Ultrafast dynamics of excitons and charge carriers in colloidal perovskite nanostructures studied by time-resolved optical spectroscopies

Carolina Villamil Franco

Thèse de doctorat

NNT : 2020UPASF012

université PARIS-SACLAY

Ultrafast dynamics of excitons and charge carriers in colloidal perovskite nanostructures studied by time-resolved optical spectroscopies

Thèse de doctorat de l'université Paris-Saclay

École doctorale n° 571, Sciences chimiques : molécules, matériaux, instrumentation et biosystèmes (2MIB)
Spécialité de doctorat: Chimie
Unité de recherche : Université Paris-Saclay, CEA, CNRS, LIDYL, 91191, Gif-sur-Yvette, France.
Référent : Faculté des sciences d'Orsay

Thèse présentée et soutenue à Saclay, le 30/09/2020, par

Carolina VILLAMIL FRANCO

Composition du Jury

Emmanuelle DELEPORTE Professeure des Universités, ENS Paris-Saclay (LUMIN), Orsay, France	Présidente du jury
Ferdinand GROZEMA Professeur, Delft University of Technology, Delf, The Netherlands	Rapporteur & examinateur
Dmitry ALDAKOV Chargé de recherche CNRS (HDR), CEA Grenoble (SyMMES/STEP), France	Rapporteur & examinateur
Benoit MAHLER Chargé de recherche CNRS, Université Claude Bernard Lyon (ILM), Villeurbanne, France	Examinateur
Thomas GUSTAVSSON Directeur de recherche CNRS, CEA Saclay (LIDYL), Gif-sur-Yvette, France	Directeur de thèse
Elsa CASSETTE Chargée de recherche CNRS, CEA Saclay (LIDYL), Gif-sur-Yvette, France	Co-encadrante & Examinatrice

To the memory of my father

– to whom I dedicate this dissertation,

you encouraged me to pursue my dreams and be myself before you left this world.

See you on the other side!

ACKNOWLEDGMENTS

I would like to express my deepest and sincerest gratitude to my supervisor, Dr. Elsa Cassette for her invaluable guidance and continuous support through this journey. Without her patient instruction, knowledge and enthusiasm, I could not have finished this manuscript on time. My truthful acknowledgments also go to my thesis director Dr. Thomas Gustavsson for his supervision, critical reading of the manuscript and remarks during the past years. Both of you dedicated considerable amount of time during our discussions which contribute to my professional growth as scientist.

I would like to thank my reporters: Ferdinand Grozema and Dmitry Aldakov for their insightful reports and questions. Also, the examinators: Emmanuelle Deleporte and Benoît Mahler for reading this manuscript. Finally, I would like to thank our collaborators: Christian Cornaggia, for his interesting talks effort to have the laser in optimal conditions, as well, Benoît for the discussions on the perovskite nanoplatelets stabilization and characterization. I want to give special thanks to the other members of DICO lab (Gerard, Stephane, Caroline, Dimitra, Akoz, Roberto, Sandrine) not only for the academical discussions, assistance in the administrative duties and enriching talks about French culture but also for your kindness. For sure, it was a pleasure to share the lunch time with all of you. Thank you very much to the graduated students and postdocs (Lara, Behnaz, Valentin, Vangelis, Houda, Jean Michel, Gina) for sharing their experiences and valuable advices.

I cannot forget my *toxic* homeless friends (Aninda, Rafa, Ben, Sandra, Kamila, Simona, Vir, Fer, Albertito, Dyvia, Livya, Oscar, Malik, Sofi, Lomello, Alex) for all the fun and adventures we had together. Also, my *serious* tennis friends who know well how to release our PhD stress (Shatha, Roberto, Sven, Dominic, Ahmed, Thomas, Hector) you were like

a light/fire/heater in the middle of a dark forest, cold mountains and tennis courts during winter. Finally, to my friends de la U (Rubencho, Paula, Tefa, Vicky, Steven, Jairo, Diego, …) to resist my madness even without knowing what I was doing in Paris. My cousins (Maleja, Diana Paola, Juanda, Christian, Sebas, Samuel, …) and all my family members for your support through all my life, I hope one day to be an inspiration of persevering as you have been for me every day. Finally, 50% of the credit goes to my mother and sister to keep my motivation, confidence and focus during this time. You both are my strength; in spite of our recent losses you have showed me that together we can always find a way to continue regardless of adversities. I won't give up just because you are with me.

ABSTRACT

Halide perovskites have emerged as very promising photoactive materials due to their outstanding optoelectronic properties combined with low-cost processability. In spite of their successful implementation in photovoltaic or light-emitting devices, a deep understanding of the dynamics of relaxation and recombination is still missing in order to enhance the device performances. For instance, the single junction solar cells with power conversion efficiencies beyond the Shockley Queisser limit (~ 33%).

This thesis focuses on the study of two major fundamental processes occurring in colloidal halide perovskite nanostructures: the hot charge carrier/exciton relaxation ("cooling"), after excitation above the optical bandgap, and the non-radiative Auger recombination, taking place after high-fluence or high-photon energy excitation. In particular, time-resolved photoluminescence and femtosecond transient absorption spectroscopy were used to investigate the confinement and composition effects in strongly confined two-dimensional (2D) lead iodide perovskite nanoplatelets (NPLs), those were synthesized following the development and optimizations of colloidal methods such as hot injection and ligand assisted reprecipitation (LARP).

For the investigation of the cooling dynamics, a global analysis method based on single value decomposition was used, where the temporal evolution of the spectral lineshapes was modeled with a sequential kinetic scheme. This method was successfully applied to effectively describe the continuous energy relaxation in weakly-confined thick $FAPbI_3$ nanoplates (FA=formamidinium) and allowed disentangling the hot phonon bottleneck from the Auger reheating effects at high excitation fluence. Furthermore, the global analysis was essential to investigate the cooling dynamics in strongly confined 2D NPLs presenting large Stark effects and discrete excitonic band-edge transition far away from

the continuum of states (exciton binding energy in several hundreds of meV). As in the weakly confined samples, the cooling rate of the NPLs decreases with the excitation fluence. However, it is faster in more-strongly confined samples, evidencing the absence of an intrinsic phonon bottleneck. Furthermore, the cooling rate and its evolution with the exciton density were found independent of the nature of the internal cations (FA, MA=methylammonium and Cs=cesium). However, when comparing with the rate measured in 2D layered perovskite thin film with equivalent quantum well thickness, the results strongly suggest a role of the surface ligands in the possibility to release the excess energy to the surrounding environment. This suggest that the ligand-mediated relaxation mechanism previously proposed for the exciton relaxation in other colloidal systems can be dominant in the thinner NPL samples with enhanced exciton/ligand vibrational mode coupling.

Then, the multiple exciton recombination dominated by non-radiative Auger recombination (AR) was studied in the strongly-confined 2D perovskite NPLs. Due to the large asymmetric geometry and the limited exciton wavefunction delocalization, the AR rate strongly depends on the exciton density via the initial average inter-exciton distance. At low fluence, this distance is in several tens of nanometers such as the AR is limited by the exciton diffusion in the 2D plane. It thus occurs on a timescale of several hundreds of picoseconds and depends on the sample dimensionality (thickness and lateral sizes). In contrast, high excitation fluences produce “overlapping” excitons with inter-exciton distances of only a few times the exciton Bohr radius, resulting in AR times of less than 10 ps and independent of the NPL composition nor geometry. Finally, the exciton population dynamics of 2D NPLs after excitation in the ultraviolet was measured. The strong dependence of the AR with the inter-exciton distance allows the identification of multiple exciton generation (MEG), which involves the reaction of “geminate biexcitons” produced by the absorption of a single high-energy photon.

Résumé en français

Les matériaux semiconducteurs de pérovskite halogénée se sont révélés très prometteurs en raison de leurs propriétés exceptionnelles et de leur capacité d'élaboration à faible coût. Malgré les progrès réalisés, une meilleure compréhension des dynamiques de relaxation et de recombinaison dans ces matériaux photo-actifs est nécessaire afin d'améliorer les performances des dispositifs opto-électroniques. Par exemple dans les cellules solaires à simple jonction avec un performance de conversion d'énergie supérieure à la limite théorique Shockley Queisser (~33%).

Cette thèse porte sur la relaxation des porteurs de charge/excitons « chauds » après excitation au-dessus de la bande interdite, et la recombinaison Auger advenant après une excitation de forte puissance ou à haute énergie. La spectroscopie de fluorescence résolue en temps et d'absorption transitoire (AT) femtoseconde sont utilisées afin d'étudier les effets du confinement et de la composition sur ces processus, en particulier dans les nanoplaquettes (NPLs) colloïdales de pérovskite bidimensionnelles (2D), dont la synthèse a été développée et optimisée au préalable. Les méthodes utilisées ici sont communément reconnues comme: injection à chaud et re-précipitation assistée par ligand (LARP).

Les dynamiques de relaxation ont été étudiées par AT en utilisant une méthode d'analyse globale où l'évolution temporelle des différentes compositions spectrales est modélisée suivant une cinétique de réactions séquentielles. Cette méthode a pu être appliquée afin de décrire efficacement la relaxation progressive dans les nanostructures de $FAPbI_3$ (FA= formamidinium) faiblement confinées, et a permis de dissocier les processus de retardement de relaxation à haute puissance d'excitation dus aux effets de « hot phonon bottleneck » et de ré-excitation par recombinaison Auger (RA). Par ailleurs, l'analyse globale de l'évolution spectrale a été essentielle afin d'examiner les dynamiques de

relaxation dans les NPLs 2D à fort confinement quantique et diélectrique, présentant des effets Stark importants et une transition de bord de bande excitonique discrète. Comme dans les systèmes faiblement confinés, le taux de relaxation dans les NPLs diminue avec la puissance d'excitation. Cependant, il est plus rapide dans les systèmes présentant un confinement plus important, mettant alors en évidence l'absence de ”phonon bottleneck” intrinsèque. La nature des cations internes (FA, MA=méthylammonium ou Cs) n’influe pas ce taux, ni son evolution en puissance. Toutefois, les mesures dans les films de pérovskite 2D présentant une épaisseur de puits quantique équivalente, suggèrent un rôle des ligands de surface dans la capacité à libérer l'excès d'énergie dans l'environnement. Ce mécanisme de relaxation à médiation par ligand proposé précédemment pour la relaxation de l'exciton dans d'autres systèmes colloïdaux peut être dominant dans les échantillons NPL plus minces avec un couplage de mode vibrationnel exciton / ligand.

Ensuite, les recombinaisons multi-excitoniques dominées par la RA non radiative ont été étudiées dans les NPLs de pérovskite 2D fortement confinées. Dû à la géométrie asymétrique de ces nanostructures et de la délocalisation limitée de l'exciton, le temps de RA dépend fortement de la densité d'excitons via la distance inter-exciton moyenne : A faible puissance d’excitation, la RA est limitée par la diffusion de l'exciton dans le plan 2D et se produit sur plusieurs centaines de picosecondes (dépendant ainsi de la géométrie de l'échantillon). En revanche, une puissance d'excitation élevée produit des excitons dont les fonctions d’onde se recouvrent spatialement, entraînant des temps de RA inférieurs à 10 ps. Finalement, les dynamiques excitoniques dans les NPLs 2D ont été mesurées par AT après excitation dans l’ultraviolet afin d'observer le processus de multiplication d’excitons. Ce dernier implique la génération de plusieurs excitons “géminés”, et donc proches spatialement, suite à l'absorption d'un unique photon de haute énergie.

CONTENTS

INTRODUCTION

Metal halide perovskite materials have attracted an enormous scientific interest in recent years. The optical and electronic properties such as high optical absorption coefficient, large defect tolerance, long diffusion lengths combined with low-cost and solution processability, contribute to their successful implementation in several photonic devices [1–5].

Over the last 10 years, solar cells based on bulk perovskite materials have turned out to be the technology with the most remarkable improvement among all emerging photovoltaics technologies (see **Figure 0.1**). For instance, technologies based on organic materials have been the subject of intense research for much longer time without attaining the comparable efficiencies. For example, dye-sensitized solar cells (DSSC) were introduced about 30 years ago, but the highest power conversion efficiency (PCE) is still limited to about 12 % and organic photovoltaics (OPVs), which emerged about 20 years ago attains 18 %. In contrast, new nanostructured semiconductors materials such as quantum dots (QDs) have almost reached a 20 % level in around 10 years. However, so far perovskite is the only material able to compete with conventional silicon technologies reaching efficiencies of about 25 %. Interestingly, perovskite/Si tandem cells show PCE values around 30 %, which is very promising.

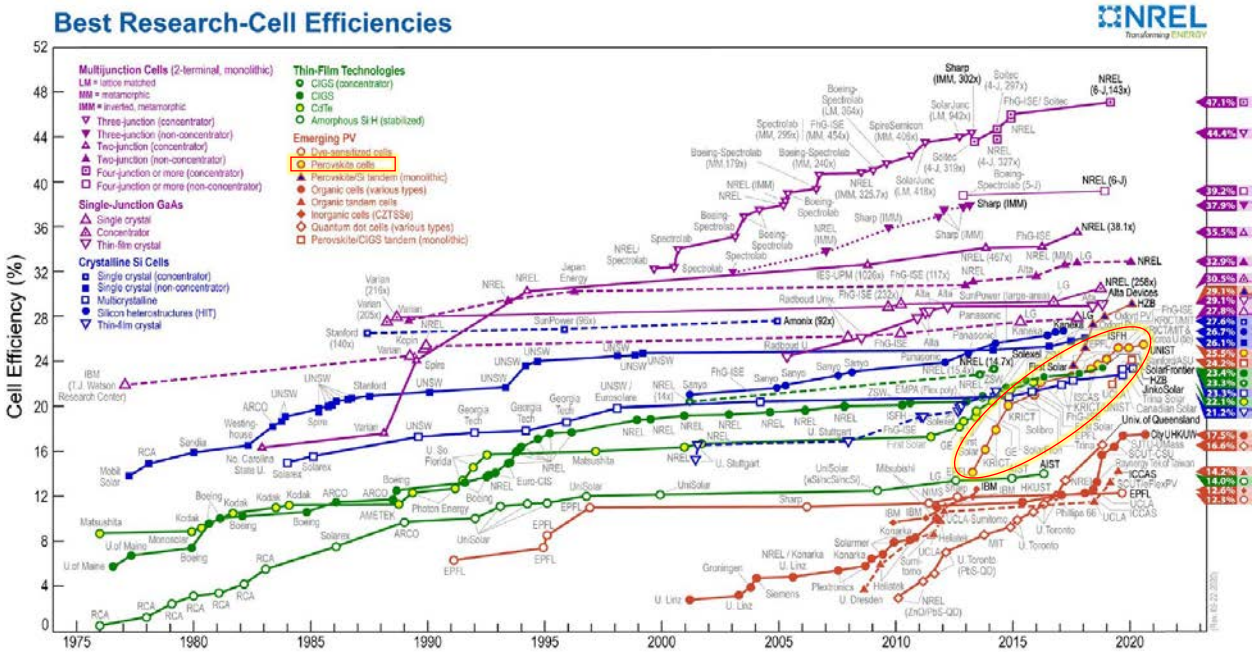

Figure 0.1. *Best research-cell efficiency chart from NREL. https://www.nrel.gov/pv/cell-efficiency.html. The performance of perovskite solar cells is highlighted.*

In spite of these outstanding performances and the many attempts to decreases the losses on the devices, there is a fundamental thermodynamic limit, which hinders single-junction solar cells to reach a power conversion efficiency (PCE) of 100 %. This limit is known as the *Shockley-Queisser (S-Q) limit* stipulating that the maximum PCE of any single junction solar cell is 33 %. This value is obtained considering charge carriers fully equilibrated with the lattice in a single active semiconductor layer where the valence and conduction bands are separated by a bandgap energy (E_g). There are two fundamental mechanisms hindering the efficient photon to current conversion that are the *transmission* and the *relaxation* losses, as shown in **Figure 0.2**. Simply speaking, for the optimize bandgap material, only one third of the absorbed sunlight photons generate charge carriers, 18 % of the photons pass right through the solar cell (not absorbed) and 47 % of the photons turn into heat (http://solarcellcentral.com/limits_page.html).

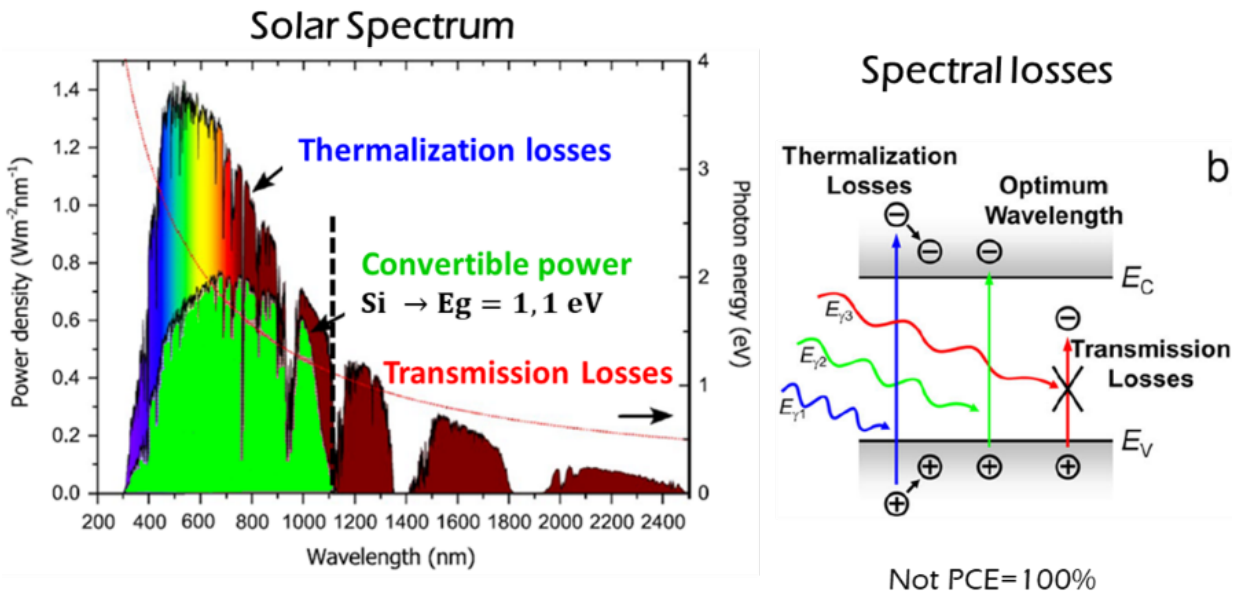

Figure 0.2. *Main principal sources of losses for a silicon semiconductor (bandgap 1.1 eV) through the solar spectrum (top line). Considering the Shockley-Queisser limit for single-junction solar cells. The thermalization (i.e. relaxation here) represents the largest loss, and increases for the high-energy region of the solar spectrum. Adapted from https://spie.org/news/4146-multiple-exciton-generation-in-a-quantum-dot-solar-cell?SSO=1*

The *transmission losses* are due to the fixed character of E_g: all photons with an energy below this value are not absorbed by the material. The *relaxation losses* are due to the fact that photons with an energy above E_g create a hot charge carrier population susceptible to release its excess energy as heat (smaller voltage reached). This process occurring in only a few hundreds of femtoseconds is also known as *cooling*. The timescale of this undesired ultrafast process is usually at least one order of magnitude faster than the typical carrier extraction times (on the picosecond time range). The ultimate PCE limit could be increased from about 33 % to about 66 % if the hot charge carriers could be extracted before losing their excess energy as heat [7].

Another consideration of the S-Q limit calculation is that one photon can produce just a single electron-hole pair. Considering that sun light also contains high-energy photons that can be several times E_g of the semiconductor material, it is in principle possible to

generate several electron-hole pairs from one high-energy photon. This process is known as *carrier multiplication* (CM). In this case, the PCE could be increased to 44 % (still assuming that rapid relaxation losses occur).In order to explore non-conventional approaches to overcome the Shockley-Queisser limit, nanoparticles have been proposed as candidates to enhance both the collection of high-energy (hot) charge carriers and to increase the current by CM. The major reason is that in nanostructures the quantum confinement increases radically the spacing between the electronic levels and thereby is expected to slow down the cooling rate (bottleneck effect, discussed in Chapter 3). Moreover, carrier multiplication is also increased in nanostructures due to the enhanced Coulomb interactions and the relaxation of the momentum conservation.

Alternatively, the colloidal nanostructures of lead halide perovskites also represent a promising material for light emitting devices such as LEDs or lasers, due to their high luminescence quantum yield and tunable narrow-band emission. In addition, the fact that the electron-hole pairs are more strongly bound to form excitons in nanoparticles helps the radiative recombination. However, non-radiative pathways such as multiexciton *Auger recombination* at high exciton density are also enhanced in small nanoparticles where the interactions between excitons are more pronounced. In such a case, the energy liberated from the exciton recombination process is transferred to an extra carrier, decreasing the efficiency in light emitting devices such as LEDs and lasers. In spite of this, the Auger recombination process has been poorly studied in colloidal perovskite systems with different morphology and dimensions. Particularly, strong confined perovskite materials such 2D nanoplateles.

Aim of research

The aim of the present thesis is to study the effects of the quantum confinement and the chemical composition on the ultrafast non-radiative processes occurring in colloidal perovskite nanostructures relevant for photonic devices such as nanostructured solar

cells, LEDs, lasers and photo-detectors. Charge carrier cooling, Auger recombination and multiple exciton generation depend on the initial charge carrier density as well as the excitation photon energy. Consequently, we investigate the ultrafast dynamics of these systems under different excitation conditions using time-resolved optical spectroscopy techniques such as time-resolved photoluminescence and femtosecond transient absorption.

Thesis outline

The thesis is organized in 4 chapters as follow:

Chapter 1: This chapter introduces the fundamental concepts necessary to the understanding of this thesis. We first describe in detail the halide perovskite materials. We discuss the relation between structure and function with a special emphasis on the origin of their unique optical properties. More precisely, we discuss the effects of quantum confinement on the electronic structure and the optical properties. Secondly, we discuss the different dynamical processes occurring in confined semiconductor systems in general. A special attention is given to the *charge carrier cooling*, *Auger recombination* and *multiple exciton generation* process and how these are modulated by the dimensionality of the nanostructures.

Chapter 2: A detailed description of the experimental methods, the spectroscopic techniques and synthetic protocol employed in this thesis, is given. A femtosecond transient absorption setup was specifically constructed and adapted for the experimental studies of this thesis. In addition, a conventional time-resolved photoluminescence technique was used in order to obtain complementary information. We then describe the

synthesis and the characterization of the perovskite nanostructures studied here. A particular attention is given to control their morphology and chemical constitution.

Chapter 3: In this chapter, we study the hot charge carrier/exciton relaxation to the band-edge (*i.e.* cooling) in weakly- and strongly confined perovskite nanostructures. In large $FAPbI_3$ nanocrystals in which the main species are free charge carriers, the cooling dynamics can be extracted by the conventional high-energy tail-fitting method. For the strongly confined 2D perovskite nanoplatelets, in which the main species are excitons, this approach fails due to discretization of the states. We propose an alternative and systematic method, based on the global data analysis and lineshape spectral analysis, to extract the full cooling dynamics. We investigate the effect of the excitation fluence and confinement effects and discuss the absence of an "intrinsic" phonon bottleneck in these strongly confined nanoplatelet systems.

Chapter 4: In this chapter, we study the non-radiative multiexcitonic Auger recombination process in strongly confined 2D nanoplatelets of different chemical compositions and thicknesses. We highlight the deviation from the expected bimolecular recombination and the effects of exciton diffusion on the timescale of the Auger recombination for moderate excitation fluence generating excitons spaced by tens of nanometers. Finally, we present strong indications for multiple exciton generation ocurring in the 2D nanoplatelets when excited with high photon energy and discuss the energy threshold found in the UV region.

REFERENCES

[1] Y. Fu, H. Zhu, J. Chen, M.P. Hautzinger, X.Y. Zhu, S. Jin, Metal halide perovskite nanostructures for optoelectronic applications and the study of physical properties,

Nat. Rev. Mater. 4 (2019) 169–188. https://doi.org/10.1038/s41578-019-0080-9.

[2] S. Adjokatse, H.H. Fang, M.A. Loi, Broadly tunable metal halide perovskites for solid-state light-emission applications, Mater. Today. 20 (2017) 413–424. https://doi.org/10.1016/j.mattod.2017.03.021.

[3] W. Zhang, G.E. Eperon, H.J. Snaith, Metal halide perovskites for energy applications, Nat. Energy. 1 (2016) 1–8. https://doi.org/10.1038/nenergy.2016.48.

[4] B.R. Sutherland, E.H. Sargent, Perovskite photonic sources, Nat. Photonics. 10 (2016) 295–302. https://doi.org/10.1038/nphoton.2016.62.

[5] L. Protesescu, S. Yakunin, S. Kumar, J. Bär, F. Bertolotti, N. Masciocchi, A. Guagliardi, M. Grotevent, I. Shorubalko, M.I. Bodnarchuk, C.-J.J. Shih, M. V. Kovalenko, No Title, ACS Nano. 11 (2017) 3119–3134. https://doi.org/10.1021/acsnano.7b00116.

[6] M.C. Beard, Multiple Exciton Generation in Semiconductor Quantum Dots, J. Phys. Chem. Lett. 2 (2011) 1282–1288. https://doi.org/10.1021/jz200166y.

[7] A.J. Nozik, Spectroscopy and hot electron relaxation dynamics in semiconductor quantum wells and quantum dots, Annu. Rev. Phys. Chem. 52 (2001) 193–231. https://doi.org/10.1146/annurev.physchem.52.1.193.

1. FUNDAMENTAL CONCEPTS

This chapter is divided in two parts. The first part introduces the crystalline structure, composition and dimensionality of the halide perovskite materials and its relation with electronic and optical properties. The different morphologies available of this semiconductor material are stablished to explain concepts such as the quantum confinement effects and the presence of charge carriers and/or excitons in the low dimensional perovskite nanostructures studied here: the weakly confined colloidal perovskite nanoparticles (quasi-3D nanocrystals) and the strongly confined 2D colloidal perovskite nanoplatelets.

The second part deals with the main ultrafast processes taking place in colloidal semiconductor nanostructures after photo-excitation. Initially, the hot exciton/charge carrier relaxation ("cooling") at high-energy photon excitation occurring in the order of hundreds of femtoseconds. Then, the non-radiative charge carrier/multiexciton recombination (Auger recombination) arising at high-density excitation is discussed. Likewise, the carrier multiplication or multiple exciton generation that could take place in the semiconductor nanostructures when the excitation photon energy is higher than twice the optical bandgap energy and competing directly with the exciton cooling is described. Finally, the radiative and non-radiative electron-hole pair recombination usually happening in few to tens of nanoseconds.

1.1. HALIDE PEROVSKITE MATERIALS

1.1.1. Bulk perovskites

1.1.1.1. Perovskite crystalline structure

Perovskite is a large class of materials with an ionic crystalline structure analogous to the oxide $CaTiO_3$ and represented by the chemical formula ABX_3, where A and B are two different cations and X, an anion. Among them, halide perovskites with the X positions occupied by halide anions such as chloride (Cl^-), bromide (Br^-) and iodide (I^-) and where B^{2+} is a divalent transition metal as lead (Pb^{2+}) or tin (Sn^{2+}), have recently emerged as promising photoactive materials for various optoelectronic applications. In this case, the structure consists in the arrangement of corner-sharing $[BX_6]^{4-}$ octahedron, with a monovalent A^+ cation located in the space formed in the center of the 8 octahedra, as depicted in **Figure 1.1.**

The nature of the A^+ cations that can fit into this cavity is limited by the Goldschmidt's tolerance factor to conserve the structural stability [1]. In the case of fully inorganic perovskite, A^+ corresponds to an atomic cation, usually cesium (Cs^+), while in the case of hybrid organic-inorganic perovskite, the small organic cations can be methylammoniums ($CH_3NH_3^+$, or MA^+) or formamidiniums ($CH(NH_2)_2^+$, or FA^+). Halide perovskites structure usually deviate from the ideal cubic phase and present several polyforms depending on the temperature and composition. For example, in the well-known $MAPbI_3$ perovskite, as the temperature decreases, the octahedral lattice framework is distorted, which results in the change of the crystallographic structure from cubic at high temperature ($T > 327$ K), to tetragonal at room temperature, then to orthorhombic at low temperature ($T < 162$ K) [2]. The defined phase transitions for the different perovskite compositions are well-described in several recent reviews [1,3,4] .

The ionic character of the lattice allows a high crystallinity of the perovskite materials at room- or fairly low temperatures. This enables processing on a range of substrates with different morphologies such as single- or poly-crystalline thin films, the growth of macroscopic single crystals, or the synthesis of colloidal nanocrystals dispersed in an non-polar organic solvent. However, the ionic character of the perovskite structure also causes a high chemical instability to moisture, air exposure, light and temperature [4].

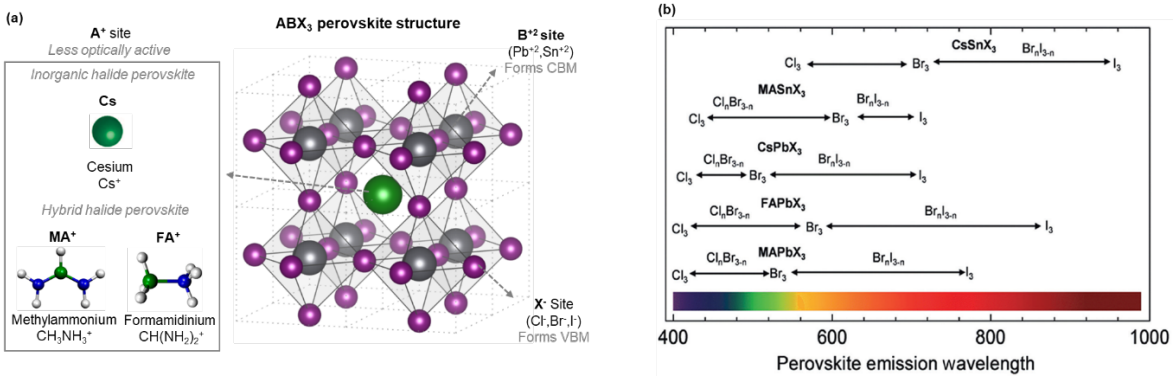

Figure 1.1. (a) *Schematics of the halide ABX_3 perovskite crystal structure adapted from reference [5].* ***(b)*** *Tunability of the halide perovskite emission peak with their chemical composition, reproduced from reference [4].*

1.1.1.2. Properties of 3D (bulk) lead halide perovskites

Electronic and optical properties

Halide perovskite materials are direct band-gap semiconductors with a high linear absorption coefficient[1] ($\approx 10^5$ cm^{-1} in their optimum energy range). The band structure of lead halide perovskites has been calculated by Even and co., including the spin-orbit coupling [6]. The conduction band minimum (CBM) is mainly composed by the p-orbitals of Pb and valence band maximum (VBM) by the p-orbitals of the halide [7,8]. Thus, the halide composition strongly affects the bandgap energy, while the nature of the A^+ cations

[1] The linear absorption coefficient μ_{lin} (cm^{-1}) in perovskite nanocrystals is comparable or larger than classical inorganic semiconductor materials. While, this μ_{lin} value is also comparable in organic semiconductor material, the absorption cross section σ_{abs} (cm^2) in perovskite materials is orders of magnitude larger.

contributes in much less proportion, indirectly *via* the distortion of the crystalline lattice [9]. For instance, changing the halide from $MAPbI_3$ to $MAPbBr_3$ notably shifts the absorption onsets from 800 nm to 570 nm and vice-versa. Replacing the MA^+ cations in $MAPbI_3$ perovskite with Cs^+, which is smaller in size, increases the wavelength corresponding to the bandgap from 700 to 716 nm, while the replacement with the slightly larger FA^+ cations decreases the bandgap to 838 nm. Additionally, the possibility to have different halides within the structure in the called "*mixed halide perovskite"* gives to this material a continuous bandgap tunability [10]. The effect of the nature of the cation and the metal on the optical properties of the halide perovskites is shown in **Figure 1.1b,** where it can be seen that the emission ranges from the deep blue to the infrared**.** This thesis focuses on the iodide-based perovskites which presents the lowest bandgap energy, in order to access various energy excitations. In spite of the fact, that perovskite nanostructures present an increased bandgap due to the quantum and dielectric confinement (see sub-sections **1.2.1** and **1.2.3**).

Free charge carriers as the main excited species

Upon the absorption of a photon with an energy at least equal to the bandgap, an electron from the valence band is promoted to the conduction band, leaving behind an effective particle with positive charge, a hole. Thus, an electron-hole (e-h) pair is created within the semiconductor. When the two charge carriers are bound by the Coulombic interaction, this bound e-h pair is considered as a quasi-particle known as an *exciton*. There two parameters to characterize an exciton: the energy needed to dissociate it into free charge carriers (free electron and hole), called the *exciton biding energy* (E_b) and the distance between the two charge carriers, known as the *exciton Bohr radius* (a_B).

The exciton binding energy is an intrinsic property of the material, which depends on its composition and dimensionality. The precise determination of E_b in halide perovskites is

still debated due to the indirect methods used to estimate it, such as the temperature-dependent photoluminescence, optical and magneto-absorption spectroscopy [11]. However, it is now commonly accepted that E_b is small in bulk lead halide perovskite materials, ranging from several to few tens of milli-electron volts (meV). As a result, the exciton rapidly dissociates into free charge carriers (electron and hole) at room temperature (RT), where E_b is smaller than the thermal fluctuation energy ($k_BT \sim 25$ meV) [12]. This is particularly true when decreasing the perovskite bandgap energy, for example from chlorine to iodine. The low E_b in perovskite bulk semiconductors is one of the reasons for the good electric conductivity of the material and its remarkable charge transport properties. This facilitates notably the charge carrier collection, which is highly desired for photovoltaic devices.

1.1.2. Confined lead halide perovskites

1.1.2.1. Quantum confinement

A system can be considered to be quantum-confined when the electronic and optical properties become size dependent on the microscopic level. This happens when at least one dimension of the material becomes comparable or lower than the exciton Bohr radius (a_B), which is typically in the nanometer range.

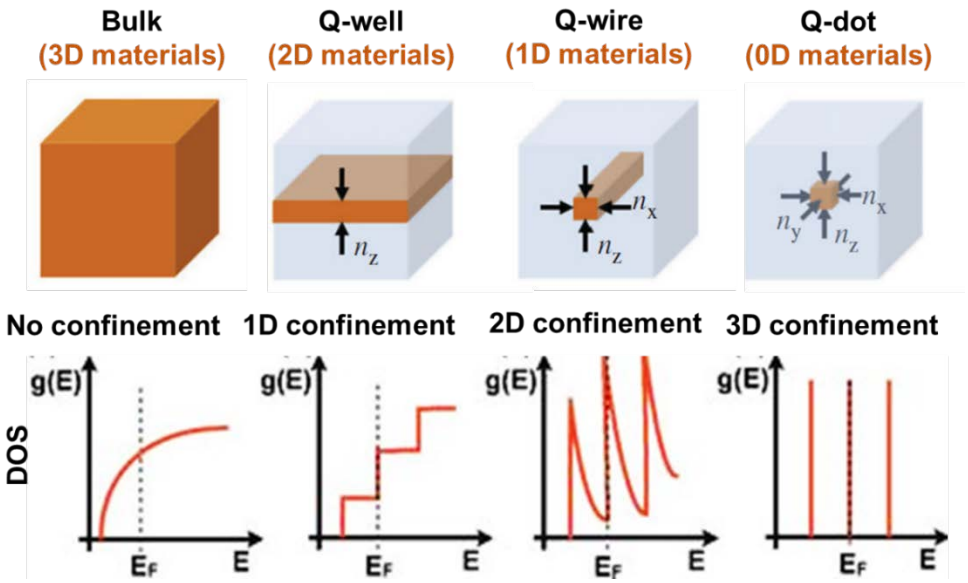

Figure 1.2. *Effect of the quantum confinement on the electronic density of states g(E) for different dimensionalities, from 3D to 0D systems. Adapted from [13].*

System dimensionality and density of states

The dimensionality of a system can be defined as a function of the degree of confinement, as shown in the **Figure 1.2.** In non-confined systems, such as three-dimensional (3D) materials, the charge carriers are free to move in all three directions. When only one of the three dimensions of the system is reduced, the charge carriers are confined in one dimension and free to move in the two others. The resulting 2D materials can then be seen as quantum wells (QWs). For 1D materials such as quantum wires (NWs) or nanorods (NRs), the charge carriers are now confined in two dimensions of space. Finally, we talk about "zero-dimensional" (0D) materials when all the three dimensions of space are confined and result in quantum dots (QDs). All *low-dimensional* materials, referred to nanostructures in this thesis, present major differences compared to bulk materials in terms of the electronic density of states, but also the bandgap energy (E_g) as well as excitonic effects (see next part).

The confinement induces a drastic change in the electronic density of states (DOS) of the electron and hole and thus of the joint DOS, that becomes highly dependent on the system dimensionality (**Figure 1.2**). From a continuous distribution that varies with the square-root of the energy E close to the bandgap in a 3D bulk semiconductor, the DOS has a step-like dependency for 2D materials and becomes discrete, with well-separated quantized energy levels near the band edges states, in 0D materials. That is why this latter system is often called "artificial atoms". These strong differences in the (joint) DOS function will directly modify the shape of the absorption spectrum of the materials. However, we should note that for semiconductor materials with continuous density of states such as 3D and 2D materials, extra discrete transitions will superpose to the continuum spectrum due to excitonic effects (see below).

Evolution of the bandgap energy with the size

Besides the drastic change of the density of states, quantum confinement induces an increase of the electronic bandgap. Solving the Schrodinger equation within the effective mass approximation for a 0D system where the exciton is confined in a spherical potential with a radius (R) leads to quantified wavefunction for the electron and the hole and quantified levels with an energy gap proportional to $1/R^2$ [14]. Thus, the electronic bandgap of a material of a given composition increases with decreasing size, as illustrated in **Figure 1.3** For 1D and 2D systems, the same trend is observed and can be calculated by taking into account the size over the confined dimension (*e.g.* NR radius or QW thickness) [14]. On the other hand, the increase of the electron-hole Coulombic interaction with decreasing size reduces the bandgap energy (see below), but only proportionally to $1/R$ with the result that the effective bandgap still undergoes a net increase when the material size along the confined dimension is reduced.

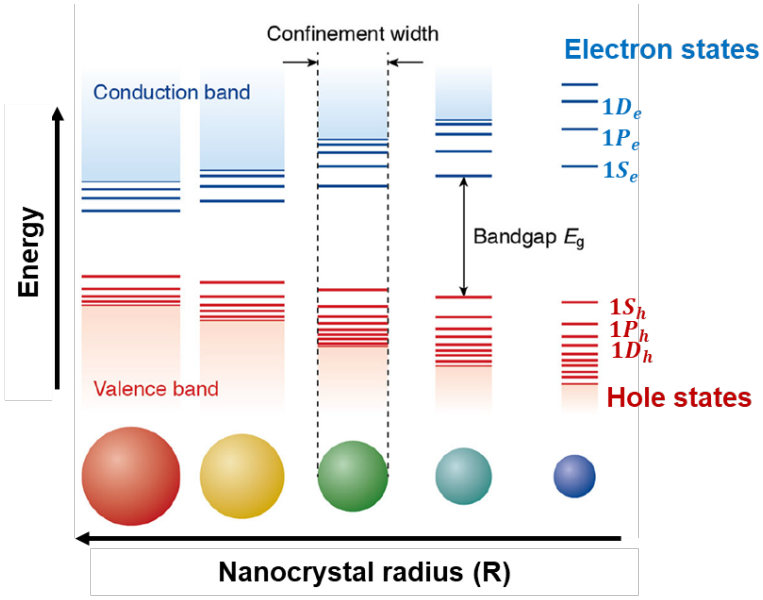

Figure 1.3. Schematic representation of the quantum confinement effects in 0D quantum dots of size R: the bandgap energy E_g of the semiconductor nanocrystal increases with decreasing size, while discrete energy levels arise at the band-edges.

Excitonic properties

Another effect of the quantum confinement is the increase of the exciton binding energy. If E_b becomes large enough, the thermal energy can no longer dissociate the exciton into free carriers and discrete excitonic resonances can be observed even at room temperature in the absorption spectrum. Due to the attractive e-h Coulomb interaction, the energy of the excitonic transition is typically lower than the electronic bandgap E_g. This implies that the structure can absorb a photon with an energy smaller than E_g. We thus talk about the *optical bandgap*. For nanostructures of dimensionality $D \geq 1$ and presenting a strong confinement (the different regimes are introduced in the confined perovskite sub-section), the discrete excitonic transitions are easily identifiable in the absorption spectrum from the (quasi)continuum of states. This is particularly true for the 2D colloidal nanoplatelets studied here (see **sub-section 1.2.3**).

Two general types of excitons exist: the Wannier-Mott excitons and the Frenkel excitons. Wannier-Mott excitons are present in semiconductors with relatively large dielectric constant, which results typically in a reduced Coulomb attraction between the electron and the hole due to the screening induced by the surrounding ions. Consequently, the exciton radius extends over several crystal lattice unit cells. In contrast, Frenkel excitons have much stronger Coulomb interactions and are present in insulators and molecular crystals. They are spatially limited to the inter-atomic distance (tightly bound excitons). The difference between Frenkel and Wannier-Mott excitons is illustrated in **Figure 1.4**. In this thesis, we only refer to Wannier-Mott excitons in the perovskite nanostructures we studied.

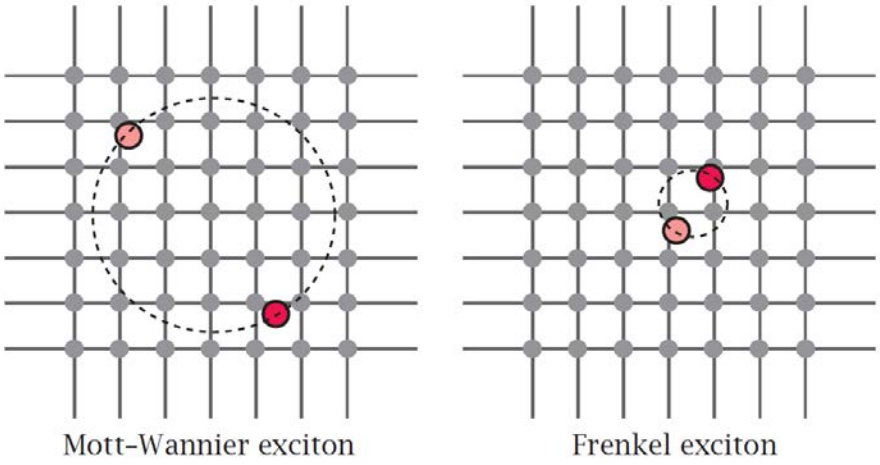

Figure 1.4. *Schematics of the extend of exciton radius for the two types of excitons, Wannier-Mott (left) and Frenkel (right) [14].*

Here, it is important to note that the exciton delocalization length within the nanostructure is related to the extent of the exciton wavefunction and not to the exciton Bohr radius, which is the electron-hole distance within the quasiparticle.

1.1.2.2. Perovskite colloidal nanocrystals: from 3D to 0D materials

Synthetic methodologies

A colloidal semiconductor nanocrystal (NC) consists of a semiconductor core with nanometer size that is coated with a stabilizing layer of (usually organic) ligand molecules. These NCs are very versatile nanomaterials that combine size-, shape-, and composition-dependent optoelectronic properties. Since the first studies of the optoelectronic properties of colloidal NCs constituted by traditional semiconductors (II−VI, III−V, and IV−VI), the studies of the quantum confinement effects are still in constant evolution with the development of more complex hetero-structures and low-dimensional nanostructures of different materials. [4,15].

The recent synthesis of colloidal hybrid perovskite NCs by Perez-prieto *and co.* in 2014, consisting of a small core of $MAPbBr_3$ stabilized by alkylamine capping ligands such as oleylamines [16], created a bridge between the well-established colloidal NC field and the new halide perovskite materials. The first adaptation of the colloidal nanocrystal synthetic routes by Kovalenko *and co.* allowed then the obtention of $CsPbX_3$ perovskite NCs (X = Cl, Br, I) with small size dispersion and high-quality crystalline phase. Moreover, the control of the size and of the composition led to tunable bandgap energies covering the entire visible spectral region with narrow and bright photoluminescence emission (**Figure 1.5**) [17]. Since then, several developments have been made in the synthesis of colloidal perovskite nanocrystals, including hybrid $MAPbX_3$ and $FAPbX_3$ materials [18,19].

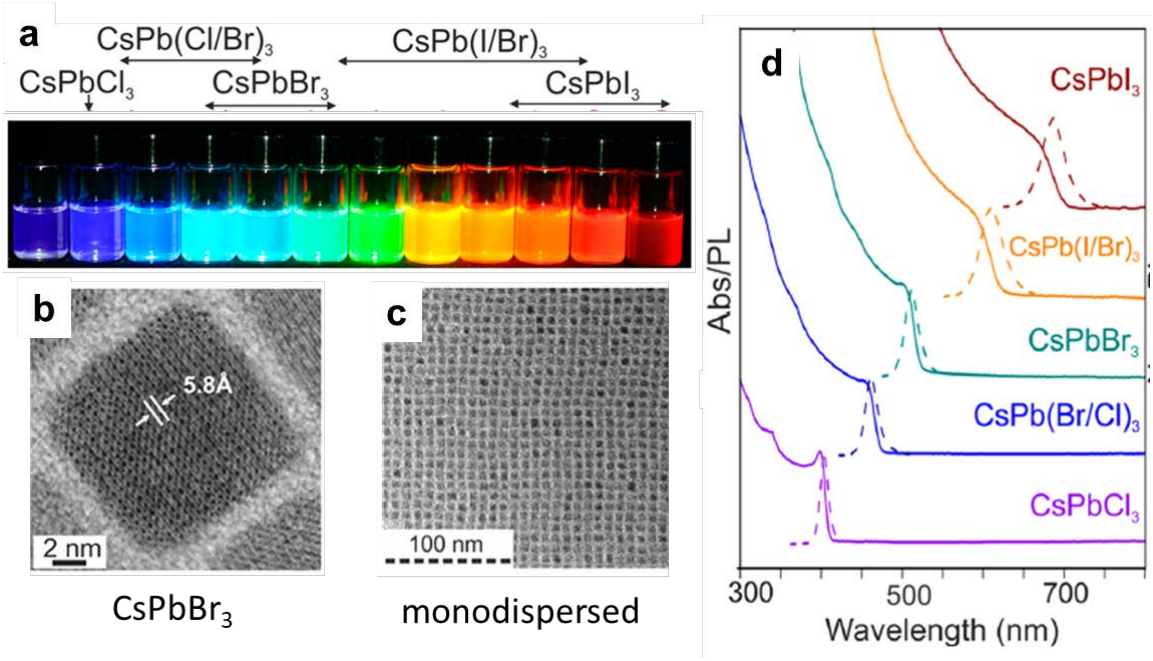

Figure 1.5. (a) *Colloidal $CsPbX_3$ NCs (X = Cl, Br, I) dispersed in toluene under UV illumination.* ***(b,c)*** *Typical transmission electron microscopy (TEM) images of the cubic-shaped $CsPbBr_3$ NCs.* ***(d)*** *Absorption (full lines) and emission (dashed lined) spectra of Cs-based NCs. Figures adapted from ref. [17].*

Degree of confinement: from weakly to more *strongly confined NCs*

Up to very recently, the size of the synthesized perovskite NCs were typically in the range of 10-20 nm, which is much larger than the exciton Bohr radius reported for bulk halide perovskites (a_B~2.5-5 nm) [20,21]. Thus, these nanostructures were only "weakly confined" and the optical properties were mostly tuned *via* the sample composition. A recent development in the synthesis of $CsPbBr_3$ NCs have allowed the control of the lateral sizes down to about 3.5 nm which is thus in the stronger quantum confined regime [22].

Optical properties of quantum-confined NCs

In spite of the high absorption cross section, the bulk perovskite materials have low photoluminescence quantum yield (PL QY), around 20 %, mainly due to their small exciton binding energy, the presence of some mobile ionic defects and low radiative recombination rate. In contrast, for perovskite NCs with sizes ranging from 5–10 nm, the colloidal suspension reaches a PL QY close to 100 % without any special surface passivation. In contrast, in order to achieve such a high PL QY value in other types of semiconductor quantum dot, such as CdSe, a complex core–shell heterostructure or surface passivation layer is required [23]. At this nanometer scale, the proportion of surface atoms *versus* those in the nanocrystal volume is very high and thus the PL QY will be strongly affected by the presence of surface defects. However, it has been calculated that the energy levels of the surface defects in perovskite nanocrystals are not located within the bandgap, making the halide perovskite defect tolerant [23,24]. Moreover, it should also be mentioned that the extent of the exciton wavefunction delocalization (center-of-mass motion) in perovskite nanocrystals is much less than in II-VI semiconductors such as CdSe, due to the more ionic character of the crystalline structure [25].

1.1.2.3. 2D layered perovskites

While layered 2D halide perovskite materials had been studied for several decades [8,26], as they regained considerable attention over the last five years following the "boom" of the 3D hybrid halide perovskites [25, 26] . In addition to their enhanced stability compared to the 3D bulk analogues, 2D nanomaterials possess a thickness of a few atomic layers that leads to unique excitonic properties. We detail below, how the 2D structure modifies the perovskite properties and explain the role of the dielectric confinement in addition to the quantum confinement previously discussed.

2D crystal structure

Thin films of two-dimensional (2D) perovskite structures are obtained when one or a few layers of the BX_6^{4-} octahedra planes are separated by large organic cations such as long chain alkylammonium ligands, that replace the small A^+ cations of the 3D ABX_3 structure following defined crystal planes (**Figure 1.6a**) [26,28,29]. For such 2D perovskite structures, the general chemical formula becomes $L_2A_{n-1}B_nX_{3n+1}$, where L is a molecular cation named here ligand to differentiate from the typical short chain A cation. Both usually have an ammonium function (NH_3^+) that participates to conserve the charge neutrality over the entire crystal structure, and n, the number of periodically ordered octahedra sheets along the direction perpendicular to the 2D structure. The most common long chain cations are the n-butylammoniums (BA^+) and 2-phenylethylammoniums (PEA^+). It is worth noting that the limit of large n corresponds to the 3D bulk perovskite, whereas $n = 1$ represents the pure 2D layered perovskites. The intermediate cases where $1<n<4$ is referred to as quasi-2D perovskites. Also, the differences of thermodynamic stability in the high-n structures become smaller, which makes it difficult to prepare pure-phase high-n structures [30]. The 2D structure confers to the material a higher stability compared to the 3D perovskites. For example, pure-phase 2D crystals can be kept under environment conditions for several days [31].

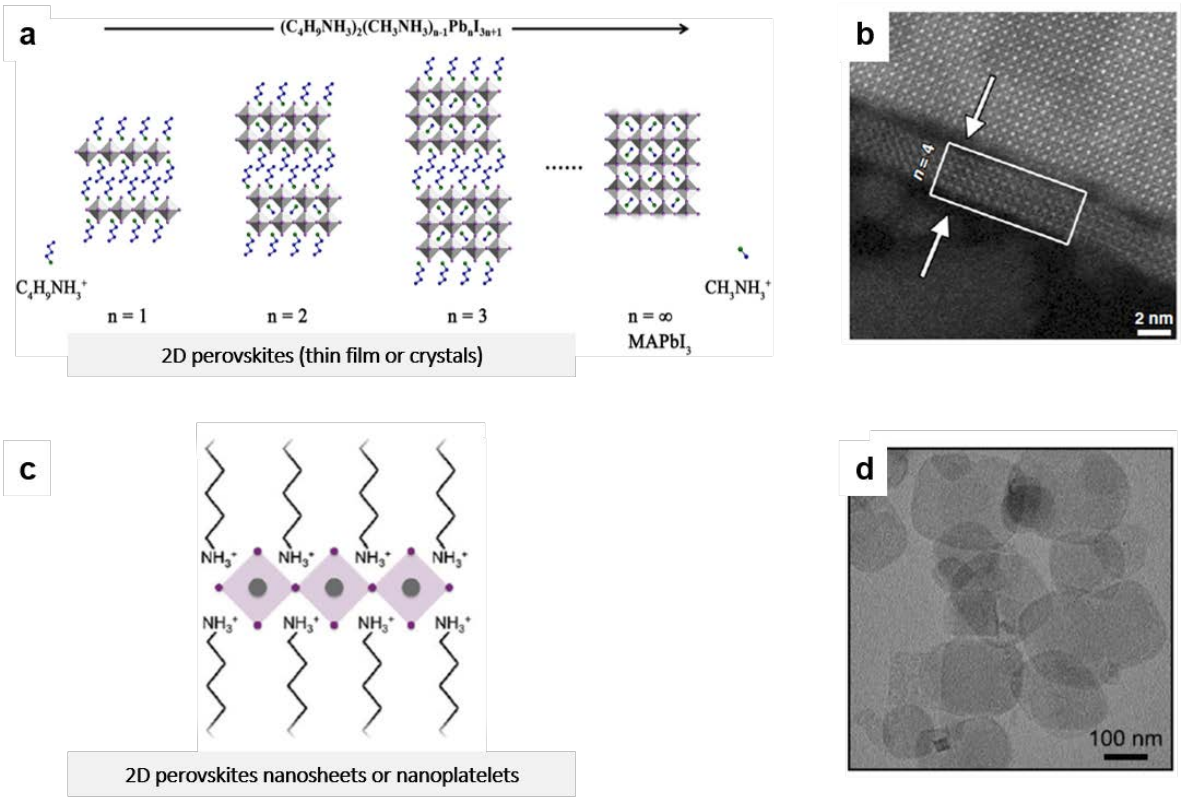

Figure 1.6. (a) *Schematics of the 2D perovskite structure (example for 2D perovskites based on methylammonium lead iodide) [32]. From left to right, the thickness increases stepwise from initially a single monolayer (n = 1) to a bulk-like value (n = +∞).* ***(b)*** *High-angle annular dark field (HAADF) scanning transmission electron microscopy (STEM) images of n=4 layered perovskite where A^+ is a mixture of MA^+ and Cs^+, B^{2+}=Pb^{2+}, X^- = Br^- and L^+ = PEA^+ [33].* ***(c)*** *Schematic representations of NPLs or single-layer nanosheet (unstacked 2D structures) in the case of 2D halide perovskite with n=1 [34].* ***(d)*** *TEM images of n = 2 $L_2[FAPbBr_3]PbBr_4$ NPLs [35].*

Single-layer perovskite nanosheets and nanoplatelets

The first reports of two-dimensional (2D) halide perovskites focused on layered perovskites thin films, grown on a substrate by solution-phase methods, where alternating stacks of organic cations surround atomically thin semiconducting sheets. In 2015, Yand *and co.* reported for the first time the direct preparation of single layer perovskite nanosheets, also grown on a substrate [36]. Unlike the 2D perovskite films, the octahedra planes in these structures are not periodically arranged but isolated by the long-chain ligands (**Figure 1.6c,d**). After this report, several groups developed ligand-assisted room temperature re-precipitation strategy for colloidal 2D perovskite nanoplatelets (NPLs), in addition to previous exfoliated methods [19,37–41]. These colloidal nanostructures are similar to the 2D nanosheets (no stacking of the different layers) but are dispersed in a solvent thanks to the ligands attached to the surface (**Figure 1.7a**). As it will be discussed in chapter II, a systematic synthetic protocol based on low cost technique where the thickness control can be reach for all composition of the colloidal perovskite NPLs and for all population of n is still missing. In this thesis I studied these 2D perovskite nanoplatelets, based on lead iodide.

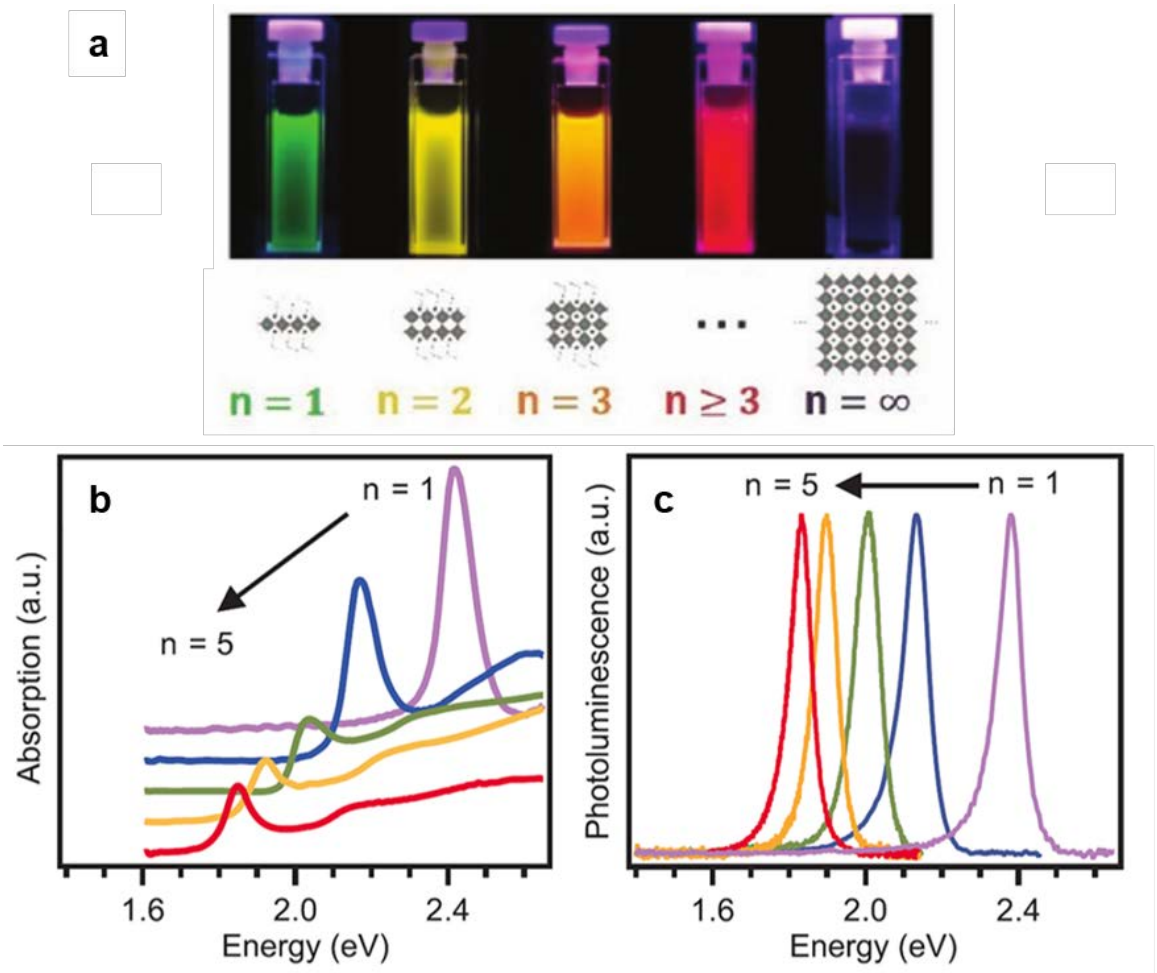

Figure 1.7. (a) *Images of cuvettes containing colloidal MAPI NPLs of different thicknesses under UV illumination [42].* ***(b)*** *Absorption and* ***(c)*** *photoluminescence* ***(****PL) spectra of* $(BA)_2(MA)_{n-1}Pb_nI_{3n+1}$ *2D layered perovskite with n varying from 1 to 5 MLs [43].*

Strong 1D quantum confinement

2D layered perovskites can be considered as quantum-well structures with semiconducting lead halide-networked sheets sandwiched between insulating organic cations. In 2D lead halide perovskite, a single monolayer of octahedral plane corresponds to a thickness of around ~0.6 nm (see for example **Figure 1.6b**). The exciton Bohr radius of halide perovskites being in the order of 2.5-5 nm [20,21], 2D and quasi-2D perovskites with $n \leq 5$ are in the strong confined regime. As a result, the corresponding bandgap energies are strongly blue-shifted compared to the bulk material and excitonic effects are

dominant close the band-edge, as it is shown in the absorption and PL spectra **Figure 1.7b,c**. At very low n, the experimentally measured exciton binding energies deviate from calculated ones based on 1D quantum confinement together with Coulombic interactions. This can be understood in term of additional *dielectric confinement* that we explain below.

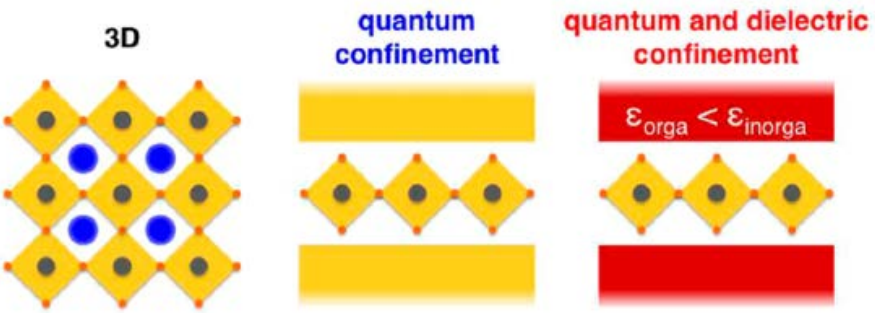

Figure 1.8. *Schematics of halide perovskites considered as a 3D material continuous dielectric constant, a 2D material with only quantum confinement, and a 2D material with both quantum and dielectric confinement [44].*

Dielectric confinement

This electrostatic effect results from the large dielectric contrast between the perovskite material with a fairly high dielectric constant ($\varepsilon_{perovskite} \approx$ 5-6) and the surrounding organic layer characterized by a lower one ($\varepsilon_{organic} \approx 2$). The proximity of the charge carriers to the organic ligands leads to the polarizability of the surface which has two major effects. First, it results in additional repulsive interactions between the charge carriers and their "virtual dielectric image" charges caused by the change of dielectric screening (mirror charges causing self-energy corrections) [28,45]. In consequence, the bandgap increases, similarly to quantum confinement, and is thus known as dielectric confinement. Secondly, the electron-hole interactions are also substantially enhanced due to the multitude interactions between each charge carrier and partner image charges [28,45]. These dielectric effects become particularly important in few nanometer-thick 2D perovskites

films and NPLs and cause notably a large increase of the exciton binding energy with decreasing layer thickness *n* (**Figure 1.8**) [46]. For example, in lead iodide perovskite the exciton binding energy in the 2D structure increases by more than an order of magnitude (*i.e.* several hundreds of meV) for $n = 1$ compared to the bulk (3D) counterpart [47]. While changing the length of the organic chain of the ligands has only a little effect on the electronic and optical properties, changing the dielectric constant of the organic cation by introducing an aromatic instead of aliphatic amines with higher dielectric constant significantly decreases the exciton binding energy in $n = 1$ 2D perovskites [47].

Properties of 2D lead halide perovskites

The most interesting optoelectronic properties of 2D perovskite materials arise from the quantum and dielectric confinement. In 2D perovskites, the electronic bandgap energy (*i.e.* the energy at which the continuum of states begins) can increase by more than 1 eV compared to the bulk materials. However, there is also a concomitant increase of the exciton binding energy, which results in strong, discrete excitonic resonances, the first one being lowered down by hundreds of meV from the continuum for low *n* (**Figure 1.7b**). Consequently, the main species at RT in 2D perovskites are excitons.

The energy of the first excitonic peak and of the corresponding emission is *quantized* according to the discrete number of monolayers ($n = 1, 2, 3, \ldots$) in the 2D layered perovskites. Indeed, the electronic and optical properties are related with the well thickness which is controlled by discrete steps and are almost independent of the lateral dimensions, as long as these latter are large enough compared to the Bohr exciton radius. The resulting emission peak is narrow, and the PL QY is high which make the 2D perovskites suitable for light emitting devices. For example, Alivisatos *and co.* reported the synthesis of cesium-based lead halide NPLs with PL QY of 84 % [48] and Brabec and co. reported for the hybrid perovskite NPLs a PL QY up to 90 % [19,41].

1.2. DYNAMICAL PROCCESSES IN SEMICONDUCTOR NANOCRYSTALS

1.2.1. Introduction

The absorption of photons by a semiconductor promotes the system to an excited state by generating bound or unbound electron-hole pairs, respectively excitons or free charge carriers (dissociated electrons and holes). The system can return to the ground state *via* radiative or a number of non-radiative processes. Depending on the excitation wavelength, the excited electrons and holes will possess a certain amount of excess kinetic energy. This excess energy is usually rapidly released to the surrounding so the system is then in a "relaxed" excited state before it returns to the ground state. Each possible pathway is related to an efficiency (rate k) and kinetics determined by the specific conditions of the systems, such as the energy of the absorbed photons (excitation energy) and the density of excited species (charge carriers or excitons). The latter initially depends on the excitation fluence, the absorption cross section of the material and eventually of its dimensionality (for nanostructures).

The main photo-physical dynamical processes occurring in semiconductor nanostructures for excitons as the main excited species are shown in the **Figure 1.9**. First, the nanostructure can be excited by absorbing a photon (1) with energy hν equal or higher than the band-gap E_g, resulting in "cold" and "hot" exciton, respectively. In the case of non-resonant excitation (hν>E_g), the created hot exciton has an excess of kinetic energy that can dissipate in an ultrafast process known as *cooling* (2, typically in 100s of femtoseconds). In principle, if the excitation photon energy hν is at least equivalent to twice E_g, several excitons can be generated from the absorption of a single photon. This process is known as multiple exciton generation (MEG, 3) and can only appears in timescales faster than cooling as these two processes are in direct competition to decrease the hot exciton population. Multiple excitons can also be generated in the nanostructure if a high excitation fluence is used. When several excitons "see" each other in a

nanostructure, a non-radiative exciton-exciton annihilation recombination known as Auger recombination (4) will occur and can be observed in tens to hundreds of picoseconds. This Auger recombination decreases the multi-exciton population until reaching a single exciton per nanostructure. Finally, the electron and hole in the "cold" exciton recombine, either non-radiatively, either radiatively by emitting a photon with equivalent energy (5). This last recombination that put back the system to its ground state (no exciton) occurs in the range of 1-10s nanoseconds in typical semiconductor nanostructures. These main relaxation and recombination pathways are explained more in detail in the following sub-sections.

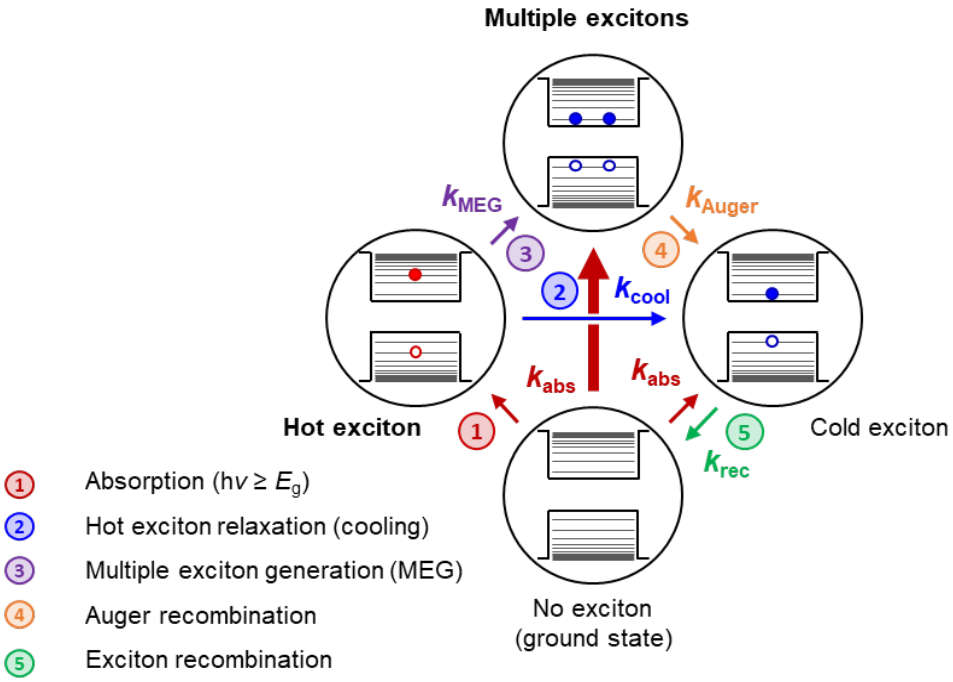

Figure 1.9. *Simplified picture of the exciton dynamical processes (relaxation and recombination) occurring in semiconductor nanostructures such as QDs, after photoexcitation. Non-excited QDs can be promoted to an excited state ("hot" or "cold" exciton) by absorption of a photon with energy hν ≥ E_g (1). The "hot" exciton may relax to a "cold" exciton by charge carrier cooling to the band-edge (2). If hν > 2Eg, two or more excitons can be created through carrier multiplication (or multiple exciton generation, MEG) (3). When multiple excitons are generated through MEG or high excitation fluence, they will recombine via Auger recombination (4). Finally, the "cold" exciton recombines which brings the system back to the ground state (5).*

1.2.2. Hot charge carrier & hot exciton relaxation: cooling

In bulk semiconductors, a pulsed excitation above the bandgap creates a non-thermal population which evolves through carrier-carrier scattering to a hot population characterized by a hot carrier temperature (T_c), higher than the lattice temperature. This thermalization process typically occurs within 100 fs. T_c reflects the distribution of the charge carriers occupying the continuous energy levels above the bandgap, characterized by a Fermi-Dirac function and often approximated by a Boltzmann distribution [49]. Then the thermalized charge carriers will equilibrate with the lattice by undergoing intra-band relaxation known as *cooling*, until T_c of the system reaches the lattice temperature [49].

1.2.2.1. Classical model of energy loss-rate

The most generally accepted cooling mechanism in bulk polar semiconductor materials is through inelastic carrier-phonon scattering. The first stage of this relaxation is governed by the coupling between charge carriers and the longitudinal optical (LO) phonon modes (Fröhlich interactions)[49,50] In perovskite, these modes are related to the Pb-I bonds. The excess kinetic energy of the charge carriers is released *via* the emission of LO phonons through electron- and hole-scattering. These emitted LO phonons then decay to low energy acoustic phonon modes through the Klemens' channel, until the carrier temperature equilibrates with the crystal lattice [49]. The temporal evolution of the carrier temperature $T_c(t)$ is complex. In particular, the characteristic rates are dependent on the temperature at a given time implying that the initial excess of kinetic energy of the charge carriers and thus the initial temperature $T_c(t=0)$, strongly affects this rate. That is why the effective energy loss rate, proportional to dT_c/dt (in $eV.s^{-1}$), is often used to compare different samples [51–53].

1.2.2.2. "Hot phonon bottleneck" at *high excitation fluence*

In addition to $T_c(t=0)$, the hot-carrier cooling rate also depends of the density of the photogenerated charge carriers. At high carrier density, typically starting at 10^{18} cm^{-3} corresponding to an average distance of 10nm between excited species, the cooling rate becomes slower. This is known as the "hot phonon bottleneck", an effect commonly observed in inorganic polar semiconductors [54,55]. Several mechanisms have been proposed to explain this bottleneck effect, notably in halide perovskite materials [49,53]. For example, at high excitation fluence, the large population of non-equilibrium optical phonons accumulates during the relaxation process of multiple photo-excited charge carriers and can no longer efficiently decay to acoustic phonons (bottleneck effect). Consequently, the LO phonons can be reabsorbed by those carriers before they decay to acoustic phonon modes [52,56,57].

1.2.2.3. "Intrinsic phonon bottleneck" in *strongly confined systems*

Apart from the "slowing-down" of the cooling rate coming from the charge carrier density, another related effect appears in the case of semiconductor nanostructures due to increased spacing between the electronic levels.

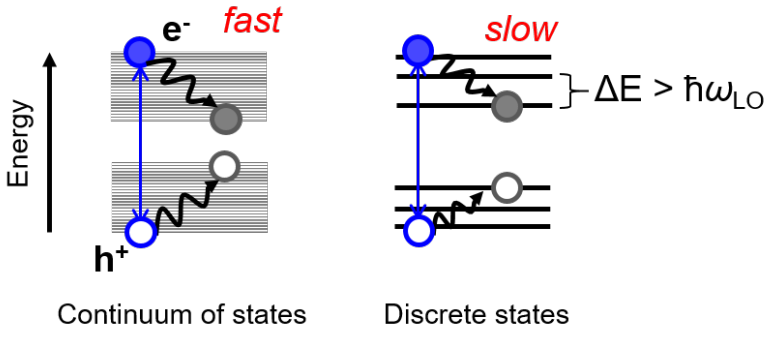

Figure 1.10. *Schematics of the intrinsic phonon bottleneck effect in confined systems. Left: fast hot charge carrier cooling in bulk polar semiconductor with continuous states. Right: slow relaxation in nanostructures with well separated electronic states close to the band-edge.*

Role of the discretization of the electronic levels

In strongly confined systems with electronic levels separated by energies higher than the discrete LO phonon modes ($\hbar\omega_{LO}$), the relaxation of hot charge carriers would require a simultaneous multi-phonon emission which is inefficient (**Figure 1.10**). Considering that the main relaxation mechanism *at low carrier density* is through the charge carrier/LO-phonon interaction, a drastic decrease of the cooling rates can be expected for nanostructures. This effect, proposed by Nozik *et al.* in the 90s, is known as the "*intrinsic phonon bottleneck"* effect and has been widely discussed in the literature due to the implications for hot carrier solar cells based on QDs [58]. However, this intrinsic phonon bottleneck is rarely observed in nanostructures due to efficient alternative pathways resulting in sub-picosecond relaxation (see below).

Mechanisms breaking the intrinsic phonon bottleneck

Several mechanisms have been proposed to explain the breaking of the expected intrinsic phonon bottleneck in colloidal semiconductor nanostructures. We will, in the following, describe some possible mechanisms.

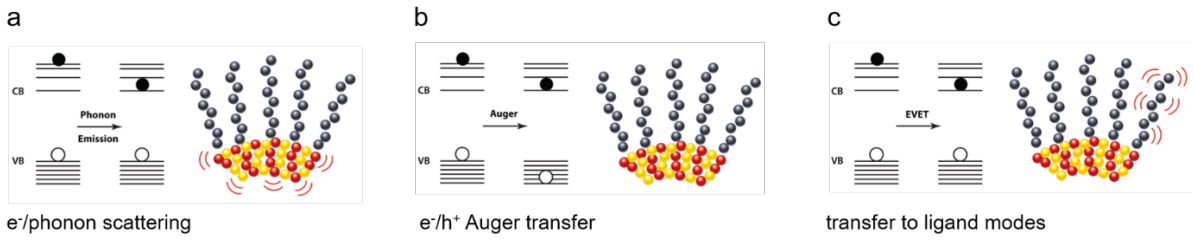

Figure 1.11. *Schematic of the possible relaxation mechanism in nanostructures: a) classical electron-phonon scattering, b) the hot electron cools down by transferring its kinetic energy to the hole that is rexcited. The later can then cooled down via the classical emission of phonons due to its higher density of states. c) hot carrier relaxation via coupling with ligand vibrational modes[59].*

- **Electron-hole Auger energy transfer:**

The first one is the electron-hole Auger transfer, that has been proposed in II-VI nanostructures such as CdSe, where it was found that the cooling rate increases in smaller-sized NCs. This mechanism involves a Auger-type energy transfer from the electron, with a low density of state, to the hole which possess a much higher density of state due to the larger corresponding effective mass (**Figure 1.11b**) [60,61]. The hot electron relax by transferring its excess energy to the hole and the latter, being re-excited to higher energy, can then more easily relax to the band-edge *via* scattering with LO phonons. The increased cooling rate in smaller-size CdSe NCs can thus be explained by the increased electron-hole coupling that enhances the Auger transfer process.

- **Surface-mediated relaxation:**

Auger transfer is not the only pathway that breaks down the intrinsic phonon bottleneck. The intraband relaxation can be also mediated by resonant energy transfer to the ligand vibrational modes [59]. Recently, Kambhampati and co. had shown that the excitonic states can directly couple with the ligand vibrations allowing efficient relaxation without resonance condition [62]. The vibronic coupling is observable in CdSe NCs with diameters ranging from 2 to 6 nm with both phosphonic acid and amine ligands.

1.2.2.4. *Auger reheating* in nanostructures

Additionally, to the hot phonon bottleneck effect that slows down the relaxation at high charge carrier density in polar semiconductor, multi-particle interactions such as Auger recombination can further reduce the cooling rate in nanostructures or in bulk semiconductors with charge carrier or exciton density as large as 10^{19} cm^{-3} [63]. Multi-particle Auger recombination results in a re-excitation of a charge carrier (or exciton) to a higher energy, this is known as Auger reheating. If this energy is high enough to eject

the carrier outside the nanostructure, we talk about Auger ionization. The Auger reheating effect results from the Auger recombination process is discussed more in detail in the next subsection.

1.2.3. Non-radiative Auger recombination

Auger recombination is a nonradiative multiparticle process that involves the recombination of an e-h pair by transferring its energy to another carrier (an electron or a hole), the latter being re-excited to a higher-energy state (**Figure 1.12a**). While in bulk materials, this multiparticle recombination process can only be observed at high carrier density, in the case of nanostructures, the Auger recombination is enhanced due to the increased Coulomb interactions and the fact that the momentum condition is relaxed [64]. In semiconductor nanostructures where the main excited species are excitons, Auger recombination is the main multiple exciton recombination pathway. Similarly, to the 3-particle interactions describe in the previous paragraph, the reaction between two excitons X can be written as follow: $X + X \rightarrow X^*$, where X^* is the re-excited exciton. For high energy excitons, the re-excitation will lead to an ionized state, resulting in a "pure" exciton-exciton annihilation ($2X \rightarrow 0$). For relatively low energetic excitons, the re-excited exciton is in a "hot" state that can further relax to the band edge ($2X \rightarrow X^* \rightarrow X$).

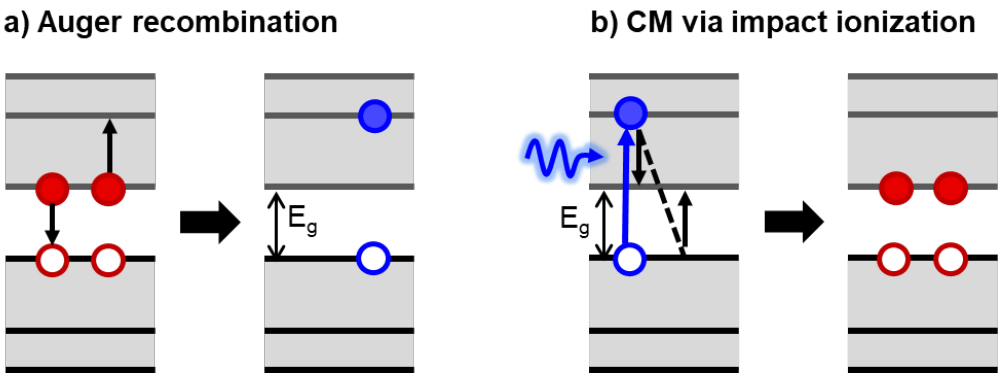

Figure 1.12. *Illustration of the Auger recombination* ***(a)*** *and carrier multiplication through impact-ionization* ***(b)****.*

1.2.4. Multiple exciton generation

Another process of particular interest is the carrier multiplication (CM) or multiple exciton generation (MEG) in case of the exciton is the major photoexcited species. CM (or MEG) can be regarded as the inverse of the Auger recombination process and may occur if the energy of the absorbed photon is at least twice the bandgap energy. In that case, a single photon can create several e-h pairs (see below), which is thus particularly interesting for photovoltaic applications. This CM or MEG was observed in various semiconductor materials. We present below the possible mechanisms.

MEG mechanisms

The CM process was first explained in bulk semiconductor using a mechanism known as *impact ionization* [58]. When the energy of the absorbed photon is much greater than the bandgap of the semiconductor, the excess kinetic energy of the resulting photoexcited e-h pair can excite a second e-h pair through an energy transfer process (**Figure 1.12b**) [65]. Although the theoretical threshold for CM or MEG is $h\nu=2E_g$, the threshold observed experimentally in bulk semiconductors is much higher and thus the resulting efficiency is very low. A. Nozik first proposed a great enhancement of the MEG efficiency in nanostructures for two principal reasons: the expected intrinsic phonon bottleneck which delays the cooling and the enhancement of the interactions between charge carriers in reduced crystal size [58]. Indeed, as already mentioned, MEG represents a pathway to depopulate the hot excited state and thus it directly competes with the cooling process. Furthermore, as MEG can be considered as the inverse process of multiexciton Auger recombination and is thus enhanced as well in nanostructures due to the increased Coulomb interactions between the charge carriers. Even though the cooling rate remains fast in colloidal nanocrystals, several groups have reported MEG in different semiconductor nanostructures [65–67]. Other theoretical models have been proposed,

such as the direct photogeneration of a coherent superposition of a high energy e-h pair and multiple low energy e-h pairs [65]. However, so far, the exact mechanism of MEG remains unknown. This is because MEG in nanostructures has mostly been observed indirectly and not in real time. In addition, several artifacts have led to an overestimation of its efficiency in nanostructures compared to bulk (see below).

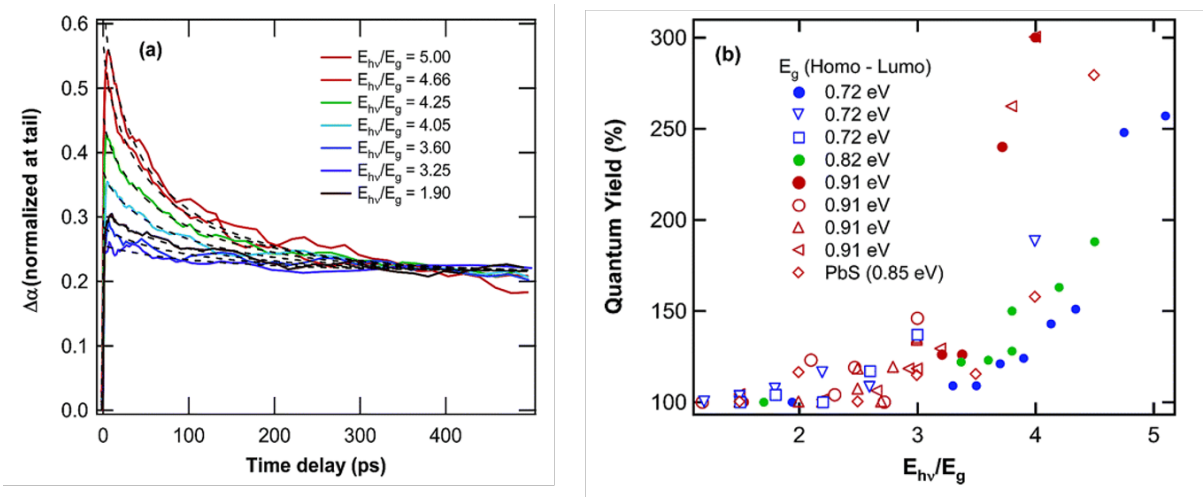

Figure 1.13. (a) *Electron-hole pair population dynamics measured in PbSe QDs through transient absorption (see Chapter II) at low excitation fluence and for different excitation energy E_{hv}. The decays are normalized at long time to highlight the extra Auger decay resulting from MEG.* ***(b)*** *Resulting quantum yield (number of e-h pairs per absorbed photons) for three different PbSe NC sizes and for one size PbS NCs, plotted versus the excitation energy E_{hv}, relative to the bandgap E_g. QY > 100 % implies MEG. Figures extracted from reference [66].*

Observation of MEG and controversy

The ultrafast time-scale at which MEG occurs (<< 100 fs) makes its direct measurement difficult using classical time-resolved optical spectroscopy techniques with time resolutions typically over 100 fs. The techniques used to probe MEG are based on the fact that multiexcitons will efficiently decay by Auger recombination in nanostructures, thus resulting in an extra recombination pathway of the exciton or charge carrier population

that can be monitored by a change of absorption or fluorescence in time-resolved spectroscopy [68]. For example, an extra decay component of about 100 ps corresponding to multi-exciton Auger recombination is observed in PbSe QDs (**Figure 1.13a)** when the excitation (photon) energy is higher than twice the bandgap, while this component is not present at lower excitation energies.

However, because multiexcitons can also be generated at high excitation fluence, in MEG experiments, the excitation fluence should remain low enough to ensure that each nanostructure absorbs less than one photon in average. Then, the observed Auger recombination of multi-exciton results from MEG occurring the high excitation photon energy and not from the high number of photons absorbed.

This indirect method to detect MEG has always been a center of controversy in the colloidal NC community due to several artifacts, such as photo-charging effects that result in another type of Auger recombination process involving trions, a charged exciton (three charged particules). The trion recombination can be misinterpreted as a multiple exciton Auger recombination [69,70]. This photo-charging effect is particularly effective when the measurements are performed on static samples, but much reduced when the excited colloidal nanostructures are refreshed through vigorous stirring of the sample solution or by using flow systems. Avoiding photo-charging effects and high excitation fluences is critical for a correct measurement of the MEG efficiency and threshold (see for example **Figure 1.13b**). Discrepancies are still observed in the reported MEG thresholds of the different nanostructures [71].

1.2.5. Radiative and non-radiative exciton recombination

The final step to return to the thermodynamic equilibrium (no e-h pair) is the interband recombination or exciton recombination [72]. The energy from the e-h pair is released

either radiatively by emitting a photon or non-radiatively. The fraction of emitted photons over the number of absorbed photons gives the photoluminescence quantum yield (PL QY). It can be linked to the radiative and non-radiative rates, k_r and k_{nr} respectively, through the following relation:

$$PL\ QY = \frac{k_r}{k_r + k_{nr}} \qquad [1.1]$$

For a monoexponential bound e-h pair recombination with characteristic decay time $\tau_X = 1/k_{tot} = 1/(k_r + k_{nr})$, we can deduce the radiative decay time $\tau_r = 1/k_r$ by determining the PL QY experimentally. In colloidal nanostructures, the exciton recombination is typically in the order or few to tens of nanoseconds.

1.2.6. Conclusion

All the processes described above have to be taken into account to describe the evolution of the different populations (no exciton, monoexcitons, multiexcitons). The diagram of these processes in **Figure 1.9** is much complex when taking into account the exciton dissociation into free carriers or charged excitons, that is not described here. The different processes have their characteristic kinetics (*i.e.* monomolecular, bimolecular…) and, for most of them, are strongly dependent on the e-h pair density. They can be in direct competition between each other.

Time resolved spectroscopy experiments with careful kinetic analysis is a powerful tool to discriminate between them. How the confinement modifies the different dynamics in colloidal nanostructures in still of major interest, particularly for the new halide perovskite materials, as it will directly affects the performances of the opto-electronic devices based on these nanostructures.

REFERENCES

[1] K. Chen, S. Schünemann, S. Song, H. Tüysüz, Structural effects on optoelectronic properties of halide perovskites, Chem. Soc. Rev. 47 (2018) 7045–7077. https://doi.org/10.1039/c8cs00212f.

[2] A. Poglitsch, D. Weber, Dynamic disorder in methylammoniumtrihalogenoplumbates (II) observed by millimeter-wave spectroscopy, J. Chem. Phys. 87 (1987) 6373–6378. https://doi.org/10.1063/1.453467.

[3] Y. Fu, H. Zhu, J. Chen, M.P. Hautzinger, X.Y. Zhu, S. Jin, Metal halide perovskite nanostructures for optoelectronic applications and the study of physical properties, Nat. Rev. Mater. 4 (2019) 169–188. https://doi.org/10.1038/s41578-019-0080-9.

[4] Y. Dong, Y. Zhao, S. Zhang, Y. Dai, L. Liu, Y. Li, Q. Chen, Recent advances toward practical use of halide perovskite nanocrystals, J. Mater. Chem. A. 6 (2018) 21729–21746. https://doi.org/10.1039/C8TA06376A.

[5] J.M. Frost, A. Walsh, Molecular motion and dynamic crystal structures of hybrid halide perovskites, in: Org. Halide Perovskite Photovoltaics From Fundam. to Device Archit., Springer International Publishing, 2016: pp. 1–17. https://doi.org/10.1007/978-3-319-35114-8_1.

[6] J. Even, L. Pedesseau, J.M. Jancu, C. Katan, Importance of spin-orbit coupling in hybrid organic/inorganic perovskites for photovoltaic applications, J. Phys. Chem. Lett. 4 (2013) 2999–3005. https://doi.org/10.1021/jz401532q.

[7] J. Even, L. Pedesseau, C. Katan, Analysis of multivalley and multibandgap absorption and enhancement of free carriers related to exciton screening in hybrid perovskites, J. Phys. Chem. C. 118 (2014) 11566–11572. https://doi.org/10.1021/jp503337a.

[8] J. Even, L. Pedesseau, C. Katan, M. Kepenekian, J.S. Lauret, D. Sapori, E. Deleporte, Solid-state physics perspective on hybrid perovskite semiconductors, J. Phys. Chem. C. 119 (2015) 10161–10177. https://doi.org/10.1021/acs.jpcc.5b00695.

[9] A. Amat, E. Mosconi, E. Ronca, C. Quarti, P. Umari, M.K. Nazeeruddin, M. Grätzel, F. De Angelis, Cation-induced band-gap tuning in organohalide perovskites: Interplay of spin-orbit coupling and octahedra tilting, Nano Lett. 14 (2014) 3608–

3616. https://doi.org/10.1021/nl5012992.

[10] S. Adjokatse, H.H. Fang, M.A. Loi, Broadly tunable metal halide perovskites for solid-state light-emission applications, Mater. Today. 20 (2017) 413–424. https://doi.org/10.1016/j.mattod.2017.03.021.

[11] K. Galkowski, A. Mitioglu, A. Miyata, P. Plochocka, O. Portugall, G.E. Eperon, J.T.-W. Wang, T. Stergiopoulos, S.D. Stranks, H.J. Snaith, R.J. Nicholas, Determination of the exciton binding energy and effective masses for methylammonium and formamidinium lead tri-halide perovskite semiconductors, Energy Environ. Sci. 9 (2016) 962–970. https://doi.org/10.1039/C5EE03435C.

[12] Z. Liu, S. Huang, J. Du, C. Wang, Y. Leng, Advances in inorganic and hybrid perovskites for miniaturized lasers, Nanophotonics. 9 (2020) 2251–2272. https://doi.org/10.1515/nanoph-2019-0572.

[13] T. Edvinsson, Optical quantum confinement and photocatalytic properties in two-, one- and zero-dimensional nanostructures, R. Soc. Open Sci. 5 (2018) 180387. https://doi.org/10.1098/rsos.180387.

[14] M. Kuno, Introductory nanoscience: Physical and chemical concepts, MRS Bull. 37 (2012) 169–170. https://doi.org/10.1557/mrs.2012.46.

[15] K. Khan, A.K. Tareen, M. Aslam, R. Wang, Y. Zhang, A. Mahmood, Z. Ouyang, H. Zhang, Z. Guo, Recent developments in emerging two-dimensional materials and their applications, J. Mater. Chem. C. 8 (2020) 387–440. https://doi.org/10.1039/c9tc04187g.

[16] L.C. Schmidt, A. Pertegás, S. González-Carrero, O. Malinkiewicz, S. Agouram, G. Mínguez Espallargas, H.J. Bolink, R.E. Galian, J. Pérez-Prieto, Nontemplate synthesis of CH3NH3PbBr3 perovskite nanoparticles, J. Am. Chem. Soc. 136 (2014) 850–853. https://doi.org/10.1021/ja4109209.

[17] L. Protesescu, S. Yakunin, M.I. Bodnarchuk, F. Krieg, R. Caputo, C.H. Hendon, R.X. Yang, A. Walsh, M. V. Kovalenko, Nanocrystals of Cesium Lead Halide Perovskites ($CsPbX_3$, X = Cl, Br, and I): Novel Optoelectronic Materials Showing Bright Emission with Wide Color Gamut, Nano Lett. 15 (2015) 3692–3696. https://doi.org/10.1021/nl5048779.

[18] F. Zhang, H. Zhong, C. Chen, X. Wu, X. Hu, H. Huang, J. Han, B. Zou, Y. Dong,

Brightly Luminescent and Color-Tunable Colloidal CH 3 NH 3 PbX 3 (X = Br, I, Cl) Quantum Dots: Potential Alternatives for Display Technology, ACS Nano. 9 (2015) 4533–4542. https://doi.org/10.1021/acsnano.5b01154.

[19] I. Levchuk, A. Osvet, X. Tang, M. Brandl, J.D. Perea, F. Hoegl, G.J. Matt, R. Hock, M. Batentschuk, C.J. Brabec, Brightly Luminescent and Color-Tunable Formamidinium Lead Halide Perovskite FAPbX 3 (X = Cl, Br, I) Colloidal Nanocrystals, Nano Lett. 17 (2017) 2765–2770. https://doi.org/10.1021/acs.nanolett.6b04781.

[20] X. Li, F. Cao, D. Yu, J. Chen, Z. Sun, Y. Shen, Y. Zhu, L. Wang, Y. Wei, Y. Wu, H. Zeng, All Inorganic Halide Perovskites Nanosystem: Synthesis, Structural Features, Optical Properties and Optoelectronic Applications, Small. 13 (2017) 1603996. https://doi.org/10.1002/smll.201603996.

[21] M. Fu, P. Tamarat, J.-B. Trebbia, M.I. Bodnarchuk, M. V. Kovalenko, J. Even, B. Lounis, Unraveling exciton–phonon coupling in individual FAPbI3 nanocrystals emitting near-infrared single photons, Nat. Commun. 9 (2018) 3318. https://doi.org/10.1038/s41467-018-05876-0.

[22] Y. Li, T. Ding, X. Luo, Z. Chen, X. Liu, X. Lu, K. Wu, Biexciton Auger recombination in mono-dispersed, quantum-confined CsPbBr 3 perovskite nanocrystals obeys universal volume-scaling, Nano Res. 12 (2019) 619–623. https://doi.org/10.1007/s12274-018-2266-7.

[23] Q.A. Akkerman, G. Rainò, M. V. Kovalenko, L. Manna, Genesis, challenges and opportunities for colloidal lead halide perovskite nanocrystals, Nat. Mater. 17 (2018) 394–405. https://doi.org/10.1038/s41563-018-0018-4.

[24] H. Huang, M.I. Bodnarchuk, S. V. Kershaw, M. V. Kovalenko, A.L. Rogach, Lead Halide Perovskite Nanocrystals in the Research Spotlight: Stability and Defect Tolerance, ACS Energy Lett. 2 (2017) 2071–2083. https://doi.org/10.1021/acsenergylett.7b00547.

[25] B.P. Zakharchenya, S.A. Permogorov, Excitons in Crystals, in: F. Bassani, G.L. Liedl, P.B.T.-E. of C.M.P. Wyder (Eds.), Encycl. Condens. Matter Phys., Elsevier, Oxford, 2005: pp. 171–179. https://doi.org/10.1016/B0-12-369401-9/01147-5.

[26] B. Saparov, D.B. Mitzi, Organic-Inorganic Perovskites: Structural Versatility for Functional Materials Design, Chem. Rev. 116 (2016) 4558–4596.

https://doi.org/10.1021/acs.chemrev.5b00715.

[27] E. Shi, Y. Gao, B.P. Finkenauer, A. Akriti, A.H. Coffey, L. Dou, Two-dimensional halide perovskite nanomaterials and heterostructures, Chem. Soc. Rev. 47 (2018) 6046–6072. https://doi.org/10.1039/c7cs00886d.

[28] C. Katan, N. Mercier, J. Even, Quantum and Dielectric Confinement Effects in Lower-Dimensional Hybrid Perovskite Semiconductors, Chem. Rev. 119 (2019) 3140–3192. https://doi.org/10.1021/acs.chemrev.8b00417.

[29] C.M. Mauck, W.A. Tisdale, Excitons in 2D Organic–Inorganic Halide Perovskites, Trends Chem. 1 (2019) 380–393. https://doi.org/10.1016/j.trechm.2019.04.003.

[30] F. Zhang, H. Lu, J. Tong, J.J. Berry, M.C. Beard, K. Zhu, Advances in two-dimensional organic–inorganic hybrid perovskites, Energy Environ. Sci. 13 (2020) 1154–1186. https://doi.org/10.1039/c9ee03757h.

[31] W. Paritmongkol, N.S. Dahod, A. Stollmann, N. Mao, C. Settens, S.L. Zheng, W.A. Tisdale, Synthetic Variation and Structural Trends in Layered Two-Dimensional Alkylammonium Lead Halide Perovskites, Chem. Mater. 31 (2019) 5592–5607. https://doi.org/10.1021/acs.chemmater.9b01318.

[32] H. Hu, T. Salim, B. Chen, Y.M. Lam, Molecularly Engineered Organic-Inorganic Hybrid Perovskite with Multiple Quantum Well Structure for Multicolored Light-Emitting Diodes, Sci. Rep. 6 (2016). https://doi.org/10.1038/srep33546.

[33] L. Na Quan, D. Ma, Y. Zhao, O. Voznyy, H. Yuan, E. Bladt, J. Pan, F.P. García de Arquer, R. Sabatini, Z. Piontkowski, A.H. Emwas, P. Todorović, R. Quintero-Bermudez, G. Walters, J.Z. Fan, M. Liu, H. Tan, M.I. Saidaminov, L. Gao, Y. Li, D.H. Anjum, N. Wei, J. Tang, D.W. McCamant, M.B.J. Roeffaers, S. Bals, J. Hofkens, O.M. Bakr, Z.H. Lu, E.H. Sargent, Edge stabilization in reduced-dimensional perovskites, Nat. Commun. 11 (2020) 1–9. https://doi.org/10.1038/s41467-019-13944-2.

[34] D. Sapori, M. Kepenekian, L. Pedesseau, C. Katan, J. Even, Quantum confinement and dielectric profiles of colloidal nanoplatelets of halide inorganic and hybrid organic–inorganic perovskites, Nanoscale. 8 (2016) 6369–6378. https://doi.org/10.1039/C5NR07175E.

[35] M.C. Weidman, M. Seitz, S.D. Stranks, W.A. Tisdale, Highly Tunable Colloidal

Perovskite Nanoplatelets through Variable Cation, Metal, and Halide Composition, ACS Nano. 10 (2016) 7830–7839. https://doi.org/10.1021/acsnano.6b03496.

[36] L. Dou, A.B. Wong, Y. Yu, M. Lai, N. Kornienko, S.W. Eaton, A. Fu, C.G. Bischak, J. Ma, T. Ding, N.S. Ginsberg, L.W. Wang, A.P. Alivisatos, P. Yang, Atomically thin two-dimensional Organic-inorganic hybrid perovskites, Science (80-.). 349 (2015) 1518–1521. https://doi.org/10.1126/science.aac7660.

[37] P. Tyagi, S.M. Arveson, W.A. Tisdale, Colloidal Organohalide Perovskite Nanoplatelets Exhibiting Quantum Confinement, J. Phys. Chem. Lett. 6 (2015) 1911–1916. https://doi.org/10.1021/acs.jpclett.5b00664.

[38] Y. Bekenstein, B.A. Koscher, S.W. Eaton, P. Yang, A.P. Alivisatos, Highly Luminescent Colloidal Nanoplates of Perovskite Cesium Lead Halide and Their Oriented Assemblies, J. Am. Chem. Soc. 137 (2015) 16008–16011. https://doi.org/10.1021/jacs.5b11199.

[39] J.A. Sichert, Y. Tong, N. Mutz, M. Vollmer, S. Fischer, K.Z. Milowska, R. García Cortadella, B. Nickel, C. Cardenas-Daw, J.K. Stolarczyk, A.S. Urban, J. Feldmann, Quantum Size Effect in Organometal Halide Perovskite Nanoplatelets, Nano Lett. 15 (2015) 6521–6527. https://doi.org/10.1021/acs.nanolett.5b02985.

[40] Y. Tong, E. Bladt, M.F. Aygüler, A. Manzi, K.Z. Milowska, V.A. Hintermayr, P. Docampo, S. Bals, A.S. Urban, L. Polavarapu, J. Feldmann, Highly Luminescent Cesium Lead Halide Perovskite Nanocrystals with Tunable Composition and Thickness by Ultrasonication, Angew. Chemie Int. Ed. 55 (2016) 13887–13892. https://doi.org/10.1002/anie.201605909.

[41] I. Levchuk, P. Herre, M. Brandl, A. Osvet, R. Hock, W. Peukert, P. Schweizer, E. Spiecker, M. Batentschuk, C.J. Brabec, Ligand-assisted thickness tailoring of highly luminescent colloidal CH3NH3PbX3 (X = Br and I) perovskite nanoplatelets, Chem. Commun. 53 (2017) 244–247. https://doi.org/10.1039/c6cc09266g.

[42] V.A. Hintermayr, A.F. Richter, F. Ehrat, M. Döblinger, W. Vanderlinden, J.A. Sichert, Y. Tong, L. Polavarapu, J. Feldmann, A.S. Urban, Tuning the Optical Properties of Perovskite Nanoplatelets through Composition and Thickness by Ligand-Assisted Exfoliation, Adv. Mater. 28 (2016) 9478–9485. https://doi.org/10.1002/adma.201602897.

[43] J.C. Blancon, H. Tsai, W. Nie, C.C. Stoumpos, L. Pedesseau, C. Katan, M.

Kepenekian, C.M.M. Soe, K. Appavoo, M.Y. Sfeir, S. Tretiak, P.M. Ajayan, M.G. Kanatzidis, J. Even, J.J. Crochet, A.D. Mohite, Extremely efficient internal exciton dissociation through edge states in layered 2D perovskites, Science (80-.). 355 (2017) 1288–1292. https://doi.org/10.1126/science.aal4211.

[44] L. Pedesseau, D. Sapori, B. Traore, R. Robles, H.-H. Fang, M.A. Loi, H. Tsai, W. Nie, J.-C. Blancon, A. Neukirch, S. Tretiak, A.D. Mohite, C. Katan, J. Even, M. Kepenekian, Advances and Promises of Layered Halide Hybrid Perovskite Semiconductors, ACS Nano. 10 (2016) 9776–9786. https://doi.org/10.1021/acsnano.6b05944.

[45] R. Benchamekh, N.A. Gippius, J. Even, M.O. Nestoklon, J.M. Jancu, S. Ithurria, B. Dubertret, A.L. Efros, P. Voisin, Tight-binding calculations of image-charge effects in colloidal nanoscale platelets of CdSe, Phys. Rev. B - Condens. Matter Mater. Phys. 89 (2014) 035307. https://doi.org/10.1103/PhysRevB.89.035307.

[46] K. Tanaka, T. Takahashi, T. Kondo, T. Umebayashi, K. Asai, K. Ema, Image charge effect on two-dimensional excitons in an inorganic-organic quantum-well crystal, Phys. Rev. B - Condens. Matter Mater. Phys. 71 (2005) 045312. https://doi.org/10.1103/PhysRevB.71.045312.

[47] D.B. Straus, C.R. Kagan, Electrons, Excitons, and Phonons in Two-Dimensional Hybrid Perovskites: Connecting Structural, Optical, and Electronic Properties, J. Phys. Chem. Lett. 9 (2018) 1434–1447. https://doi.org/10.1021/acs.jpclett.8b00201.

[48] J. Shamsi, Z. Dang, P. Bianchini, C. Canale, F. Di Stasio, R. Brescia, M. Prato, L. Manna, Colloidal Synthesis of Quantum Confined Single Crystal CsPbBr3 Nanosheets with Lateral Size Control up to the Micrometer Range, J. Am. Chem. Soc. 138 (2016) 7240–7243. https://doi.org/10.1021/jacs.6b03166.

[49] J. Fu, Q. Xu, G. Han, B. Wu, C.H.A. Huan, M.L. Leek, T.C. Sum, Hot carrier cooling mechanisms in halide perovskites, Nat. Commun. 8 (2017) 1300. https://doi.org/10.1038/s41467-017-01360-3.

[50] S. Kahmann, M.A. Loi, Hot carrier solar cells and the potential of perovskites for breaking the Shockley–Queisser limit, J. Mater. Chem. C. 7 (2019) 2471–2486. https://doi.org/10.1039/C8TC04641G.

[51] C.A. Leatherdale, M.G. Bawendi, Electron and hole relaxation pathways in semiconductor quantum dots, Phys. Rev. B - Condens. Matter Mater. Phys. 60

(1999) 13740–13749. https://doi.org/10.1103/PhysRevB.60.13740.

[52] Y. Yang, D.P. Ostrowski, R.M. France, K. Zhu, J. Van De Lagemaat, J.M. Luther, M.C. Beard, Observation of a hot-phonon bottleneck in lead-iodide perovskites, Nat. Photonics. 10 (2016) 53–59. https://doi.org/10.1038/nphoton.2015.213.

[53] M. Li, S. Bhaumik, T.W. Goh, M.S. Kumar, N. Yantara, M. Grätzel, S. Mhaisalkar, N. Mathews, T.C. Sum, Slow cooling and highly efficient extraction of hot carriers in colloidal perovskite nanocrystals, Nat. Commun. 8 (2017) 14350. https://doi.org/10.1038/ncomms14350.

[54] V. Klimov, P. Haring Bolivar, H. Kurz, Hot-phonon effects in femtosecond luminescence spectra of electron-hole plasmas in CdS, Phys. Rev. B. 52 (1995) 4728–4731. https://doi.org/10.1103/PhysRevB.52.4728.

[55] R.P. Joshi, D.K. Ferry, Hot-phonon effects and interband relaxation processes in photoexcited GaAs quantum wells, Phys. Rev. B. 39 (1989) 1180–1187. https://doi.org/10.1103/PhysRevB.39.1180.

[56] M. Li, J. Fu, Q. Xu, T.C. Sum, Slow Hot-Carrier Cooling in Halide Perovskites: Prospects for Hot-Carrier Solar Cells, Adv. Mater. (2019) 1802486. https://doi.org/10.1002/adma.201802486.

[57] P. Papagiorgis, L. Protesescu, M. V. Kovalenko, A. Othonos, G. Itskos, Long-Lived Hot Carriers in Formamidinium Lead Iodide Nanocrystals, J. Phys. Chem. C. 121 (2017) 12434–12440. https://doi.org/10.1021/acs.jpcc.7b02308.

[58] A.J. Nozik, Spectroscopy and hot electron relaxation dynamics in semiconductor quantum wells and quantum dots, Annu. Rev. Phys. Chem. 52 (2001) 193–231. https://doi.org/10.1146/annurev.physchem.52.1.193.

[59] M.D. Peterson, L.C. Cass, R.D. Harris, K. Edme, K. Sung, E.A. Weiss, The Role of Ligands in Determining the Exciton Relaxation Dynamics in Semiconductor Quantum Dots, Annu. Rev. Phys. Chem. 65 (2014) 317–339. https://doi.org/10.1146/annurev-physchem-040513-103649.

[60] A.L. Efros, V.A. Kharchenko, M. Rosen, Breaking the phonon bottleneck in nanometer quantum dots: Role of Auger-like processes, Solid State Commun. 93 (1995) 281–284. https://doi.org/10.1016/0038-1098(94)00760-8.

[61] P. Guyot-Sionnest, M. Shim, C. Matranga, M. Hines, Intraband relaxation in CdSe

quantum dots, Phys. Rev. B - Condens. Matter Mater. Phys. 60 (1999) R2181–R2184. https://doi.org/10.1103/PhysRevB.60.R2181.

[62] T.G. Mack, L. Jethi, M. Andrews, P. Kambhampati, Direct Observation of Vibronic Coupling between Excitonic States of CdSe Nanocrystals and Their Passivating Ligands, J. Phys. Chem. C. 123 (2019) 5084–5091. https://doi.org/10.1021/acs.jpcc.8b11098.

[63] M. Achermann, A.P. Bartko, J.A. Hollingsworth, V.I. Klimov, The effect of Auger heating on intraband carrier relaxation in semiconductor quantum rods, Nat. Phys. 2 (2006) 557–561. https://doi.org/10.1038/nphys363.

[64] V.I. Klimov, Multicarrier Interactions in Semiconductor Nanocrystals in Relation to the Phenomena of Auger Recombination and Carrier Multiplication, Annu. Rev. Condens. Matter Phys. 5 (2014) 285–316. https://doi.org/10.1146/annurev-conmatphys-031113-133900.

[65] A. Shabaev, C.S. Hellberg, A.L. Efros, Efficiency of Multiexciton Generation in Colloidal Nanostructures, Acc. Chem. Res. 46 (2013) 1242–1251. https://doi.org/10.1021/ar300283j.

[66] R.J. Ellingson, M.C. Beard, J.C. Johnson, P. Yu, O.I. Micic, A.J. Nozik, A. Shabaev, A.L. Efros, Highly efficient multiple exciton generation in colloidal PbSe and PbS quantum dots, Nano Lett. 5 (2005) 865–871. https://doi.org/10.1021/nl0502672.

[67] A.J. Nozik, Exciton multiplication and relaxation dynamics in quantum dots: Applications to ultrahigh-efficiency solar photon conversion, Inorg. Chem. 44 (2005) 6893–6899. https://doi.org/10.1021/ic0508425.

[68] V.I. Klimov, Spectral and Dynamical Properties of Multiexcitons in Semiconductor Nanocrystals, Annu. Rev. Phys. Chem. 58 (2007) 635–673. https://doi.org/10.1146/annurev.physchem.58.032806.104537.

[69] M.C. Beard, Multiple Exciton Generation in Semiconductor Quantum Dots, J. Phys. Chem. Lett. 2 (2011) 1282–1288. https://doi.org/10.1021/jz200166y.

[70] R.D. Schaller, V.I. Klimov, High Efficiency Carrier Multiplication in PbSe Nanocrystals: Implications for Solar Energy Conversion, Phys. Rev. Lett. 92 (2004) 186601. https://doi.org/10.1103/PhysRevLett.92.186601.

[71] D.J. Binks, Multiple exciton generation in nanocrystal quantum dots - Controversy,

current status and future prospects, Phys. Chem. Chem. Phys. 13 (2011) 12693–12704. https://doi.org/10.1039/c1cp20225a.

[72] J. Shah, Ultrafast Spectroscopy of Semiconductors and Semiconductor Nanostructures, Springer Berlin Heidelberg, Berlin, Heidelberg, 1999. https://doi.org/10.1007/978-3-662-03770-6.

Chapter 2. EXPERIMENTAL METHODS

This chapter, divided in two parts, presents the experimental methods employed. The first part deals with the optical spectroscopic techniques used to characterize the perovskite nanostructures in term of steady-state and time-resolved optical properties. A description of the absorption and photoluminescence phenomena is introduced. The two main spectroscopic setups used in this thesis are explained in detail. The home-built time-resolved photoluminescence setup based on time-correlated single photon counting (TCSPC) technique and the cutting-edge femtosecond broad-band transient absorption (fs-TA) setup.

The second part describes the synthetic approaches of the perovskite nanomaterials used in this thesis. It starts with a short review of the wet chemical methods available in the literature for the preparation of colloidal perovskite nanostructures, such as the hot injection (HI) and the ligand assisted reprecipitation (LARP). Then, these methods are applied to the synthesis of the colloidal perovskite nanostructures of interest and optimized in terms of population dispersion and stability.

2.1. Optical spectroscopy techniques

Optical spectroscopy refers to the study of the matter by using its interaction with electromagnetic radiation (light). Historically, *steady-state* spectroscopy includes all methods of characterization based on the detection of an optical signal dispersed in frequency, energy or wavelength, such as absorption, photoluminescence and light scattering. Time-resolved optical spectroscopy goes a step further following the changes of matter induced by an external perturbation, for example, a light flash. To investigate ultrafast changes, short pulses are needed, such that obtained with pulsed lasers. In this thesis, both steady-state and time-resolved optical spectroscopy experiments were performed at room temperature, with the colloidal perovskite nanostructures dispersed in organic solvents for the time resolved experiments, a flow system was used to avoid the sample degradation.

2.1.1. Steady-state optical spectroscopy

2.1.1.1. Absorption spectroscopy

A beam of light passing through a solution of absorbing material decreases progressively in intensity. The measured intensity (I) of the transmitted light is:

$$I = I_0 exp(-\varepsilon C l) \quad [2.1]$$

with I_0, the initial intensity of the light, C, the concentration of absorbers in $mol \cdot L^{-1}$, l, the length of the path in cm and ε, the linear extinction coefficient in $L \cdot mol^{-1} \cdot cm^{-1}$, the latter being wavelength dependent. The absorption A can be written as follow:

$$A(\lambda) = log\left(\frac{I_0(\lambda)}{I(\lambda)}\right) = \varepsilon(\lambda) l C \quad [2.2]$$

The second part of the equation is known as the Beer-Lambert's law [1]. The dependence of the absorbance on the frequency of light can be displayed by plotting A (or ε) as a function of the frequency (υ), the wavelength (λ), or the energy which is the *absorption spectrum*.

2.1.1.1.1. Spectrophotometer

All the absorption measurements were carried out with a UV/Vis Lambda 850 spectrophotometer (Perkin Elmer) covering the 175-900 nm spectral range. We used two light sources: a deuterium arc lamp with good continuity, intensity a low noise level in the ultraviolet (UV) region (180-350 nm) and a tungsten filament-halogen lamp with good intensity and stability over a part of the UV and the whole visible range (330-900 nm). The detector is a high-sensitivity photomultiplier tube on the full range UV-Vis coverage from 175 to 900 nm. We used steps of 1 nm which much larger than the intrinsic spectral resolution of the spectrophotometer with a spectral resolution up to 1 nm. The measurements were typically performed in a 1 mm quartz cells from Hellma using a single beam configuration. The calibration of the instrument at 0 % transmittance was made without any sample (auto-zero) and the 100 % transmittance (baseline) was set using a *blank* with the same solvent used for the sample synthesis. For the UV absorption measurements, the spectrum was acquired without a baseline correction due to the absorption of the toluene in this region.

2.1.1.2. Photoluminescence spectroscopy

The photoluminescence (PL) spectrum of a colloidal dispersion of nanostructures is measured by exciting the sample at fixed excitation energy, typically higher than the bandgap, and by scanning the resulting emission in wavelength. It is particularly interesting to visualize the purity of the synthesized nanocrystals as only the lowest bright excited state is emitting.

The photoluminescence excitation (PLE) spectrum of sample solutions can be measured by fixing the emission wavelength and scanning the excitation energy. This PLE spectrum corresponds to the absorption spectrum of the excited species that emit at the specifically

selected wavelength if the PL QY of the sample is independent of the excitation wavelength. PLE spectra are usually more well-defined than the absorption ones due to the absence of scattering signal and non-emitting species. The PLE at selective emission wavelength also helps to identify different nanoparticles populations in the solution.

2.1.1.2.1. Fluorometer

Photoluminescence measurements were carried out with a Fluorolog 3-22 spectrofluorometer (HORIBA JOBIN-YVON) equipped with a double monochromator (optimized for 500 nm), a R928P photomultiplier tube detector (200-870 nm) and a continuous-wave Xenon arc lamp (450 W, 250-2500 nm). A UV enhanced silicon photodiode reference detector monitors and compensates for variation in the Xenon lamp intensity. The sensitivity of the detection system (optics, gratings, detector) as a function of emission wavelength and light intensity of the excitation were corrected. The experiments were performed in quartz cuvettes, 10 mm × 10 mm (Hellma) with an excitation wavelength centered typically at 400 nm and with a corresponding absorption below 0.1 to avoid reabsorption effects. The aperture of the slit in excitation and emission are fixed to 1 nm.

2.1.1.2.2. Measurement of the PL quantum yield

The photoluminescence quantum yield (PL QY), as defined in **Chapter 1, part 2**, can be measured using the absolute or the relative method. The relative measurement relies on the comparison with well-characterized reference standards (dyes), with known PL QY values and optical properties closely matching the sample of interest. The PL QY value Φ_s of the sample is estimated using the following formula [2]:

$$\Phi_s = \Phi_{ref} \frac{I_s A_{ref} n_s^2}{I_{ref} A_s n_{ref}^2} \quad [2.3]$$

with Φ_{ref}, the known PL QY value of the reference standard used; A_{ref} and A_s, the absorption value at the excitation wavelength of the reference and the sample, respectively; n_{ref} and n_s, the refractive index corresponding to the respective solvent and I_{ref} and I_s, the measured integrated fluorescence intensity of the reference and sample, respectively.

For simplicity, and because we do not expect the PL QY to be wavelength-dependent in the visible region, the excitation wavelength can be chosen at a crossing point between the two samples in the absorption spectrum (nanoparticle and reference dye solutions). This relative PL QY determination is an estimation, that can be strongly affected by the scattering of the colloidal solution of nanoparticles. An improvement would be to use an integrating sphere in the detection of the absorption setup [3]. The PL QY of the synthesized perovskite NPL samples dispersed in toluene are displayed in **Table 2.1**.

NPL samples	Estimated PLQY (%)	Reference dye	Reference PLQY (%)	Solvent refractive index (*n*)
MAPI *n*=3	31	Cresyl violette	54 [1]	Methanol (1.32)
MAPI *n*=2	1*	Rhodamine B	70 [1]	Ethanol (1.36)
FAPI *n*=2	9	Rhodamine 101	98 [1]	Toluene (1.50)
CsPI *n*=2	20	Rhodamine 101	98 [1]	

***** The dilution causes nanoplatelets instability which makes difficult to determine the PL QY in this sample in spite of the visible emission in the pristine solution.

Table 2.1. *Photo-luminescence quantum yield estimations for the different samples.*

2.1.2. Time-resolved optical spectroscopy

2.1.2.1. Pulsed laser excitation sources

The high-energy and short-pulsed laser can be exploited to reach extremely high-power densities. This allows non-linear processes required for some of the time-resolved spectroscopic experiments such as TA (third order signal) and also to control the

wavelength of the excitation source facilitating spectroscopic experiments by using harmonic generation or optical parametrical amplifier/oscillator.

The commercial Ti:sapphire (Ti:Sa) *oscillators* are mostly exploiting passive mode-locking configurations to generate short pulses with individual time duration in the range of 100 fs or below and with repetition rates of up to 100 MHz. The energy of an individual pulse from a Ti:Sa *oscillator* is in the range of 1-25 nJ, which is orders of magnitude higher than the average power in a continuous wave (CW) laser or a conventional lamp as the ones used in steady-state spectroscopy. However, it is several orders of magnitude lower than the energies needed for ultrafast pump-probe techniques. Such energies can only be delivered by *amplified* laser systems based on *chirped pulse amplification (CPA)* [4].

For instance, the excitation beam in the TR-PL setup detailed in the next section corresponds to the second harmonic generation (SHG) (400 nm) of a the fundamental beam (800 nm) from a commercial Ti:Sa *oscillator* with a peak power of ~ 2 $x10^5$ W. This is enough to produce certain non-linear optical (NLO) phenomena such as SHG. However, for third order NLO phenomena, such as the white-light continuum generation, a home-built regenerative *amplified* laser with a peak power of ~$2x10^{10}$ W was required.

2.1.2.2. Time-resolved photoluminescence (TR-PL)

Time-resolved photoluminescence spectroscopy uses a short light pulse at a given excitation wavelength (λ_{exc}) to optically excite a sample and measures the intensity of the emitted photons at a given emission wavelength (λ_{em}) as a function of time delay following the excitation. The excited population gradually decays radiatively and non-radiatively to the ground state and hence, the photoluminescence intensity, which is proportional to this population, diminishes as a function of time.

Several techniques are used to measure photoluminescence lifetimes. One approach is to excite a sample repeatedly with short pulses of light and measure the times at which individual emitted photons are detected after the excitation pulses. This is called time-correlated single-photon counting (TCSPC).

2.1.2.2.1. Principle of TCSPC

In TCSPC, the excitations are used to construct a histogram of the numbers of photons detected at various times after the excitation, which will form the photoluminescence decay. This method requires a precise measurement of the time delay between the first measured photons and the reference excitation pulse. To do so, a fraction of the excitation pulse is extracted and sent to a fast photo-detector, usually a photodiode, generating the reference electronic signal. The other fraction of the laser pulse intensity is directed to the sample, using appropriate optics and suitable attenuation of the light level, to maintain single-photon emission conditions of this technique [5]. The detection of the emitted photons is done with high-sensitivity photomultipliers (PMT) or avalanche photodiodes (APD) generating the single-photon luminescence electronic signal. These types of detectors give typically nanosecond pulses. A more performant detector is the microchannel plate photomultiplier (MCT-PM) producing an electronic pulse of a few 100s of picoseconds. The heart of a TCSPC setup is the high-performant electronics that measure the time between the reference and the luminescence signals. This requires fast electronics performing pulse-shaping, time-to-amplitude conversion, and amplitude-to-memory sorting. In modern setups, all this is implemented on a dedicated board or computer plugin-card. To construct the histogram mentioned above, the experiment must be repeated many times to collect photons with sufficient counting statistics throughout the complete fluorescence emission decay curve. This is no real problem with modern laser

sources having a repetition-rate of several tens of MHz. However, to obtain reliable histograms, the count-rate must be set much lower than the excitation rate. The reason is that, after having detected the first photon, the detector (PMT, APD) remains "blind" for several nanoseconds, which may lead to subsequent photons to be omitted if the rate is too high. A rule-of-thumb is to set the count-rate to 1/1000 of the excitation rate. Also, the reference and luminescence signals can be interchanged to decrease the effective cycle rate to the actual luminescence count rate, which decreases the load (and the heating, etc.) of the card. This is called "inverse mode" TCSPC. The recorded histogram is thus the "complement" of the real one and needs simply to be inverted in time.

The "time-resolution of a TCSPC experiment depends of course on the detectors used and the temporal widths of the generated signals but even more on the relative "timing" between the two signals. By carefully chose the optics, the time-resolution using a ns PM can be reduced to a few hundreds of ps, and when using a fast MCP-PM, time-resolutions down to a few tens of ps.

2.1.2.2.2. Setup description

We used a home-built TCSPC setup described in the reference [6]. The laser source is a commercial mode-locked Ti: Sa oscillator (MIRA 900, Coherent) pumped by a continuous-wave (CW) solid-state laser (VERDI V10, Coherent). The oscillator provides 120 fs pulses at 76 MHz repetition rate, with wavelength-tunable between 720 and 950 nm and an average power about 2 W. The repetition rate was reduced to 200 kHz using a pulse picker (Model 9200, Coherent). The experimental setup is illustrated in **Figure 2.1.**

The output pulse train was frequency-doubled using a β-barium borate (BBO) crystal (type I, 5 nm-thick) mounted on a tilt stage, providing vertically polarized pulses tunable between 360 and 475 m. The residual fundamental beam passes through a dichroic

mirror, is reduced in intensity, and is focused on a photodiode (Thorlabs PDA-10). The polarization of the 400 nm excitation beam was controlled by a Fresnel rhomb (EKSMA) mounted in a motorized rotation stage (DMT65, OWIS). It was set vertically, but we should note that our colloidal nanostructures do not present a specific dipole orientation at high-energy excitation (*cf* **Chapter 3**).

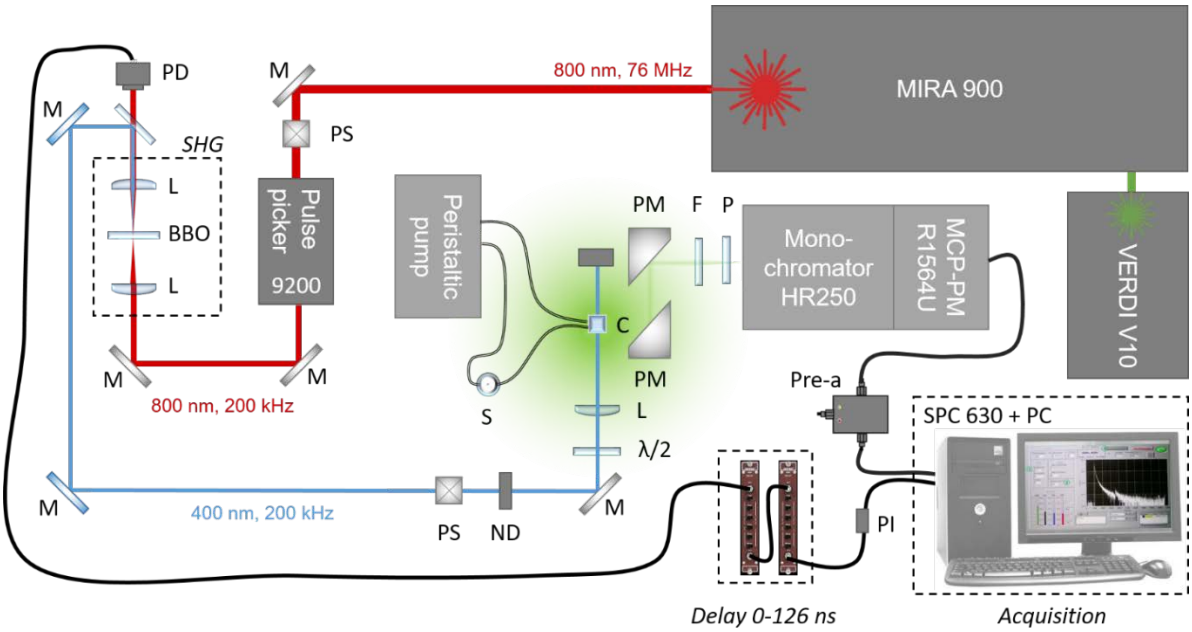

Figure 2.1. *Schematics of the TCSPC apparatus with the SHG for the excitation beam. M: flat mirror, PS: periscope, L: lens, BBO: frequency doubling BBO crystal, PD: photodiode, ND: neutral density filter, λ/2: half-waveplate, C: flow cell, S: sample solution, PM: parabolic mirror, F: filter, P: polarizer, MCP-PM: microchannel plate photomultiplier, PI: pulse inverter, Pre-a: pre-amplification.*

The excitation power was controlled using a set of neutral density filters. The excitation beam was focused at the center of the fluorescence flow cell (Hellma 176.751, 3 × 3 mm) with a 60 mm focal length lens. The estimated beam waist at the focus was 50 µm. The fluorescence was collected and transported by a set of two parabolic mirrors to a monochromator (HR250, Jobin-Yvon). A Schott WG 420 filter to cut the diffused excitation light and a Glan-Thompson polarizer, set parallel to the excitation, were both positioned

in front of the entrance slit of the monochromator. The fluorescence signal was detected with a microchannel plate photomultiplier (MCP-PM R1564U, Hamamatsu). For all the fluorescence lifetime experiments, the sample was refreshed within the 3 mm-thick flow-cell with a peristaltic pump and adapted tubing. This avoids photo-damage and photo-charging effects that strongly affects the measured fluorescence decay.

The TCSPC setup in our laboratory functions in the “inverse mode”, such that the first collected photon by the MCP-PM triggers the start signal and the PD the stop one. Both signals are sent to a single photon counting module (card SPC 630, Becker & Hickl GmbH) for accurate timing delay recording.

2.1.2.2.3. Instrument response function (IRF)

The TCSPC technique allows the measurement, with great accuracy, of the photo-luminescence emission lifetimes in a temporal range from 3 ns up to 2 microseconds (an electronic delay can replace the manual temporal delays normally used in the setup **Figure 2.1**). The overall temporal resolution is characterized by the instrument response function (IRF). As described above, the IRF is limited by the duration of the excitation pulse, the detector response, and electronic accuracy (jitter). The IRF was measured by recording the Raman scattering signal of the solvent as shown in **Figure 2.2**.

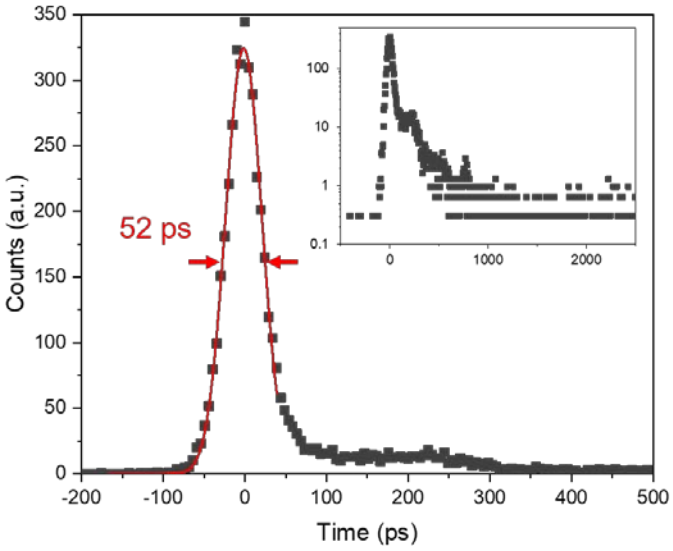

Figure 2.2. *Instrument response function (IRF) of our TCSPC technique, measured using the Raman scattering signal of the toluene detected at 455 nm (excitation 400 nm). The accumulated counts are displayed on the linear scale and a logarithm scale in the inset. The main lobe of the response (80 % of the signal) can be approximated with a Gaussian function of FWHM 52 ps.*

The main lobe of the IRF signal can be approximated by a Gaussian function with the full width at half maximum (FWHM) around 50-60 ps. A range of 20 ns was chosen, giving a sampling time of 20 ns / 4000 channels = 5 ps, which is 10 time below the IRF.

2.1.2.2.4. Data treatment and fitting

For the excitation fluence dependent experiments, where the intensity of the pump beam was controlled using various ND filters, different collection times were required to avoid the detector saturation and to keep the condition of the single-photon detection. As a consequence, all the decays were normalized by their respective collection time prior comparison. Additionally, the data points before time zero were averaged to construct the baseline used to correct the all data points.

Except mentioned otherwise, we use multi-exponential decay functions convoluted with the instrument response function (IRF) to fit the PL decays $I(t)$. First, a free software (DecayFit from FluorTools) was used to fit the PL decays using the setup IRF that allows

us to extract the deconvoluted exponential decay components. We noticed that we obtain similar results by using an analytical formula to fit the experimental decay that is a convolution of the multi-exponential decay and Gaussian IRF function [7]:

$$I(t) = \sum_i^m \frac{A_i}{2} exp(-k_i t)\ exp\left(k_i\left(t_0 + \frac{k_i}{2}\tilde{\Delta}^2\right)\right)\left[1 + erf\left(\frac{t-\left(t_0+k_i\tilde{\Delta}^2\right)}{\sqrt{2}\tilde{\Delta}}\right)\right] \quad [2.4]$$

The first two terms correspond to the convolution between the exponential decay function, with amplitude A_i and rate k_i, and the Gaussian IRF centered at time zero (t_0) with full-width at half maximum (FWHM) Δ. We have $\tilde{\Delta} = \Delta/\left(2\sqrt{ln(2)}\right)$, such that:

$$IRF(t) = \frac{1}{\tilde{\Delta}\sqrt{2\pi}} exp\left[-\frac{(t-t_0)^2}{\tilde{\Delta}^2}\right] \quad [2.5]$$

The last term corresponds to a step function used to fit the whole dynamics from $t \ll t_0$ to $t \gg t_0$. It can be seen as the convolution between the heavy-side step function and the Gaussian IRF.

2.1.2.3. Femtosecond transient absorption spectroscopy (fs-TA)

In this part, the principal technique to study the ultrafast photophysical processes occurring in colloidal perovskite nanostructures is presented: the femtosecond transient absorption (TA) spectroscopy. In contrast with TCSPC spectroscopy, TA is a pump-probe technique based on differential absorption measurement. Here, the temporal resolution is no longer limited by the detection system which allows to study ultrafast processes even on the femtosecond timescale.

2.1.2.3.1. Principle of fs-TA

The fundamental idea is to use an intense light pulse of a short time duration to perturb the equilibrium of a system and follow the appearance and the evolution in time of *transient species*. In this type of pump-probe measurement, the sample is excited using a first intense short laser pulse while another pulse, called the probe, arrives sometime after to measure how the absorption of the sample is altered by the first pulse. Using broadband probe pulse and detection (1D or 2D array detectors), the differential absorption spectrum is recorded. By scanning the pump-probe delay time t, we can measure the entire time-dependence of the absorption spectrum change ($\Delta A(\lambda,t)$ [7]:

$$\Delta A(\lambda, t) = -log\left[I(\lambda, t)_{pumped}/I(\lambda)_{unpumped}\right] \quad [2.6]$$

where $I_{\text{pumped}}(\lambda,t)$ is the wavelength-dependent intensity of the probe measured with the pump "ON" at a time delay t and $I_{\text{unpumped}}(\lambda)$ is the reference probe spectrum measured in the absence of pump pulse interaction (pump "OFF"). The strength of this pump-probe spectroscopy technique is that the time resolution is mainly limited by the duration of the laser pump pulse. Ideally, the probe pulse should not affect the system but only interrogate it, while the pump pulse must be strong enough to produce measurable populations of the excited states. Thus, the probe beam is typically much weaker than the pump.

2.1.2.3.2. fs-TA setup description

The home-made fs-TA spectrometer was built just before the beginning of this thesis, then several parts were improved during this period. The setup schematics are presented in **Figure 2.3.** The Ti: Sa oscillator (800 nm, 2 nJ at 76 MHz, MIRA from Coherent) seeds a regenerative amplifier using a powerful pump laser (Nd: YLF, 10 mJ, 3 kHz, Amplitude Technology). This amplifier function in the chirped pulse amplification (CPA) mode.

Briefly, the seed pulses are first stretched temporally to several hundreds of picoseconds in order to not damage the cavity optics and the crystal during the amplification. A combination of two Pockels cells and a quarter waveplate is used to create the "mirrors" of the cavity with the Ti: Sa crystal inside as the gain medium. This allows the generation of energetic pulses at a much-reduced repetition rate (3 kHz). The pulses are then recompressed to 40 fs by a grating compressor.

This mode-locked Ti: Sa amplified laser, delivering 40 fs pulses at 800 nm with an energy of about 0.6 mJ/pulse at 3 kHz repetition rate, is separated in two beams using a 50-50 % beamsplitter. One of the beams is used to pump a home-built non-collinear optical parametric amplifier (NOPA) based on previous publication [8] to generate tunable, relatively narrowband, pump pulses in the visible range (see below). The second beam is used generate the probe pulse.

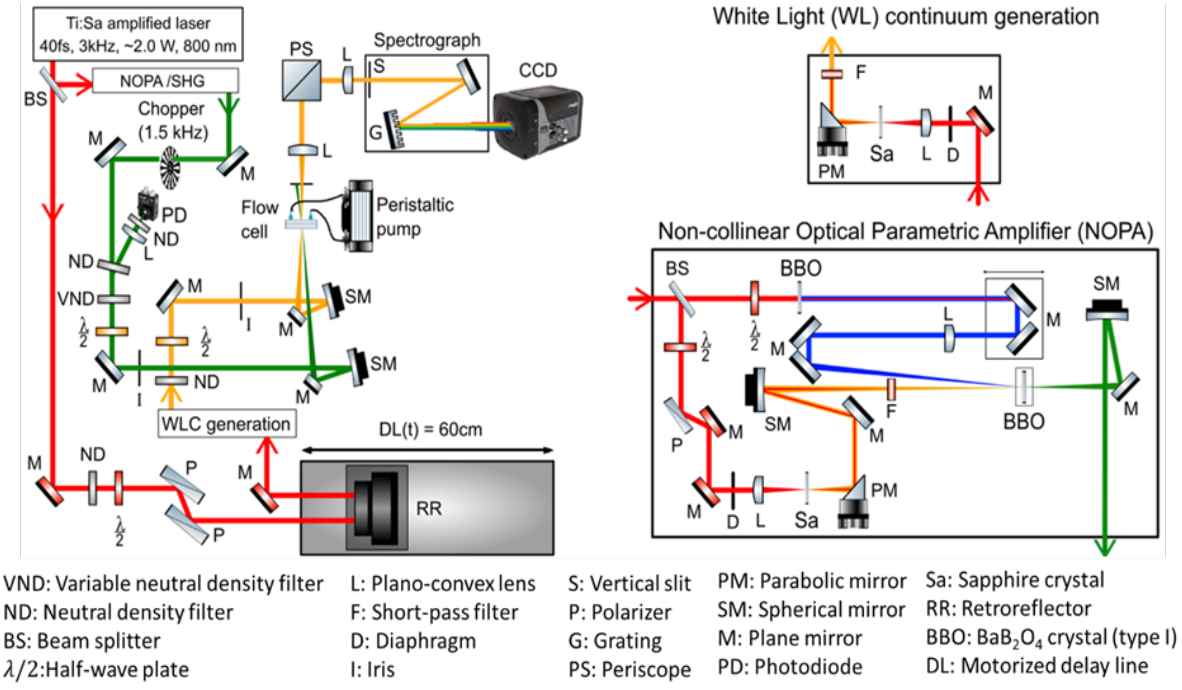

Figure 2.3. *Schematics of the fs-TA apparatus with the white light (WL) continuum generation for the probe beam and the non-collinear optical parametric amplifier (NOPA) or second harmonic generation (SHG) for the pump beam. Temporal compressors based on chirped mirror pairs and prisms were added in the pump path (not represented here). The schematics of the WL continuum generation and NOPA are presented on the right.*

2.1.2.3.3. Visible non-collinear optical parametric amplifier (NOPA)

The principle of NOPA is based on non-linear optical effects whereby a spectral portion of a white light continuum is amplified by a high-amplitude pump beam. A picture is shown in **Figure 2.4** and the schematics in **Figure 2.3**. First, a small fraction (about 5 %) at the center of the 800 nm beam is focused on a thin Sapphire plate (2 mm thick) to generate a white-light (WL) continuum from about 450 nm to wavelengths above 800 nm. These new frequencies are generated through a third-order non-linear process implicating mainly *self-phase modulation* [9]. Its intensity is controlled by a set of a half-waveplate and polarizer in the 800 nm path. The WL beam is then recollimated using a parabolic mirror mounted on an X-Y-Z stage to control its spatial mode (see the picture in the inset of **Figure 2.5**). The remaining 800 nm radiation is filtered out using a filter (cut-off wavelength 750 nm). At this point the WL polarization is vertical and the different colors are dispersed in time (*i.e.* "chirped"). The WL is then focused onto the thin amplifying BBO crystal with a long focal length concave mirror. In parallel, the remaining 95 % of the 800 nm is frequency-doubled and focused as well in the amplifying BBO crystal after filtering out the residual fundamental with the use of dichroic mirrors. On the crossing plane of the BBO crystal, the 400 nm pump, horizontally polarized, will transfer a part of its energy to the weak WL continuum through a wave-mixing process called *optical parametric amplification* (see below) [10]:

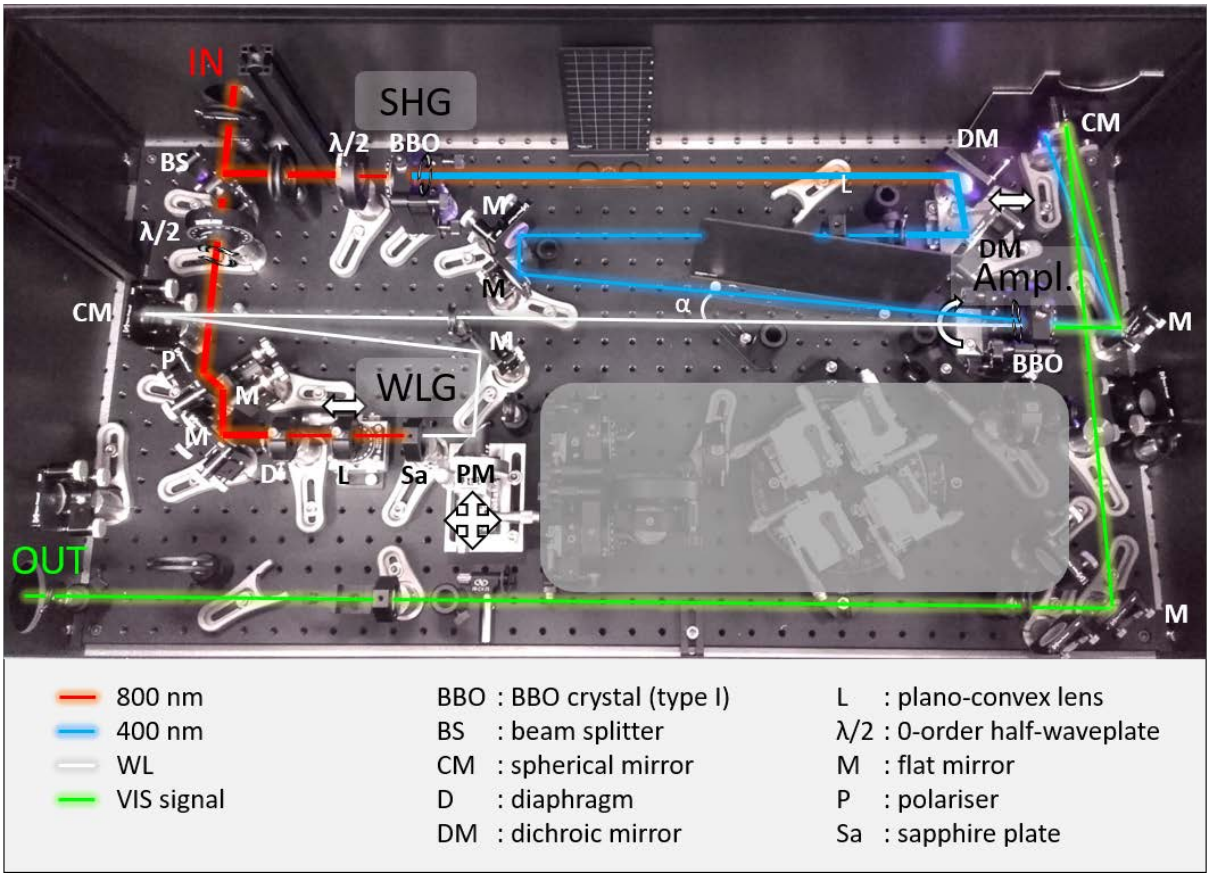

Figure 2.4*. Non-collinear optical parametric amplifier (NOPA) setup. It displays the second harmonic generation (SHG) part for the pump, the white-light (WL) generation, and its amplification (Ampl.). For clarity, the different beams were drawn and the different optic elements listed (legend below).*

Optical parametric amplification is a second-order nonlinear optical effect based on difference-frequency generation. It can occur under specific conditions in a birefringent medium (such as a nonlinear crystal) presenting a non-zero second-order susceptibility (*e.g.* BBO), in response to intense electromagnetic fields such as laser pulses. In an optical parametric amplifier (OPA), the energy transfers from a high-frequency (ω_p) and intense beam (the *pump*) to a lower intensity beam (the *signal) of frequency* ω_s, resulting in an amplification of this beam, whereas an additional beam (the *idler*), with frequency ω_i, is generated to fulfill energy and momentum conservation [10]:

$$\hbar\omega_p = \hbar\omega_s + \hbar\omega_i \qquad [2.7]$$

and,

$$\overrightarrow{k_p} = \overrightarrow{k_s} + \overrightarrow{k_i} \quad [2.8]$$

This second equation, linking the different beam wavevectors k, is called the *phase-matching condition*. The frequency of the amplified signal can then be varied over a certain range, as long as the phase-matching condition is satisfied. The non-collinear geometry of a NOPA compared to OPA gives an extra degree of freedom to satisfy this phase matching condition, the angle between the pump and signal beam, and, also allows to spatially separate the three beams.

We choose a type-I BBO crystal cut at 27.5°, with the crystal set perpendicular to the WL beam, to satisfy the phase-matching on a wide range of wavelengths for a phase-matching angle α between the pump and signal beams ranging from 4° to 6° [10]. The wavelength of the NOPA spectrum is tuned from 500 to above 650 nm by adjusting α, with the set of two dielectric mirrors, and timing Δt, with a delay stage on a manual translation stage, between the WL continuum and pump beam. We also can tilt the BBO crystal in the horizontal plane if needed as it is mounted on a rotational stage. The pump intensity is controlled with the size of an iris located before the focalization lens. Typical resulting spectra are shown in **Figure 2.5**. This allows us to selectively excite a chosen optical transition of the investigated samples. Some glass can be added in the WL path before amplification, chirping it further, to reduce the spectral bandwidth of the NOPA spectrum since only the part of the WL, which overlaps temporally with the pump will be amplified.

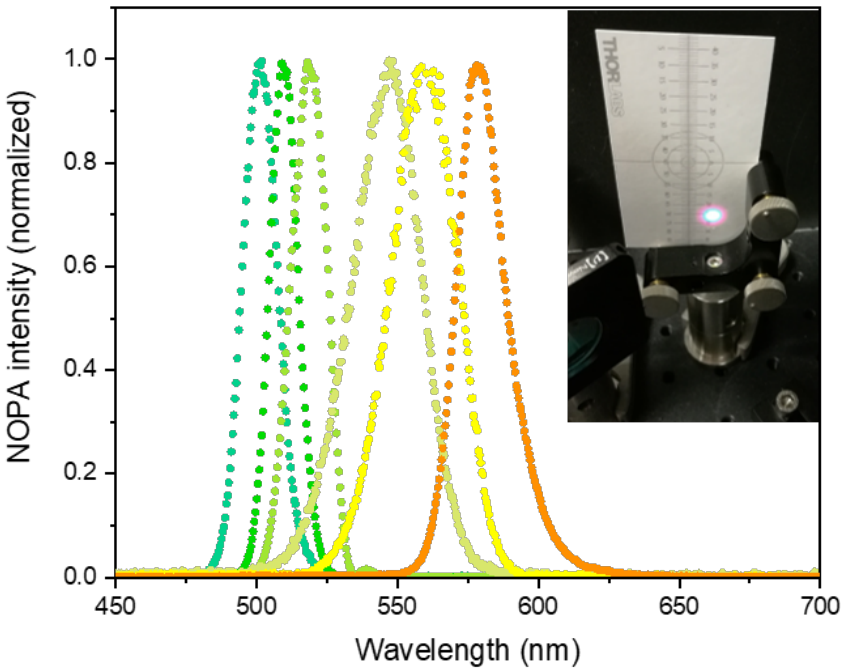

Figure 2.5. *Examples of NOPA spectrum used for the TA experiments, recorded with an optic fiber connected to a mini spectrometer (Flame, Ocean Optics). A picture of the WL beam before amplification is shown on the inset.*

2.1.2.3.4. 400 nm excitation (SHG)

In the case of 400 nm excitation, the 800 nm beam was just frequency-doubled using a type-I BBO crystal (1 mm thick, cut at 29.2°), and the residual fundamental beam filtered out using dichroic mirrors. This BBO crystal is much thinner than the one used for the SHG in TCSPC. Moreover, the laser beam does not need to be focused to get a good conversion efficiency. This is due to the much higher pulse energy.

2.1.2.3.5. Pump pulse compression

The pulses from the SHG and NOPA beam contain some "*chirp*". The different colors propagate at different velocities so that, after passing through the optical material, different wavelengths experience different delays, a ubiquitous effect called group-delay dispersion (GDD). In *positively* chirped pulses, the longer wavelengths (red) propagate

faster than the shorter (blue) ones in a medium with a refractive index $n(\lambda)$. This is particularly true for the broadband ultrashort pulses coming from the NOPA amplification, meaning that their temporal envelope can be minimized by removing the temporal dispersion between the different wavelengths. The earliest strategy to compensate for the GDD is based in the fact that the angular dispersion of a parallel pair of gratings or prisms induces a *negative* GDD as it is shown in **Figure 2.6.** This geometrical approach can compensate for dispersion without introducing losses [11].

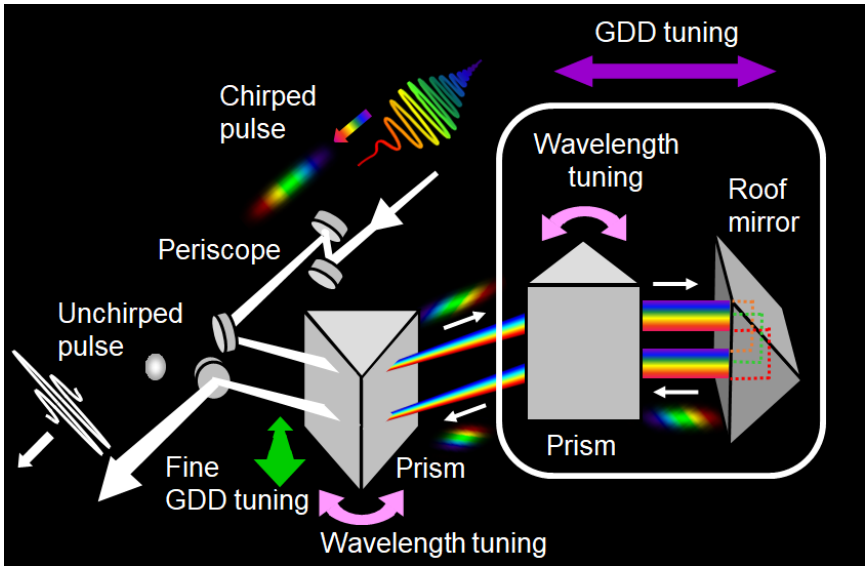

Figure 2.6. *Principle of a two-prism compressor. This device avoids the need for maintaining equal prism separations (note only one thick purple arrow). The chirped pulse beam profile is indicated in each step. The angular dispersion caused by the first prism generates also a pulse-front tilt which is corrected by the second prism. However, the opposite crossing pathway through the two prisms using the roof mirror is needed to correct the spatial chirp. Finally, an unchipped beam with the minimum spatio-temporal distortions can be obtained. See: Trebino group at GIT, https://frog.gatech.edu/pulse-compression.html).*

On the other side, a pair of chirped mirrors offer an alternative method for arbitrary order dispersion compensation. These dielectric mirrors consist of alternating pairs of transparent high- and low- refractive index layers. If the optical thickness of all layers is

chosen to be equal to $\lambda_B/4$, interference of all Fresnel reflections generated by the index discontinuity at the layer interfaces will constructively add up for the Bragg-wavelength λ_B. Varying the optical layer thickness along with the mirror structure during deposition then results in dependence of Bragg wavelength λ_B on penetration depth z, therefore allowing to delay the longer wavelengths relative to the shorter ones introducing the wanted *negative* GDD as it is shown in the **Figure 2.7**.

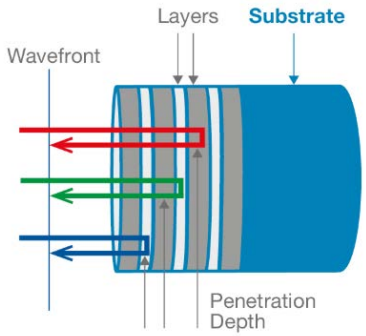

Figure 2.7. *Principle of a chirped mirror (Optics Balzers).*

A schematic layout of both compressors is shown in **Figure 2.7** for the pathway of the SHG beam (400 nm drawn in blue) and NOPA beam (visible drawn is green). Thus, both were compressed by several reflections on a pair of chirped mirrors (-25 and -40 fs^2 per bounce for 400 nm and visible beam respectively, from Layertec). Furthermore, the two-prism compressor was built for the visible NOPA beam. Both prisms, set at the minimum of deviation and with minimum of glass amount crossed by the beam, can be rotated by precisely the same amount using the large rotating plate (thick curved pink arrows in the **Figure 2.6**). This geometrical design requires a complex arrangement for fine-tuning the GDD and avoiding the remained angular dispersion, spatial chirp, and pulse front tilt.

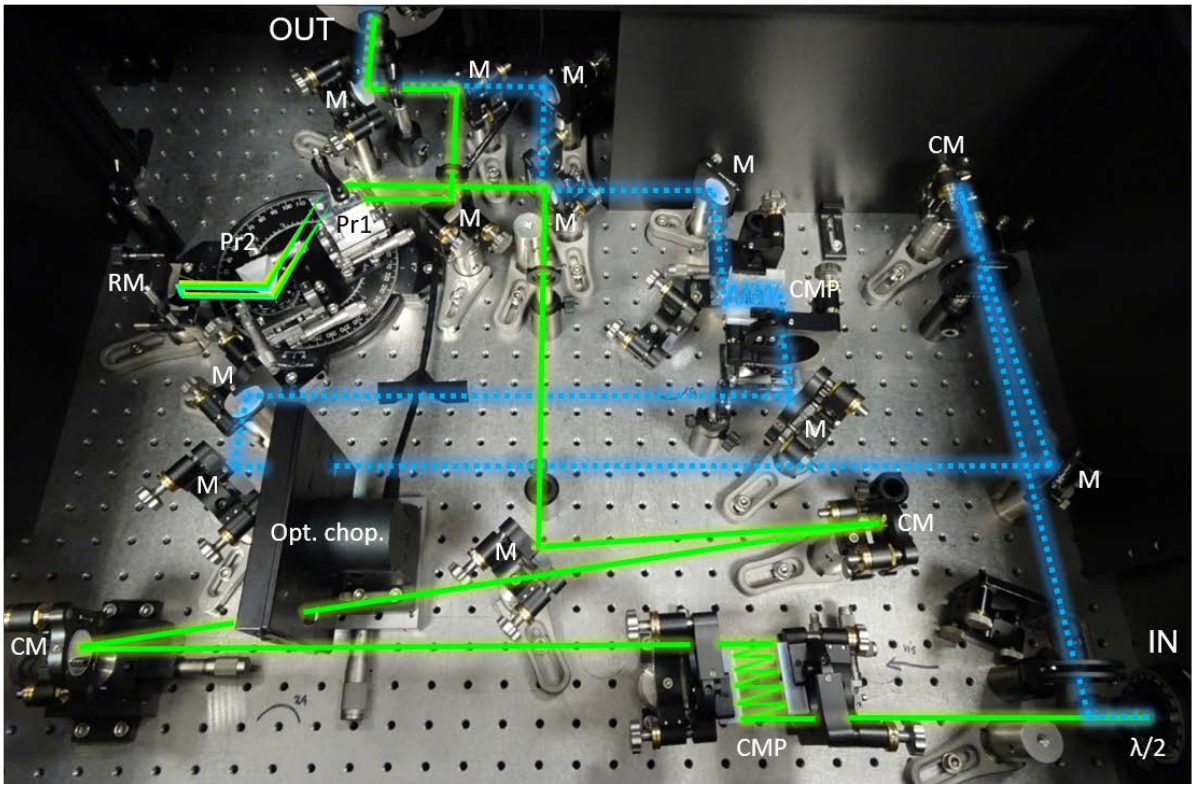

Figure 2.8*. Picture of the pump compressor box using chirped mirror pairs and two-prism compressor. Legend: λ/2: half-wave plate (here achromatic), CMP: chirped mirror pair, CM: concave mirror, Opt. chop.: optical chopper wheel, M: flat mirror, Pr1&Pr2: SF10 prisms, RM: roof mirror.*

2.1.2.3.6. UV excitation (SHG of the NOPA beam)

For the UV pump beam generation, the compressed visible NOPA beam was focalized on a type-I BBO crystal (3 mm-thick, cut at about 50°) for SHG (**Figure 2.9**). The frequency-doubled beam was collimated back with a plano-convex lens. The residual visible beam is filtered out using a polarizer and adapted dielectric UV mirrors in the path of the UV beam. The UV output was maximized in intensity by tilting the BBO crystal along the vertical plane to adapt the phase matching angle (horizontal incoming beam polarization).

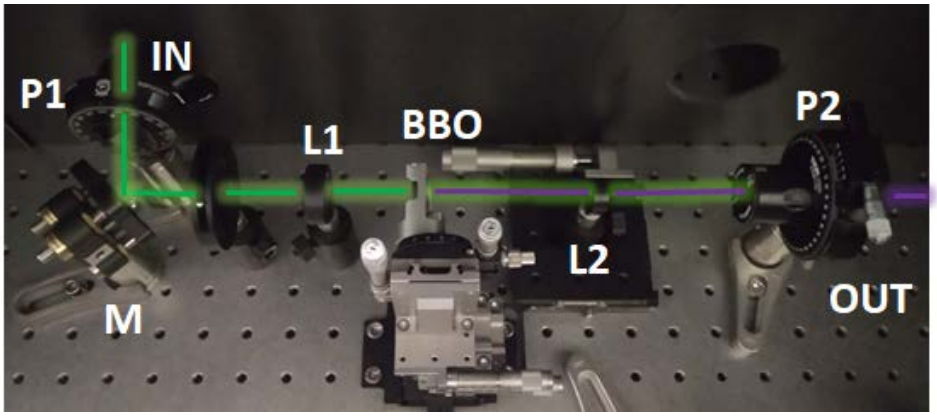

Figure 2.9. *Picture of the UV generation from the SHG of the compressed NOPA beam. Legend: P1: thin film polarizer, M: flat mirror, L1 & L2: plano-convex lenses, BBO: NLO crystal (type I), P2: cube polarizer.*

2.1.2.3.7. Details of the TA spectrometer

A picture of the fs-TA setup is shown in **Figure 2.10** to complete the previous schematics (**Figure 2.3).** While half of the fundamental 800 nm laser beam was used to pump the NOPA, the other 50 % was used to generate the probe beam through WL generation. Prior WL generation, the travel distance was adapted to compensate the long path length of the pump (NOPA or SHG + compressor distance) and then its pulse train is delayed with a retroreflector (UBBR2.5-1S, from Newport) mounted on a motorized translation stage (60 cm long, IMS600CCHA from Newport).

The mechanical translation stage plays a very important role in the pump-probe setup since it defines the time-axis. It can be moved with high precision (here 200 nm) and serves to introduce a temporal delay in the probe beam. Since the speed of light is constant, this temporal delay can be directly calculated as $\Delta t = 2\Delta x/c$, where Δx is the spatial displacement of the platform with the retroreflector introducing a path of $2 \times \Delta x$ in the 800 nm beam and c is the speed of light, which is constant and determined very precisely. To illustrate the power of this approach, a displacement of 150 ± 0.2 µm corresponds to a temporal delay of 1.001 ± 0.001 picoseconds.

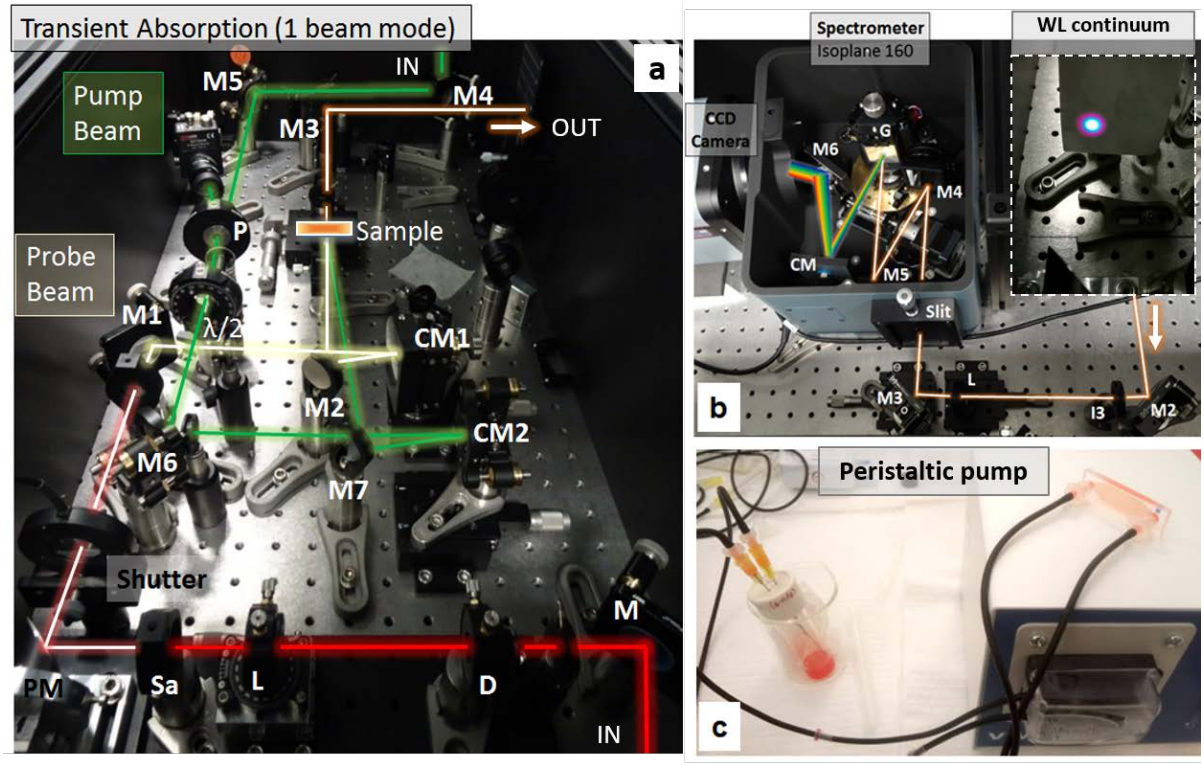

Figure 2.10. ***(a)*** *Picture of the TA box. The laser beams are drawn in red (800 nm fundamental), white (WL probe), and green (pump beam from NOPA or SHG). Legend: M: flat mirror, D: diaphragm, L: lens, Sa: Sapphire plate, PM: parabolic mirror, CM: concave mirror, P: polarizer, λ/2: half waveplate.* ***(b)*** *The detection system of the WL spectra using a spectrograph coupled to a CCD camera. The WL is focused on the entrance slit of the spectrograph using a lens (L). Its intensity is adjusted with ND filters to maximize the signal on the detector without saturation. A picture of the WL is shown in the inset. For the measurement, the red ring was cut off.* ***(c)*** *Picture of the flow system using a 1 mm-thick quartz cuvette, a peristaltic pump, and tubing adapted to organic solvents such as toluene and chloroform.*

Finally, a broadband white-light (WL) continuum probe beam is generated, just before the sample, in a thin Sapphire plate using a small fraction of the delayed 800 nm beam (this WL continuum is generated identically to that used in the NOPA part). After filtering, the typical WL spectra are shown in **Figure 2.11**.

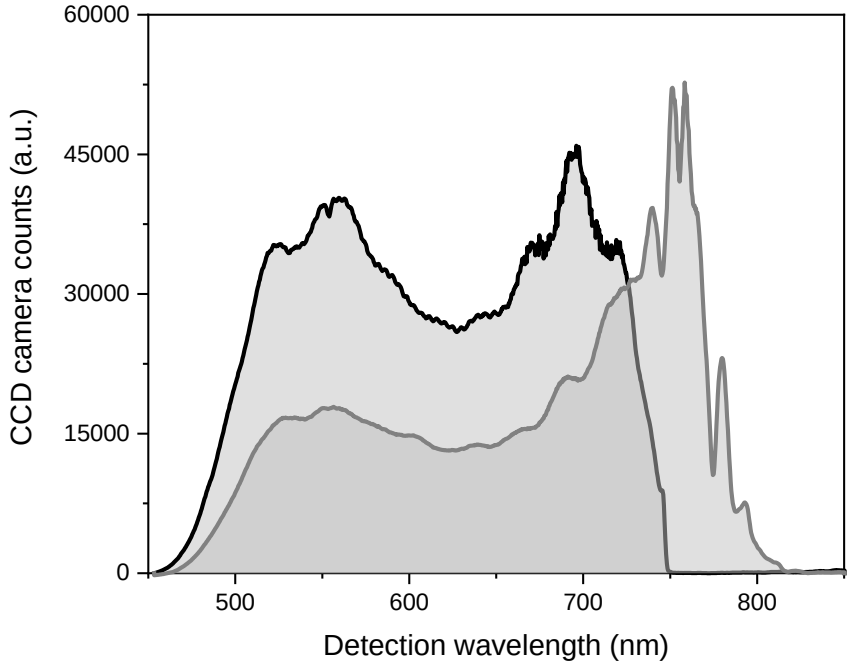

Figure 2.11. *Typical white-light spectra recorded with the CCD camera (sample: solvent only) with a short pass 750 nm filter (black, for NPL experiments) and with a combination of filters for a smoother cut (grey, for measurements on weakly-confined NC measurements with smaller bandgap energy).*

The polarization of the pump and probe beam were set vertical using an achromatic half waveplate. Before the sample, the pump power was controlled using neutral density filters. The WL was filtered to remove the residual 800 nm and reduced by 10 in intensity by a neutral density filter (ND). The probe and pump beams were focalized and adjusted to overlap at the center of the flow cell with a concave mirror (focal length 200 and 250 mm respectively). The beam waist at the focus was measured to be 39 ± 1 µm for the probe and 119.7 ± 0.7 µm for the pump beam at 400 nm (larger for visible wavelengths, see **ANNEXE 2**). After the sample, the transmitted probe beam is recollimated with a plano-convex lens and its spectrum was registered at 3 kHz by a commercial spectrograph (IsoPlane 160, Princeton Instruments) coupled to a CCD camera (ProEM-HS 1024B, Princeton Instruments). The intensity of the pump pulse is measured using a photodiode

(PD) using a back-reflection. This measure allows correcting data a posteriori for eventual pump intensity fluctuations in the case of low excitation fluence (see below).

All measurements of the colloidal perovskite nanostructures were carried out at room temperature in a 1 mm-thick flow cell connected to a peristaltic pump to refresh the sample at the focus position. This limits photodamage build-up and photo-charging effects. Flexible and organic solvent compatible F-5500-A fluoroelastomer (Saint-Gobain®) tubing and Teflon adaptors were used to build the flow system. The employed sample solutions were prepared with optical density (OD) below 0.3 at the excitation wavelength and longer wavelengths in anhydrous toluene or chloroform.

2.1.2.3.8. TA electronics

Even though the laser system works at 3 kHz, the repetition rate of the pump is reduced to half (1.5 kHz) to block one pulse out of two, allowing for measures with and without the pump as described below. This is achieved with an optical chopper (Newport 3502).

A transistor-transistor logic (TTL) signal at 3 kHz extracted from the laser Pockels cells was used as the reference for the electronics of the TA apparatus, to synchronize the frequency of the optical chopper in the pump arm, to trig a low jitter digital delay generator (Stanford Research Systems DG645) and a gated integrator (Stanford Research Systems SR250). The delayed TTL was used to trig the charge-couple device (CCD) camera to measure WL spectra at 3 kHz (*shot-to-shot*). The timing was set in order that the WL pulse arrives on the CCD during the exposition time. The gate integrator was used to integrate the intensity of each pump pulse through a photodiode (PD, 200-1100 nm, Thorlabs DET10A/M, at 3 kHz, to 1) register the pump fluctuations (output voltage proportional to the PD intensity integrated over the gate) and 2) to identify the ON and OFF pump pulses (pump at 1.5 kHz). Its output was sent to a data acquisition (DAQ) card (National Instruments USB-6211, 250 kS/s). This DAQ card was triggered by a TTL signal

of the CCD corresponding to the exposure time (3 kHz, rising edge). The motorized translation stage and the optical shutter in the probe and pump arms were directly controlled by LabVIEW software (National Instruments). The CCD camera was indirectly controlled by LabVIEW *via* LightField software (Princeton Instruments). To measure a spectrum of 1024 pixels at 3 kHz with the CCD camera (3000 frames/s), we use a fast-custom acquisition mode with a vertical binning of 64 pixels (13 µm each) over the region of interest (ROI) closest to the chip and an exposure time of 1 µs.

2.1.2.3.9. Signal detection and pre-treatment

The collected CCD data (WL spectra) measured at 3 kHz were transferred by a peripheral component interconnect (PCI) express port. The TA signal was calculated as follow:

$$\Delta A(\lambda, t) = -log\left(\frac{1}{m}\sum_{k=0}^{m-1}\frac{I_{2k}^{ON}(\lambda,t)-I_{fluo}(\lambda)}{I_{2k+1}^{OFF}(\lambda,t)-I_{dark}(\lambda)}\right) \quad [2.9]$$

with $I(\lambda,t)$ the WL spectrum measured at a pump-probe time delay t with the pump "ON" for a pulse $2k$ (even) and the pump OFF for the following pulse $2k$+1 (odd), $I_{\text{fluo}}(\lambda)$ the spectrum recorded with the probe beam blocked, $I_{d\text{ark}}(\lambda)$ the spectrum measured with both pump and probe blocked and m the number of ON/OFF kinetic cycle pairs to average at one position of the translation state (for each different t).

Both $I_{\text{fluo}}(\lambda)$ and $I_{d\text{ark}}(\lambda)$ correspond to background spectra that need to be subtracted before performing the ratio of the WL spectrum. They are collected just before the scan collection, averaged over 3000 pulses. This is a quasi- shot-to-shot measurement based on the fact that two consecutive pulses have strongly correlated intensity. Thus, the measured differential spectrum results from the pump interaction effect on the sample absorption and not from the change of intensity of the WL pulses over time, which can be

assumed to be negligible. The sensitivity of the measured ΔA signal is about ± 2.10^{-4} (optical density) for m= 250, in the optimum wavelength range (480-740 nm), before scan averaging. The number of measured scans was typically varied from 1 to 10 for excitation fluence dependency measurements due to the finite stability of the recirculating sample. At low excitation fluence, the TA signal is directly proportional to the pump power. In this linear regime, ΔA can be further corrected by the pump fluctuations measured with the PD and boxcar integrator. The full 2D TA spectrum, resolved in wavelength and in time, is called a TA map.

2.1.2.3.10. The temporal resolution of the fs-TA setup

The temporal resolution is estimated from the measurement of the non-resonant response of the solvent, a signal occurring only during the pump-probe temporal overlap in the sample cell due to cross-phase modulation and often referred to as a "*coherent artifact*" (**Figure 2.12**).

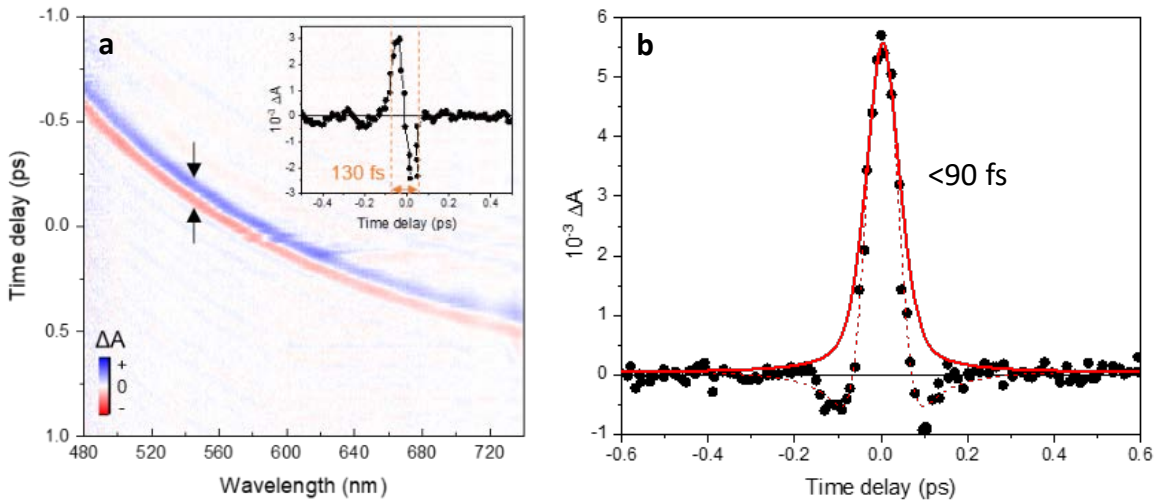

Figure 2.12. ***(a)*** *TA map of the solvent response (toluene) excited at 400 nm. The chirp of the WL is seen by the change of the position of t=0 with the wavelength. At a given wavelength, the width of the non-resonant signal gives an estimation of the temporal resolution. An average over the wavelength (chirp corrected) gives the graph in the inset, with a signal within 127 fs.* ***(b)*** *Solvent response time trace recorded with chirped mirror pair in the 400 nm beam path.*

In TA, the temporal resolution is limited by the pump and WL pulse duration. From the TA map of the solvent response shown in **Figure 2.12a**, we can see that the probe pulse presents a large chirp, as the time-zero is wavelength-dependent. This chirp was corrected posteriori using a routine program (see below), such that the corrected TA spectra, like the single-wavelength TA decay traces, are limited essentially by the duration of the pump pulse. Here we remark that to perform this correction successfully, the TA spectrum must be sampled very densely during the whole duration of the chirp, *i.e.* the first picosecond.

Without compressor in the pump path, the temporal resolution was measured to be about 130 fs in FWHM (inset **Figure 2.12a**). By building the compressor(s) and using mainly reflective optics in the spectrometer (ND in reflection), the temporal resolution was decreased to about 90 fs (**Figure 2.12b**). From the bandwidth of the pump spectrum, we would expect a minimal temporal resolution of about 50 fs for the 400 nm beam (transform-limited energy to time product for a Gaussian pulse) and lower in the case of the NOPA beam. Nevertheless, the compression down to sub-100 fs was essential for the cooling measurement of NPLs presented in **Chapter 3**.

2.1.2.3.11. Data treatment

The TA data acquired from Labview® were analyzed using a home-written program in Octave®. It consists of averaging the datasets, removing the static scatter (signal at t<200 fs), and correcting the group velocity dispersion (chirp) of the white-light to extract the accurate TA spectra in case of t < 1 ps. For the chirp correction, first, the wavelength-dependent time-zero $t_0(\lambda)$ in ps was fitted with a polynomial function:

$$t_0(\lambda) = \mu_0 + \mu_1\lambda + \mu_2\lambda^2 \qquad [2.10]$$

Where, λ_0 is the central wavelength in nm typically taken at the maximum signal amplitude and μ_0, μ_1 and μ_2 the 0-, 1- and 2-order polynomial constant. The polynomial parameters can be extracted after retrieving manually several $t_0(\lambda)$ points in the experimental solvent TA spectra or given by the Glotaran global analysis program (see below) of the sample TA map (see below). Then the 2D matrix $\Delta A(\lambda,t)$ is modified by shifting the vertical data in time at each wavelength to "align" the time-zeros horizontally to have a common time-zero (see **Figure 2.13**)

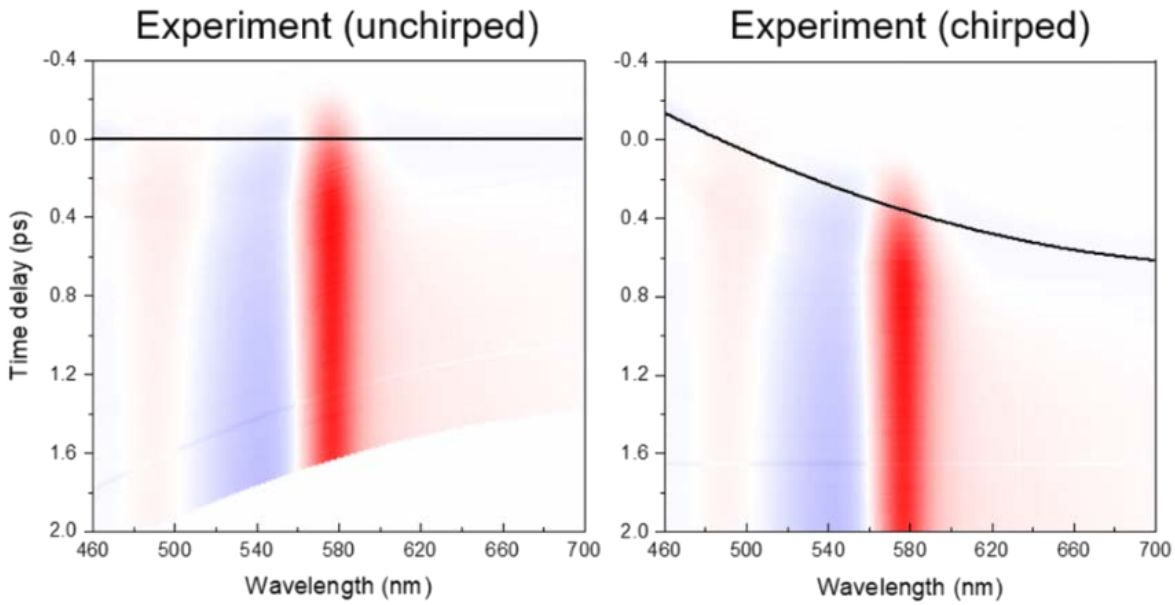

***Figure 2.13**. Example plot of the TA maps of colloidal NPLs (n=2) excited at high fluence at 400 nm, after (left), and before (right) chirp correction. The black lines are a visual aid corresponding to t=0.*

2.1.2.3.12. Origin of the TA signals and spectral lineshapes

Transient spectra present a more complex structure than TR-PL ones as they contain several different contributions. Two main effects contribute to the TA signal $\Delta A(\lambda)$ in confined semiconductor nanostructures: state filling due to Pauli exclusion, and the Stark effects due to Coulomb interactions [12].

State filling or photoinduced bleach

The signals from the first effect arise to the fact that the optical pump creates a population of excitons, which results in a decrease of the absorption of all-optical transitions related to the corresponding excited electron and hole states. Indeed, electrons (and holes) are fermions particles that cannot occupy the same quantum state within the same place (Pauli exclusion principle). Thus, state filling gives rise to strong bleach features of the *discrete* optical transitions involving excited states populated with electron and hole [12]. The reduction of absorption leads to an increased number of photons on the detector and thus these photoinduced bleach (PIB) features are purely negative in the TA signal convention specified earlier (**Equation 2.6**). This can be simulated by Lorentzian or Gaussian functions depending on the optical transition (see **Figure 2.14a**). The evolution of the bleach signal in time allows us to follow the population and depopulation of the excited states and thus is essential to investigate the dynamics in semiconductor nanostructures.

Stark effects

Stark signals have a large contribution to the TA signals of nanostructures. On one hand, it can be understood as a shift in the energy of the probed optical transitions due to local fields originating from the presence of charge carriers photo-generated by the pump pulse (carrier-induced Stark effects) [12]. We should note that this is a non-selective effect as all the optical transitions involving populated and unoccupied states are affected. On the other hand, Coulomb interactions arising from exciton-exciton interactions also lead to a spectral shift, which is the biexciton binding energy [13]. Both cases give first derivative-like features of the differential spectrum $\Delta A(\lambda)$, centered at the optical transition energy, with equal negative and positive signals (**Figure 2.14c**). The amplitude and sign of the Stark signals are given by the value of the energy shift [12].

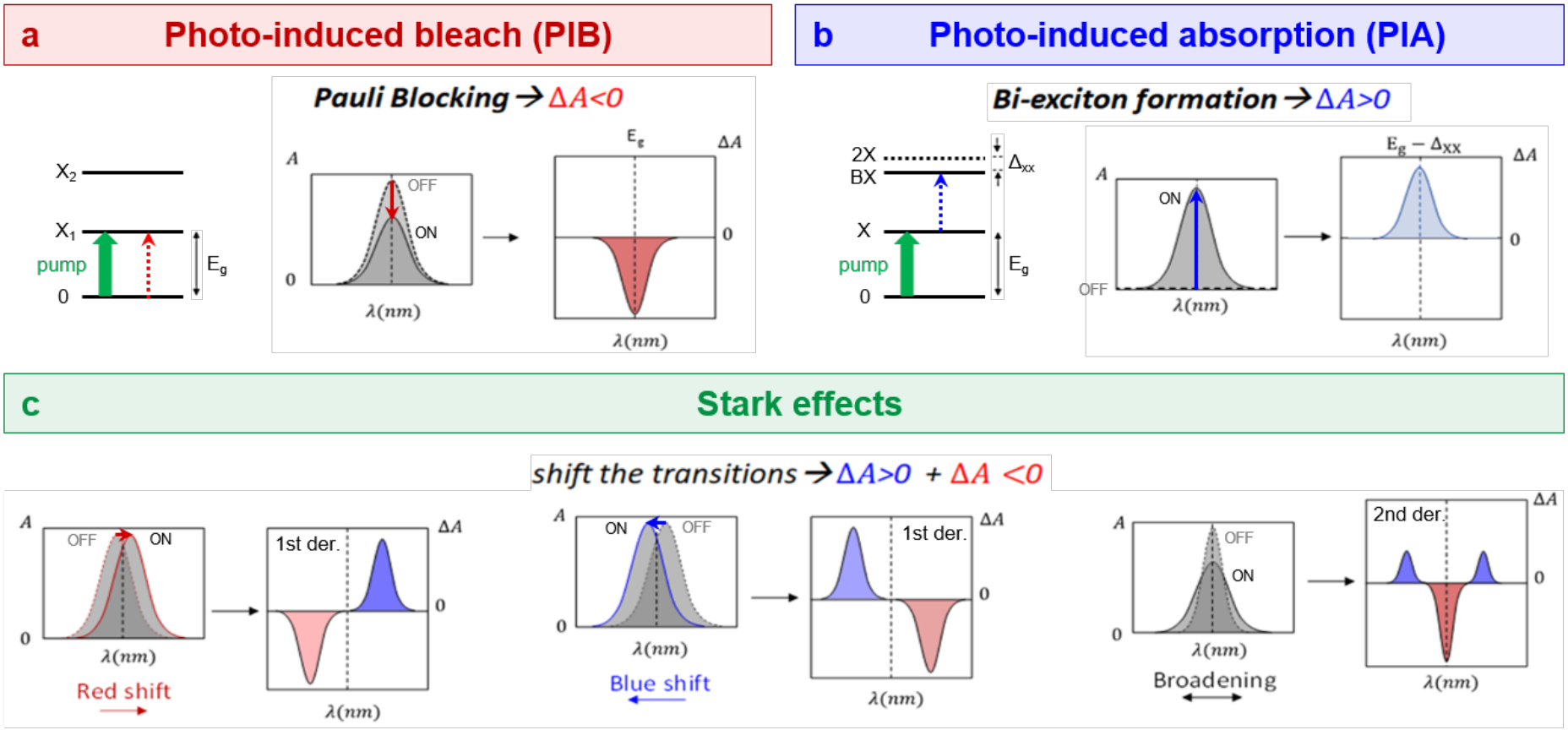

Figure 2.14. *Schematic of the origin of the transient signals ΔA due to photo-induced bleach* ***(a)****, photo-induced absorption (****b****, in the case of excited state absorption), and pure Stark effects* ***(c)****. In* ***(c)****, the related linear absorption spectra for "OFF" and "ON" pump pulses are displayed for three the different possibilities: low-energy shift (left), high-energy shift (middle), and broadening (right). The positive (negative) TA signal is displayed in blue (red).*

For the carrier-induced Stark effect, we expect the sign of the shift (*i.e.* blue- or red-shift) to depend on the relative orientation between the dipole of the optical transition and the electric field. For example, destabilization of the exciton by spatially separating the electron from the hole should result in a decrease of the exciton binding energy and thus a blue shift of the optical transition. Furthermore, Stark shifts will be particularly important when the intrinsic electric field is in the direction of the confinement, as it modifies the energy of the electron and hole (or exciton) states. For example, a large red-shift was measured in quantum wells when an external electric field was applied perpendicularly to the plane [14]. In case of non-selective excitation dipole orientation, *e.g.* in the dense high-energy excited states, the resulting random electric field should lead to a broadening of the probed optical transitions, similarly to the spectral diffusion broadening observed in the PL spectrum (integrated in time) of single colloidal semiconductor NCs [15]. This effective broadening of the transitions gives an overall second derivative lineshape in the TA spectra (**Figure 2.14c)**.

As for exciton-exciton interaction, it usually leads to a redshift of the transitions (stabilization) but can result in a blue shift in the case of reduced overlap between the hole and electron wavefunction (more electron-electron and hole-hole interactions than electron-hole ones) [16].

Other TA signals

Positive signals can arise from the absorption of new species appearing in time or new possible transition from populated excited states (**Figure 2.14.b**). In the first case we talk about photoinduced absorption (PIA). In the second case we referred to the excited state absorption (ESA), which in semiconductor nanostructures is mainly link to the biexciton absorption (X state to BX state).

Carrier induced Stark effects strongly shifts the discrete excitonic states of confined perovskite materials but also modified the energy of the electronic bandgap. This band gap renormalization (BGR) is seen in bulk and in confined nanostructure [17].

2.1.2.3.13. Data fitting

Global analysis for early time dynamics

The foundation of global analysis based on singular value decomposition (SVD) is the superposition principle, which states that the evolution in time of the complex TA measured data $\Delta A(\lambda,t)$ result from the overlapping spectral components from the different states/species of the system. The main assumption is that time and wavelength properties are separable, which means that the spectra of states/species are constant, only their amplitudes change in time. This model is known as a compartmental model.

In a simple sequential kinetic model, each state is characterized by a unique spectral component called "Evolution Associated Spectra" (EAS_i). These are related by decreasing rate constants. The full dataset $\Delta A(\lambda,t)$ can thus be described as:

$$\Delta A(\lambda,t) = \sum_{i=1}^{n}\left(M_i EAS_i(\lambda) - M_{i-1} EAS_i(\lambda)\right) \qquad [2.11]$$

with the associated time-dependent amplitude $M_i(t)$:

$$M_0 = 0$$

$$M_i(t) = \frac{1}{2} exp(-k_i t) exp\left[k_i\left(t_0 + \frac{k_i\tilde{\Delta}^2}{2}\right)\right]\left[1 + erf\left[\frac{t-(t_0+k_i\tilde{\Delta}^2)}{\sqrt{2}\tilde{\Delta}}\right]\right] \; for\; i > 0 \qquad [2.12]$$

Assuming a Gaussian instrument response function (IRF), with full width at half maximum Δ and centered at t_0 (time zero of the pump probe overlap) [18]. We have $\tilde{\Delta} = \Delta/\left(2\sqrt{ln(2)}\right)$. In this first order approximation, M_i is a mono-exponential decay function (first term) that is convoluted with the IRF (giving the second term). The last term is a step function, more or less smooth depending on Δ, to generate the signal starting around t_0.

Glotaran® software[19] was used with a sequential model to fit the global TA map with 2-3 exponential kinetic parameters. Here, the global analysis considers the IRF as a Gaussian function. Also, it compensates for the dispersion using a polynomial function (2^{nd} order). In the case of high excitation fluence, an extra coherent artifact can be introduced.

In **Chapter 3**, we will see that the lineshapes of the measured transient spectra at early times (t < 1 ps for the NPL) strongly evolve as their physical origin. For the weakly confined perovskite samples, spectral changes still occur up to a few hundreds of ps.

Single decay trace fit for longer time dynamics

We found that the TA spectra do not evolve much in terms of lineshape for the perovskite NPL samples at t > 1 ps, but only change in amplitude. In this case, the TA signal can be analyzed in terms of a single decay trace. This decay trace can then be analyzed in the same way as in TR-PL decay traces using a convolution between the IRF and multiexponential function. In that case, however, the IRF approximated by a Gaussian present a much reduced temporal FWHM (between 70 to 90 fs) for the experiments with the pump compressed.

2.2. Synthesis of colloidal perovskite nanostructures

2.2.1. Introduction to the wet chemical methods

Solution-phase methods represent probably the most viable synthetic routes for the production of nanomaterials in terms of relatively easy implementation and low cost for several applications. Among them, colloidal synthesis had become an approach of choice for the fabrication of nanostructures with well-defined size, with low size dispersion and high crystallinity, that are so important to control the resulting optical properties of the nano-objects. In this bottom-up strategy, the chemical reaction and the nucleation process are controlled by several parameters, such as the temperature, the solvents and the precursor concentration. Also, the addition of ligands (surfactant molecules) plays a major role in the nucleation step in term of reactivity of the precursors and in the growth that they regulate in term of size and morphology. Moreover, these long chain molecules insure the colloidal stability of the dispersion of nanostructures and their surface passivation [20].

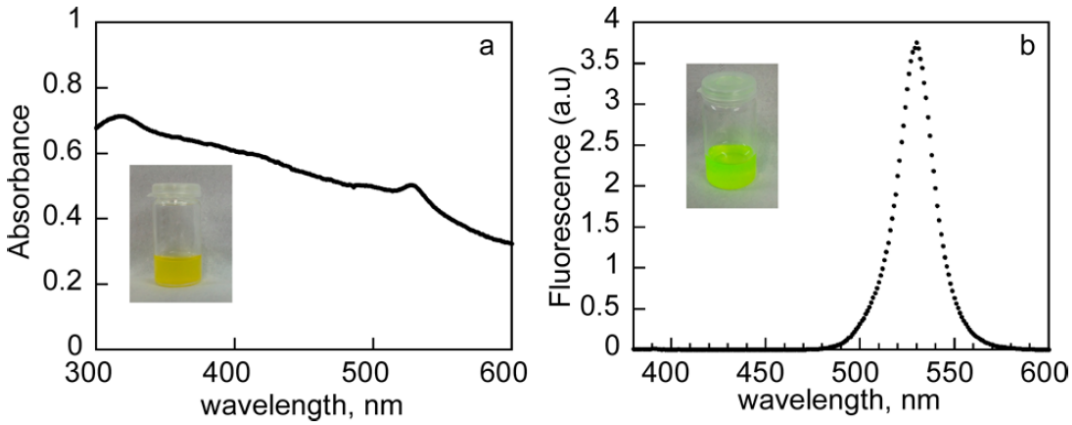

Figure 2.15. *Absorption (a) and photoluminescence (b) spectra of $MAPbBr_3$ NCs dispersed in toluene. Inset: pictures of the sample under ambient light (a) and UV illumination(b). Spectra from reference* [21]. *The lack of well-defined feature in the absorption spectrum is due to scattering signals resulting from large nanoparticles in suspension.*

The group of Pérez-Prieto in 2014 reported the first proof of concept of the synthesis of halide perovskite nanocrystals dispersed in toluene using a precipitation method [21]. The

resulting $MAPbBr_3$ NCs had good crystallinity but suffer from low size dispersion control, as can be seen in the corresponding spectrum **Figure 2.15**. This work was followed by the development of several synthetic routes, based on precipitation, to obtain halide perovskite colloidal nanostructures of various compositions and shapes [22]. The two major approaches are the hot-injection and the ligand assisted re-precipitation methods presented below **(Figure 2.16)**.

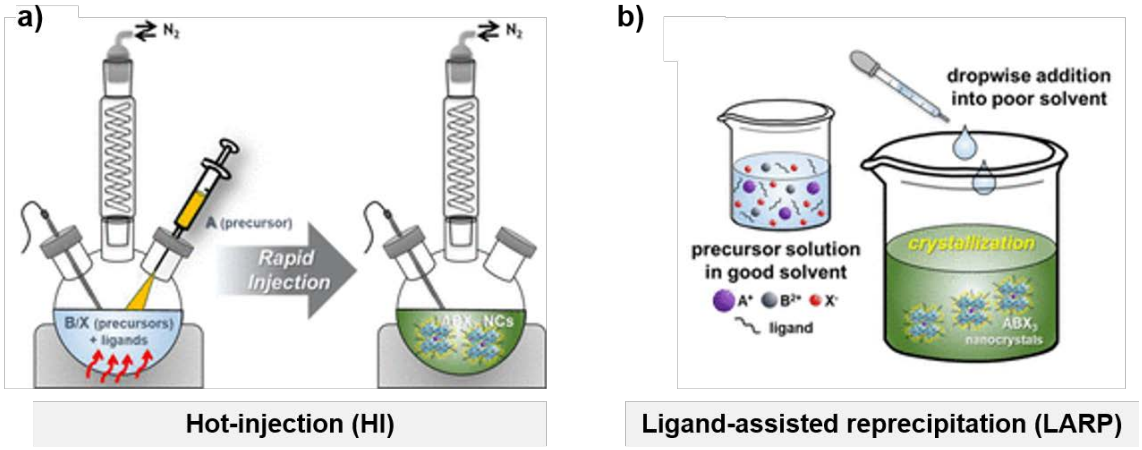

Figure 2.16. *Schematic description of the two representative synthetic methods to prepare colloidal halide perovskite nanocrystals:* ***(a)*** *the hot-injection and* ***(b)*** *the ligand assisted re-precipitation (LARP) methods* [23].

2.2.1.1. Hot-injection (HI) method

The hot-injection technique is a well-established method to prepare high-quality colloidal NCs, which was developed in 1993 for metal chalcogenide semiconductor NCs [24]. The synthesis of monodispersed colloids is achieved by the rapid injection of a hot reactant solution into other dissolution of the precursor solubilized in an organic solvent at high temperature and under inert atmosphere. By injecting the precursor solution as quickly as possible, the monomer concentration increases rapidly to reach the threshold of nucleation (called the "burst of nucleation" [24]. The formation of nuclei induces a drastic decrease of the monomer concentration under the nucleation threshold where the

nanocrystals can only grow. The separation of the nucleation and growth step allows to obtain nanoparticles with very good size dispersion. Then, the subsequent growth is stopped by the decrease of the temperature (quenching). The nanocrystal size can be varied with the injection temperature, the relative compositions of precursors and ligands, and/or the crystal growth period.

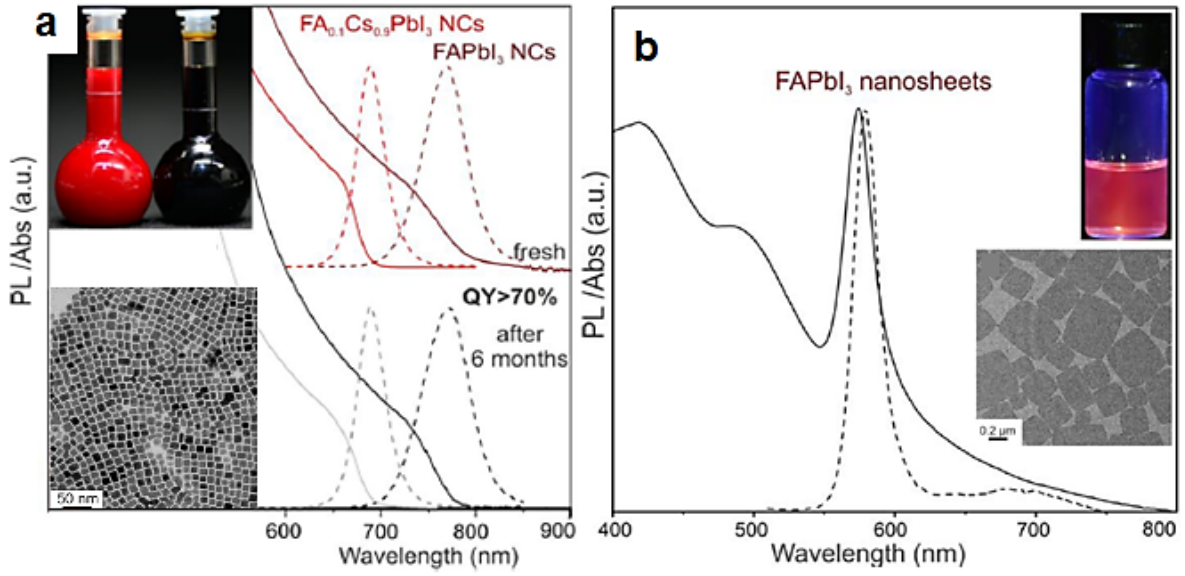

Figure 2.17 (a) *Absorption (full lines) and PL (dashed lines) spectra of $FAPbI_3$ and $FA_{0.1}Cs_{0.9}PbI_3$ NCs before (up) and after time aging (down). The solution flask and TEM pictures are also displayed.* ***(b)*** *PL and absorption spectra of FA-Pb-I nanosheets.* ***Inset:*** *picture of the colloidal solution under UV illumination and TEM image of the nanosheets. Adapted from* [25].

2.2.1.1.1. Adaptation of the HI method to perovskite

The adaptation of this protocol for halide perovskites NCs was developed in 2015 by Kovalenko and coworkers in the case of $CsPbX_3$ (X=Br,Cl, I) [26]. Solution of cesium oleate was injected at moderated temperature (140-200 °C) into a reaction flask containing the lead halide precursors dissolved in a non-coordinating organic solvent (1-octadecene, ODE) with ligand molecules as long chain amines (usually oleylamine, OLAm) and carboxylic acids (oleic acid, OA), all under inert gas atmosphere (**Figure 2.16a**). This

results in high-quality cubic NCs of 4-15 nm in size that can be redispersed in toluene. Recently, the methodology was extended to the $FAPbI_3$ composition by the same group with lower injection temperature (80 °C) [25]. $FAPbI_3$ and FA-doped $CsPbI_3$ nanocubes of 10-15 nm were synthesized with an emission wavelength extended up to the near-IR (**Figure 2.17a**). In the same article, the authors also reported the synthesis of n=2 nanosheets with lateral sizes of 100-600 nm formed with the same HI procedure but at temperatures below 50 °C (**Figure 2.17b**).

Advantages and drawback of the HI method

In the HI method, the complete dissolution of the precursors is generally required. For halide perovskite NCs, this can imply an overnight heating of the precursors in a 1-octadecene solution together with the ligands. Moreover, the precursor solution and NC synthesis are prepared under controlled (inert) atmosphere at moderate temperature which involves a full chemical synthesis setup with a double Schlenk line, flask with heating mantle, temperature probe and controller.

The perovskite NCs synthesized by the HI method have a high crystallinity due to high-temperature growth, as well as uniform particle sizes (about 5-10 % deviation from the mean size). Typically, the cubic NCs synthesized by the HI method present the highest PL QY reported for halide perovskite NCs (e.g. > 70 % for $FAPbI_3$).

2.2.1.1.2. Toward different morphologies

The impact of the temperature and of the type of ligands on the morphology of perovskite nanostructures in the HI method was studied in cesium lead bromide perovskite nanostructures by Pan *et al.* [27]. The authors found that a higher injection temperature results in general to isotropic nanocubes (there at 170 °C) while lower temperature (140

°C) always leads to nanoplatelets (see **Figure 2.18**), similarly to the work of Alivisatos *and co.* [28] and in agreement with the more recent publication of Kovalenko *and co.* for $FAPbI_3$ [25]. The 2D growth can be understood as a difference of reaction kinetics between different crystal facets enhanced at low and moderated temperature [29]. It can also results from a templating effect from the van der Waals attraction between the sidechains of ligands attached to the surface [28]. Interestingly the authors found that shorter chain of linear amines result in thinner NPLs [27].

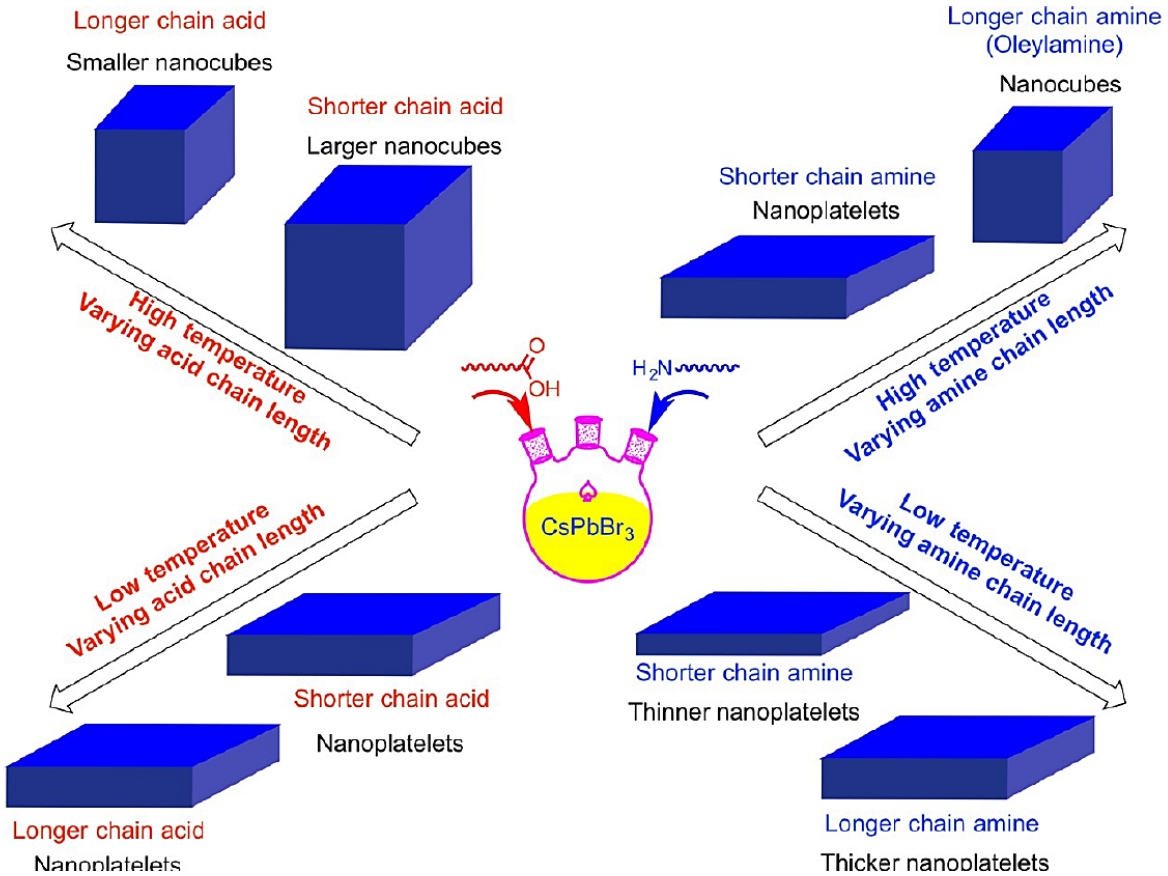

Figure 2.18. *Summary of the shape and size dependence on the chain length of carboxylic acids and amines on $CsPbBr_3$ perovskite colloidal nanocrystals* [27].

2.2.1.2. Ligand-assisted re-precipitation (LARP) method

The relatively low formation energy for ionic bonds in halide perovskite structures allows the synthesis of these materials at room temperature. However, as mentioned previously,

the HI method requires the complex task to dissolve the ionic precursors in a non-polar solvent, which is often completed at elevated temperature with the help of amines and carboxylates.

An alternative method consists in the use of a small amount of polar solvents to dissolve the precursor salts. The mixture of precursors is then added quickly to a nonpolar solvent to induces a recrystallization process that will form the perovskite structure (**Figure 2.16b**) [30]. This new method, known as *ligand assisted re-precipitation* (LARP), was proposed by Zhang *et al.* in 2015 to synthesize hybrid $MAPbX_3$ NCs.

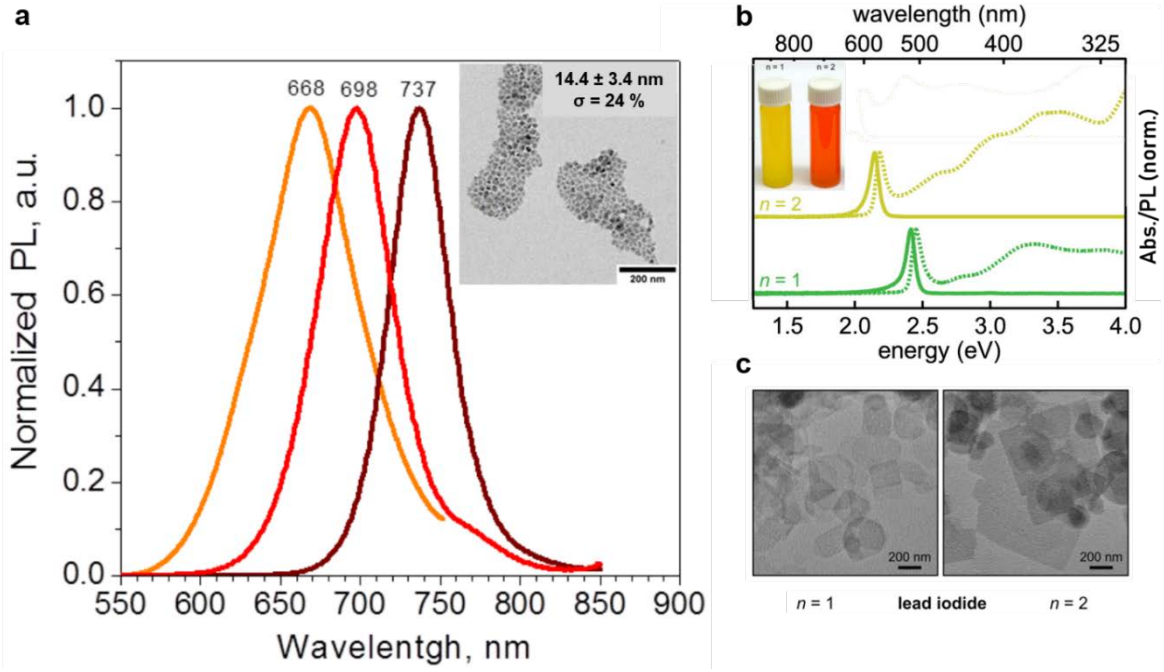

Figure 2.19. (a) *Photoluminescence spectra of colloidal $FAPbI_3$ NCs using different amounts of oleylamine ligands (larger amounts give smaller sizes and thus bluer PL emission). Inset: TEM picture of $FAPbI_3$ NCs and corresponding size distribution. Extracted from ref* [31]. ***(b)*** *Absorption (dotted lines) and PL (solid lines) spectra of n = 1 (L_2PbI_4) and n = 2 ($L_2[FAPbI_3]PbI_4$) colloidal NPLs. Inset: NPLs suspensions in toluene under ambient lighting.* ***(c)*** *Corresponding TEM images*[32].

The quantity of polar solvent must be minimal to ensure the stability of the perovskite structure (*i.e.* to not dissolve it). Moreover, it needs to be at least partially miscible with the nonpolar solvent. The dissolution of the precursors salts, AX and BX_2, is obtained in

dimethylformamide (DMF), as well with the ammonium ligand molecules (*L*X). One drop of this mixture is added to a large amount of a poor solvent such as anhydrous toluene or chloroform, eventually with the presence of carboxylic acids and alkyl amines. All this process can be realized at RT under ambient atmosphere.

Brabec *et al.* used the LARP method to synthesized large $FAPbX_3$ colloidal NCs [31]. By changing the oleylamine ligand quantity used in the synthesis, several sizes can be obtained, as shown with the corresponding PL spectra of the NCs presenting weak quantum confinement effect (**Figure 2.19a**).

2.2.1.2.1. 2D colloidal nanoplatelets using LARP

The LARP methodology was also employed for the synthesis of 2D perovskite nanoplatelets. Since 2015 Tisdale and coworkers reported the synthesis of methyl-ammonium lead bromide (MAPBr) NPLs with the LARP procedure [33]. One year later, the same group reported the extended protocol to other compositions, using other cations (FA, Cs, in addition to MA), other halides (Cl, I, in addition to Br) and Sn in addition to Pb [32]. An example of this is displayed in **Figure 2.19 b,c** for the cases of n=1 and n=2 (formamidinium) lead iodide perovskite NPLs. The procedure to obtain NPLs with a well-defined thickness population (the number of monolayers n and distribution ± Δn) consists in preparing stock solutions (AX, BX_2, *L*X) in DMF and to mix them within a specific stoichiometric ratio before injecting the mixture in the toluene, at RT, under vigorous stirring (**Figure 2.20**). The stoichiometric ratio *L*X:BX_2:AX is defined by the final expected ratio in the NPLs, which formula can be written as $(LX)_2(BX_2)_n(AX)_{n-1}$. For example, for n=1 a stoichiometric ratio of 2:1:0 is used whereas for n=2 it is 2:2:1.

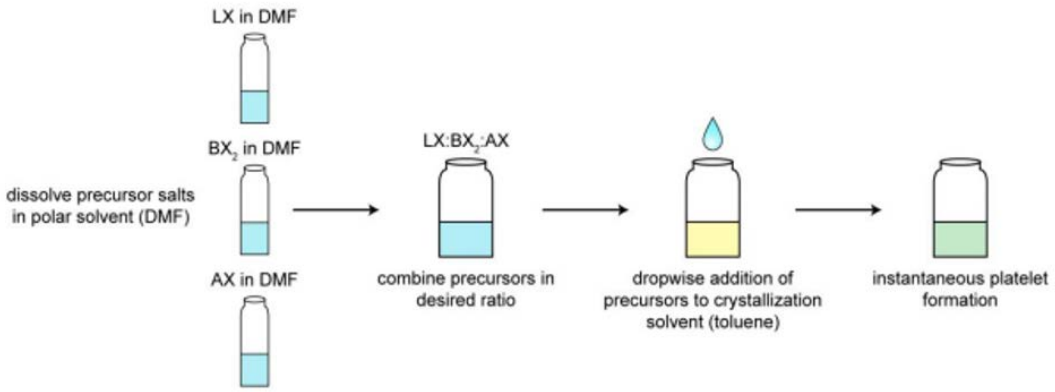

Figure 2.20. *Schematic of the LARP procedure to synthesize colloidal halide perovskite NPLs* [32] .

2.2.1.2.2. Advantages and drawback of the LARP method

The LARP method has the advantage to be an easy procedure to synthesize colloidal perovskite nanostructures. Moreover, the possibility to implement it under ambient conditions (room temperature, under air) without complicated equipment allows the possibility to upscale it to a high-scale level [34].

However, the low temperature preparation might imply a lower crystallinity and stability of the perovskite nanostructures compared to the ones synthesized *via* the HI method [35]. In particular, the morphology and the size dispersion of the NCs synthesized with the LARP method are not as well-defined as the cubic NCs obtained with the HI method, but they exhibit a high PL QY of about 55% [31]. In addition, the LARP method applied to NCs often requires a post separation and purification steps for the thickness control and size dispersion, respectively [35].

Unlike halide perovskite NCs, 2D NPLs synthesized from LARP can have a very well-defined thickness distribution that can be controlled to a high precision with the precursors/ligand ratio used. The remarkable optical properties of these objects make the LARP method a method of choice for us to synthesize the perovskite NPLs during this thesis.

2.2.1.2.3. Other synthetic methods: external stimuli-induced colloidal methods.

In addition to the HI and LARP, other methods have been employed to synthesize colloidal perovskite nanostructures. In 2016, Tong et al. first reported a single step *ultrasonication-assisted* synthesis to produce $CsPbX_3$ NCs with a tunable halide composition. However, the thickness and morphology was not well-controlled [36].

On the other side, the *exfoliation* using sonication allowed the synthesis of different colloidal NPLs. However, a mixture of NPL population is obtained and then requires further separation steps [37].

2.2.2. Experimental syntheses protocols developed

The main objective of this thesis is to study ultrafast processes, such as hot exciton relaxation and Auger recombination, in colloidal perovskite nanostructures. As previously described, these phenomena are enhanced in confined systems. To investigate how the confinement affects these processes, a precise control of the nanostructure dimensions is required.

The first approach was to synthesize both weakly confined $FAPbI_3$ NCs and strongly confined FAPI NPLs using reported protocols. In the case of the NPLs samples, a well-defined thickness (i.e. number of monolayers) with other chemical compositions such as CsPI and MAPI NPLs was desirable. The chemical list of all the reactants used in the different syntheses can be found in the **ANNEXE 2**.

2.2.2.1. Synthesis of weakly confined $FAPbI_3$ nanosystems.

2.2.2.1.1. Synthesis of $FAPbI_3$ nanocubes by the "hot injection" method.

First, the $FAPbI_3$ nanocubes were synthesized using the HI method developed by Kovalenko and *co.* [35]. This synthesis requires a Schrenk line that was not available at LIDYL laboratory, so it was done in collaboration with Benoît Mahler at ILM in Lyon as follows:

A solution of PbI_2 was prepared by dissolving 0.187 mmol of PbI_2 in a mixture of vacuum-dried ODE (5 mL), OA (1 mL) and OLAm (0.5 mL) at 80°C under argon. FA-oleate (~0.25 M) was prepared by dissolving FA-acetate (5 mmol) in a mixture of ODE/OA (16/4 mL, vacuum-dried) at 130 °C under argon. The mixture was then dried under vacuum for 30 min at 50 °C. The solution was preheated at 100 °C under argon before use in order to avoid precipitation.

2 mL of the FA-oleate solution were introduced in a 3-neck flask at 100°C under argon followed by injecting 6.5 mL of the PbI_2 solution. After 1 min, the reaction is quenched with an ice bath. The resultant solution was centrifuged for 10 min at 13000 rpm. The supernatant was discarded and the precipitate re-dispersed in toluene. The NCs solution was then centrifuged for 5 min at 3000 rpm and only the supernatant was kept in order to eliminate the large aggregates present in the suspension. No further washing step was employed.

A picture of the synthesized $FAPbI_3$ NCs at the end of the synthesis and after redispersion in toluene is shown in **Figure 2.21a** and **b**, respectively. The obtained NCs are cubic in shape, with a lateral size of 12 ± 2 nm (**Figure 2.21c**). Details on the TEM characterization are given in the **ANNEXE 2**.

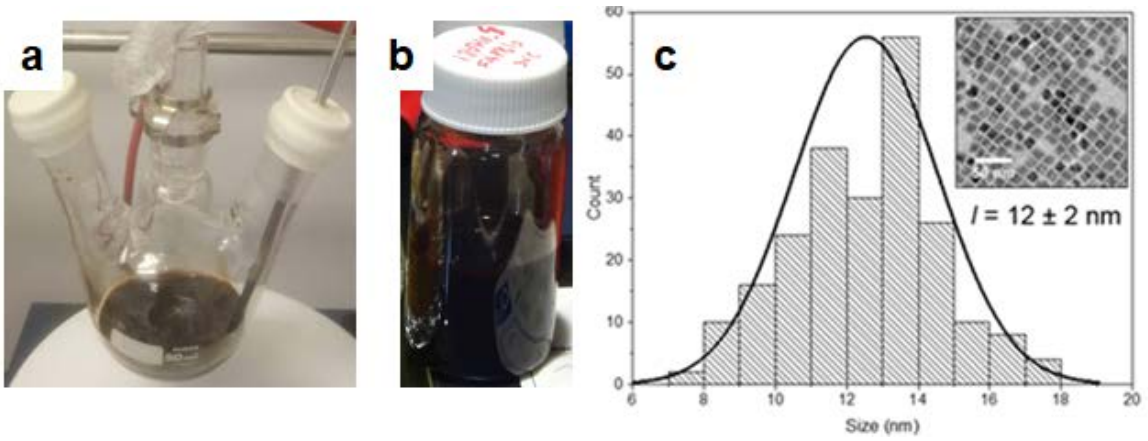

Figure 2.21. (a) *Photograph of the 3-neck flask containing the colloidal* $FAPbI_3$ *NCs solution obtained with the HI method.* ***(b)*** *Same NCs after redispersion in toluene.* ***(c)*** *Histogram of the size distributions of the NC sample obtained from TEM analysis. A typical picture is shown in inset.*

2.2.2.1.2. Synthesis of thick $FAPbI_3$ nanoplates by the LARP method.

As the HI method requires a specific chemical setup, the synthesis protocol used for the $FAPbI_3$ NCs at LIDYL was based in the the LARP method reported by Brabec and *co.* [31]. This method has the advantages that it does not involve controlled atmosphere and can be performed at room-temperature (RT).

Solutions of PbI_2 and FA-I at 0.2 M in DMF were prepared by dissolving 0.2 mmol of each salt in 1 mL of DMF. At RT and aerobic atmosphere, 125 µL of the PbI_2 solution at 0.2 M was mixed with 125 µL of the FA-I solution at 0.2 M. Then, the ligands OA (50 µL) and OLAm (40 µL) were added. This mixture (~340 µL) was injected into 15 mL of chloroform under strong stirring. The crude solution was separated in 1 mL aliquots and a chloroform/acetonitrile mixture (100 µL, ratio 1:1) was added for precipitation. The solution was centrifuged at 5.0 rcf (relative centrifugal force) for 20 min. Then, the supernatant was discarded and the precipitate re-dispersed in chloroform to reach the adequate optical density for the experiments (see **Figure 2.22a**).

Whereas, we were expecting cubic NCs, the TEM pictures reveal that the $FAPbI_3$ NCs synthesized by the LARP method have the shape of a hexagonal plate (**Figure 2.22 b,c**). The lateral dimensions are about 70 ± 20 nm (in diameter) and the thickness is about 11 ± 3 nm. Using a lattice parameter of 0.6 nm, we can estimate that these thick nanoplates (NPs) are composed of an equivalent of 18 ± 5 MLs.

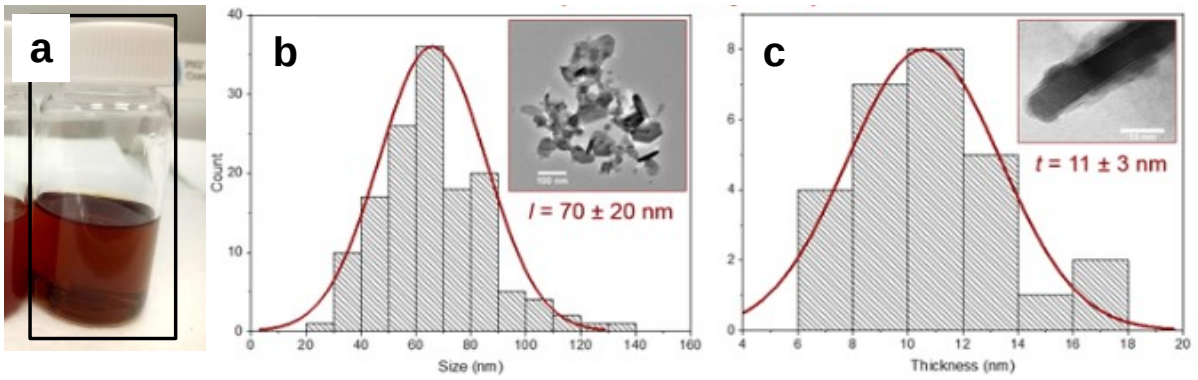

Figure 2.22. (a) *Photograph of the colloidal $FAPbI_3$ thick NPs synthesized with the LARP method in chloroform.* ***(b, c)*** *Histograms of the size distributions of the $FAPbI_3$ NP sample obtained from the TEM images and displaying their lateral length (l) and thickness (t). Typical TEM pictures are shown in the insets.*

2.2.2.1.3. Optical characterization of the $FAPbI_3$ samples

The steady-state absorption and emission spectra of the synthesized hybrid $FAPbI_3$ perovskite nanostructures are displayed **Figure 2.23**. The absorption spectra of both nanocube and thin NPs $FAPbI_3$ samples extend to the near-infrared and present no well-defined excitonic structures, as expected in these materials presenting a weak confinement. The cubic-shaped NCs exhibit a photoluminescence (PL) peak centered around 750 nm (1.65 eV) while the PL maximum of the thick nanoplates is at 770 nm (1.61 eV). These results suggest some degree of confinement when compared with the typical 820-840 nm PL emission of bulk $FAPbI_3$ thin films [38] and macrocrystals [39]. The NP thickness is similar to the average size of the cubic NCs while its optical spectrum is slightly red-shifted in comparison due to its larger lateral dimensions.

The sizes and linear spectra of both samples are in agreement with a weak confinement regime when compared with the ≈ 5 nm exciton Bohr radius reported for $FAPbI_3$ [40].

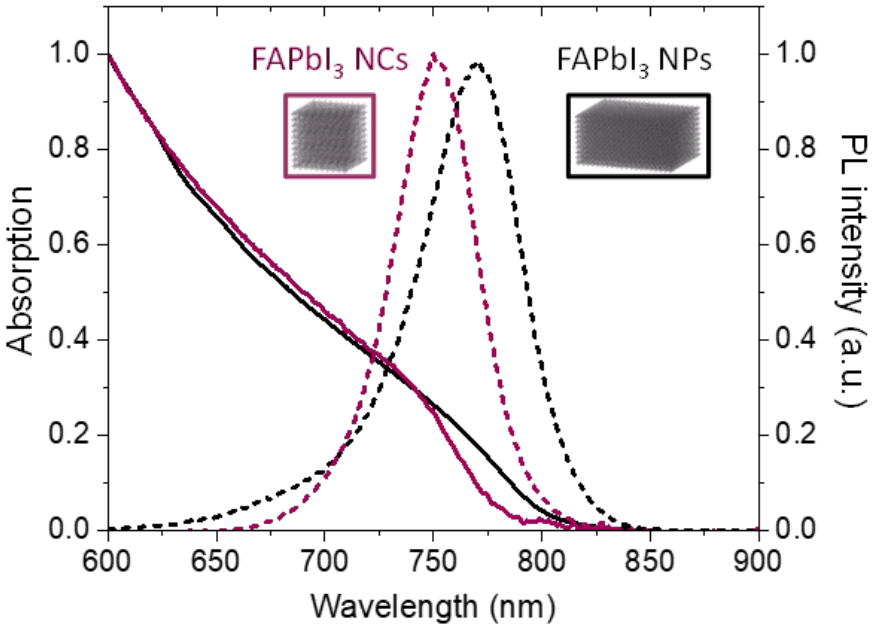

Figure 2.23. *Absorption (full lines) and photoluminescence (dashed lines) spectrum of the colloidal $FAPbI_3$ samples (cubic NCs in purple, thick NPs in black).* ***Inset:*** *schematics of the nanostructures.*

2.2.2.2. Synthesis of the strongly confined FAPI nanoplatelets

2.2.2.2.1. Synthesis of FAPI NPLs by the HI method

The synthesis protocol used at at ILM in Lyon was based in the HI method reported by Kovalenko and co. [26]. The NPLs obtained after the synthesis are shown in **Figure 2.24.** While the FAPI NPLs synthesized with the HI method are of high quality in terms of thickness control (isolated n=2 MLs) and PL QY, the samples were not stable enough in time for transportation to LIDYL in order to perform the time-resolved spectroscopic investigations. Thus, all the NPL samples described in the following were synthesized directly at LIDYL, using the LARP method adapted from the report of Tisdale *and co.* [32].

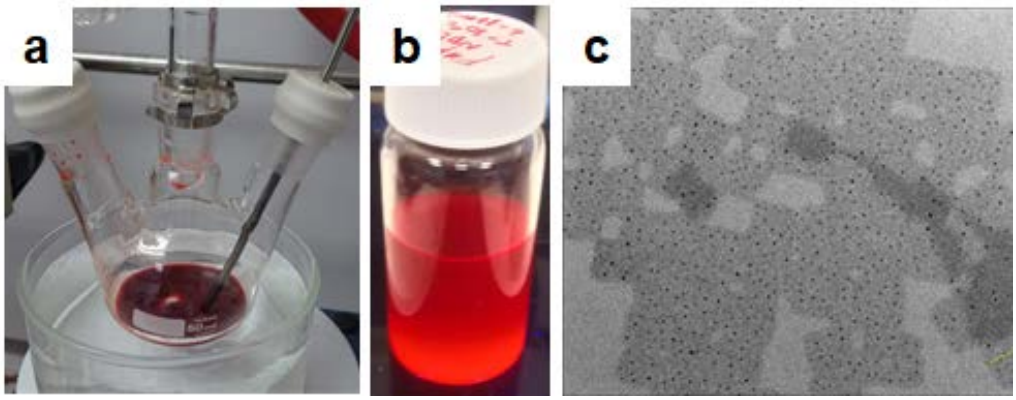

Figure 2.24. *Photograph of the colloidal FAPI n=2 NPLs solution synthesized with the HI method in the three-neck flash* ***(a)*** *and after redispersion in toluene (b). TEM picture of the synthesized FAPI NPL sample. The small black dots are due to some recrystallization under the electron beam.* ***(c)***

2.2.2.2.2. Synthesis of perovskite NPLs by the LARP method

Hybrid perovskites nanoplatelets with controlled number of monolayers (*n=1* and *n=2*) were synthesized by injecting in toluene a fresh mixture of a precise ratio of the three precursor solutions, PbI_2, butyl-ammonium iodide and FA-I, all three dissolved separately at 0.5 M in DMF, under vigorous stirring.

For *n=1* NPLs (L_2PbI_4), the stoichiometric ratio employed was 2:1:0 (alkyl-ammonium iodide:PbI_2:FA-I) so the precursor mixture was prepared with 40 µL of 0.5 M alkyl-ammonium iodide solution and 20 µL of the 0.5 M PbI_2 solution.

For *n=2* NPLs ($L_2[FAPbI_3]PbI_4$), the same protocol was employed but using a stoichiometric ratio for the precursor solution of 2:2:1, with 20 µL of the alkyl-ammonium iodide solution, 20 µL of the PbI_2 solution and 10 µL of the FA-I solution.

Stability in time.

We found that the purity of the toluene is of major importance for the reaction of precipitation. We use anhydrous toluene from Sigma-Aldrich (see **ANNEXE 2**). We use

either butyl-ammonium or octyl-ammonium as the alkyl-ammonium iodide precursors. In either case, the sample was not stable for more than one day, even when a larger proportion of ligand was used (see **Figure 2.25**).

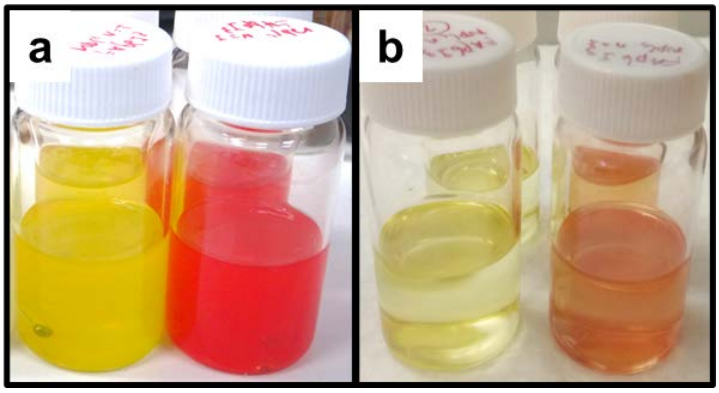

Figure 2.25. (a) *Photograph of the n=1 (left) and FAPI n=2 (right) NPLs as synthesized in toluene using the LARP method. The samples were prepared with octyl-ammonium ligands with a* stoichiometric *ratio of precursors of 2:1:0 and 10:2:1 (alkyl-ammonium iodide:PbI_2:FA-I).* ***(b)*** *Same samples after 1 day.*

Tisdale's protocol was thus slightly modified by adding a small volume of a OLAm solution (0.5 M in toluene) to the toluene flask prior to injection of the precursor solution. It was found that the stability of the prepared NPLs was improved by adding 20 µL of this OLAm solution without dissolving the sample. Furthermore, less scatter was observed in the dispersion of synthesized NPLs with a little amount of OLAm, evidencing the better stability of the samples (absence of large aggregates, see **Figure 2.26**). It was also found that when using short alkyl-ammoniums (butyl-), a better dispersion is obtained by adding a little amount of OA in the toluene prior injection.

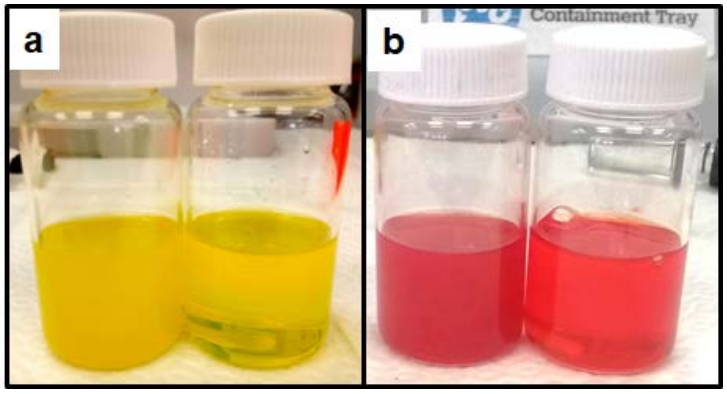

Figure 2.26. *Photograph of the colloidal perovskite NPLs synthesized with the LARP method without (left flask) and with (right flask) adding 20 µL of the OLA solution, in the case of n=1* ***(a)*** *and FAPI n=2* ***(b)***.

Redispersion effect.

As synthesized, the NPL dispersion should contain some unreacted precursors and excess ligands that can participate to the evolution of the sample in time. Thus, we tried to wash to synthesized NPLs. The reaction solutions were centrifugated and we tried to redisperse the NPLs deposited on the botton in toluene.

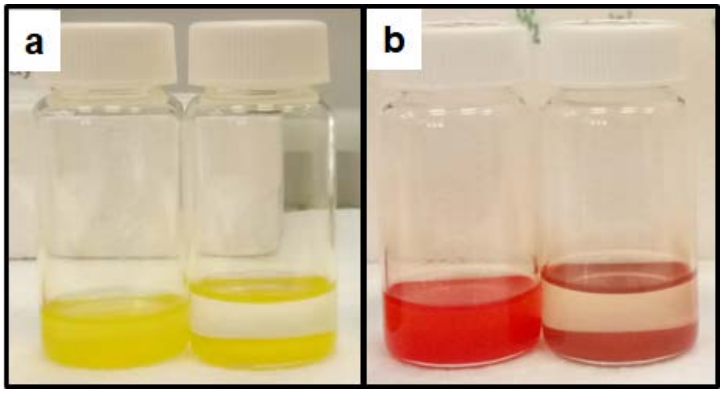

Figure 2.27. *Photograph of the colloidal n=1 (a) and FAPI (n=2) NPL samples before (left flask) and after (right flask) washing.*

However, the colloidal stability was compromised, as shown in **Figure 2.27**, probably because the change of equilibrium between the free ligands in the solution and those

attached at the surface of the NPLs. Thus, the samples were measured as prepared in the time-resolved experiments.

Sample characterizations.

The modified LARP method allows a layer by layer control of the synthesized perovskite NPLs directly from precursor stoichiometry as previously reported by Tisdale *et co*. This avoids further separation steps as in the ligand-assisted exfoliation method employed for MA-based lead iodide NPLs. The thickness of the thin NPLs was deduced from their first excitonic transition energy using steady-state optical spectroscopy results from previous reports. In spite that X-ray diffraction experiments were carried out a full description of the XRD patterns in this samples can be found in the reference [32].

The lateral dimension was determined using TEM as it is shown in the **Figure 2.28.**

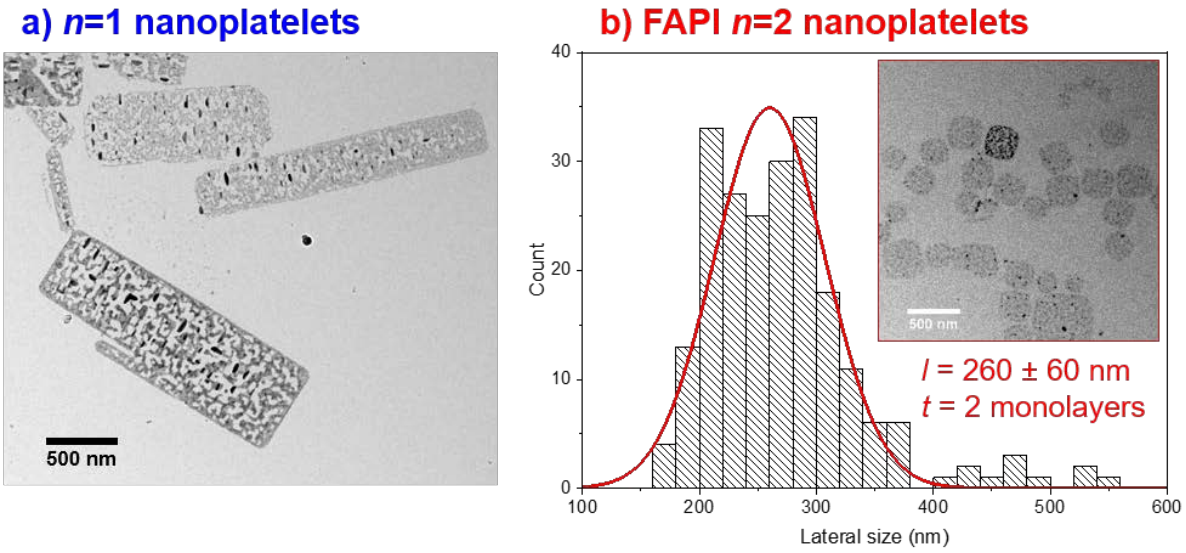

Figure 2.28. *(a) TEM picture of n=1 NPLs synthesized with the LARP method. (b) Histogram of the lateral size distribution of FAPI n=2 NPLs synthesized by the LARP method. Inset: typical corresponding TEM picture.*

As it corresponds to one and two 2D layers of corner-sharing PbI_6 octahedra (phase-pure samples), the inorganic layer thickness should be 0.6 and 1.2 nm, respectively, in the case of a thickness along the <100 > crystallographic direction and without taking into account some possible deformation of the lattice induced by the ligands. One monolayer thick nanoplatelets show rectangular shape with lateral dimensions larger than those of FAPI n=2 NPLs (see **Figure 2.28**), but no accurate size distribution could be extracted from TEM due to their tendency to assemble (pearly effect in solution).

Both n=1 and n=2 NPLs are in the strong confinement regime, as can be clearly observed in the spectra displayed in **Figure 2.29**. In both samples, the first absorption transition and PL peaks are dramatically blue-shifted compared to the quasi-3D $FAPbI_3$ nanoplates and large NCs, due to the strong quantum and dielectric confinements (*cf* **Chapter 1, part 1**). Due to the high control of the thickness distribution (one or two monolayers) along the confinement direction, the absorption spectra display a well-defined first excitonic transition with a Lorentzian lineshape and narrow full-width at half maximum (FWHM). This bandedge optical transition, centered at 515 nm (2.40 eV) for n=1 and about 576 nm (2.15 eV) for FAPI n=2 NPLs, is well separated from the continuum of states due to the large exciton binding energy of these 2D materials (about 10-times their bulk counterpart) [41]. The Lorentzian PL emission is centered at 518 nm (2.39 eV) for n=1 and 578 nm (2.14 eV) for n=2 NPLs, with narrow FWHMs of 70 meV and 67 meV, respectively. This contrasts with the Gaussian PL line-shape of the $FAPbI_3$ samples having a FWHM of about 112 meV. The assignment of the number of monolayers n of our NPL samples was made by comparison with the first excitonic transition energy reported in the literature for colloidal NPLs [32] and in agreement with the values of 2D perovskite films [42]. We noticed however slightly lower peak energies for our NPL samples and narrower FWHM that we attribute to the larger lateral dimensions of our samples.

Finally, a weak red-tail was observed in the NPL PL spectra. We interpreted this signal as some radiative recombination involving excitons in shallow trap states.

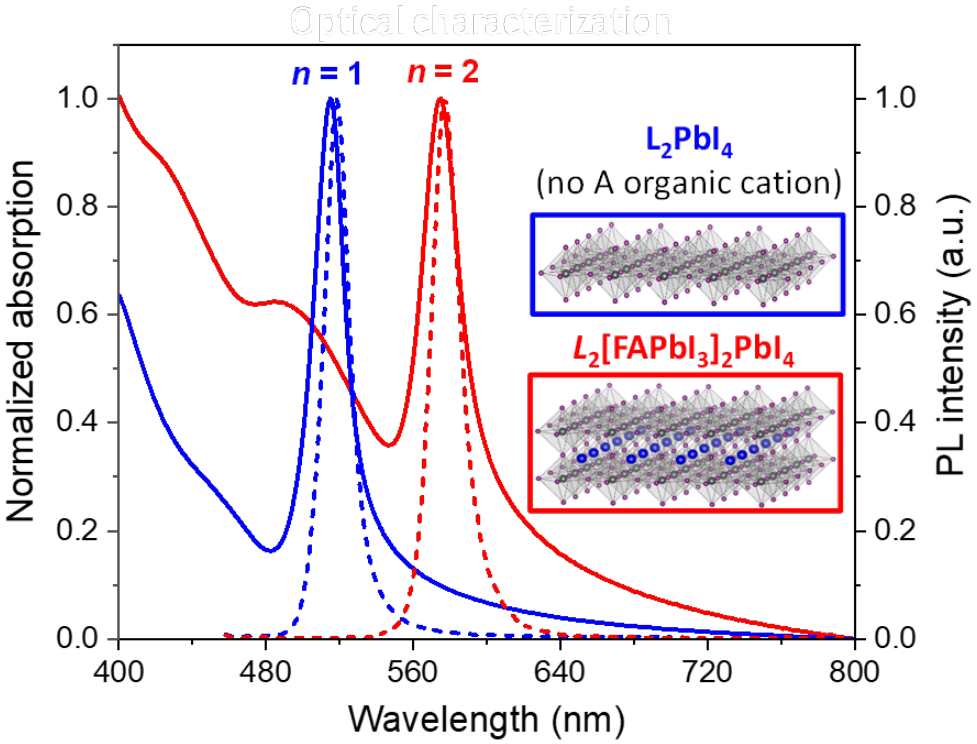

Figure 2.29. *Absorption (full line) and photoluminescence (dashed line) spectra of colloidal NPLs of one (blue) and two monolayers (red). Inset: schematics of the colloidal nanostructures with corresponding formula.*

Effect of the ligand chain in n=1 NPLs.

We notice that the *n*=1 NPL sample, synthesized with butyl-ammonium ligands and oleylamine, presents a color change in time. From yellow to orange under ambient light after few days. This effect can be seen in the absorption spectrum (**Figure 2.30**), where the first absorption transition switches from 515 to 558 nm, close to the value of *n*=2 NPL. As there is no A^+ cation precursor in this synthesis, it cannot be due to a simple evolution of the sample to larger thickness. The change of energy is large, discrete and not continuous, suggesting a modification of the crystallographic structure of the sample in time. The proportion of ligands added in excess seems to influence this modification. More

specific structural characterization as X-ray diffraction measurement could give an insight on this effect in such samples. This phenomenon was suppressed when using longer alkyl-ammonium ligand in the synthesis as oleylamonium. We thought additionally to the Van der Waals interactions between adjacent oleylamine ligands, the doble bond present in this ligand can cause a template effect stabilizing in time a particular crystalline structure. For n=1 NPLs, the more stable samples were obtained by using oleylammonium iodide.

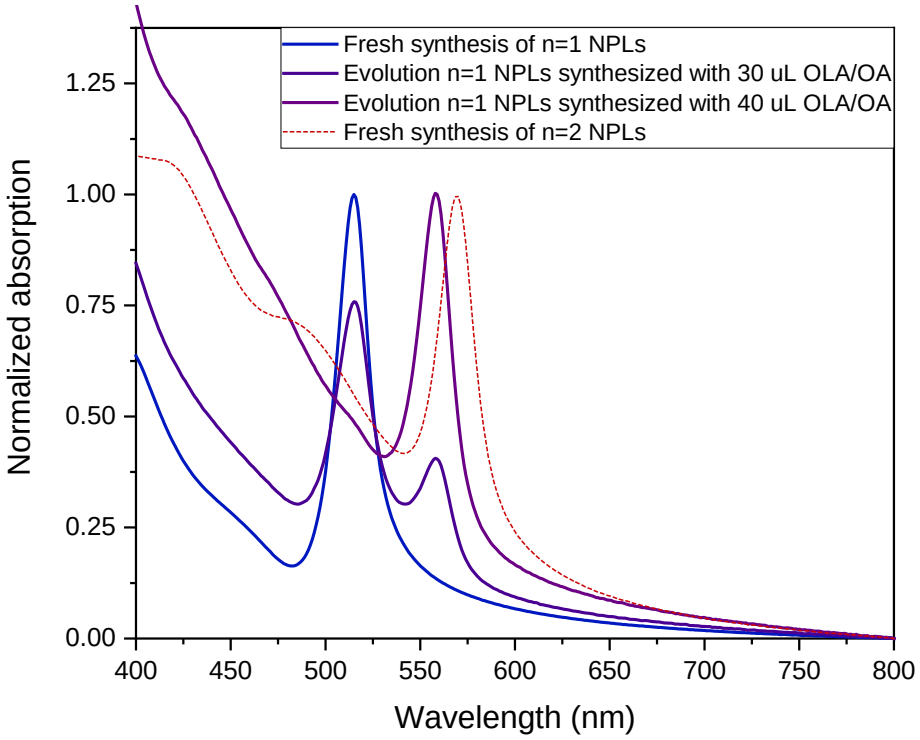

Figure 2.30. *Evolution of the absorption of n=1 NPL sample when synthesized with butyl-ammoniums and a small excess of oleylamonium (OLA) and oleic acid (OA) ligands. The absorption of the fresh sample is shown in blue. The evolved spectrum are in purple. For comparison, we also display the spectrum of FAPI n=2 NPLs (red dashed line).*

2.2.2.3. LARP method extended to the synthesis of CsPI and MAPI NPLs

2.2.2.3.1. *Modified synthesis of CsPI n=2 NPLs*

Tisdale and co. reported the first synthesis of CsPI *n*=2 NPLs but these NPLs evolved into thicker ones in several minutes and hours [32]. They attribute this to the smaller size of the Cs^+ cations with its ability to diffuse within the crystalline structure. The synthesis protocol was reproduced in our laboratory, with important issue of stability: almost all the CsPI NPLs disappear in a few minutes.

Then, the use of OLAm to improve the stability of this sample (as previous seen for FAPI NPLs), a ligand study was carried out using different lengths of alkyl-ammoniums. Ligands such as butyl- (C4), octyl- (C8) and dodecyl- (C12) ammonium iodide precursors were mixed in different proportions. The **Figure 2.31** shows the samples synthesized using the different ligand ratios, in absence and presence of OLAm.

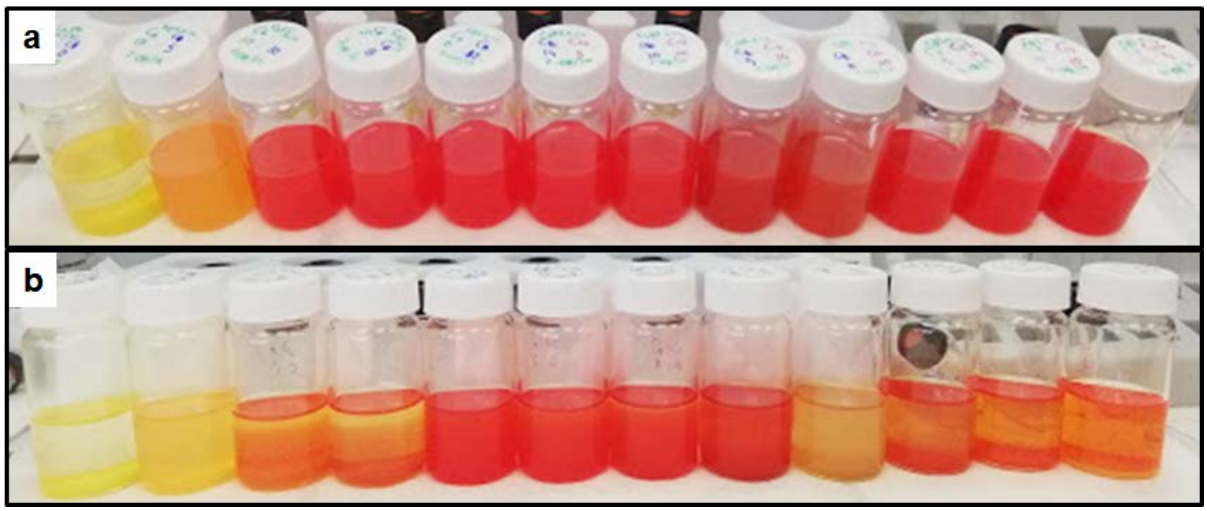

Figure 2.31. *Picture of the colloidal suspension of CsPI n=2 NPLs using different ligands ratios, (a) with OLAm and (b) without. From the left to the right: C4:C8 (20:0), C4:C8 (15:5), C4:C8 (10:10), C4:C8 (5:15), C8:C12 (0:20), C8:C12 (5:15), C8:C12 (10:10), C8:C12 (5:15), C8:C12 (20:0), C4:C12 (5:15), C4:C12 (10:10), C4:C12 (15:5).*

It is clear that the OLAm ligands improve considerably the colloidal stability of the samples in all cases but the ammonium ligand ratio allowed a finer control. We found that the most stable sample was obtained using the longest ligand available (dodecylammonium iodide, C12).

Optical characterizations of CsPI n=2 NPLs

The steady-state absorption and photoluminescence spectra of the synthesized CsPI NPLs dispersed in toluene are shown in **Figure 2.32**. The energy peak corresponding to the first exciton transition matches the previous reports of strongly confined 2D CsPI NPLs [32] with an absorption maximum near 550 nm, while the PL emission peaks at 561 nm. The 2D CsPI NPL samples display some degree of confinement in one of the lateral dimensions. Indeed, they look like nanoribbons, with a width of 17 ± 3 nm and a length of several hundreds of nm. The spectrum of Cs-based perovskite *n*=2 NPL is blue shifted compared to that of FA- (and MA-, see below) based counterparts as expected [32].

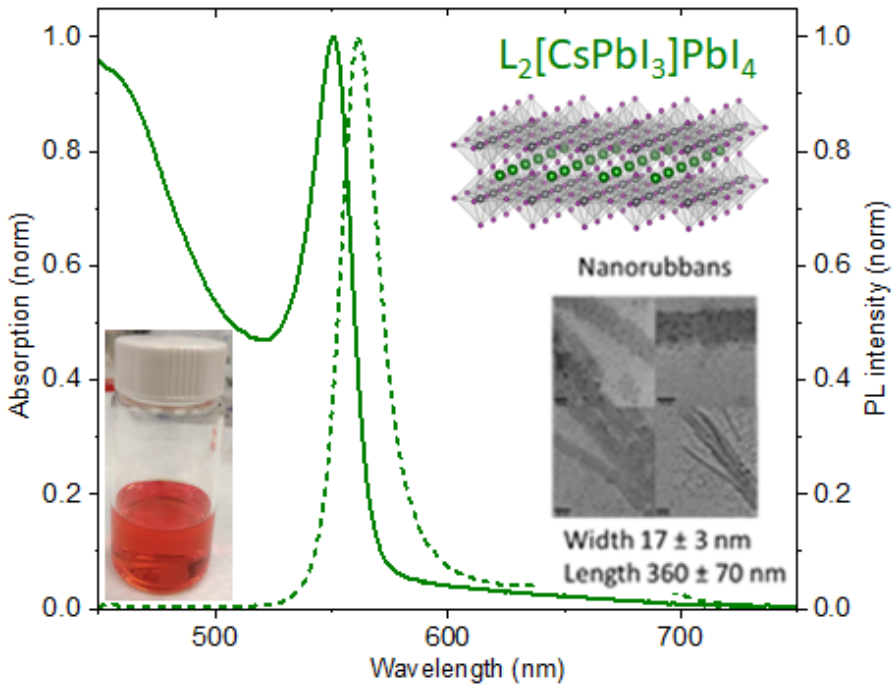

Figure 2.32. *Absorption (full line) and PL (dashed line) spectrum of colloidal CsPI n=2 NPLs synthesized with C12 and OLA. Inset: picture of the sample under ambient light, schematics of the nanostructure and TEM images.*

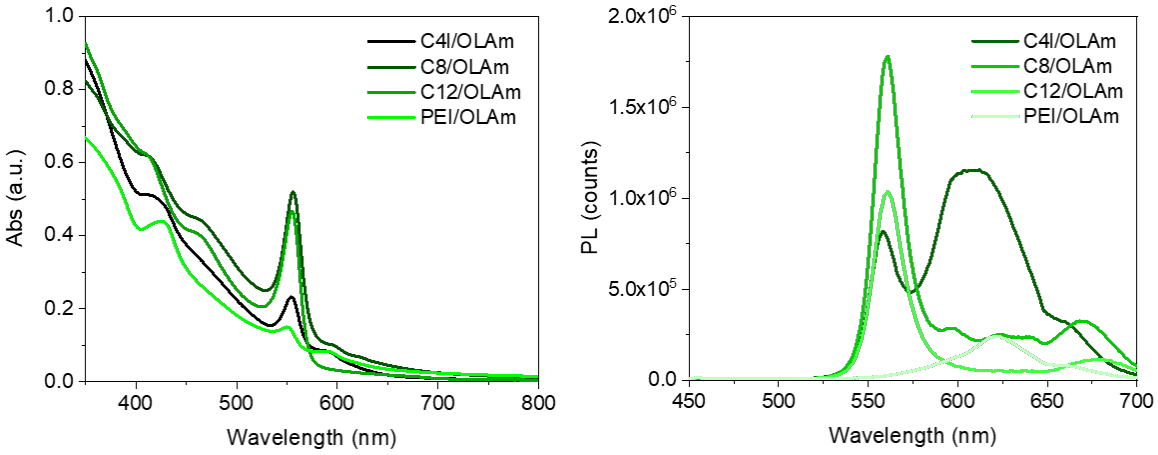

Figure 2.33. (a) *Absorption and* ***(b)*** *photoluminescence spectra of colloidal NPLs synthesized with different alkyl-ammonium chains (C4, C8, C12 and phenylethyl- PE).*

Comparing the spectra of the differently synthesized CsPI NPLs confirmed that the sample with just C12 as ligands and OLAm possesses a better thickness control and surface passivation compared to the other NPLs with shorter ligands (**Figure 2.33**).

Synthesis of n=2 and n=3 MAPI NPLs

The previous study of CsPI NPLs showed the effect of the ligands on the stability but also on the control of the different thickness populations. We extended the synthesis of perovskite NPLs to MAPI for which we were able to synthesize both n=2 and n=3, while no thickness larger than 2 MLs could be obtained in FAPI and CsPI. Similar difficulties were encountered to synthesize particular members of the 2D perovskite crystals containing FA or Cs in the A-site cation [43]. This observation suggests that n=2 might be the most thermodynamically stable product among the lead iodide perovskite thin film with FA cations.

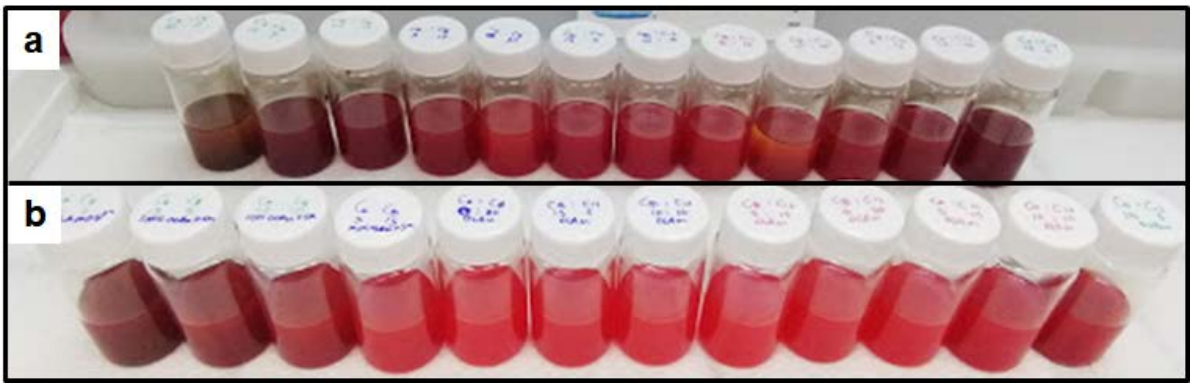

Figure 2.34. *Pictures of the colloidal suspension of MAPI NPLs synthesized using different ratios of ligand length, without (a) and with (b) OLA. From the left to the right: C4:C8 (20:0), C4:C8 (15:5), C4:C8 (10:10), C4:C8 (5:15), C8:C12 (0:20), C8:C12 (5:15), C8:C12 (10:10), C8:C12 (5:15), C8:C12 (20:0), C4:C12 (5:15), C4:C12 (10:10), C4:C12 (15:5).*

By changing the length of the alkyl-ammonium chain, we were able to synthesize MAPI NPL samples of pure n=2 and n=3 monolayers (**Figure 2.34a** and **2.35b**). We found that the short C4 or relatively short C8 ligands were necessary to obtain the n=3 NPLs. The presence of OLA in the toluene prior injection prevents from the formation of n=3 NPLs. However, we found it necessary to inject a small amount after several minutes to keep a good stability. In the case of MAPI n=2 NPLs, a longer chain ligand (C18, see **ANNEXE 2**) was synthesized in order to have a better control of the thickness. Additionally, OLAm was added to the toluene before the injection.

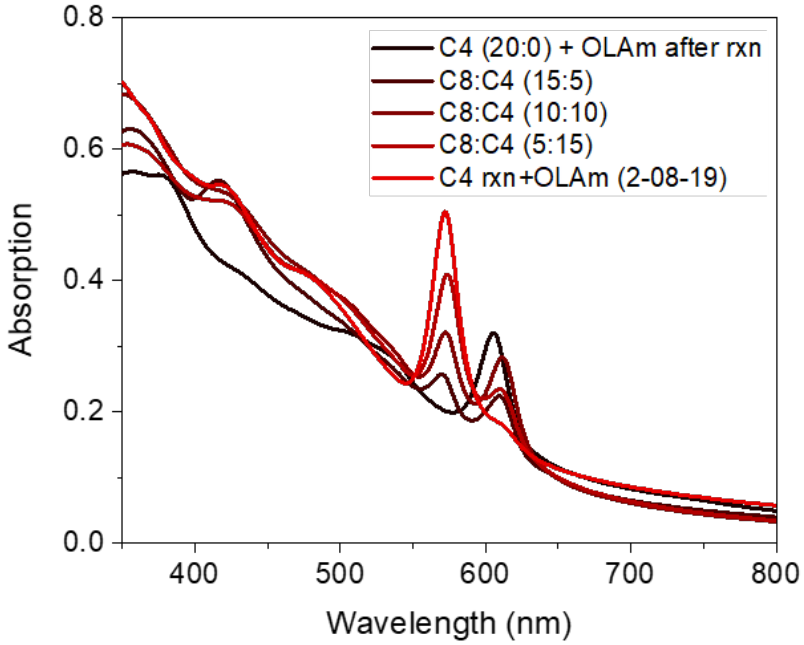

Figure 2.35. *Absorption spectra of different MAPI NPL reaction by using different ligand length molar ratio.*

Final protocol for MAPI n=2 and n=3 NPLs

Oleylammonium iodide ($C_{18}I$) was prepared as described by Kovalenko and coworkers [44] (see **ANNEXE 2**). MAPI NPLs with a controlled number of monolayers (*n=2* and *n=3*) were synthesized by injecting a fresh mixture of the precursor solutions (ligand: C_4I and $C_{18}I$, metal: PbI_2 and cation: MA-I, all three dissolved separately at 0.5 M in DMF) at a precise ratio in a non-polar solvent (toluene).

For *n=2* NPLs ($L_2[MAPbI_3]PbI_4$), the stoichiometric ratio employed was 2:2:1 ($C_{18}I$:PbI_2:MA-I).The precursor mixture was consequently prepared with 20 µL of $C_{18}I$ 0.5 M solution, 20 µL of 0.5 M PbI_2 solution and 10 µL of FA-I solution. Before injection, OLA (20 µL, 0.5 M in toluene) was added to 10 mL of toluene as anti-solvent. Then, 20 µL of the freshly mixed precursor solution was rapidly injected in the toluene solution under vigorous stirring.

For *n=3* NPLs ($L_2[MAPbI_3]_2PbI_4$), a similar protocol was employed but using a stoichiometric ratio for the precursor solution equivalent to 2:2:2 with 15 µL of solution C_4I, 5 µL of C_8I solution, 20 µL of the PbI_2 solution and 20 µL of the MA-I solution. However, OLA was added after the injection of the precursor mixture in the toluene.

Characterizations of MAPI NPLs

MAPI *n*=3 NPLs present absorption and PL peaks that are red-shifted compared to the *n*=2 sample (**Figure 2.36**), as expected from the lower confinement effects. The position of the first exciton transition is 573 nm and 610 nm, for *n*=2 and *n*=3, respectively, in agreement with the reported values of MAPI 2D perovskite thin films and exfoliated crystals [45,46]. The shape of the *n*=3 sample could not be well determined (see TEM picture in **Figure 2.36b**) but looks like slightly faceted plates. The lateral size is about 140 nm in diameter.

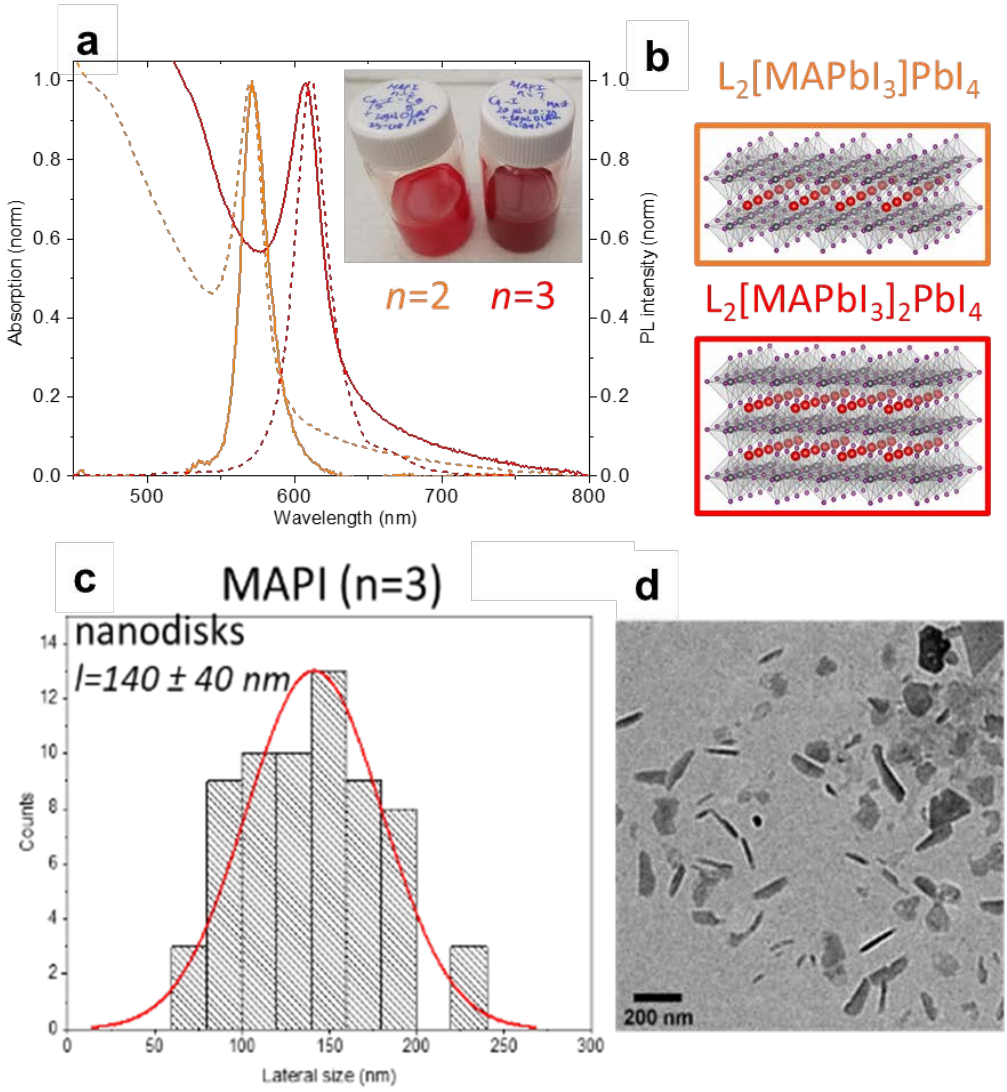

Figure 2.36. (a) *Absorption (dashed lines) and photoluminescence (full lines) spectra of colloidal perovskite MAPI NPLs of two (orange) and three (red) monolayers.* ***(b)*** *Corresponding schematics are displayed on the right.* ***(c)*** *Histogram of the size distributions of the MAPI n=3 NPL sample with lateral length (l) extracted from the TEM images* ***(d)***.

ANNEXE 2.

Transmission electron microscopy (TEM)

The shape and size of the prepared colloidal perovskite nanostructures were determined by Benoît Mahler at ILM using transmission electronic microscopy (TEM) using a JEOL 2100 equipped with a LaB_6 filament and operating at 200 kV. The sample sizes were extracted from ImageJ program. Minimum electron flux was used to limit the damages under the electron beam.

Chemical list

Lead iodide (PbI2 99.999%), formamidinium iodide (FA-I, anhydrous, > 99%), n-butyl-ammonium iodide (98%) N,N-dimethylformamide (DMF, anhydrous, 99.8%), chloroform (anhydrous, 99%), toluene (anhydrous, 99.8%) and acetonitrile (anhydrous, 99.8%) Ethanol (absolute, > 99.8%), Diethhyl ether (contains BHT as inhibitor >99.8%) were purchased from Sigma-Aldrich.

Oleic acid (OA, 99%) and 1-Octylamine (99%) were purchased from Alfa Aesar. Oleylamine (OLAm, 90%) was purchased from Acros Organics. Hydriodic acid, for analysis. 57 wt% aqueous solution (Acros organics), Oleylamine (OLAm, 90%), Hydriodic acid (57 wt% aqueous solution for analysis, distilled, unestabilized) was purchased from Acros Organics. Octadecene (ODE), Formamidinium acetate (FA-acetate). Methylamoninium iodide (MA-I, anhydrous, > 99%), cesium iodide (Cs-I, anhydrous, > 99%), n-butyl-ammonium iodide (C4I, 98%), n-octyl-ammonium iodide (C8I, 98%), dodecyl were purchased from Great cell solar materials.

Beam characterization in TA

Assuming a Gaussian beam, the waist of a beam can be estimated by measuring the beam power after placing pinholes of well-known diameter in the focus plane (**Figure 1**). The pinholes are placed perpendicularly to the beam we want to characterize and at the focus position (maximum of transmitted power).

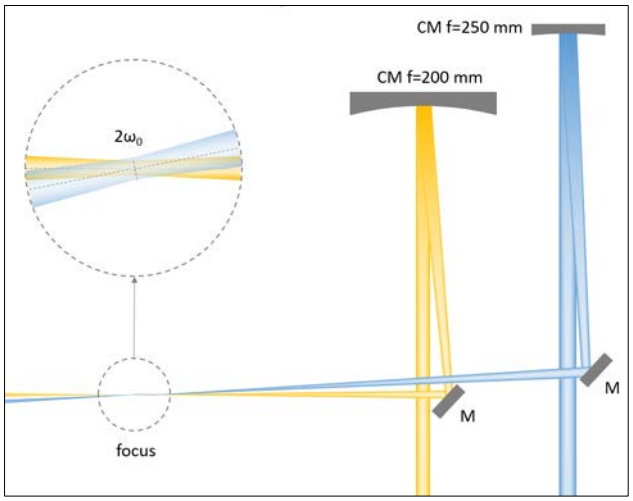

Figure A2.1. *Pump-probe overlap region schematics.*

Characterization of the WL beam:

For the WL probe beam, the measured powers after removing the ND filter in the patch and adding a pinhole through a set are displayed in **Table A2.1**.

Table A2.1. *Power measurement in function of the pinhole aperture for probe beam (WL).*

Aperture	Measured power, iris fully open	Power, iris cut red/blue ring of WL
25 µm pinhole	3 µW	3 µW
50 µm pinhole	9-10 µW	8 µW
75 µm pinhole	15 µW	12 µW
100 µm pinhole	17-18.5 µW	13 µW
No pinhole	28-29 µW	14-15 µW

Then, the gaussian beamwaist (ω_0) was estimated using the different powers corresponding to the different pinhole aperture and the following equation:

$$P(r) = P(\infty)\left[1 - exp\left(-\frac{2r^2}{\omega_0^2}\right)\right] \quad [A2.1]$$

P(r) is the power measured for an aperture diameter of 2r, P(∞) is the power measured without aperture, and ω_0 is the beam waist.

We get for the iris fully open ω_0 = 60 ± 4 µm and with the iris in the experimental model (cut the red and blue ring of the WL) ω_0 = 39 ± 1 µm.

Characterization of the 400 nm pump beam

For a 400 nm pump beam, a pinhole was fixed at overlap position with the WL beam at the focus.

Table A2.2. *Power measurement in function of the pinhole aperture for 400nm pump beam.*

Aperture	Measured power
25 µm pinhole	2 µW
50 µm pinhole	7 µW
75 µm pinhole	15 µW
100 µm pinhole	24 µW
Without pinhole	82-83 µW

Using the same formula, we get ω_0 = 119.7 ± 0.7 µm.

The extent to another pump in the visible region

The 400 nm pump beam has a diameter on the spherical mirror CM of 6 mm. The focal length of this CM is 250 mm. The size of the waist (at focus) ω_0 is dependent on the beam energy following the formula:

$$2\omega_0 = M^2 \frac{4}{\pi} \frac{\lambda f}{D} \quad [A2.2]$$

Where λ is the beam wavelength, f the focal length of the CM (or lens), D is the diameter of the beam before focalization (measured on the CM) and M^2 is the beam quality factor ($M^2 = 1$ for a Gaussian beam).

By using the same optics and keeping a beam diameter of 6 mm, the beam waist for the different wavelength $\omega_0(\lambda)$ is proportional to ω_0 measured at 400 nm, with a factor corresponding to the ratio of the two wavelengths.

REFERENCES

[1] W.W. Parson, Modern Optical Spectroscopy, Springer, 2015. http://link.springer.com/10.1007/978-3-662-46777-0_4 (accessed May 14, 2019).

[2] J.R. Lakowicz, Principles of fluorescence spectroscopy, Springer, 2006.

[3] C. Würth, M. Grabolle, J. Pauli, M. Spieles, U. Resch-Genger, Relative and absolute determination of fluorescence quantum yields of transparent samples, Nat. Protoc. 8 (2013) 1535–1550. https://doi.org/10.1038/nprot.2013.087.

[4] D. Strickland, G. Mourou, Compression of amplified chirped optical pulses, Opt. Commun. 56 (1985) 219–221. https://doi.org/10.1016/0030-4018(85)90120-8.

[5] Desmond V. O'Connor;David Phillips, Time-Correlated Single Photon Counting, Elsevier, 1984. https://doi.org/10.1016/b978-0-12-524140-3.x5001-1.

[6] J. Brazard, A.K. Thazhathveetil, I. Vayá, F.D. Lewis, T. Gustavsson, D. Markovitsi, Electronic excited states of guanine-cytosine hairpins and duplexes studied by fluorescence spectroscopy, Photochem. Photobiol. Sci. 12 (2013) 1453–1459. https://doi.org/10.1039/c3pp50088h.

[7] I.H.M. Van Stokkum, D.S. Larsen, R. Van Grondelle, Global and target analysis of time-resolved spectra, Biochim. Biophys. Acta - Bioenerg. 1657 (2004) 82–104. https://doi.org/10.1016/j.bbabio.2004.04.011.

[8] D.B. Turner, K.E. Wilk, P.M.G. Curmi, G.D. Scholes, Comparison of electronic and vibrational coherence measured by two-dimensional electronic spectroscopy, J. Phys. Chem. Lett. 2 (2011) 1904–1911. https://doi.org/10.1021/jz200811p.

[9] H.H. Telle, A. González Ureña, Laser spectroscopy and laser imaging : an introduction, 2018. https://books.google.fr/books?id=2SJWDwAAQBAJ&printsec=frontcover&dq=Laser+Spectroscopy+and+Laser+Imaging+An+Introduction&hl=en&sa=X&ved=0ahUKEwj2nLuQubrdAhVSvxoKHRpzCYcQ6AEIJzAA#v=onepage&q=Laser Spectroscopy and Laser Imaging An Introduction&f=false (accessed September 14, 2018).

[10] C. Manzoni, G. Cerullo, Design criteria for ultrafast optical parametric amplifiers, J. Opt. 18 (2016) 103501. https://doi.org/10.1088/2040-8978/18/10/103501.

[11] S. Akturk, X. Gu, M. Kimmel, R. Trebino, Extremely simple single-prism

ultrashort- pulse compressor, Opt. Express. 14 (2006) 10101. https://doi.org/10.1364/oe.14.010101.

[12] V.I. Klimov, Nanocrystal Quantum dots -2nd edition, 2010. https://doi.org/10.1017/CBO9781107415324.004.

[13] P. Kambhampati, Unraveling the structure and dynamics of excitons in semiconductor quantum dots, Acc. Chem. Res. 44 (2011) 1–13. https://doi.org/10.1021/ar1000428.

[14] G. Walters, M. Wei, O. Voznyy, R. Quintero-Bermudez, A. Kiani, D.-M. Smilgies, R. Munir, A. Amassian, S. Hoogland, E. Sargent, The quantum-confined Stark effect in layered hybrid perovskites mediated by orientational polarizability of confined dipoles, Nat. Commun. 9 (2018) 4214. https://doi.org/10.1038/s41467-018-06746-5.

[15] J. Cui, A.P. Beyler, L.F. Marshall, O. Chen, D.K. Harris, D.D. Wanger, X. Brokmann, M.G. Bawendi, Direct probe of spectral inhomogeneity reveals synthetic tunability of single-nanocrystal spectral linewidths, Nat. Chem. 5 (2013) 602–606. https://doi.org/10.1038/nchem.1654.

[16] D. Oron, M. Kazes, U. Banin, Multiexcitons in type-II colloidal semiconductor quantum dots, Phys. Rev. B - Condens. Matter Mater. Phys. 75 (2007) 035330. https://doi.org/10.1103/PhysRevB.75.035330.

[17] Y. Yang, D.P. Ostrowski, R.M. France, K. Zhu, J. Van De Lagemaat, J.M. Luther, M.C. Beard, Observation of a hot-phonon bottleneck in lead-iodide perovskites, Nat. Photonics. 10 (2016) 53–59. https://doi.org/10.1038/nphoton.2015.213.

[18] I.H.M. Van Stokkum, D.S. Larsen, R. Van Grondelle, Global and target analysis of time-resolved spectra, Biochim. Biophys. Acta - Bioenerg. 1657 (2004) 82–104. https://doi.org/10.1016/j.bbabio.2004.04.011.

[19] J.J. Snellenburg, S.P. Laptenok, R. Seger, K.M. Mullen, I.H.M. Stokkun, Glotaran : A Java -Based Graphical User Interface for the R Package TIMP, J. Stat. Softw. 49 (2012) 1–22.

[20] Q.A. Akkerman, G. Rainò, M. V. Kovalenko, L. Manna, Genesis, challenges and opportunities for colloidal lead halide perovskite nanocrystals, Nat. Mater. 17 (2018) 394–405. https://doi.org/10.1038/s41563-018-0018-4.

[21] L.C. Schmidt, A. Pertegás, S. González-Carrero, O. Malinkiewicz, S. Agouram, G.

Mínguez Espallargas, H.J. Bolink, R.E. Galian, J. Pérez-Prieto, Nontemplate synthesis of CH3NH3PbBr3 perovskite nanoparticles, J. Am. Chem. Soc. 136 (2014) 850–853. https://doi.org/10.1021/ja4109209.

[22] J. Shamsi, A.S. Urban, M. Imran, L. De Trizio, L. Manna, Metal Halide Perovskite Nanocrystals: Synthesis, Post-Synthesis Modifications, and Their Optical Properties, Chem. Rev. 119 (2019) 3296–3348. https://doi.org/10.1021/acs.chemrev.8b00644.

[23] J. Sun, J. Yang, J.I. Lee, J.H. Cho, M.S. Kang, Lead-Free Perovskite Nanocrystals for Light-Emitting Devices, 9 (2018) 1573–1583. https://doi.org/10.1021/acs.jpclett.8b00301.

[24] A.L. Rogach, Semiconductor nanocrystal quantum dots : synthesis, assembly, spectroscopy and applications, Springer, 2008.

[25] L. Protesescu, S. Yakunin, S. Kumar, J. Bär, F. Bertolotti, N. Masciocchi, A. Guagliardi, M. Grotevent, I. Shorubalko, M.I. Bodnarchuk, C.-J. Shih, M. V. Kovalenko, Dismantling the "Red Wall" of Colloidal Perovskites: Highly Luminescent Formamidinium and Formamidinium–Cesium Lead Iodide Nanocrystals, ACS Nano. 11 (2017) 3119–3134. https://doi.org/10.1021/acsnano.7b00116.

[26] L. Protesescu, S. Yakunin, M.I. Bodnarchuk, F. Krieg, R. Caputo, C.H. Hendon, R.X. Yang, A. Walsh, M. V. Kovalenko, Nanocrystals of Cesium Lead Halide Perovskites ($CsPbX_3$, X = Cl, Br, and I): Novel Optoelectronic Materials Showing Bright Emission with Wide Color Gamut, Nano Lett. 15 (2015) 3692–3696. https://doi.org/10.1021/nl5048779.

[27] A. Pan, B. He, X. Fan, Z. Liu, J.J. Urban, A.P. Alivisatos, L. He, Y. Liu, Insight into the Ligand-Mediated Synthesis of Colloidal $CsPbBr_3$ Perovskite Nanocrystals: The Role of Organic Acid, Base, and Cesium Precursors, ACS Nano. 10 (2016) 7943–7954. https://doi.org/10.1021/acsnano.6b03863.

[28] Y. Bekenstein, B.A. Koscher, S.W. Eaton, P. Yang, A.P. Alivisatos, Highly Luminescent Colloidal Nanoplates of Perovskite Cesium Lead Halide and Their Oriented Assemblies, J. Am. Chem. Soc. 137 (2015) 16008–16011. https://doi.org/10.1021/jacs.5b11199.

[29] D. Zhang, S.W. Eaton, Y. Yu, L. Dou, P. Yang, Solution-Phase Synthesis of Cesium

Lead Halide Perovskite Nanowires, J. Am. Chem. Soc. 137 (2015) 9230–9233. https://doi.org/10.1021/jacs.5b05404.

[30] F. Zhang, H. Zhong, C. Chen, X. Wu, X. Hu, H. Huang, J. Han, B. Zou, Y. Dong, Brightly Luminescent and Color-Tunable Colloidal CH 3 NH 3 PbX 3 (X = Br, I, Cl) Quantum Dots: Potential Alternatives for Display Technology, ACS Nano. 9 (2015) 4533–4542. https://doi.org/10.1021/acsnano.5b01154.

[31] I. Levchuk, A. Osvet, X. Tang, M. Brandl, J.D. Perea, F. Hoegl, G.J. Matt, R. Hock, M. Batentschuk, C.J. Brabec, H. Perovskite, F.X. Cl, I.C. Nanocrystals, I. Levchuk, A. Osvet, X. Tang, M. Brandl, J. Dar, F. Hoegl, G.J. Matt, R. Hock, M. Batentschuk, C.J. Brabec, Brightly Luminescent and Color-Tunable Formamidinium Lead Halide Perovskite FAPbX 3 (X = Cl, Br, I) Colloidal Nanocrystals, Nano Lett. 17 (2017) 2765–2770. https://doi.org/10.1021/acs.nanolett.6b04781.

[32] M.C. Weidman, M. Seitz, S.D. Stranks, W.A. Tisdale, Highly Tunable Colloidal Perovskite Nanoplatelets through Variable Cation, Metal, and Halide Composition, ACS Nano. 10 (2016) 7830–7839. https://doi.org/10.1021/acsnano.6b03496.

[33] P. Tyagi, S.M. Arveson, W.A. Tisdale, Colloidal Organohalide Perovskite Nanoplatelets Exhibiting Quantum Confinement, J. Phys. Chem. Lett. 6 (2015) 1911–1916. https://doi.org/10.1021/acs.jpclett.5b00664.

[34] G. Li, K.J. Jiang, Y.F. Li, S.L. Li, L.M. Yang, Efficient structural modification of triphenylamine-based organic dyes for dye-sensitized solar cells, J. Phys. Chem. C. 112 (2008) 11591–11599. https://doi.org/10.1021/jp802436v.

[35] D. Chen, X. Chen, Luminescent perovskite quantum dots: synthesis, microstructures, optical properties and applications, J. Mater. Chem. C. 7 (2019) 1413–1446. https://doi.org/10.1039/C8TC05545A.

[36] Y. Tong, E. Bladt, M.F. Aygüler, A. Manzi, K.Z. Milowska, V.A. Hintermayr, P. Docampo, S. Bals, A.S. Urban, L. Polavarapu, J. Feldmann, Highly Luminescent Cesium Lead Halide Perovskite Nanocrystals with Tunable Composition and Thickness by Ultrasonication, Angew. Chemie Int. Ed. 55 (2016) 13887–13892. https://doi.org/10.1002/anie.201605909.

[37] J.A. Sichert, Y. Tong, N. Mutz, M. Vollmer, S. Fischer, K.Z. Milowska, R.G. Cortadella, B. Nickel, C. Cardenas-Daw, J.K. Stolarczyk, A.S. Urban, J. Feldmann, Quantum Size Effect in Organometal Halide Perovskite Nanoplatelets, (2015).

https://doi.org/10.1021/ACS.NANOLETT.5B02985.

[38] H.-H. Fang, L. Protesescu, D.M. Balazs, S. Adjokatse, M. V. Kovalenko, M.A. Loi, Exciton Recombination in Formamidinium Lead Triiodide: Nanocrystals versus Thin Films, Small. 13 (2017) 1700673. https://doi.org/10.1002/smll.201700673.

[39] A.A. Zhumekenov, M.I. Saidaminov, M.A. Haque, E. Alarousu, S.P. Sarmah, B. Murali, I. Dursun, X.-H. Miao, A.L. Abdelhady, T. Wu, O.F. Mohammed, O.M. Bakr, Formamidinium Lead Halide Perovskite Crystals with Unprecedented Long Carrier Dynamics and Diffusion Length, ACS Energy Lett. 1 (2016) 32–37. https://doi.org/10.1021/acsenergylett.6b00002.

[40] K. Galkowski, A. Mitioglu, A. Miyata, P. Plochocka, O. Portugall, G.E. Eperon, J.T.W. Wang, T. Stergiopoulos, S.D. Stranks, H.J. Snaith, R.J. Nicholas, Determination of the exciton binding energy and effective masses for methylammonium and formamidinium lead tri-halide perovskite semiconductors, Energy Environ. Sci. 9 (2016) 962–970. https://doi.org/10.1039/c5ee03435c.

[41] J.-C.C. Blancon, A. V. Stier, H. Tsai, W. Nie, C.C. Stoumpos, B. Traoré, L. Pedesseau, M. Kepenekian, F. Katsutani, G.T. Noe, J. Kono, S. Tretiak, S.A. Crooker, C. Katan, M.G. Kanatzidis, J.J. Crochet, J. Even, A.D. Mohite, B. Traoré, J. Even, A. V. Stier, H. Tsai, C.C. Stoumpos, F. Katsutani, J.-C.C. Blancon, M. Kepenekian, L. Pedesseau, G.T. Noe, A.D. Mohite, J.J. Crochet, W. Nie, J. Kono, S.A. Crooker, M.G. Kanatzidis, C. Katan, Scaling law for excitons in 2D perovskite quantum wells, Nat. Commun. 9 (2018) 1–10. https://doi.org/10.1038/s41467-018-04659-x.

[42] X. Wu, M.T. Trinh, X. Zhu, Excitonic Many-Body Interactions in Two-Dimensional Lead Iodide Perovskite Quantum Wells, J. Phys. Chem. C. 119 (2015) 14714–14721. https://doi.org/10.1021/acs.jpcc.5b00148.

[43] W. Paritmongkol, N.S. Dahod, A. Stollmann, N. Mao, C. Settens, S.L. Zheng, W.A. Tisdale, Synthetic Variation and Structural Trends in Layered Two-Dimensional Alkylammonium Lead Halide Perovskites, Chem. Mater. 31 (2019) 5592–5607. https://doi.org/10.1021/acs.chemmater.9b01318.

[44] L. Protesescu, S. Yakunin, S. Kumar, J. Bär, F. Bertolotti, N. Masciocchi, A. Guagliardi, M. Grotevent, I. Shorubalko, M.I. Bodnarchuk, C.-J. Shih, M. V. Kovalenko, Dismantling the “Red Wall” of Colloidal Perovskites: Highly

Luminescent Formamidinium and Formamidinium–Cesium Lead Iodide Nanocrystals, ACS Nano. 11 (2017) 3119–3134. https://doi.org/10.1021/acsnano.7b00116.

[45] X. Wu, M.T. Trinh, X.-Y. Zhu, Excitonic Many-Body Interactions in Two-Dimensional Lead Iodide Perovskite Quantum Wells, J. Phys. Chem. C. 119 (2015) 14714–14721. https://doi.org/10.1021/acs.jpcc.5b00148.

[46] V.A. Hintermayr, L. Polavarapu, A.S. Urban, J. Feldmann, Accelerated Carrier Relaxation through Reduced Coulomb Screening in Two-Dimensional Halide Perovskite Nanoplatelets, ACS Nano. 12 (2018) 10151–10158. https://doi.org/10.1021/acsnano.8b05029.

Chapter 3. HOT CHARGE CARRIER AND EXCITON RELAXATION IN COLLOIDAL PEROVSKITE NANOSTRUCTURES

In this chapter, hot charge carrier and hot exciton cooling dynamics were studied using femtosecond transient absorption (TA) in two different colloidal perovskite nanosystems: weakly confined $FAPbI_3$ nanostructures and strongly confined 2D perovskite nanoplatelets (NPLs) with different compositions. The first part deals with the effect of high excitation fluence on the carrier relaxation process in $FAPbI_3$ nanocrystals (NCs) and thick nanoplates (NPs). In these systems, the cooling dynamics were determined by the extraction of the time-dependent carrier temperature following the Burstein-Moss shift of the band-edge bleach. A global analysis method was found to be more practical to follow the full relaxation dynamics compared to previous methodologies. As it was expected we obtained a large contribution from hot phonon bottleneck and Auger reheating effect, both of which decrease the hot charge carrier relaxation rates.

In the second part, the strong quantum and dielectric confinement in the 2D NPLs lead to discrete excitonic band-edge transitions and large Stark effects that prevent the use of conventional analysis methods to investigate the exciton cooling dynamics. Consequently, we apply also in this case a global data analysis method based on the spectral lineshape evolution from an initial "hot" state to a relaxed state, that we interpreted in terms of photo-induced bleach and spectral shifts. The extracted cooling rate was found to be faster than in the weakly confined samples, evidencing the absence of an intrinsic phonon bottleneck and thus suggesting another efficient relaxation pathway than the phonon-related one. While the nature of the cations inside the crystalline structure in the NPLs does not affect this rate strongly, we found an effect of the surface ligands through excitation fluence dependent experiments by comparing with 2D perovskite thin films. These results suggest the existence of a surface-mediated relaxation mechanism that becomes dominant in the strongly confined perovskite structures.

3.1. Introduction

Thanks to their outstanding properties, 3D and 2D lead halide perovskites have emerged as extremely promising low cost processing materials for several optoelectronic applications [1–9]. For all these applications, it is important to characterize the rate at which hot charge carriers and excitons relax to the band-edge and identify the properties affecting its rate in order to control it. While, the cooling has been the subject of intense research in 3D and quasi-3D (weakly confined NCs) halide perovskites over the last few years, corresponding investigations in strongly confined structures remain limited and have led to conflicting conclusions (see below).

Several groups have investigated the hot charge carrier relaxation in bulk perovskite films [10–15] Typically, the hot carrier relaxation is analyzed by fitting the high-energy tail of the band-edge bleach in transient absorption spectra with a Maxwell-Boltzmann distribution function. This allows the extraction of the carrier temperature T_c, whose time-evolution gives the cooling rate. The latter was found to be strongly dependent on the instantaneous charge carrier density. From the order of hundreds of femtoseconds at low or moderate excitation fluence, this time is strongly increased by several orders of magnitude at high excitation fluence (starting at about 10^{18} cm^{-3}) [10–12]. This *hot phonon bottleneck* effect is commonly observed in inorganic polar semiconductors where the dominant relaxation pathway is through carrier-longitudinal optical (LO) phonon scattering (*cf* **Chapter 1, part 2**). This has been the subject of several reports in bulk hybrid halide perovskite materials (thin films) [10–12,18,19]. In weakly confined halide perovskite nanocrystals, this method can still be applied as long as the energy-level spacing remains below the thermal temperature [20–24]. A recent review summarizes the findings regarding hot carrier cooling of several halide perovskite materials studied previously with TR-PL and TA spectroscopy [16].

In more confined structures, a strong reduction of the cooling rate is expected at low excitation fluence when the material energy level separations become larger than the energy of relevant optical phonon modes (*intrinsic phonon bottleneck* effect). Although predicted in the early 90s for confined semiconductor NCs, this *intrinsic phonon bottleneck*, originating from an inefficient multiphoton emission process, is rarely observed due to the presence of other fast relaxation pathways [25,26]. In halide perovskite, a slightly slower cooling rate was observed within smaller sized $MAPbBr_3$ NCs [20], whereas in more recent studies, comparable rates were reported for $CsPbBr_3$, $CsPbI_3$ and $FAPbBr_3$ NCs over a larger size range [23,24,27]. Apart from that, a much larger decrease of the hot charge carrier cooling rate was reported for confined perovskite NCs compared to bulk thin films when increasing the excitation fluence. The reason for this was attributed to the Auger reheating effect (*cf* **Chapter 1, part 2**). While this resonant energy transfer is difficult to achieve in bulk materials, it becomes highly efficient in nanostructures due to the enhanced carrier-carrier interactions.

In 2D nanostructures such as perovskite NPLs, the substantial quantum and dielectric confinements lead to discrete excitonic band-edge transition and strong carrier-induced Stark signals. This prevents the use of conventional analysis methods for the extraction of the carrier temperature or the build-up of the band-edge bleach amplitude. Analyses of hot exciton cooling in halide perovskite 2D structures with well-defined population (*i.e.* with an unique number of monolayers, n) have led to divergent cooling times; sub-150 fs [28] and 360-400 fs [29]. While both studies were carried out on n=1 lead iodide films, the 2D perovskite film samples were based on two different ligands, phenylethyl- *versus* butyl-ammoniums and two different excitation wavelengths were employed for the experiments (about 440 and 350 nm, respectively). In another study, Feldmann *and co.* have attempted to compare the cooling rate of quasi-3D colloidal $MAPbI_3$ nanoplates and 3 monolayer 2D nanoplatelets in solution (MAPI n=3) [30]. The authors found a faster

relaxation of 240 fs in the thin NPL sample based on oleylammonium ligands. Importantly, this rate, measured *within the continuum of states*, was found independent on the excitation fluence. In contrast, another report on exciton cooling in MA-based lead iodide 2D perovskite nanoplatelets (n=3) with n-butylammonium ligands has surprisingly led the authors to assume the presence of an enhanced hot phonon bottleneck [31]. In all these reports, the apparent discrepancies could be explained mainly by the different methods of analysis employed to extract the cooling dynamics rather than a difference in the materials.

Here, employing fs-TA spectroscopy, we examine the role of confinement effects in the cooling dynamics by comparing the dynamics of hot charge carriers and hot excitons in weakly-confined NCs and strongly-confined 2D NPLs, respectively. We propose a systematic method based on a temporal analysis of the transient spectral lineshapes. This approach rationalizes the results of weakly confined $FAPbI_3$ samples with the conventional analysis of the carrier temperature, while pointing out its inaptness in the investigation of 2D perovskites in a strong 1D confinement regime. We find a faster cooling rate in the more confined 2D perovskite NPLs compared to the weakly confined $FAPbI_3$ NCs, which is also dependent on the excitation fluence. This absence of an intrinsic phonon bottleneck in the strongly-confined systems suggests here the presence of an efficient cooling mechanism mediated by the coupling between the exciton and surface ligand vibrational modes.

3.2. Carrier relaxation in weakly confined $FAPbI_3$ nanostructures

We begin by describing the charge carrier relaxation dynamics in thick $FAPbI_3$ nanoplates and cubic $FAPbI_3$ nanocrystals, in both of which the confinement is weak. The hot charge

carrier cooling rate of thick colloidal $FAPbI_3$ nanoplates (NPs) synthetized with the LARP method (see **Chapter 2, part 2**) was studied using femtosecond TA spectroscopy, with a pump energy of 1.97 eV (630 nm) and several excitation fluences. This excitation above the bandgap corresponds to an excess of energy of about 350 meV. The TA spectra of these thick colloidal NPs is displayed in **Figure 3.1b**.

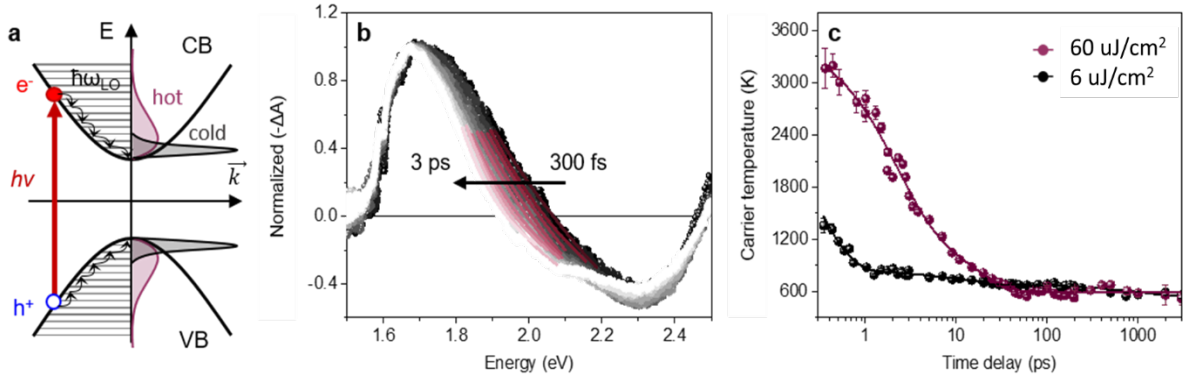

Figure 3.1. (a) *Schematics of the relaxation from a hot to cold charge carrier distribution in the case of a continuum of energy levels above the bandgap.* ***(b)*** *Example of normalized TA spectra at short time range (dots, excitation 630 nm, 60 µJ/cm², chirp-corrected) with their high energy tail fitted by a Boltzmann distribution (full lines). In this graph the bleaches appear positive and the PIA negative while their sign is opposite before normalization of ΔA(λ) to the first bleach feature.* ***(c)*** *Time-dependent carrier temperatures T_c of thick $FAPbI_3$ nanoplates extracted over four decades from the TA spectra for a 630 nm pump excitation of 6 µJ/cm² (black dots) and 60 µJ/cm² purple dots). Three-exponential fits of these decays are displayed in full lines (parameters in* ***Table 3.1****).*

Here, we should note that the sign of the TA spectra was inversed before normalization such as the negative features appear positive and inversely. The TA spectra show characteristic features of hybrid perovskite thin films [32]: 1) a large bleach signal at about 1.7 eV corresponding to band-edge state filling and which extends to higher energies at early time, 2) a second bleach signal at higher energy (>2.6 eV, not resolved entirely) involving a higher energy transition and 3) a broad photo-induced absorption (PIA) signal in between.

3.2.1. Classical method of the tail-fitting to extract T_c

The high energy tail (1.9-2.1 eV) of the band-edge bleach at early time reflects the hot charge carrier occupancy of the continuous energy levels above the bandgap and is much pronounced at high excitation fluence (Burstein-Moss effect) [10,11]. Previous reports in 3D perovskite thin films and weakly confined NCs have shown that the relaxation process can be examined considering a continuous band filling dominated by free charge carriers [16,20,21]. Here, the continuous high-energy tail of $FAPbI_3$ thick NPs reflects the distribution of the thermalized charge carriers occupying the quasi continuous high-energy levels as well, since the energy spacing remains small in comparison with k_BT at room temperature (**Figure 3.1a**) [20,21]. This follows a Fermi-Dirac distribution that can be approximated by a Maxwell-Boltzmann function [33]:

$$\Delta A(h\nu) = A_0 \, exp\left(-\frac{h\nu - E_{eff}}{k_B T_c}\right) + PIA \qquad [3.1]$$

where A_0 is a constant, $h\nu$ is the detected energy, k_B the Boltzmann constant and T_c charge carrier temperature. PIA corresponds to a non-zero background due to the broadband photoinduced absorption signal. E_{eff} corresponds to the center energy of the bleach signal and results from the time-dependent bandgap energy (Burstein-Mott shift).

Using this equation to fit the extent of the high-energy tail of the band-edge bleach of each TA spectrum (see for example **Figure 3.1b**), carrier temperatures were extracted from 300 fs to 3 ns, for moderate (6 µJ/cm^2) and high excitation fluence (60 µJ/cm^2), and displayed in **Figure 3.1c**. The average density of excitons created per pulse for these two fluences are estimated to be 1.2×10^{18} and 1.2×10^{19} cm^{-3}, respectively (see calculation in **ANNEXE 3**). The overall behavior of the carrier temperature decay curves in time can be effectively described by a multiexponential function, similarly with reported relaxation

dynamics of $FAPbI_3$ NCs [21], with two or three time constants over the full nanosecond time range. The fit parameters of **Figure 3.1c** presented in **Table 3.1** present a first component of hundreds of femtoseconds to picoseconds, a second component of tens of ps and a last component in several hundreds of ps to ns.

Excitation Fluence	A_1 (%)	τ_1 (ps)	A_2 (%)	τ_2 (ps)	A_3 (%)	τ_3 (ps)	T_0 (K)
6 µJ/cm²	90 ± 30	0.25 ± 0.05	5.7 ± 0.5	11 ± 2	5 ± 2	1030 ± 860	540 ± 60
60 µJ/cm²	2100 ± 200	2.1 ± 0.6	900 ± 100	14 ± 2	-	-	588 ± 8

Table 3.1. *Fit parameters for a two- and tri-exponential decay of the charge carrier temperature in time at moderate and high excitation fluence (**Figure 3c**):* $T_c = T_0 + \sum_i^3 a_i \, exp\left(-{}^{t}/_{\tau_i}\right)$ *and* $A_i = \frac{100\, a_i}{\sum_j a_j}$.

Several mechanisms can participate in the charge carrier relaxation dynamics in these weakly confined samples: hot-charge carrier cooling through LO-phonon scattering, Auger recombination (Auger heating) and electron-hole recombination. The associated processes can lead to different recombination orders (*e.g.* mono-, bi- or tri-molecular), depending on their physical nature. To try to give a physical meaning of the different timescales of relaxation obtained in the thick nanoplates, we investigated the evolution of the lineshape and the amplitude of the signals in the transient spectra along these three different time scales. Although the classical tail-fitting method extracting T_c in TA and plotting the energy-loss rate *versus* this temperature allows to compare cooling dynamics between different samples or for a given sample with different initial excess energies [12,20], we found it quite sensitive on the energy range used for the fit. Some authors suggest a minimum range of 0.2 eV [21], whereas for an extended energy range the overlap of the band-edge bleach with the PIA signal might introduce some errors in T_c extraction. Moreover, for a high density of photogenerated charge carriers, a non-negligible bandgap renormalization, occurs causing an important red-shift of the bleach [34]. This Coulomb

screening effect has an opposite trend than the Burstein-Mott shift. Even if the *Eeff* value is modified by the band-gap renormalization its incidence on the *T*c remains unclear for us and thus might compensate it at least partially [19]. Finally, the final carrier temperature we obtained was higher than the expected lattice temperature at room conditions *T*~300 K. This difference can be understood by the presence of the smaller-sized nanoplates within the sample synthesized by the "LARP" method, as corroborated by the high energy tail observed in the corresponding PL spectrum (**Figure 2.23** in **Chapter 2**). Thus, carrier temperature extraction in confined systems can be artificially overestimated with a large distribution of sizes.

3.2.2. Global analysis of TA data

Alternatively, relaxation dynamics can be accessed using global and target analysis methods to follow the global evolution of the bleach signal in time even in the presence of other overlapping spectral components [15,22,34,35]. Here, we used Glotaran [36] to perform a global fit analysis of the full TA data ($\Delta A(t,\lambda)$) of the thick NPs, using a sequential kinetic model involving spectral components called "Evolution Associated Spectra" (EAS) and exponential components defined by their rate constants (k). This global analysis allows to relate the evolution of the integrated amplitude of the TA signal with the dynamics of the photoexcited charge carriers (explanation below) in order to identify the underlying relaxation processes. In order to cover the full nanosecond range, we perform the global analysis on three different time ranges that can be related to the multiexponential fit of the Tc (see above): the short-time range up to 4 ps with 20 fs step, the middle range up to 200 ps with 1 ps step and the long time range up to 3.2 ns with 20 ps step.

3.2.2.1. Short-time dynamics

We first concentrate on the picosecond time range where the weight of the associated time constant represents 90 % of the total relaxation in terms of temperature decay at moderate excitation fluence and 70 % at high fluence. With two rate constants k_1 and k_2 and two EASs EAS_1 and EAS_2, the TA data could be perfectly reproduced for all the excitation fluences. Including a larger number of components did not significantly improve the quality of the fit. In this model, the EAS_1 rises during the interaction with the pump pulse (*e.g.* in about 100 fs) and decays exponentially following k_1, while the EAS_2 rises with k_1 and then decays exponentially following k_2 (schematic **Figure 3.2a**).

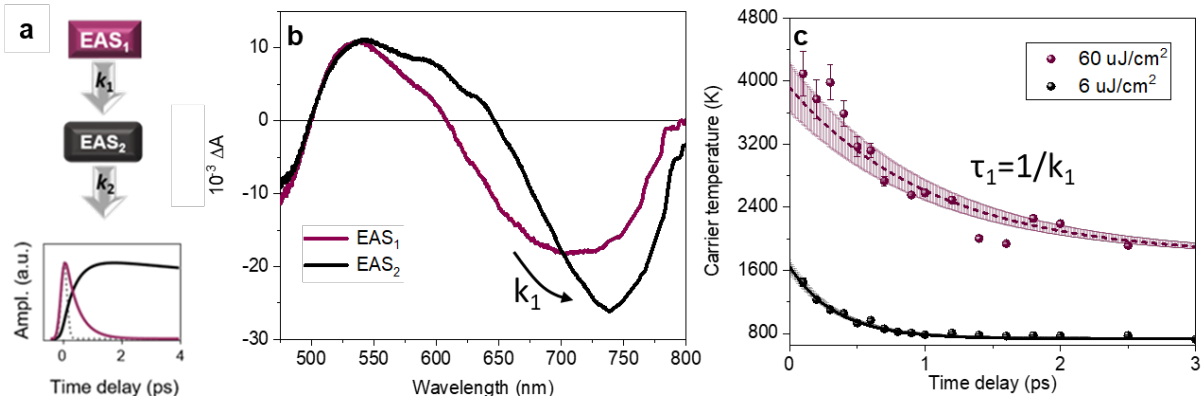

Figure 3.2. *Global analysis of TA data of thick $FAPbI_3$ nanoplates. The TA data can be simulated by a kinetic model schematized in* ***(a)*** *with two rate constants k_1 and k_2 and two spectral components EAS_1 and EAS_2 displayed in* ***(b)*** *(here for an excitation fluence of 6 $\mu J/cm^2$). The continuous spectral shift of the experimental TA spectra are simulated by a linear combination of the EASs with time-dependent amplitude related to k_1, k_2 and the IRF.* ***(c)*** *Comparison between T_c extracted from the classical analysis (dots) and the exponential simulation using global fit parameters (lines with associated errors) at low (black) and high (purple) excitation fluences.*

The good agreement between the experimental and the fitted data can be seen in the decay traces at band-edge and in the PIA signals (**Figure 3.3**). The corresponding EAS are shown in **Figure 3.4** for the different excitation fluences. The band-edge bleach of EAS_1 displays a characteristic high-energy tail and a pronounced blue shift compared to that of EAS_1 (see also the direct comparison in **Figure 3.2b**). The resulting lifetime

associated with this fast dynamics (EAS_1 to EAS_2), $\tau_1 = 1/k_1$, increases with the excitation fluence from 360 ± 20 fs at 6 μJ/cm² to 970 ± 80 fs at 60 μJ/cm². We attribute the evolution from EAS_1 to EAS_2 with a rate constant k_1 to the early-stage relaxation of the hot charge carriers to the band-edge.

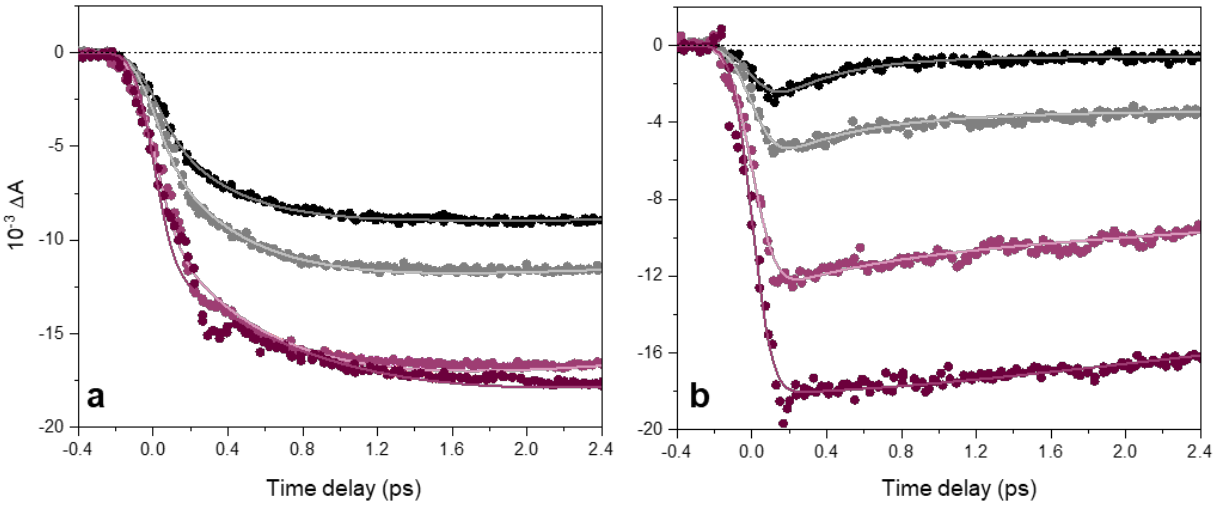

Figure 3.3. *Experimental TA decay traces (dots) and fitted traces (lines, from global analysis) of thick $FAPbI_3$ nanoplates detected (a) at the band-edge (765 nm) and (b) above (700 nm). The excitation was at 630 nm for fluences of 6 (black), 15 (grey), 30 (pink) and 60 (purple) μJ/cm².*

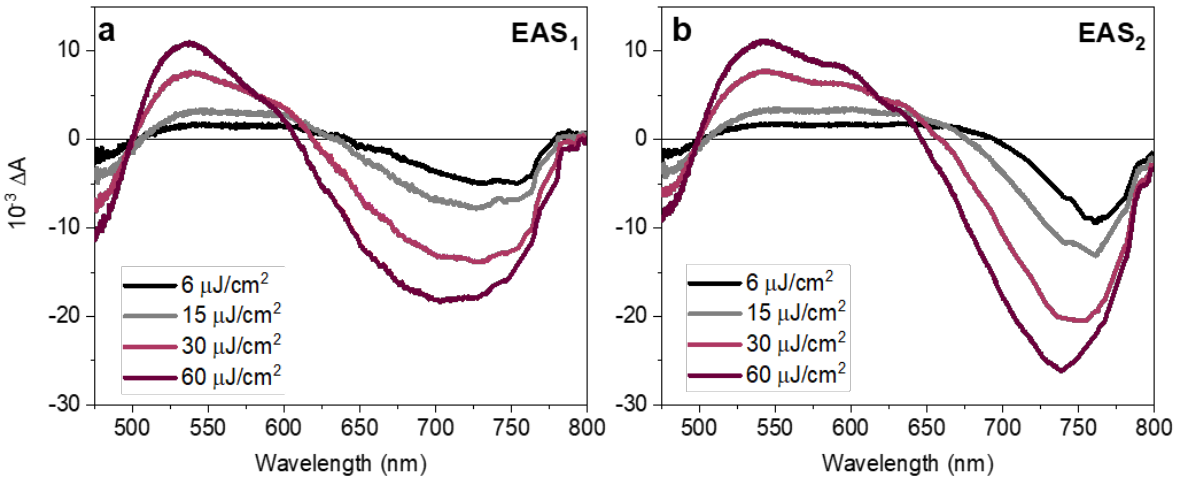

Figure 3.4. *Initial (EAS_1, **a**) and final (EAS_2, **b**) evolution associated spectra of thick $FAPbI_3$ nanoplates for four different excitation fluences, extracted from TA data at short time scale (few ps).*

There are two objections one could made about this model. First it describes an evolution from a specific state, a "hot" state of the system, represented by EAS_1, to another specific state EAS_2, while physically the system really evolves through a continuum of states, each of them described by its proper T_c. However, as EAS_1 and EAS_2 overlap over an important spectral range, a linear combination of them, as indeed obtained along all the time range of the experiment, result in an effective continuous shift of the band-edge bleach and successive reduction of the extent of its high-energy tail in time (see below). Secondly, the kinetics of relaxation are expected to be much more complex than simple exponential dynamics, as previously equated with the energy loss rate evolution for charge carrier-LO phonon scattering and high-order kinetic recombination such as Auger reheating [37]. We discuss this approximation in the following.

During the first picosecond time range, EAS_1 decays with a characteristic rate k_1 to the EAS_2 state, presenting much reduced high-energy tail. Assuming a thermalized distribution of the charge carriers, the initial and final (within this time range) carrier temperatures can be extracted from EAS_1 and EAS_2 respectively. Furthermore, the time constant $\tau_1 = 1/k_1$ obtained from the global data analysis can be used to simulate the evolution of the carrier temperature within this time range:

$$T_c(t) = \left(T_i - T_f\right) exp\left(-\frac{t}{\tau_1}\right) + T_f \qquad [3.2]$$

where T_i and T_f are the initial and final carrier temperatures extracted by fitting the high energy tail of the band-edge bleach of the EAS_1 and EAS_2 spectra, respectively, with a Boltzmann distribution. The results are displayed within the TA maps of the thick $FAPbI_3$ nanoplates sample in **Figure 3.5**.

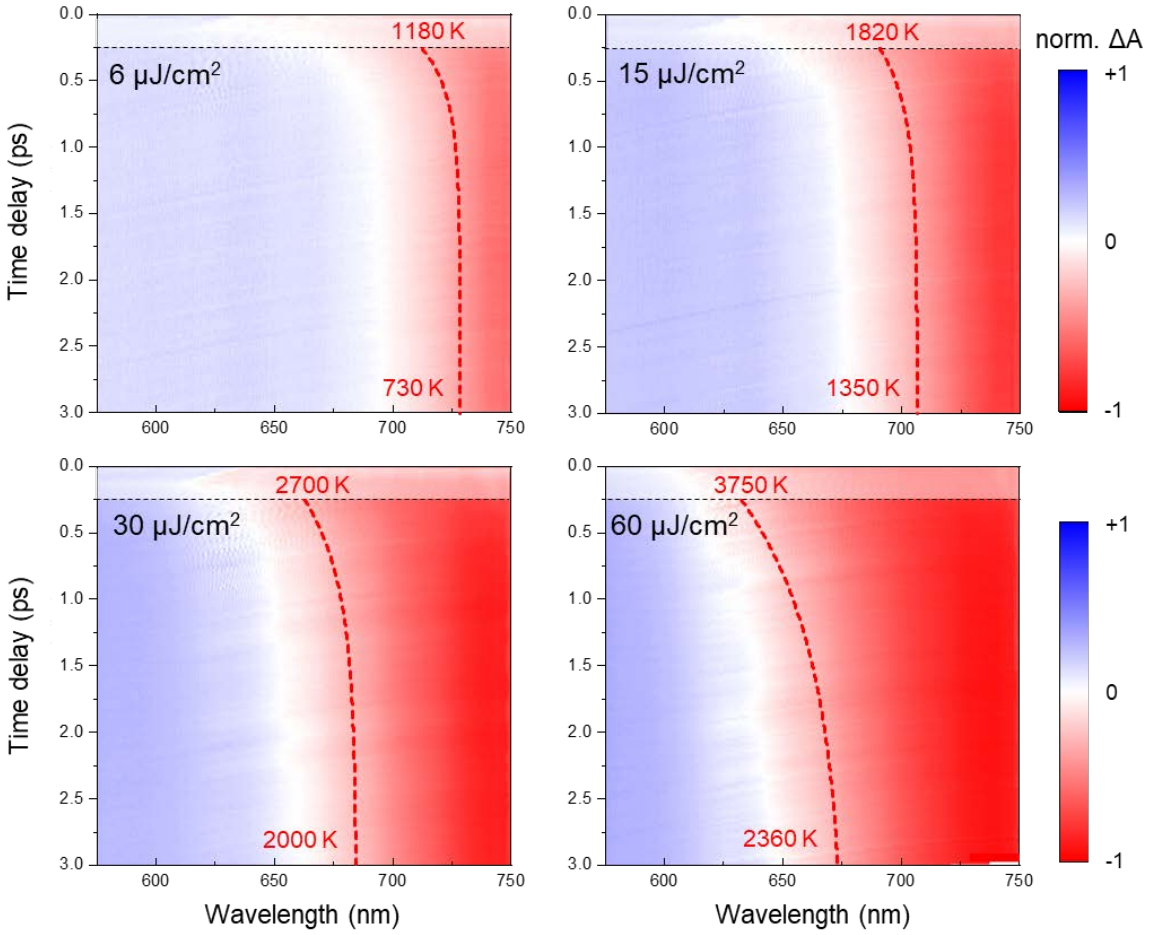

Figure 3.5. *Early time TA maps, corrected from the chirp, of thick $FAPbI_3$ nanoplates for a pump excitation at 630 nm from 6 to 60 µJ/cm². The initial and final carrier temperatures T_c extracted from the EAS spectra are displayed, as well as a visual aid of the time dependent energy corresponding to $k_BT_c+E_{eff}$ (exponential fit, dashed red line). The first 250 fs were not analyzed (white shaded parts) in order to take into account only the thermalized charge carrier distributions.*

The comparison between the carrier temperature decays obtained for thick $FAPbI_3$ NPs using the classical high energy-tail fitting method (dots) and the simulated decay using the **Equation 3.2** with the global analysis parameters are in good agreement in this first picosecond time range (**Figure 3.2c**). We then performed the same analysis of the data measured at a higher excitation photon energy (520 nm, excess energy of about 760 meV) and for the cubic $FAPbI_3$ NCs excited at 650 nm (about 240 meV above the bandgap energy

of 1.67 eV). All the relaxation k_1 rates extracted at different excitation fluences are plotted in **Figure 3.6a**.

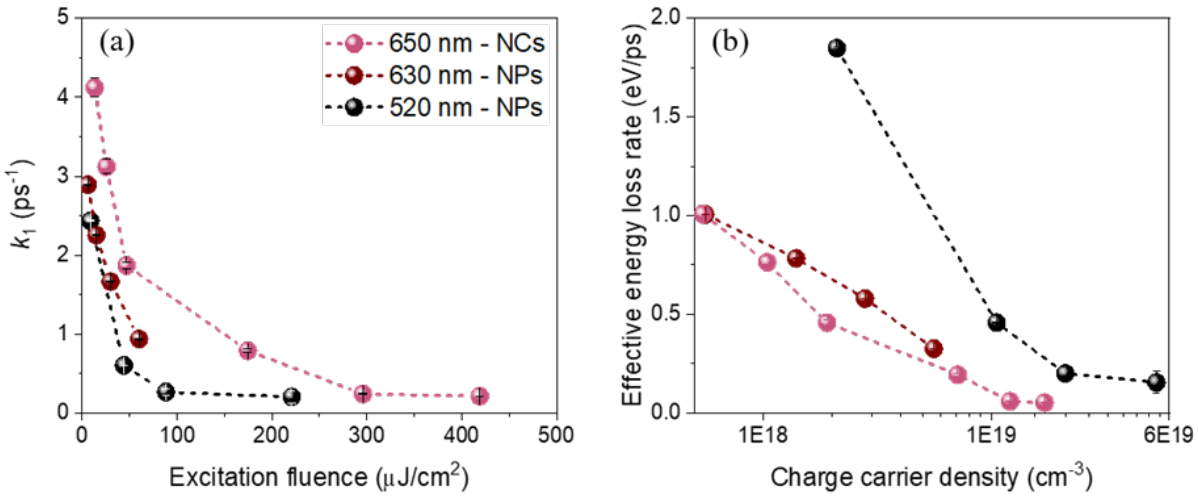

Figure 3.6. **a)** *Extracted cooling rates k1 of FAPbI3 NCs (pink dots, excitation 650 nm) and thick nanoplates (excitation 630 nm: wine dots, excitation 520 nm: black dots) plotted versus the excitation fluence.* **b)** *Plot of the corresponding energy loss rate versus the charge carrier density (number of initial electron-hole pairs per nanocrystal volume).*

At the lowest fluences, the cooling is relatively fast and depends on the excitation photon energy: $\tau_1=1/k_1 \approx 411 \pm 1$ fs for the thick $FAPbI_3$ nanoplates excited at 520 nm and 350 ± 10 fs when excited at 630 nm. While physically, it takes longer time to fully relax to the band-edge in the case of a higher excess energy, the "global energy loss rate" defined as the initial excess energy ($\Delta E=h\upsilon-E_g$) divided by the cooling time (τ_1) is 1.9 and 1.0 eV/ps, respectively (see **Figure 3.6b)**. It is higher when it is excited at 520 nm than at 630 nm. For the cubic $FAPbI_3$ NCs excited at 650 nm, we obtained $\tau_1 \approx 242$ fs, corresponding to the global energy loss rate about 0.99 eV ps^{-1}. At higher carrier densities, the initial cooling time τ_1 increases up to few picoseconds for the two $FAPbI_3$ samples, comparable to previous reported values for $FAPbI_3$ NCs [21]. This corresponds to a global energy loss rate of about 0.4 eV ps^{-1} for the NPs excited at 630 nm. These values will be compared with those measured of strongly confined 2D nanoplatelets in **Part 3.3**.

3.2.2.2. Middle and long-time dynamics

To further investigate the relaxation processes, we analyzed the longer time TA dynamics of thick $FAPbI_3$ nanoplates, up to 3 ns. Indeed, within this time range, the high-energy tail of the bleach is still evolving, in particular at high excitation fluence, indicating some additional slower mechanism in the hot charge carrier cooling. For these longer time ranges, three kinetic time constants and corresponding EASs were needed to reproduce the data well (**Figure 3.7**).

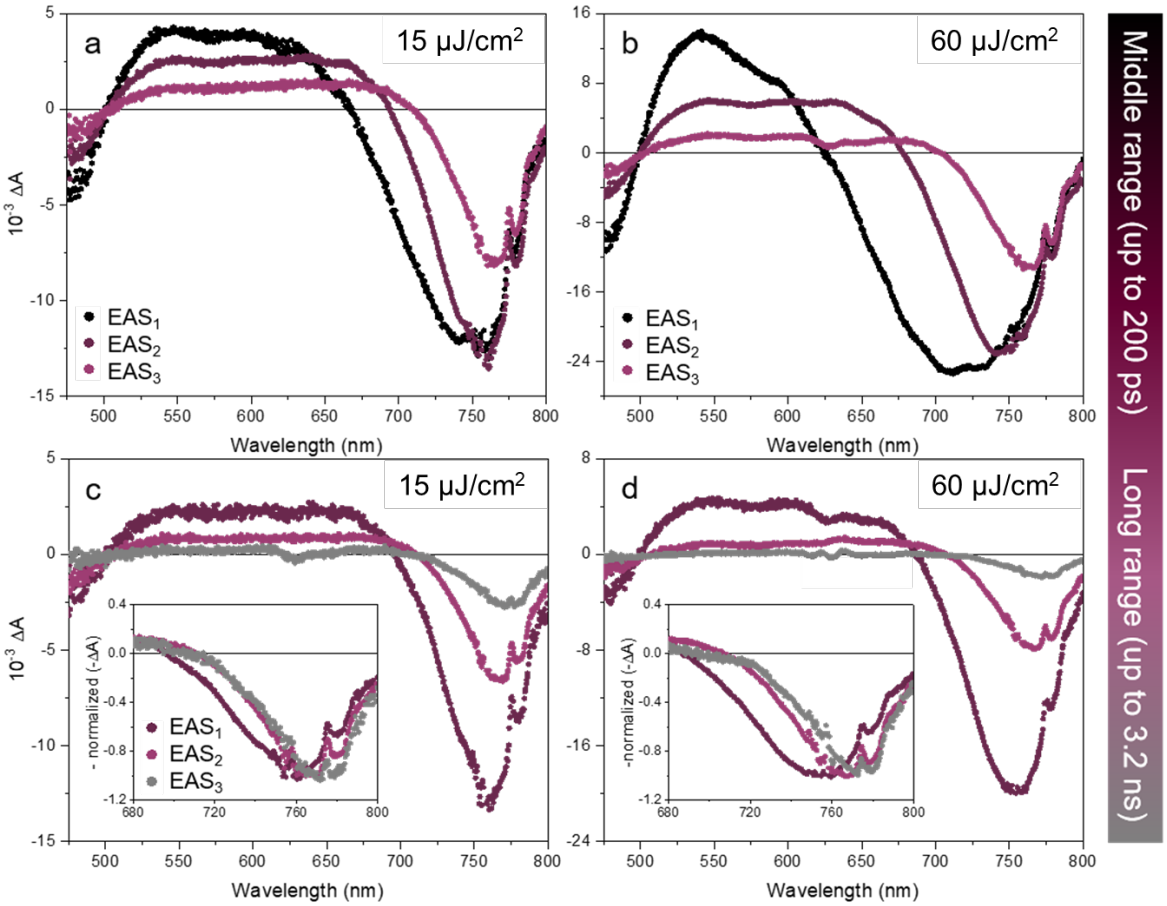

Figure 3.7. *Evolution Associated Spectra of thick $FAPbI_3$ NPs excited at 630 nm at middle* ***(a,b)*** *and long* ***(c,d)*** *time ranges, for medium* ***(a,c)*** *and high* ***(b,d)*** *excitation fluences. For*

the middle time range analysis, the characteristic time corresponding to the evolution from EAS_1 to EAS_2 is increasing from several hundreds of fs to few ps with the excitation fluence, while the second- and third-time constants remain about 25-40 ps (EAS_2 to EAS_3) and 270-500 ps (decay of EAS_3) respectively. For the long-time range, the characteristic times are about 60-80 ps (EAS_1 to EAS_2), 500-800 ps (EAS_2 to EAS_3) and 5-20 ns (decay of EAS_3). Inset: Normalized EASs.

The summarized parameters are displayed in the following **Table 3.2.**

Excitation fluence	time range					
	short	middle		long		
	$\tau_1 = 1/k_1$	$\tau_{1,m}=1/k_{1,m}$	$\tau_{2,m}=1/k_{2,m}$	$\tau_{1,l}=1/k_{1,l}$	$\tau_{2,l}=1/k_{2,l}$	$\tau_{3,l}=1/k_{3,l}$
($\mu J/cm^2$)	(ps)	(ps)	(ps)	(ps)	(ps)	(ns)
6	0.36 ± 0.02	0.31 ± 1	42.9 ± 0.3	82 ± 1	597 ± 10	9.8 ± 1
15	0.44 ± 0.02	4.9 ± 1	34.5 ± 0.2	63.0 ± 0.6	517 ± 10	8.5 ± 1
30	0.62 ± 0.02	4.3 ± 1	29.41 ± 0.09	58.8 ± 0.3	635 ± 10	20.1 ± 1
60	0.97 ± 0.08	3.6 ± 1	25.09 ± 0.07	58.9 ± 0.4	811 ± 10	14 ± 1

Table 3.2. *Fit parameters for a two- and tri-exponential decay extracted from global analysis at different excitation fluence.*

The first time constant $\tau_{1,m}$ covering the time-range from sub-ps to a few picoseconds in the middle range experiments and increasing with the excitation fluence corresponds well to the initial stage of relaxation described above by τ_1 in the short time range. It can be seen by comparing EAS_1 and EAS_2 in **Figure 3.7a,b** that the total amplitude of the band-edge bleach does not evolve much during the first 10 ps. This means that the population (*i.e.* number of charge carriers) remains approximately constant during this initial stage

of relaxation while the corresponding time constant increases with the excitation fluence. We thus attribute the origin of this first relaxation stage to charge carrier - longitudinal optical (LO) phonon scattering, with a hot phonon bottleneck effect, in agreement with previous work reported in bulk and bulk-like hybrid lead halide perovskites [10–12,17,20,21]. Although the exact mechanism of the hot phonon bottleneck effect is still under debate [16], the optical phonon mode(s) involved can be assigned to the Pb-I inorganic lattice with no (or weak) contribution from the organic cation vibrational modes [13,38]. The good agreement between the experimental data and a simple mono-exponential decay in this short time range is rather surprising since a more complex T_c evolution in time is expected [11,12,17,20].

While the total areas of the EAS_1 and EAS_2 bleach signals in the middle time range experiments are rather similar, a strong diminution of the signal was observed during the second stage, covering several tens of ps. This can be observed by comparing EAS_2 to EAS_3 in the middle range experiments associated with time constant $\tau_{2,m}$ (**Figure 3.7a,b**) or EAS_1 to EAS_2 in the long time range data with associated with the $\tau_{1,l}$ (**Figure 3.7c,d**).

At longer times, we found almost no evolution of the spectral lineshapes while the amplitude still evolves with characteristic times $\tau_{2,l}$ of few hundreds of picoseconds and with $\tau_{3,l}$ in several nanoseconds (**Figure 3.7c,d** with inset). The change in time of the bleach amplitude ΔA gives information on the evolution of the carrier concentration due to mono-, bi- and trimolecular recombinations, depending on the nature of the photo-created species (exciton *versus* free carriers) and of the processes taking place [39,40]. Here, only non-radiative Auger recombination can explain the diminution of the bleach amplitude occurring over several tens of ps. Indeed, neither charge carrier trapping [41] nor geminate (or non-geminate) electron-hole recombination should occur on this timescale considering the moderate excitation fluence. From the initial number of electron-hole pairs created per NC volume (*i.e.* e-h pair density), 1.2×10^{18} and 1.2×10^{19}

cm^{-3} corresponding to the two excitation fluences, we can calculate the average distance[1] between these pairs to be about 8.5 and 4 nm, respectively. These values are consistent with a fast three-body recombination [42]. Thus, we attribute the further diminution of the high energy tail taking place during this time range to the effect of the non-radiative Auger recombination in the cooling mechanism (*i.e.* Auger reheating), as previously discussed in hybrid perovskite nanocrystals [20,21] (*cf* **Chapter 1, part 2**).

In agreement with this interpretation, the evaluated Auger recombination time constants $\tau_{2,m}$ or $\tau_{1,l}$ decrease with the excitation fluence (see **Table 3.2**). Furthermore, the Auger time constant $\tau_{1,l}$ extracted from the analysis at long time range are about twice as large as the value $\tau_{2,m}$ extracted at middle time range. This shows that the non-radiative Auger recombination rate is time-dependent and cannot be assigned to a well-defined time constant. Indeed, carrier-carrier interactions depend strongly on the charge carrier concentration which changes in time. This will be discussed in **Chapter 4**.

3.2.3. *Conclusion: Global analysis method*

The global analysis method could be easily and uniformly used to investigate the relaxation (*i.e.* cooling) dynamics in perovskite materials including nanostructures. The evolution of the lineshape and signal amplitude in time extracted from global TA data analysis allows to disentangle the different processes underlying the hot charge carrier relaxation in these samples. The extracted kinetic parameters at short times (first few picoseconds) following exponential dynamics give a good description of the main cooling dynamics through LO phonon emission, with important hot phonon bottleneck effects increasing the relaxation time to almost 1 ps for an excitation fluence of 60 µJ/cm². While,

[1] For 2D material with a surface ($S = V/l$), the average number of excitons per nanocrystal ($\langle N \rangle = j\sigma_{abs}$) can be expressed by the 2D exciton density in cm^{-2} ($\tilde{n} = < N > /S$). Then, the exciton-exciton distance (d) can be estimated using the following expression: $d = \sqrt{1/\tilde{n}}$

more sophisticated analysis compared an exponential decay could be applied at longer times, a sequential kinetic model demonstrates the importance of Auger reheating in both the cooling and the recombination mechanisms, with relatively fast characteristic times on the order of tens of ps for a charge carrier density of 10^{18}-10^{19} cm^{-3}.

3.3. Hot exciton cooling in strongly-confined 2D nanoplatelets

We then turn to the relaxation dynamics in thin colloidal NPLs. In all NPL samples, the first absorption transition and emission peaks are dramatically blue-shifted compared to the corresponding bulk materials (*cf* **chapter 2, part 2**), due to the strong quantum and dielectric confinements (*cf* **Chapter 1, part 1**). We thus use a relatively high excitation photon energy, 3.1 eV (400 nm), in order to excite the NPLs well above their band-edge. In the first TA measurements we fully describe the analysis of the cooling dynamics in FAPI *n*=2 NPLs. These data were acquired without compressing the pump pulse, which was about 130 fs. In the second stage, we performed the same analysis in the other NPL samples, *n=1* (without A^+ cation), CsPI and MAPI *n*=2, with the pump compressed to about 90 fs.

3.3.1. Transient absorption experiments in FAPI *n*=2 nanoplatelets

3.3.1.1. Description of the TA data

We started by investigating the dynamics during the first few picoseconds. Where, the cooling is expected to be the main relaxation process. At low excitation fluence, the transient spectra of $L_2[FAPbI_3]_2PbI_4$ (FAPI *n*=2*)* NPLs are dominated by a strong and narrow negative feature around 576 nm (2.15 eV) (**Figure 3.8a)**. This matches the energy of the first excitonic transition (*i.e*, the band-edge transition) in the linear absorption spectra (**Figure 2.29** in **chapter 2**). Two strong positive signals surround the negative signal at early time and persist well after the pump duration. This gives an overall second derivative lineshape (*cf* **Figure 2.14** in **Chapter 2**).

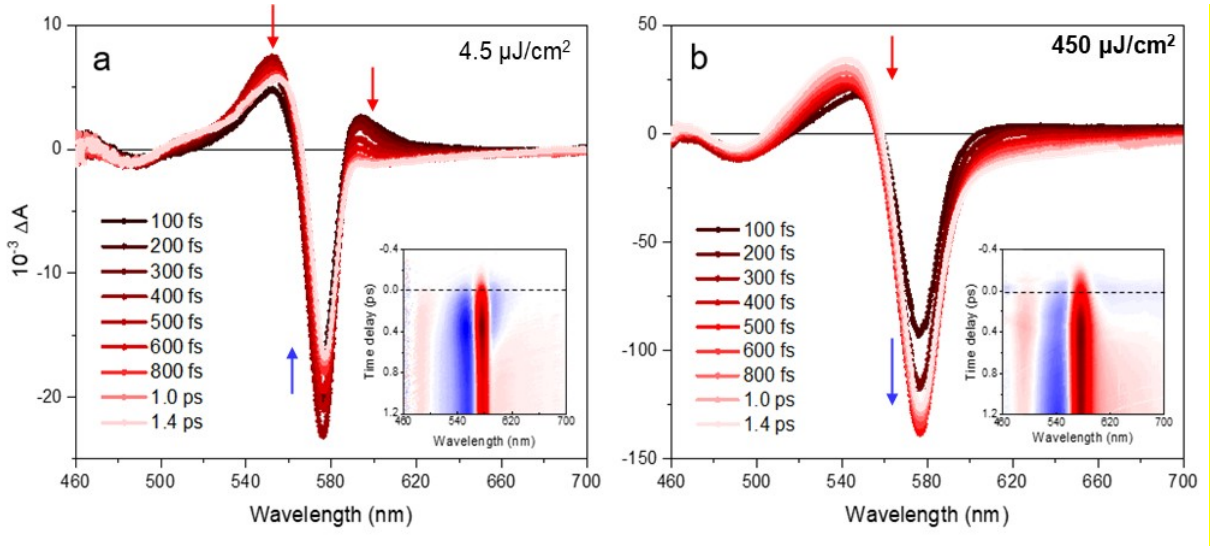

Figure 3.8. *Unchirped transient absorption spectra at different time delays of* FAPI *n=2 NPLs for 400 nm excitation at low* ***(a)*** *and high* ***(b)*** *excitation fluence.* ***Inset:*** *Full TA maps (unchirped, positive and negative signals are displayed in blue and red, respectively).*

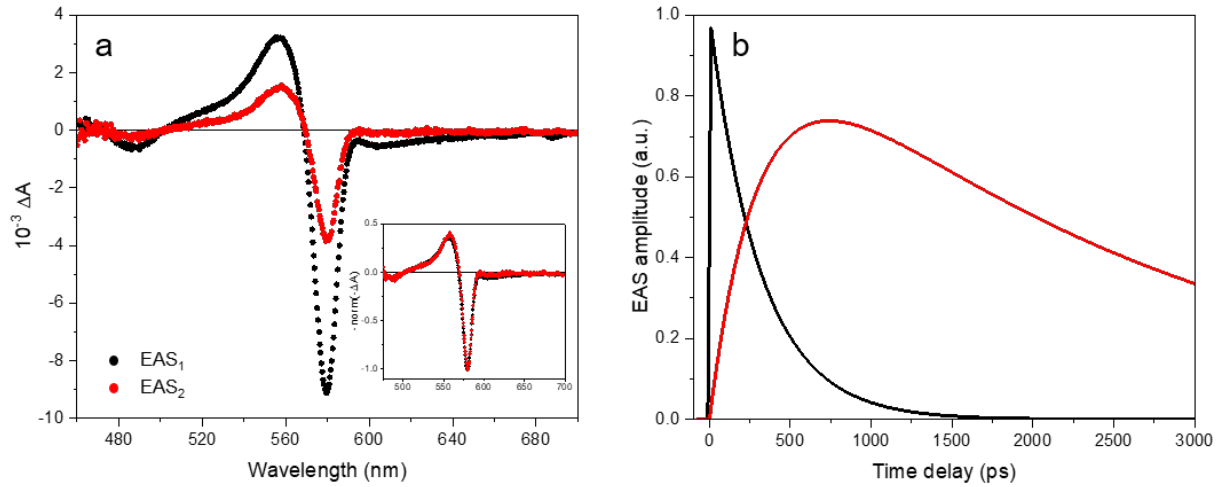

Figure 3.9. a) *Long time EASs of FAPI n=2 NPLs samples excited at 400 nm.* ***b)*** *Associated decays. Both were obtained from a global analysis using two kinetic and spectral components. The exponential decay time constants are 314 ps (EAS₁ to EAS₂) and 2.4 ns (amplitude decay of EAS₂). As EAS₁ and EAS₂ are only different in amplitude the dynamics are only due to depopulation (same normalized lineshape, see* ***inset of a****).*

At times longer than 300 fs, the low-energy positive signal becomes weaker and changes sign. This leads to a broad negative signal observed at long time on the low energy side of

the band-edge feature (576 nm), up to 650 nm. Using global analysis with Glotaran, we notice that the spectra do not change further in shape after a few ps when comparing with the long-time TA spectra (see **Figure 3.9**).

In order to explore the effect of the initial excess energy, we performed experiments at three different excitation wavelengths (400, 515 and 580 nm), all at low fluence (**Figure 3.10**). From the global analysis, we found that the picosecond spectra EAS_2 are independent of the initial excitation photon energy (**Figure 3.10b**). The EAS_1 spectra will be discussed further down in the sub-section **3.3.1.2.** The longtime negative signal at 576 nm reflects at least in part the bleach of the first excitonic transition due to state filling of the band-edge. The extra positive signals are consistent with carrier-induced Stark effects as detailed in the next section (**3.3.1.2**).

The low energy tail of the bleach feature at long time can be assigned to optical transitions involving high-density trap states inside the gap (see **ANNEXE 3**). During this thesis, the initial synthetic protocol of these FAPI n=2 NPLs was slightly modified by changing the length of the ligand chain. Which allowed the suppression of the broadband low-energy tail of the band-edge bleach. (see **chapter 2, part 2**).

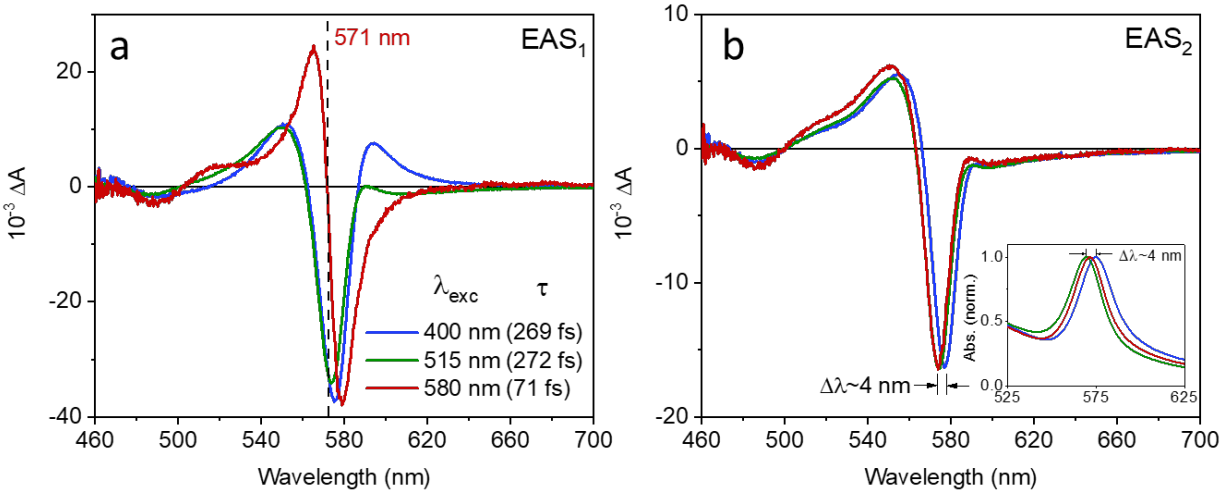

Figure 3.10. *Spectral components EAS_1* ***(a)*** *and EAS_2* ***(b)*** *obtained from a global analysis of the short-time range TA of FAPI n=2 NPLs at low excitation fluence for different excitation wavelengths. In each case, the spectra where normalized (opposite sign) by the value of the negative signal of EAS_2 at about 576 nm. While the initial EAS_1 spectra present different lineshapes, the EAS_2 for all the excitation energies can be superposed as they correspond to the same final state of the system. From the linear absorption spectra (inset of* ***b****), we can link the small shift in energy to a light difference in the synthesis of the samples prepared for the different experiments.*

At high excitation fluence, **Figure 3.8b**, similar but broader features are observed in the transient spectra of FAPI *n*=2 NPLs. Importantly, no high energy tail was observed as the features are symmetrically broadened, as previously observed in CdSe NPLs [43]. In 2D perovskite films and NPLs, with a first exciton binding energy of several hundreds of meV, the continuum of states is well above the lowest energy state and thus the first excitonic transition is discrete [44]. This clearly rules out the possibility of analyzing the cooling dynamics in these 2D samples by fitting the high energy tail of the lowest energy TA bleach by a Boltzmann distribution function, in contradiction with the work of Ding *and co.* [31].

Feldmann *and co.* have thus proposed to extract the relaxation dynamics of *n*=3 MA-based perovskite NPLs by fitting the high-energy tail of a higher energy peak (second lowest optical transition), which overlaps with the continuum of states in energy [30]. From our point of view, such approach probes the relaxation from higher continuum-like levels and does not inform on any confinement effects on the cooling dynamics.

Overall, the transient spectra in terms of photo-induced bleach and Stark signals reflect the state of the system (*e.g.* hot or relaxed state) and thus, their evolution in time can be used to extract the cooling dynamics, as previously reported in colloidal nanocrystals of other semiconductor materials [45–47]. We thus again use the global analysis to fit the

evolution of the transient spectra during the first hundreds of femtoseconds to a few picoseconds and from the lineshape evolution over time we extract the global exciton cooling rate.

3.3.1.2. Kinetic model of relaxation in strongly confined 2D perovskites

Model of analysis.

We performed global data analyses of the time-dependent TA spectra of colloidal FAPI *n=2* NPLs during the first few picoseconds in the same manner as the one used previously for the weakly confined $FAPbI_3$ nanostructures. The results are displayed in **Figure 3.11** for low- (14 μJ/cm²) and high-excitation fluence (1.4 mJ/cm²), see calculation of the corresponding exciton density in **ANNEXE 3**.

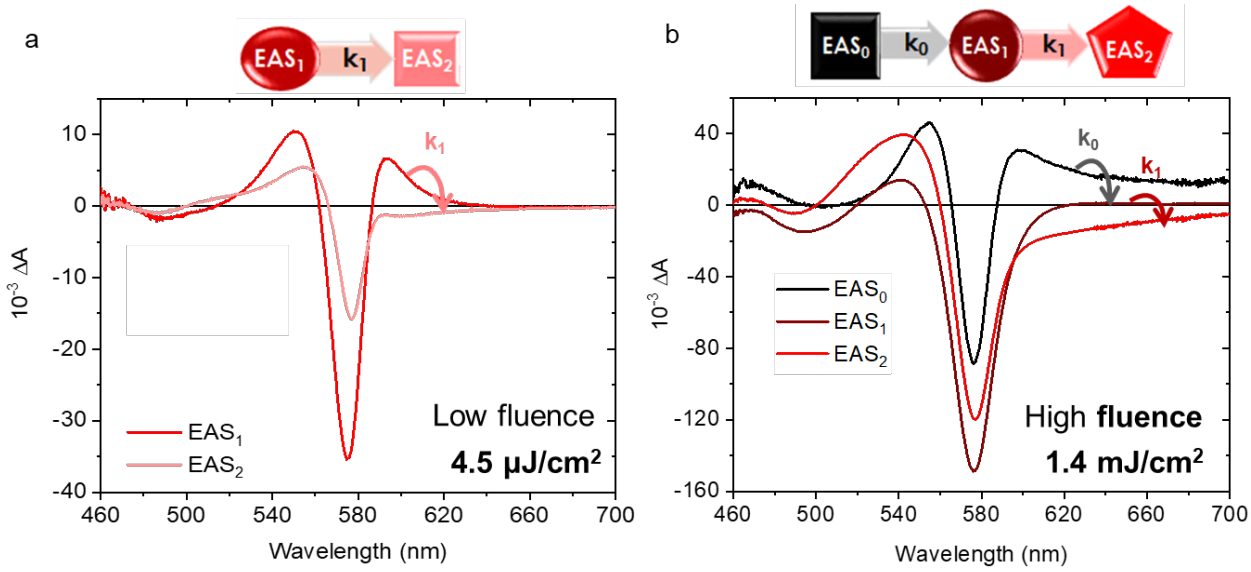

Figure 3.11. *Evolution Associated Spectra (EAS) corresponding to the sequential analysis model of FAPI n=2 NPLs with two and three spectral components for low* ***(a)*** *and high* ***(b)*** *excitation fluence at 400 nm, respectively.*

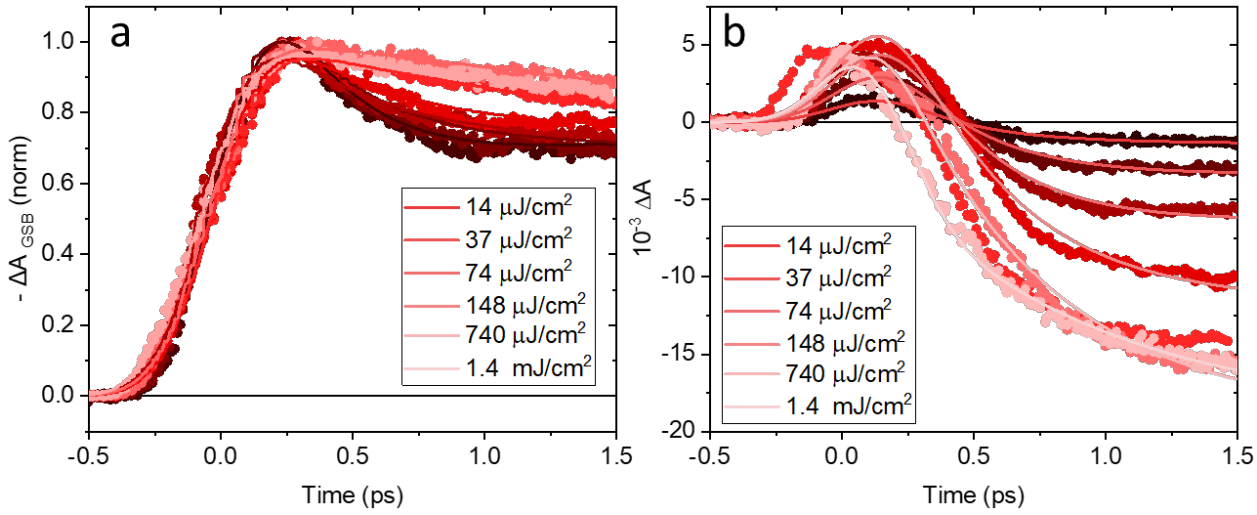

Figure 3.12. *Amplitude evolution in time at (a) band-edge and (b) low energy PIA wavelength at different excitation fluence.*

- At low excitation fluence

At 14 μJ/cm², the TA data are well-modelized by two main spectral and kinetic components: EAS_1 appearing within the pump pulse duration and decaying exponentially with $\tau_1=1/k_1$ = 269 fs and EAS_2 growing exponentially with τ_1 and decaying in amplitude with a characteristic time $\tau_2=1/k_2$ in the tens of ps (outside the time window of this measurement). A very good agreement is found by comparing the experimental spectra **Figure 3.8a** and modelization by the EASs **Figure 3.11a**, as well with the corresponding dynamics (selected decay traces shown in **Figure 3.12**).

- At high excitation fluence:

The same analysis was performed on the TA data obtained with a higher excitation fluence. An additional kinetic component was needed to fit the data satisfactory at excitation fluences above 148 μJ/cm² (**Figure 3.11b**). This is seen by comparing the root mean square (RMS) deviation of the fit with two and three components (**Figure 3.13**). There, no improvement of the fit is obtained by using more than two components below 148 μJ/cm2, while higher excitation fluences require the third component to modelize well the data.

In addition, the simulated TA maps generated using Glotaran parameters in the **Figure 3.14** show not difference between two and three components at low excitation fluence but reproduce better the profile at earliest time at high excitation fluence. We thus use a pre-component EAS_0 that rises within the pump pulse duration and decays with $\tau_0 = 1/k_0$. Consequently, the EAS_1 now grows with τ_0, whereas the other following dynamics are unchanged compared to the previous model involving two components.

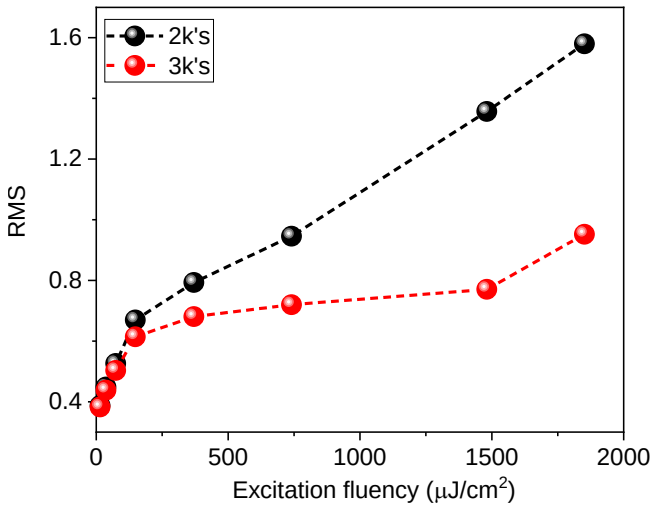

Figure 3.13. *Root mean square (RMS) deviation resulting from the fit of the TA map of FAPI n=2 NPLs, using two and three kinetic components.*

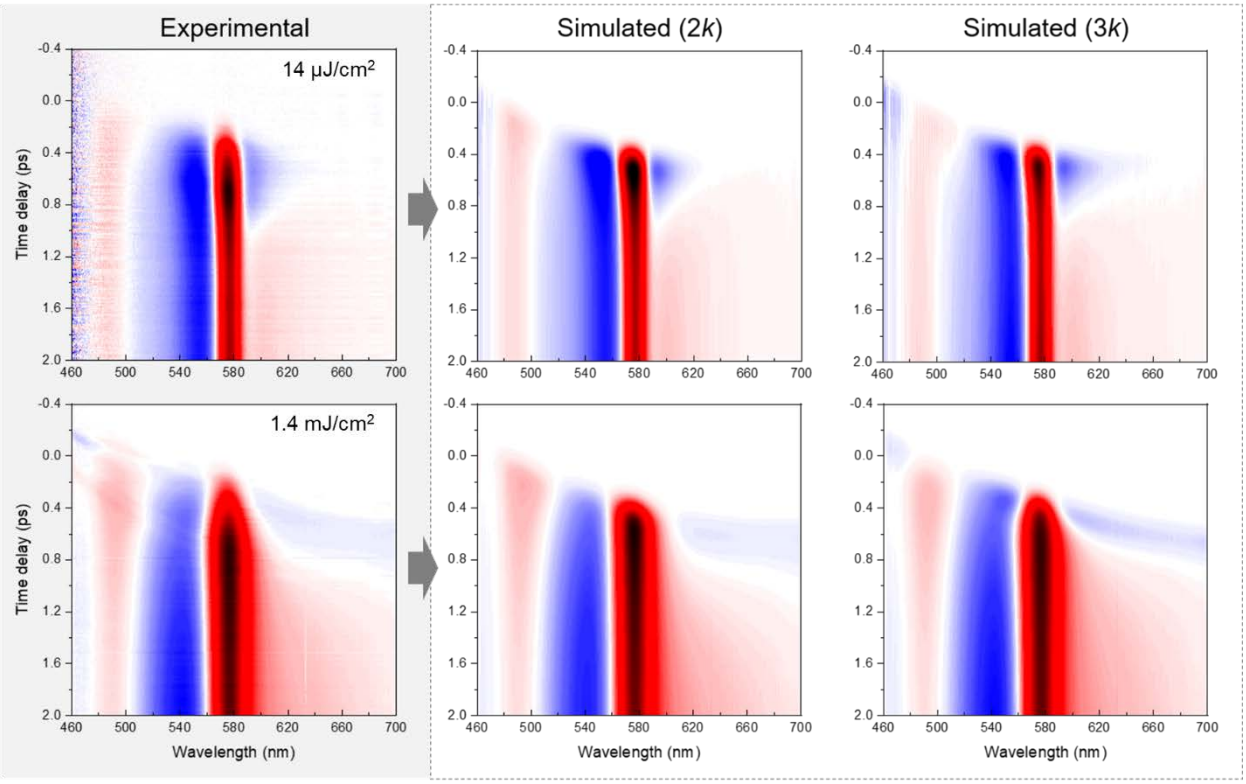

Figure 3.14*. TA maps of* FAPI *n=2 NPLs at low (top) and high (bottom) excitation fluence at 400 nm. The first column displays experimental TA data (uncorrected chirp, arbitrary time delay). Simulations with parameters obtained from Glotaran fit with two (2k) and three (3k) kinetic components are shown in the middle and the right column, respectively.*

Interpretation of the EASs.

In the following, we rationalize the EASs obtained from the global analysis and explain how the kinetic components can be related to the cooling dynamics. We simulated the transient spectrum of the EASs by the difference between the absorption spectra with the pump "ON" and the pump "OFF", each of them described by the sum of a Lorentzian function for the band-edge transition and a Gaussian function for the second excitonic transition with independent parameters (see **ANNEXE 3**).

- Initial EAS_1:

The shape of the EAS_1 spectrum in the case of a low excitation fluence (< 148 µJ/cm²) at 400 nm was reproduced in terms of a broadening of the absorption lineshape with the

pump “ON” (“shift” in both low- and high-energy directions), without relevant “bleach” contribution. Indeed, by simulating the EAS_1 spectra (**Figure 3.15a**), the relative change in linewidth (FWHM) of the band-edge absorption, $(\omega_{ON}-\omega_{OFF})/\omega_{ON} = \Delta\omega/\omega_0$, is about 16 % for the smallest excitation fluence while the relative change in area, $(f_{ON}-f_{OFF})/f_{ON} = \Delta f/f_0$, is smaller than -0.7 % (**Figure 3.15 c,d**).

This shows that for 400 nm excitation, initially both the electron and the hole populate states higher in energy than the excited state corresponding to the band-edge transition at 576 nm. EAS_1 corresponds thus to the system in its hot state. The pure broadening in the absorption of the band-edge transition can be explained by Stark effects: the energetic charge carriers created by the high photon energy pump pulse induce an electric field that shifts the energy of all transitions probed by the white light continuum pulse. Thus, the corresponding transient signal ΔA at the band-edge displays both positive and negative features, as previously observed in other semiconductor nanostructures [45].

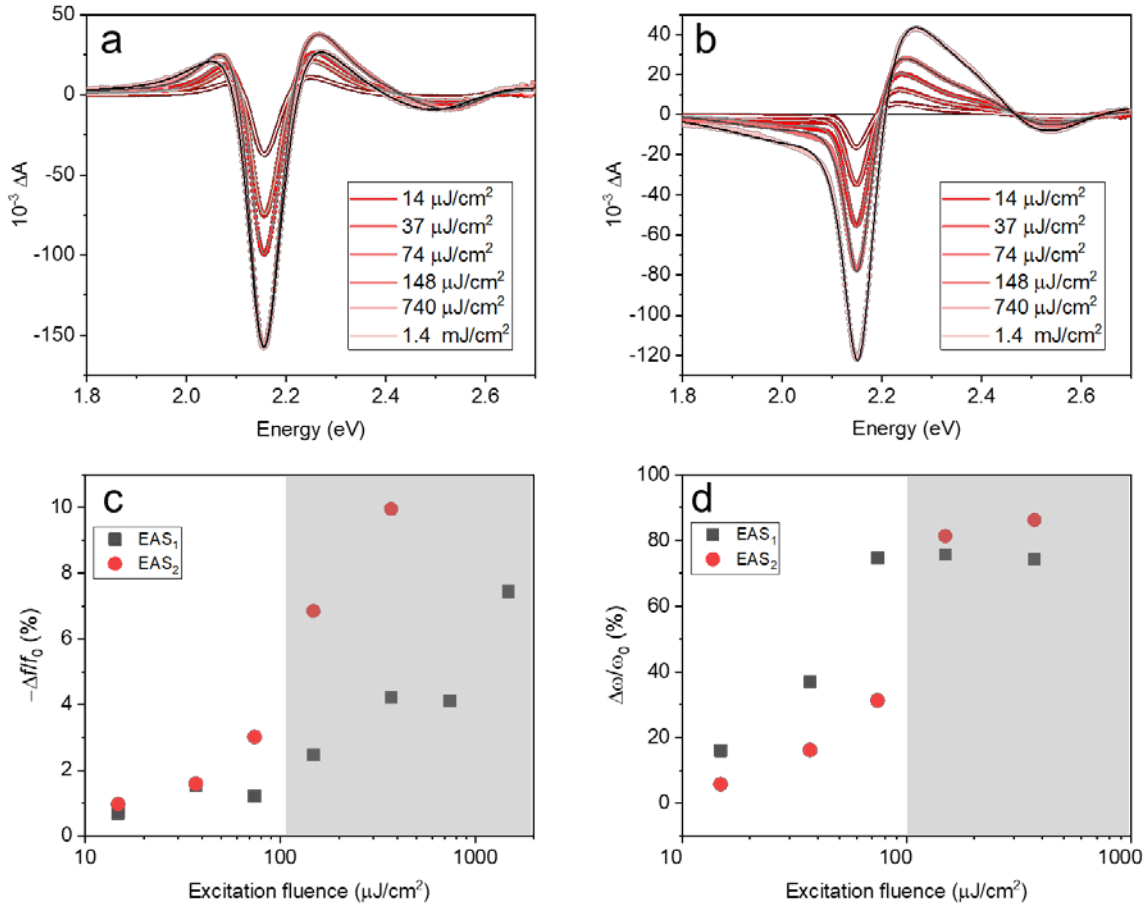

Figure 3.15. (a) *Initial EAS_1 and* **(b)** *final EAS_2* spectra (full dots) obtained from a global analysis of the TA data of FAPI n=2 NPLs excited at 400 nm, at different excitation fluences (two components). The resulting fit curves are displayed in solid lines. **(c, d)** Ratio of the isolated band-edge absorption area (f) and full-width at half maximum (ω) between the pump "OFF" and "ON", in the case of the fit of EAS_1 (black squares) and EAS_2 (red dots), respectively. The grey area highlights the range of excitation fluences where strong exciton-exciton interactions induce an extra broadening of the spectral lineshape.

For this well-defined excitonic transition, a second derivative lineshape is obtained rather than a first derivative one as the excitation well above the bandgap generates carrier-induced local electric fields with statistically random orientations (*cf* **Chapter 2, part 1**). Indeed, at this energy far away from the band-edge, confinement effects are negligible and, as the NPLs are randomly oriented, multiple resonant transitions are excited by the polarized excitation, corresponding to both transition dipoles parallel and perpendicular to the NPL 2D plane.

We note that at excitation fluence of 148 µJ/cm^2 and larger, the relative change in the absorption area ("bleach" component) becomes non-negligible as it starts to increase linearly with the excitation fluence. This can be explained by a change of oscillator strength due to exciton-exciton interactions rather by a state filling effect, as seen previously by Lauret *and co* [28].

- Final EAS_2:

Per opposition to EAS_1, the EAS_2 spectra corresponding to the final state display a decrease in the area of the band-edge absorption when the pump is "ON" (**Figure 3.15b**), characteristic of a state filling effect (*cf* **Chapter 2, part 1**). This spectrum is thus characteristic of cooled-down exciton, even if we still notice a large proportion of a derivate character (mostly high-energy PIA), resulting mostly from a high-energy shift the band egde transition. This can still be explained by the Stark effect on the probed optical transition due to the presence of the relaxed exciton. As the dipole associated with the first excitonic transition is expected to be in the 2D plane of the NPLs, the carrier-induced Stark effect induces some spatial separation of the electron and hole wavefunctions, leading to a decrease of the exciton binding energy. Consequently, the transition is shifted toward high-energies. This blue shift causes the first derivative-like lineshape seen in the EAS_2 corresponding to the transient spectrum of FAPI n=2 at long time.

- Effect of the high excitation fluence

As already discussed, the TA data corresponding to excitation fluences of about 148 µJ/cm^2 and above are better described by three kinetic and spectral components than two. However, while the decay time of EAS_1 (τ_1) is much larger than the temporal resolution of the setup, the evolution from EAS_0 to EAS_1 characterized by τ_0 is about or less than 130 fs at high excitation fluence. This can be seen in the graph showing the evolution of these two times in function of the excitation fluence (**Figure 3.16**). Thus, from our point of view

this first stage is not related to a relaxation process of the system but to a purely *optical Stark effect* only present during the pump pulse duration. In this case, it is the pump electric field that shifts the energy of the sample optical transitions [48].

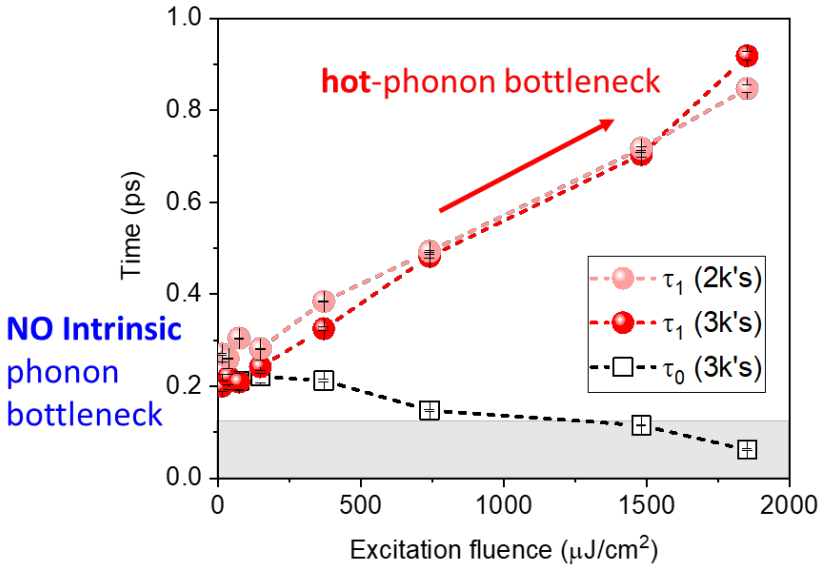

Figure 3.16. *Pump fluency dependence of the lifetimes obtained from the global data analysis of FAPI n=2 NPLs excited at 400 nm, using two (pink dots) and three (red dots and empty squares) kinetic components. The relevant times of the cooling process are the* τ_1.

- Effect of the excitation photon energy:

Going back to the experiments performed at different excitation photon energies (corresponding to 400, 515, 580 nm), we can now interpret the lineshape of each EAS_1 spectrum **(Figure 3.10a)**. For 400 nm excitation wavelength, the observed 2nd derivative lineshape corresponds to the system in a hot state, as discussed just before. For 515 nm excitation, the lineshape is similar to the spectra for the relaxed state except for a less pronounced low-energy tail. This shows that for this excitation wavelength, at least one of the charge carriers (*i.e.* the electron or the hole) is in its lower excited state (presence

of bleach contribution). Surprisingly, the evolution to EAS_2 occurs with the same characteristic time than for an excitation at 400 nm (about 270 fs).

Finally, for a band-edge excitation at 580 nm, the EAS_1 has a pure 1st derivative lineshape indicating a specific direction of the optical transition shift without any bleach component (*cf* **Chapter 2, part 1**). The dynamics associated to EAS_1 to EAS_2 are very fast (about 70 fs) allowing us to interpret the EAS_1 spectrum to a pure *optical Stark effect* involving an electric field along the 2D plane of the NPLs and thus resulting in a high energy shift. Indeed, this excitation energy corresponding to the band-edge transition involve a specific dipole orientation within the 2D plane, as expected for 2D sample [49–51].

Conclusion on the cooling analysis.

From the analysis of the EAS spectra, we can conclude that the cooling dynamics in colloidal NPLs can be extracted from global analysis with the relevant rate k_1 between EAS_1 and EAS_2, at low and high excitation fluence. For FAPI n=2 NPLs excited at 400 nm, we summarize the lifetimes extracted from global analysis using two and three kinetic components (k's) in **Figure 3.16**. Similarly, with the cooling time of thick $FAPbI_3$ nanoplates, the cooling lifetime of FAPI n=2 NPLs increases with the excitation fluence up to almost 1 ps, which can thus be assigned to the *hot* phonon bottleneck effect. Furthermore, because the global analysis method can be applied to investigate the cooling dynamics in both weakly-confined samples and strongly confined 2D NPLs, this allows us to compare the cooling rates of these samples and thus the real effect of the confinement on this process (see below).

Another approach to measure the cooling dynamics in strongly confined nanostructures would consist in following the band-edge state population from the growth of the corresponding bleach signal at selected wavelength [22]. However, as we seen here, the

band-edge signal never grows and even decreases at low excitation fluence (**Figure 3.12**). This is due to "instantaneous" apparition (*i.e.* with the pump pulse) of the carrier-induced Stark signals that cannot be neglected in these strongly-confined 2D perovskite NPLs. In consequence, a global analysis method, as the one used here, is the only relevant method to use to analyze the cooling dynamics.

3.3.2. Comparison of the cooling dynamics in different nanostructures.

Using the global approach described above for FAPI *n=2* NPLs, we determined the cooling rate of *n=1*, CsPI and MAPI *n*=2 NPLs in order to compared them and identify the role of the confinement and composition in this process.

3.3.2.1. Confinement effect

Bulk-like versus 2D perovskite.

The FAPI *n*=2 NPLs presents at least two times faster carrier cooling times at low excitation fluence compared the thick $FAPbI_3$ nanoplates. This evidences the absence of *intrinsic* phonon bottleneck in 2D NPLs compared the bulk-like hybrid perovskites. There, the excess energy was about twice larger (≈ 950 meV) for FAPI *n*=2 NPLs excited at 400 nm compared with the $FAPbI_3$ NPs (≈ 410 meV) excited at 520 nm. Additionally, the cooling times in the strong confined FAPI *n*=2 NPLs showed no dependence with the excitation wavelength (515 nm and UV versus 400 nm excitation).

Thickness-dependent cooling rates in 2D NPLs.

To further confirm the absence of such *intrinsic* phonon bottleneck effect in halide perovskite nanostructures, we measured the cooling dynamics in a sample with a smaller thickness and thus larger confinement effects: *n*=1 colloidal NPLs. The initial and final

EAS spectra are displayed in **Figure 3.17a,b** for a low and high excitation fluence. The time constant and RMS deviation are shown in **Figure 3.17c,d**.

At low excitation fluence, we found an exciton cooling time of 240 ± 10 fs for the *n=1* NPLs. Thus, the higher confinement in *n*=1 NPLs compared to *n*=2 NPLs leads to a faster cooling time, confirming the absence of an intrinsic phonon bottleneck effect. All TA measurements in the following were performed by compressing the pump pulses to 90 fs for a better accuracy of the extracted cooling times.

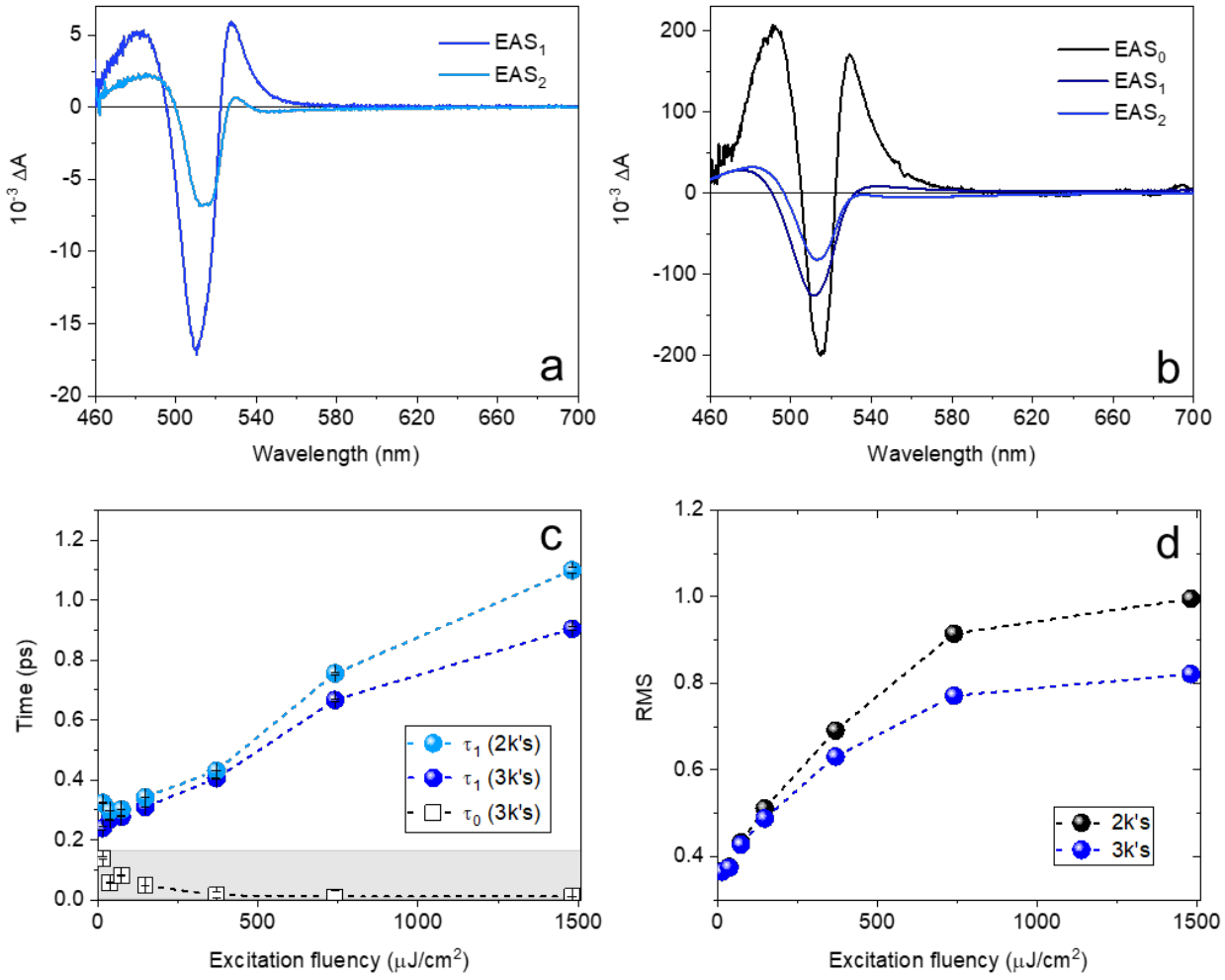

Figure 3.17. *EAS spectra for n=1 NPLs at* ***(a)*** *at low (4.5 μJ/cm²)* *and* ***(b)*** *high* ***(****450 μJ/cm²****)*** *excitation fluence at 400 nm.* ***(c)*** *Extracted time constants as a function of the*

pump fluence. ***(d)*** *Root mean square (RMS) deviation for the fit with two and three kinetic components.*

3.3.2.2. Cation effect: *hybrid versus fully-inorganic n=2 NPLs*

In hybrid perovskite materials, several efforts have been made to investigate the effect of the organic cations MA^+ or FA^+ in the cooling dynamics [13,22]. The hot phonon bottleneck was found to be more pronounced in fully inorganic Cs-based perovskites than in its hybrid counterpart [13]. In addition, the intrinsic cooling lifetime (*i.e.* measured at low excitation fluence) was found to be longer [22,23]. Both effects were explained mainly by the role of molecular vibrational modes and/or dynamic disorder due to the A^+ organic cation rotation. Here, we performed fs-TA experiments on *n*=2 NPLs with various A^+ cations, Cs^+, FA^+ and MA^+. The results from FAPI *n*=2 NPLs give a cooling time of 251 ± 9 fs at low excitation fluence, which is close to the previous value obtained with other FAPI *n*=2 NPL samples without pump compression (239, 266 and 269 fs, see above).

The transient spectra of CsPI *n*=2 NPLs at low and high excitation fluences are shown in **Figure 3.18**. We can see the absence of the low-energy tail in the band-edge bleach of this sample, evidencing the better surface passivation obtained with the longer alkylammonium ligand.

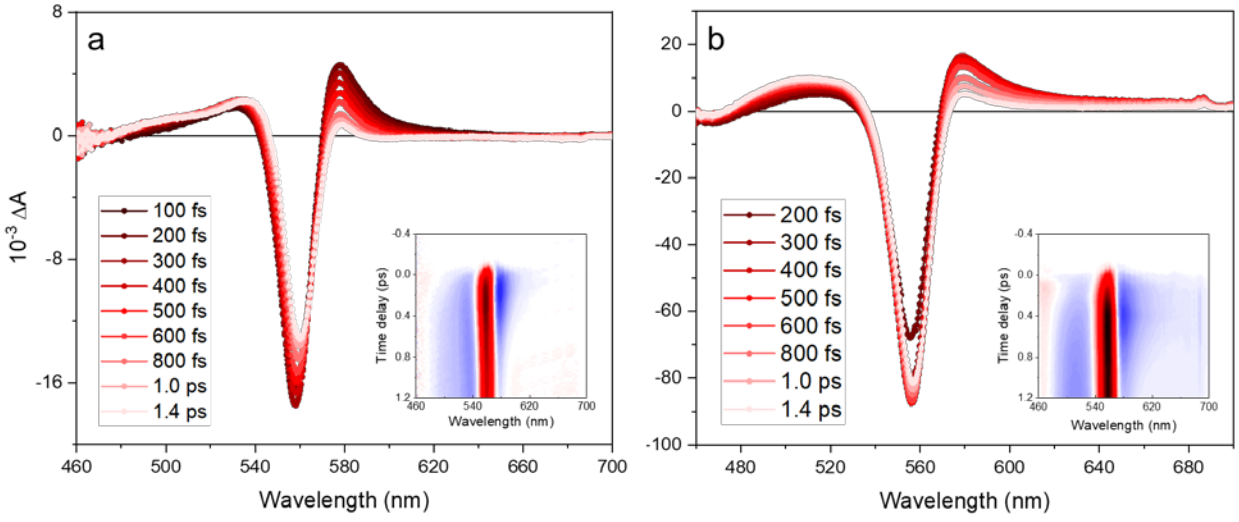

Figure 3.18. *Unchirped TA spectra of CsPI n=2 NPLs excited at 400 nm at* ***a)*** *low- (3 µJ/cm²) and* ***(b)*** *high- (79 µJ/cm²) excitation fluence.* ***Inset:*** *full TA map.*

By comparing the cooling rates of FAPI and CsPI *n*=2 NPLs (**Figure 3.19)**, no clear difference could be seen, neither in the *intrinsic* cooling time, nor in the slope at high excitation fluences which can be related to the hot phonon bottleneck effect. These similarities between fully-inorganic and hybrid perovskite NPLs add to our conviction that the cooling process in these 2D nanostructures is dominated by a different mechanism than the classical energy dissipation *via* carrier-LO phonon scattering. Furthermore, this mechanism is independent of the nature of the internal cation.

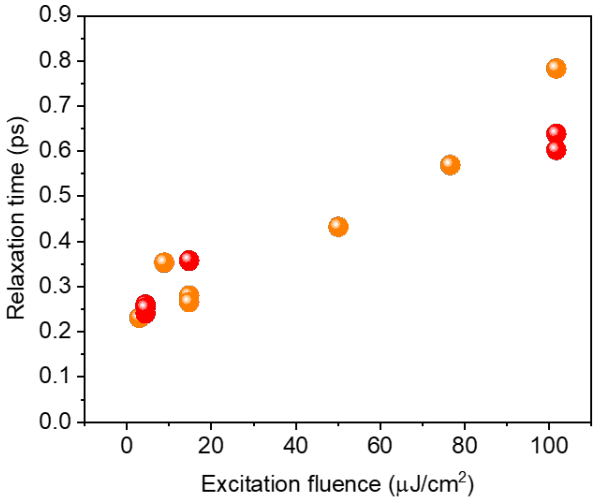

Figure 3.19. *Comparison of the cooling times of CsPI n=2 (orange dots) and FAPI n=2 NPLs (red dots) excited at 400 nm for various fluences. These values were obtained by global analysis.*

3.3.2.3. Ligand effect: *colloidal nanoplatelets versus 2D thin films*

Several mechanisms have already been proposed to explain the breaking of the expected intrinsic phonon-bottleneck in colloidal II-VI and III-V semiconductor nanostructures: relaxation mediated by Auger transfer between electron and hole with asymmetric density of states, efficient multi-phonon emission in spatially confined systems and

relaxation assisted by ligand vibrational modes (*cf* **Chapter I, part 2**). In small nanocrystals and 2D perovskite, the absence of an *intrinsic* phonon bottleneck was suggested to result from non-adiabatic relaxation pathways [28,30], in particular involving interactions with surface ligands [27].

Here, the 2D n=1 perovskite was selected as model samples to study the ligand effects on the *hot* exciton relaxation process. However, as the ammonium ligands are part of the perovskite crystalline structure, they cannot be exchanged easily. Moreover, the relaxation mechanism involving the classical resonant energy transfer between the hot charge carrier and the ligand vibration modes [52] should not be efficient in our NPL samples. This is because the main ligands attached on the perovskite surface are the alkylammonium ligands [53], which have a weak infra-red absorption bands at the relevant energies (see below).

Indeed to achieve an efficient exciton relaxation in n=2 NPLs excited at 400 nm the energy of the ligand vibrational mode should be around 7000 cm^{-1} (400 nm to the bandedge) or a at least ~ 3000 cm^{-1} to match the energy difference between the first two excitonic transitions. This latter energy difference is relatively close to the N-H stretching vibrations of the primary alkylamines (3200-3400 cm^{-1}) as n-butylamine (C4). However, for the specific case of the ligands used here, the *cis*-9-octadecenylamine (OLAm), including its corresponding ammonium salt does not present a strong IR absorption at energies higher than 3000 cm^{-1}. These findings suggest, in principle, that the relaxation through ligands can take place efficiently only if thought an non-adiabatic transfer, as proposed by Kambhampati *and co.* [54] and in agreement with the work of Wu *and co.* in small $CsPbBr_3$ nanocrystals [27].

Thus, instead of changing the nature of the ligand function (here NH_3^+), we decided to compare the exciton cooling rate in samples where the mobility of the ligands attached on

the surface is different. In particular, we studied the n=1 NPLs with short (butyl-) and long (oleyl-) ammonium ligands and compare with 2D perovskite thin film with identical number of MLs (n=1) synthesized by Gaëlle Allard, in collaboration with the NanoOptics and Spectroscopy group at LUMIN laboratory. The corresponding steady-state spectra are shown in **Figure 3.20a**.

The shift observed in the position of the band edge transition can be explained either by a difference of lateral size in the 2D plane or by a strain effect due to the different ligands. In colloidal NPLs, the ligands attached to the surface are in continuous equilibrium with the ligands present in the solution. The interactions between the long chains might result in a more stable binding to the perovskite surface. This templating effect is used in the synthesis of anisotropic nanostructures [55]. In contrast, the ligands in 2D layered perovskite thin film are expected to be "frozen" in between layers.

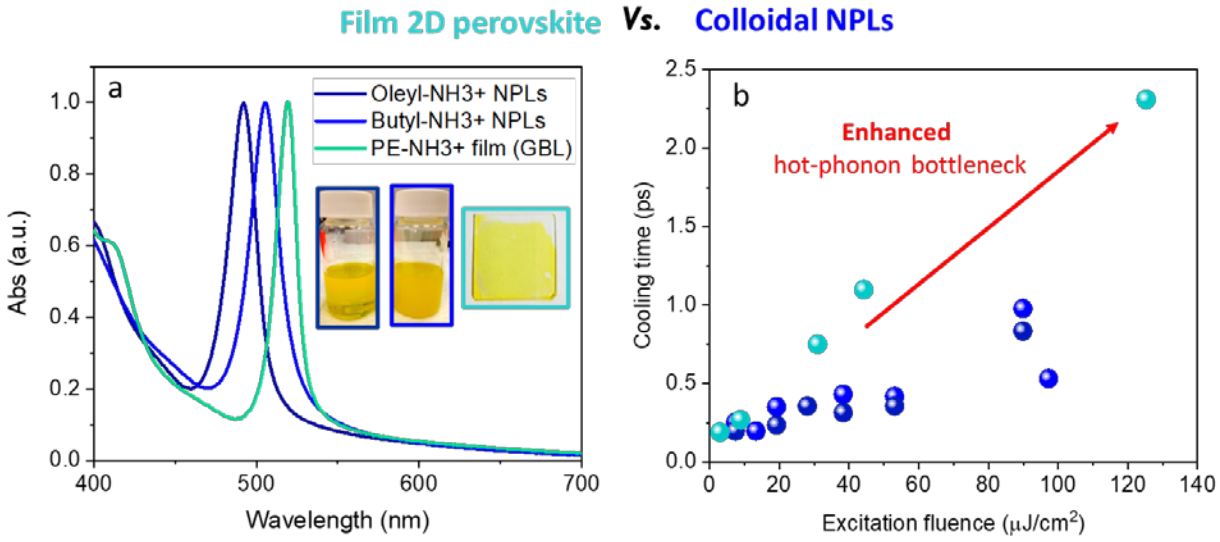

Figure 3.20. (a) *Normalized absorption of the n=1 perovskite sample: n=1 colloidal NPLs synthesized with oleyl- (dark blue) and butyl- (light blue) ammonium ligands and 2D layered thin film synthesized with phenyl-ethyl (PE) ammoniums (green).* ***(b)*** *Comparison of the corresponding hot exciton cooling times obtained from global analysis for an excitation at 400 nm using different fluences.*

The excitation fluence dependent cooling times of the three different samples are presented in **Figure 3.20b**. From the graph, we clearly see that the cooling time becomes significantly longer in the thin film sample at high excitation fluence compared to the ones measured in the colloidal NPLs. This enhanced hot phonon bottleneck cannot just result from the difference of the absorption cross sections of the samples since the relevant value is the number of created excitons created *per surface* (the exciton density), which here is directly proportional to the excitation fluence with the same factor.[2]

3.3.3. Conclusion

Per opposition with the internal organic cations A^+, ligands in the colloidal NPL systems are in direct contact with the surrounding medium (solvent) and can thus easily release the excess energy, limiting thus the "hot phonon bottleneck" effect at high excitation fluence.

[2] The absorption cross-section σ_{abs} in cm^2 is proportional to volume of the nanocrystal (V) ; $\sigma_{abs} = \mu_{abs} V$, the linear absorption coefficient μ_{abs} in cm^{-1} is characteristic of each material and independent of the volume. In consequence, the exciton density (ñ) is the only parameter directly proportional to the excitation fluence (j): $\tilde{n} = < N > /S = j\sigma_{abs}/S = j\,\mu_{abs} V/S = \boldsymbol{j}\,\mu_{abs} l$, where S is the area that describes the lateral dimensions of the 2D of the nanoparticle and l is the thickness.

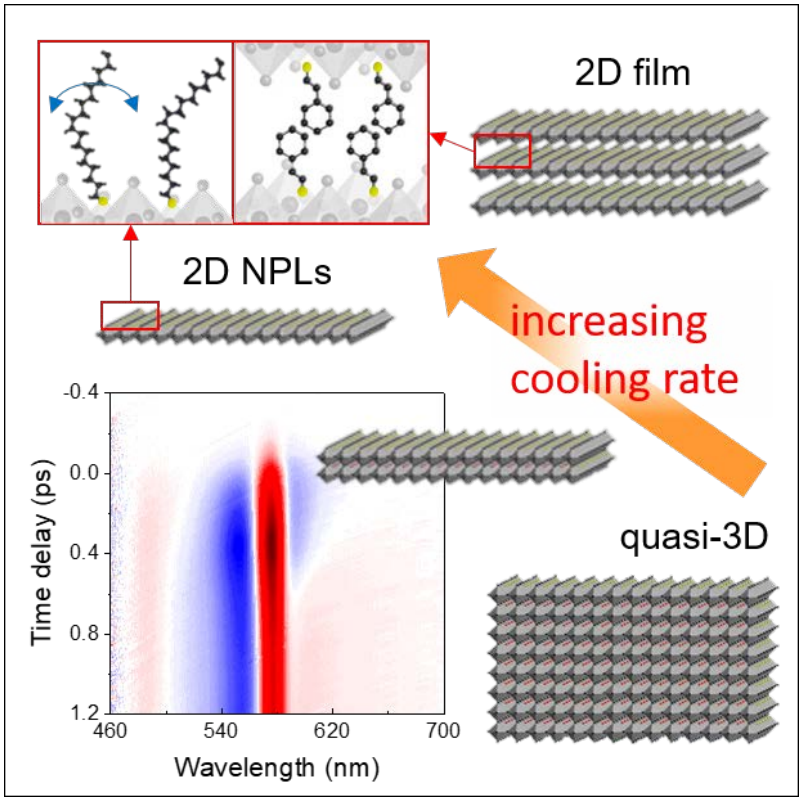

Figure 3.21. *Schematic of the evolution of the cooling rate with the confinement effect (NPL thickness) and effect of the dynamics of the surface ligands in the cooling mechanism. The colloidal systems present a decrease on the colling rates with the sample thickness. On the other side, the 2D n=1 layered thin films with same thickness as n=1 NPLs presents a slower relaxation (enhanced hot phonon bottleneck).*

The role played by the surface ligands in the cooling mechanism explains why faster cooling times are measured within the more strongly-confined system: the decrease of thickness enhances the coupling between the ligand vibrational modes and the exciton which wavefunction is more delocalized outside the lattice framework. These results are summarized in **Figure 3.21**. Here, we should note that the Auger transfer process cannot play any role to break the phonon bottleneck in 2D perovskite with strong quantum and dielectric confinement since the discrete states are due to the exciton species and are well-separated from the continuum energy levels.

ANNEXE 3.

Calculation of the exciton density

The excitation fluence per-pulse (J) in J/cm^2 is:

$$J = \frac{E_{pulse}}{\Sigma_{laser}}$$

Where the E_{pulse} is the pump energy per pulse can be calculated with the expression $E_{pulse} = P_0/RR$ with RR as the pump repetition rate (1.5 KHz for TA) and P_0, the average power of the pump beam. On the other side, $\Sigma_{laser} = \pi(\omega_0)^2$ is the section of the pump laser beam with a beam waist (ω_0) at the focus position for the different wavelengths. For example, the ω_0=120 µm corresponds to the $\Sigma_{laser} = 4.52 \times 10^{-4}$ cm^2 at 400nm pump beam. To calculate the average photogenerated excitons per nanoparticle (<N>) the following expression is used:

$$\langle N \rangle = j\sigma_{abs}$$

There, the photon fluence per pulse (j) is expressed in photons/cm^2 calculated dividing the J (J/cm^2) by the excitation energy per one photon (J). The absorption cross-section σ_{abs} (cm^2) at specific wavelength was estimated as follows.

Absorption cross-section

Away from the confinement effects, the absorption cross section should scale linearly with the volume of the nanoparticle [56]. Previously, Fang *et al.* have determined the absorption cross section of 13 ± 3 nm cubic $FAPbI_3$ NCs to be 5.2×10^{-13} cm^2 at 400 nm [57]. We used this value to estimate the cross section of our $FAPbI_3$ NCs at 630 nm and estimate the cross section of n=2 NPLs at 400 nm.

$FAPbI_3$ cubic NCs and thick NPs.

The volume estimated for the cubic NCs with l = 12 ± 2 nm is $V_{NC} \approx 1970$ nm^3 and for the thick NPs (hexagonal shape) with lateral size l = 70 nm ± 20 nm and thickness t = 11 ± 3 nm, the section is $S_{NP} \approx 3773$ nm^2 and the volume is $V_{NP} \approx 39925$ nm^3.

Then, the deduced absorption cross section at 400 nm was 4.7×10^{-13} cm² for the NCs and 9.4×10^{-12} cm² for the thick NPs. From the absorption spectrum (of a diluted sample) which is proportional to the cross section, we get an absorption cross section of 4.7×10^{-14} cm² for the cubic NCs at 650 nm and 1.3×10^{-12} cm² for the thick NPs at 630 nm. For the NCs, the beam waist is about 195 µm for the pump at 650 nm, the number of electron-hole pairs created per pulse is $N_{NC} \approx 2.7$ (in term of density 1.2×10^{18} cm^{-3}) for an excitation of 6 µJ/cm² at 650 nm. For the thick NPs excited at 630 nm with a beam waist of about 188 µm, $N_{NP} \approx 66$ (density 1.6×10^{18} cm^{-3} or 1.7×10^{12} cm^{-2}) and $N_{NP} \approx 660$ (density 1.2×10^{19} cm^{-3} or 1.2×10^{18} cm^{-2}) at 6 and 60 µJ/cm², respectively.

Colloidal FAPI n=2 NPLs.

From the lateral sizes and thickness, the volume of n=2 NPLs was estimated to V_{NPL} = 81120 nm³. Thus, the absorption cross section at 400 nm was estimated to about 1.9×10^{-11} cm². For the lowest excitation density 4.5 µJ/cm², it corresponds to $N \approx 692$, or $\tilde{n} = 1 \times 10^{12}$ cm^{-2}. For the higher excitation density 445 µJ/cm², $N \approx 69200$ and $\tilde{n} = 1 \times 10^{14}$ cm^{-2}.

Dense surface energy traps within the gap

Previously, Zhu *and co.* have reported the existence of excitonic trap states in 2D layered perovskites (1 to 3 monolayer thick, based on methylammonium lead iodide) [58]. In our case, the trap states seem also to be related to the surface interface because the magnitude of the bleach tail on washed samples is less pronounced, as shown in **Figure A3.1**. However, we found the samples were unstable after washing as they evolve to thicker nanoplatelets (discrete TA signals at around 640 nm corresponding to *n=3* NPLs. Therefore, the unwashed sample were preferred for the experimental purposes, and no clear difference was noticed in the associated dynamics.

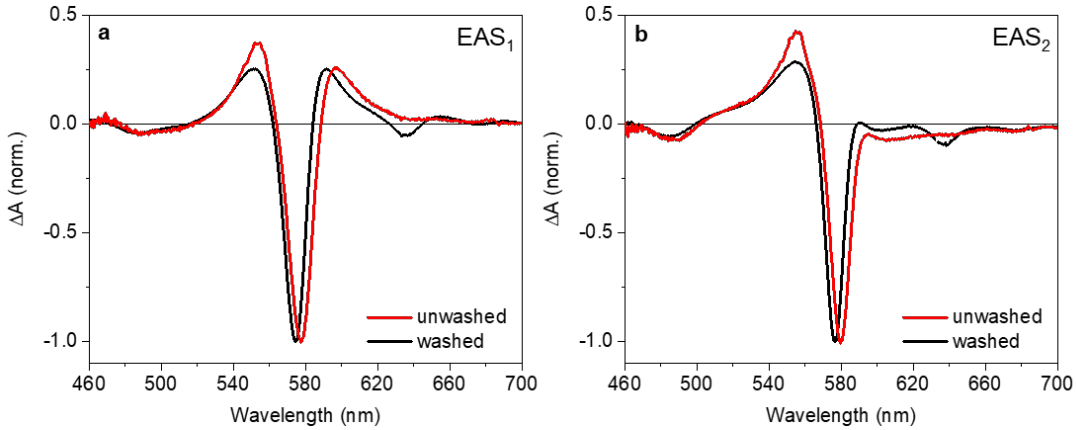

Figure A3.1. *Comparison of the spectral components EAS_1* ***(a)*** *and EAS_2* ***(b)*** *obtained from a global analysis for n=2 NPLs in the case of washed sample (black) and unwashed one (red). For the washed sample, we get $\tau_1 = 1/k_1 = 266$ fs, and for the unwashed sample $\tau_1 = 239$ fs, while the red tail is much less pronounced in EAS_2. The error associated to the time constant of a single fit is pretty small (1 to 2 fs), while several fits give a determination of τ_1 within ±15 fs. The extra negative peaks for the washed sample correspond to the bleach of the first excitonic transition of some proportion of n=3 and n=4 NPLs.*

We performed time-resolved PL experiments to identify the longer dynamics expected to the trap-assisted carrier recombination (red curve in the **Figure A3.2a**) from the exciton recombination dynamics at the band-edge (black curve in the **Figure A3.2a**) as reported by Mohite *et co.* using PL microscopy. They compared the exfoliated crystal 2D layered perovskite dynamics with different *n* thickness with the 2D perovskite thin films [59]. They found that in thin films, the free carriers after exciton dissociation are trapped in deep electronic states located at layer edges. Then, a higher PL efficiency and the longer lifetime of those trap states (red tail) as compared with those of the exciton higher-energy states are related with the non-radiative decay mechanisms such as electron-phonon coupling or electronic impurities. The fact that after photogeneration of excitons can either decay through classical processes ($n \leq 2$) or dissociated to free carriers potentially that can be trapped ($n > 2$) suggests the reason why MAPI n=3 presents at higher PL QY as we will see in the next chapter.

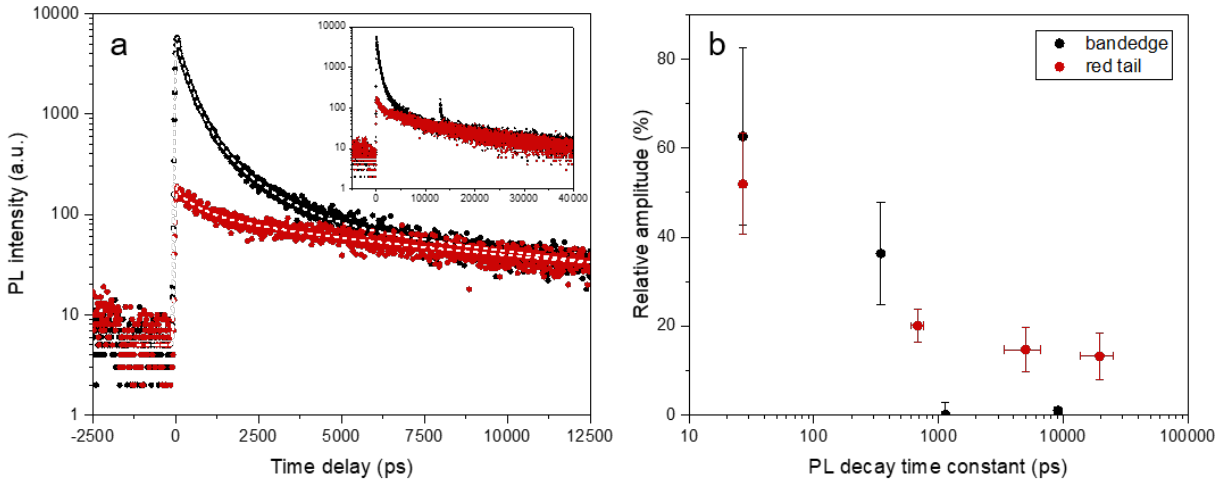

Figure A3.2. (a) *Time-resolved photoluminescence traces of FAPI n=2 NPLs excited at 400 nm for a detection at the band-edge (black) and at the red tail (red). The longer decays are displayed in inset. For the fit, we used a multiexponential decay function convoluted with an instrument response function (IRF, Gaussian with a FWHM of about 75 ps).* ***(b)*** *Relative amplitude of the decay time constants plotted over their value for the two detection wavelengths.*

Simulation of the EAS spectra

The transient absorption spectra $\Delta A(E)$, or $\Delta A(\lambda)$ as defined in **Chapter 2, part 1, Equation 2.6**, can be approximated by the difference of the absorption spectra with the pump "ON" and with the pump "OFF". As the white light continuum covers a range starting from about 450 nm, we only probe the first and the second excitonic transitions of the NPL system. The absorption of each transition can be described by a pseudo-Voigt function:

$$PSV_i(E) = f_i\left[(\mu_i)\frac{2}{\pi}\frac{\omega_i}{4(E-E_i)^2+\omega_i{}^2} + (1-\mu_i)\frac{\sqrt{4ln(2)}}{\sqrt{\pi}\omega_i}exp\left(-\frac{4ln(2)}{\omega_i{}^2}(E-E_i)^2\right)\right] \qquad [A3.1]$$

with parameters f_i, E_i, ω_i and μ_i, corresponding respectively to the area (proportional to the transition oscillator strength), the central energy, the full-width at half maximum and the profile shape factor. This latter parameter μ is linked to the lineshape of the transition, which value is included between 0 (pure Gaussian) and 1 (pure Lorentzian).

To simulate the low-energy tail in the bandedge bleach of the transient spectra, we used a biphasic Hill function in a purely phenomenological manner:

$$BiHill(E) = \frac{P_m}{\left[1+\left(\frac{K_a}{E}\right)^{Ha}\right]\left[1+\left(\frac{E}{K_i}\right)^{H_i}\right]} \quad [A3.2]$$

where P_m is the maximum of the tail amplitude, K_a and K_i the energies corresponding to the position of the half maximum of the curve in the activation and inhibitory slope, respectively. H_a and H_i are the activation and inhibitory Hill coefficients determining the "smoothness" of the slope. This tail modifies the integrated area of the transition absorption and thus has to be taken into account for the real, effective *f* area.

The function used to fit the EAS spectrum using the Origin program is:

$$\Delta A(E) \approx PSV_{1,ON}(E, f_{1,ON}, E_{1,ON}, \omega_{1,ON}) + PSV_{2,ON}(E, f_{2,ON}, E_{2,ON}, \omega_{2,ON}) - PSV_{1,OFF}(E, f_{1,OFF}, E_{1,OFF}, \omega_{1,OFF}) - PSV_{2,OFF}(E, f_{2,OFF}, E_{2,OFF}, \omega_{2,OFF}) - BiHill(E, P_m, K_a, K_i, H_a, H_i) \quad [A3.3]$$

The parameters of $PSV_{1,OFF}$ and $PSV_{2,OFF}$ are initialized using the steady-state absorption spectrum. The area $f_{1,OFF}$ and $f_{2,OFF}$ are fixed as it is the differential absorption we are simulating. An example of the resulting absorption spectra of the bandedge transition with pump "OFF" and "ON" is shown in **Figure A3.3** in the case of the fit of EAS_2 of FAPI *n*=2 NPLs excited at 400 nm at different fluences.

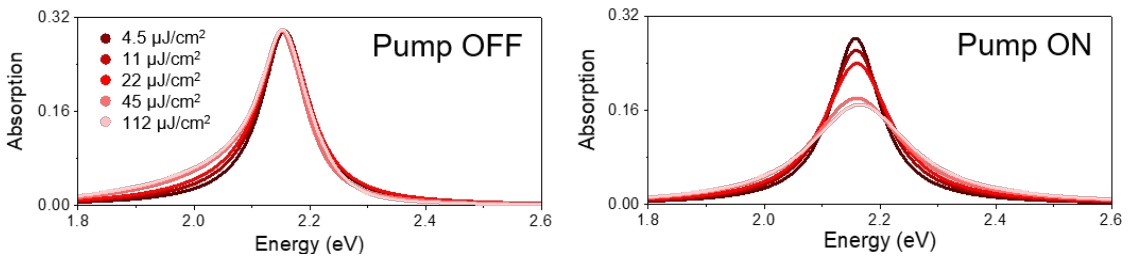

Figure A3.3. *Simulated bandedge absorption in the case of the long time EAS_2 spectra of FAPI n=2 NPLs excited at 400 nm. We arbitrary choose to display the low-energy tail as a positive feature in the pump "OFF" spectrum, which is equivalent of having a reduction of absorption in the pump "ON" spectrum.*

REFERENCES

[1] H.J. Snaith, Perovskites: The emergence of a new era for low-cost, high-efficiency solar cells, J. Phys. Chem. Lett. 4 (2013) 3623–3630. https://doi.org/10.1021/jz4020162.

[2] H. Tsai, W. Nie, J.C. Blancon, C.C. Stoumpos, R. Asadpour, B. Harutyunyan, A.J. Neukirch, R. Verduzco, J.J. Crochet, S. Tretiak, L. Pedesseau, J. Even, M.A. Alam, G. Gupta, J. Lou, P.M. Ajayan, M.J. Bedzyk, M.G. Kanatzidis, A.D. Mohite, High-efficiency two-dimensional ruddlesden-popper perovskite solar cells, Nature. 536 (2016) 312–317. https://doi.org/10.1038/nature18306.

[3] Q. Zhao, A. Hazarika, X. Chen, S.P. Harvey, B.W. Larson, G.R. Teeter, J. Liu, T. Song, C. Xiao, L. Shaw, M. Zhang, G. Li, M.C. Beard, J.M. Luther, High efficiency perovskite quantum dot solar cells with charge separating heterostructure, Nat. Commun. 10 (2019) 2842. https://doi.org/10.1038/s41467-019-10856-z.

[4] L. Dou, Y.M. Yang, J. You, Z. Hong, W.H. Chang, G. Li, Y. Yang, Solution-processed hybrid perovskite photodetectors with high detectivity, Nat. Commun. 5 (2014) 1–6. https://doi.org/10.1038/ncomms6404.

[5] M.I. Saidaminov, V. Adinolfi, R. Comin, A.L. Abdelhady, W. Peng, I. Dursun, M. Yuan, S. Hoogland, E.H. Sargent, O.M. Bakr, Planar-integrated single-crystalline perovskite photodetectors, Nat. Commun. 6 (2015) 1–7. https://doi.org/10.1038/ncomms9724.

[6] Z.K. Tan, R.S. Moghaddam, M.L. Lai, P. Docampo, R. Higler, F. Deschler, M. Price, A. Sadhanala, L.M. Pazos, D. Credgington, F. Hanusch, T. Bein, H.J. Snaith, R.H. Friend, Bright light-emitting diodes based on organometal halide perovskite, Nat. Nanotechnol. 9 (2014) 687–692. https://doi.org/10.1038/nnano.2014.149.

[7] N. Wang, L. Cheng, R. Ge, S. Zhang, Y. Miao, W. Zou, C. Yi, Y. Sun, Y. Cao, R. Yang, Y. Wei, Q. Guo, Y. Ke, M. Yu, Y. Jin, Y. Liu, Q. Ding, D. Di, L. Yang, G. Xing, H. Tian, C. Jin, F. Gao, R.H. Friend, J. Wang, W. Huang, Perovskite light-emitting diodes based on solution-processed self-organized multiple quantum wells, Nat. Photonics. 10 (2016) 699–704. https://doi.org/10.1038/nphoton.2016.185.

[8] B.R. Sutherland, E.H. Sargent, Perovskite photonic sources, Nat. Photonics. 10 (2016) 295–302. https://doi.org/10.1038/nphoton.2016.62.

[9] H. Zhu, Y. Fu, F. Meng, X. Wu, Z. Gong, Q. Ding, M. V. Gustafsson, M.T. Trinh, S. Jin, X.-Y. Zhu, Lead halide perovskite nanowire lasers with low lasing thresholds and high quality factors, Nat. Mater. 14 (2015) 636–642. https://doi.org/10.1038/nmat4271.

[10] M.B. Price, J. Butkus, T.C. Jellicoe, A. Sadhanala, A. Briane, J.E. Halpert, K. Broch, J.M. Hodgkiss, R.H. Friend, F. Deschler, Hot-carrier cooling and photoinduced refractive index changes in organic-inorganic lead halide perovskites, Nat. Commun. 6 (2015) 8420. https://doi.org/10.1038/ncomms9420.

[11] Y. Yang, D.P. Ostrowski, R.M. France, K. Zhu, J. Van De Lagemaat, J.M. Luther, M.C. Beard, Observation of a hot-phonon bottleneck in lead-iodide perovskites, Nat. Photonics. 10 (2016) 53–59. https://doi.org/10.1038/nphoton.2015.213.

[12] J. Fu, Q. Xu, G. Han, B. Wu, C.H.A. Huan, M.L. Leek, T.C. Sum, Hot carrier cooling mechanisms in halide perovskites, Nat. Commun. 8 (2017) 1300. https://doi.org/10.1038/s41467-017-01360-3.

[13] T.R. Hopper, A. Gorodetsky, J.M. Frost, C. Müller, R. Lovrincic, A.A. Bakulin, Ultrafast Intraband Spectroscopy of Hot-Carrier Cooling in Lead-Halide Perovskites, ACS Energy Lett. 3 (2018) 2199–2205. https://doi.org/10.1021/acsenergylett.8b01227.

[14] H. Zhu, K. Miyata, Y. Fu, J. Wang, P.P. Joshi, D. Niesner, K.W. Williams, S. Jin, X.Y. Zhu, Screening in crystalline liquids protects energetic carriers in hybrid perovskites, Science (80-.). 353 (2016) 1409–1413. https://doi.org/10.1126/science.aaf9570.

[15] M.T. Trinh, X. Wu, D. Niesner, X.Y. Zhu, Many-body interactions in photo-excited lead iodide perovskite, J. Mater. Chem. A. 3 (2015) 9285–9290. https://doi.org/10.1039/c5ta01093d.

[16] M. Li, J. Fu, Q. Xu, T.C. Sum, Slow Hot-Carrier Cooling in Halide Perovskites: Prospects for Hot-Carrier Solar Cells, Adv. Mater. (2019) 1802486. https://doi.org/10.1002/adma.201802486.

[17] J. Yang, X. Wen, H. Xia, R. Sheng, Q. Ma, J. Kim, P. Tapping, T. Harada, T.W. Kee, F. Huang, Y.B. Cheng, M. Green, A. Ho-Baillie, S. Huang, S. Shrestha, R. Patterson, G. Conibeer, Acoustic-optical phonon up-conversion and hot-phonon bottleneck in lead-halide perovskites, Nat. Commun. 8 (2017) 14120.

https://doi.org/10.1038/ncomms14120.

[18] J. Yang, X. Wen, H. Xia, R. Sheng, Q. Ma, J. Kim, P. Tapping, T. Harada, T.W. Kee, F. Huang, Y.B. Cheng, M. Green, A. Ho-Baillie, S. Huang, S. Shrestha, R. Patterson, G. Conibeer, Acoustic-optical phonon up-conversion and hot-phonon bottleneck in lead-halide perovskites, Nat. Commun. 8 (2017) 14120. https://doi.org/10.1038/ncomms14120.

[19] H.H. Fang, S. Adjokatse, S. Shao, J. Even, M.A. Loi, Long-lived hot-carrier light emission and large blue shift in formamidinium tin triiodide perovskites, Nat. Commun. 9 (2018) 1–8. https://doi.org/10.1038/s41467-017-02684-w.

[20] M. Li, S. Bhaumik, T.W. Goh, M.S. Kumar, N. Yantara, M. Grätzel, S. Mhaisalkar, N. Mathews, T.C. Sum, Slow cooling and highly efficient extraction of hot carriers in colloidal perovskite nanocrystals, Nat. Commun. 8 (2017) 14350. https://doi.org/10.1038/ncomms14350.

[21] P. Papagiorgis, L. Protesescu, M. V. Kovalenko, A. Othonos, G. Itskos, Long-Lived Hot Carriers in Formamidinium Lead Iodide Nanocrystals, J. Phys. Chem. C. 121 (2017) 12434–12440. https://doi.org/10.1021/acs.jpcc.7b02308.

[22] J. Chen, M.E. Messing, K. Zheng, T. Pullerits, Cation-Dependent Hot Carrier Cooling in Halide Perovskite Nanocrystals, J. Am. Chem. Soc. 141 (2019) 3532–3540. https://doi.org/10.1021/jacs.8b11867.

[23] B.T. Diroll, R.D. Schaller, Intraband Cooling in All-Inorganic and Hybrid Organic–Inorganic Perovskite Nanocrystals, Adv. Funct. Mater. 29 (2019) 1901725. https://doi.org/10.1002/adfm.201901725.

[24] M. Cong, B. Yang, J. Chen, F. Hong, S. Yang, W. Deng, K. Han, Carrier Multiplication and Hot-Carrier Cooling Dynamics in Quantum-Confined CsPbI3 Perovskite Nanocrystals, J. Phys. Chem. Lett. 11 (2020) 1921–1926. https://doi.org/10.1021/acs.jpclett.0c00188.

[25] A.J. Nozik, Spectroscopy and hot electron relaxation dynamics in semiconductor quantum wells and quantum dots, Annu. Rev. Phys. Chem. 52 (2001) 193–231. https://doi.org/10.1146/annurev.physchem.52.1.193.

[26] S. Xu, A.A. Mikhailovsky, J.A. Hollingsworth, V.I. Klimov, Hole intraband relaxation in strongly confined quantum dots: Revisiting the “phonon bottleneck”

problem, Phys. Rev. B - Condens. Matter Mater. Phys. 65 (2002) 1–5. https://doi.org/10.1103/PhysRevB.65.045319.

[27] Y. Li, R. Lai, X. Luo, X. Liu, T. Ding, X. Lu, K. Wu, On the absence of a phonon bottleneck in strongly confined CsPbBr3 perovskite nanocrystals, Chem. Sci. 10 (2019) 5983–5989. https://doi.org/10.1039/c9sc01339c.

[28] K. Abdel-Baki, F. Boitier, H. Diab, G. Lanty, K. Jemli, F. Lédée, D. Garrot, E. Deleporte, J.S. Lauret, Exciton dynamics and non-linearities in two-dimensional hybrid organic perovskites, J. Appl. Phys. 119 (2016) 064301. https://doi.org/10.1063/1.4941345.

[29] X. Wu, M.T. Trinh, X.-Y. Zhu, Excitonic Many-Body Interactions in Two-Dimensional Lead Iodide Perovskite Quantum Wells, J. Phys. Chem. C. 119 (2015) 14714–14721. https://doi.org/10.1021/acs.jpcc.5b00148.

[30] V.A. Hintermayr, L. Polavarapu, A.S. Urban, J. Feldmann, Accelerated Carrier Relaxation through Reduced Coulomb Screening in Two-Dimensional Halide Perovskite Nanoplatelets, ACS Nano. 12 (2018) 10151–10158. https://doi.org/10.1021/acsnano.8b05029.

[31] X. Jia, J. Jiang, Y. Zhang, J. Qiu, S. Wang, Z. Chen, N. Yuan, J. Ding, Observation of enhanced hot phonon bottleneck effect in 2D perovskites, Appl. Phys. Lett. 112 (2018) 143903. https://doi.org/10.1063/1.5021679.

[32] T.C. Sum, N. Mathews, G. Xing, S.S. Lim, W.K. Chong, D. Giovanni, H.A. Dewi, Spectral Features and Charge Dynamics of Lead Halide Perovskites: Origins and Interpretations, Acc. Chem. Res. 49 (2016) 294–302. https://doi.org/10.1021/acs.accounts.5b00433.

[33] J. Shah, Ultrafast Spectroscopy of Semiconductors and Semiconductor Nanostructures, Springer Berlin Heidelberg, Berlin, Heidelberg, 1999. https://doi.org/10.1007/978-3-662-03770-6.

[34] A. Mondal, J. Aneesh, V. Kumar Ravi, R. Sharma, W.J. Mir, M.C. Beard, A. Nag, K. V. Adarsh, Ultrafast exciton many-body interactions and hot-phonon bottleneck in colloidal cesium lead halide perovskite nanocrystals, Phys. Rev. B. 98 (2018) 115418. https://doi.org/10.1103/PhysRevB.98.115418.

[35] M.N. Ashner, K.E. Shulenberger, F. Krieg, E.R. Powers, M. V. Kovalenko, M.G.

Bawendi, W.A. Tisdale, Size-dependent biexciton spectrum in cspbbr3 perovskite nanocrystals, ACS Energy Lett. 4 (2019) 2639–2645. https://doi.org/10.1021/acsenergylett.9b02041.

[36] J.J. Snellenburg, S.P. Laptenok, R. Seger, K.M. Mullen, I.H.M. Stokkun, Glotaran : A Java -Based Graphical User Interface for the R Package TIMP, J. Stat. Softw. 49 (2012) 1–22.

[37] M. Achermann, A.P. Bartko, J.A. Hollingsworth, V.I. Klimov, The effect of Auger heating on intraband carrier relaxation in semiconductor quantum rods, Nat. Phys. 2 (2006) 557–561. https://doi.org/10.1038/nphys363.

[38] D.M. Monahan, L. Guo, J. Lin, L. Dou, P. Yang, G.R. Fleming, Room-Temperature Coherent Optical Phonon in 2D Electronic Spectra of CH 3 NH 3 PbI 3 Perovskite as a Possible Cooling Bottleneck, J. Phys. Chem. Lett. 8 (2017) 3211–3215. https://doi.org/10.1021/acs.jpclett.7b01357.

[39] L.M. Herz, Charge-Carrier Dynamics in Organic-Inorganic Metal Halide Perovskites, Annu. Rev. Phys. Chem. 67 (2016) 65–89. https://doi.org/10.1146/annurev-physchem-040215-112222.

[40] L.T. Kunneman, M.D. Tessier, H. Heuclin, B. Dubertret, Y. V. Aulin, F.C. Grozema, J.M. Schins, L.D.A. Siebbeles, Bimolecular auger recombination of electron-hole pairs in two-dimensional CdSe and CdSe/CdZnS core/shell nanoplatelets, J. Phys. Chem. Lett. 4 (2013) 3574–3578. https://doi.org/10.1021/jz401970p.

[41] N. Mondal, A. De, S. Das, S. Paul, A. Samanta, Ultrafast carrier dynamics of metal halide perovskite nanocrystals and perovskite-composites, Nanoscale. 11 (2019) 9796–9818. https://doi.org/10.1039/c9nr01745c.

[42] L.M. Herz, Charge-Carrier Dynamics in Organic-Inorganic Metal Halide Perovskites, Annu. Rev. Phys. Chem. 67 (2016) 65–89. https://doi.org/10.1146/annurev-physchem-040215-112222.

[43] M. Pelton, S. Ithurria, R.D. Schaller, D.S. Dolzhnikov, D. V Talapin, Carrier Cooling in Colloidal Quantum Wells, Nano Lett. 12 (2012) 6158–6163. https://doi.org/10.1021/nl302986y.

[44] C. Katan, N. Mercier, J. Even, Quantum and Dielectric Confinement Effects in Lower-Dimensional Hybrid Perovskite Semiconductors, Chem. Rev. 119 (2019)

3140–3192. https://doi.org/10.1021/acs.chemrev.8b00417.

[45] P. Kambhampati, Unraveling the structure and dynamics of excitons in semiconductor quantum dots, Acc. Chem. Res. 44 (2011) 1–13. https://doi.org/10.1021/ar1000428.

[46] V.I. Klimov, D.W. McBranch, Femtosecond 1 P -to- 1 S Electron Relaxation in Strongly Confined Semiconductor Nanocrystals, Phys. Rev. Lett. 80 (1998) 4028–4031. https://doi.org/10.1103/PhysRevLett.80.4028.

[47] M.T. Trinh, M.Y. Sfeir, J.J. Choi, J.S. Owen, X. Zhu, A hot electron-hole pair breaks the symmetry of a semiconductor quantum dot, Nano Lett. 13 (2013) 6091–6097. https://doi.org/10.1021/nl403368y.

[48] Y. Yang, M. Yang, K. Zhu, J.C. Johnson, J.J. Berry, J. Van De Lagemaat, M.C. Beard, Large polarization-dependent exciton optical Stark effect in lead iodide perovskites, Nat. Commun. 7 (2016) 1–5. https://doi.org/10.1038/ncomms12613.

[49] E. Cassette, B. Mahler, J.M. Guigner, G. Patriarche, B. Dubertret, T. Pons, Colloidal CdSe/CdS dot-in-plate nanocrystals with 2D-polarized emission, ACS Nano. 6 (2012) 6741–6750. https://doi.org/10.1021/nn3024255.

[50] R. Scott, J. Heckmann, A. V. Prudnikau, A. Antanovich, A. Mikhailov, N. Owschimikow, M. Artemyev, J.I. Climente, U. Woggon, N.B. Grosse, A.W. Achtstein, Directed emission of CdSe nanoplatelets originating from strongly anisotropic 2D electronic structure, Nat. Nanotechnol. 12 (2017) 1155–1160. https://doi.org/10.1038/NNANO.2017.177.

[51] D. Pommier, R. Bretel, L.E.P. López, F. Fabre, A. Mayne, E. Boer-Duchemin, G. Dujardin, G. Schull, S. Berciaud, E. Le Moal, Scanning Tunneling Microscope-Induced Excitonic Luminescence of a Two-Dimensional Semiconductor, Phys. Rev. Lett. 123 (2019) 027402. https://doi.org/10.1103/PhysRevLett.123.027402.

[52] P. Guyot-Sionnest, B. Wehrenberg, D. Yu, Intraband relaxation in CdSe nanocrystals and the strong influence of the surface ligands, J. Chem. Phys. 123 (2005) 074709. https://doi.org/10.1063/1.2004818.

[53] M.C. Weidman, M. Seitz, S.D. Stranks, W.A. Tisdale, Highly Tunable Colloidal Perovskite Nanoplatelets through Variable Cation, Metal, and Halide Composition, ACS Nano. 10 (2016) 7830–7839. https://doi.org/10.1021/acsnano.6b03496.

[54] R.R. Cooney, S.L. Sewall, K.E.H. Anderson, E.A. Dias, P. Kambhampati, Breaking the phonon bottleneck for holes in semiconductor Quantum dots, Phys. Rev. Lett. 98 (2007). https://doi.org/10.1103/PhysRevLett.98.177403.

[55] N. Castro, C. Bouet, S. Ithurria, N. Lequeux, D. Constantin, P. Levitz, D. Pontoni, B. Abécassis, Insights into the Formation Mechanism of CdSe Nanoplatelets Using in situ X-ray Scattering, (2019). https://doi.org/10.26434/CHEMRXIV.8299382.V2.

[56] J. Maes, L. Balcaen, E. Drijvers, Q. Zhao, J. De Roo, A. Vantomme, F. Vanhaecke, P. Geiregat, Z. Hens, Light Absorption Coefficient of CsPbBr3 Perovskite Nanocrystals, J. Phys. Chem. Lett. 9 (2018) 3093–3097. https://doi.org/10.1021/acs.jpclett.8b01065.

[57] H.-H. Fang, L. Protesescu, D.M. Balazs, S. Adjokatse, M. V. Kovalenko, M.A. Loi, Exciton Recombination in Formamidinium Lead Triiodide: Nanocrystals versus Thin Films, Small. 13 (2017) 1700673. https://doi.org/10.1002/smll.201700673.

[58] X. Wu, M.T. Trinh, D. Niesner, H. Zhu, Z. Norman, J.S. Owen, O. Yaffe, B.J. Kudisch, X.-Y. Zhu, Trap States in Lead Iodide Perovskites, J. Am. Chem. Soc. 137 (2015) 2089–2096. https://doi.org/10.1021/ja512833n.

[59] J.C. Blancon, H. Tsai, W. Nie, C.C. Stoumpos, L. Pedesseau, C. Katan, M. Kepenekian, C.M.M. Soe, K. Appavoo, M.Y. Sfeir, S. Tretiak, P.M. Ajayan, M.G. Kanatzidis, J. Even, J.J. Crochet, A.D. Mohite, Extremely efficient internal exciton dissociation through edge states in layered 2D perovskites, Science (80-.). 355 (2017) 1288–1292. https://doi.org/10.1126/science.aal4211.

Chapter 4. AUGER RECOMBINATION AND MULTIPLE EXCITON GENERATION IN STRONGLY CONFINED COLLOIDAL 2D PEROVSKITE NANOPLATELETS

In this chapter, the multiexciton dynamics in strongly confined colloidal 2D perovskite nanoplatelets (NPLs) is studied using time-resolved photoluminescence (TR-PL) and femtosecond transient absorption (fs-TA) spectroscopy, under high excitation fluence and high excitation photon energy. The Auger recombination (AR) lifetimes from the TR-PL decays were measured by time-correlated single photon counting (TCSPC). These measurements were completed using fs-TA in the visible range to access much higher temporal resolution. Due to the limited exciton wavefunction delocalization and relatively long diffusion length in these halide perovskite materials, the effective AR rate is strongly dependent on the initial exciton density, ñ, via the average inter-exciton distance: typical Auger lifetime decreases from several hundreds of picoseconds at moderate exciton density to sub-10 ps when the photo-generated excitons spatially overlap ($\tilde{n} > 10^{11}$ cm^{-2}).

The intrinsic (i.e. not diffusion-limited) fast AR rate in these 2D materials can be explained by the enhanced interactions between the multiple, spatially confined excitons. Similarly, the inverse process of multiple exciton generation (MEG) should be efficient as well in these colloidal 2D NPLs. While MEG reports have often been judged controversial in semiconductor nanostructures, we found evidence for it in 2D MAPI n=3 perovskite nanoplatelets when exciting at very low fluence with photon energy excitation above twice the bandgap in the ultraviolet region. The strong dependency of the Auger rate on the inter-exciton distance allows us to interpret the fast picosecond decay component as an indirect observation of multiple exciton generation (MEG), implying the formation of two close excitons that ultimately recombine through AR.

4.1. Introduction

By combining outstanding strong photoluminescence, color purity and enhanced stability with easy and cheap solution-processing fabrication, 2D halide perovskites have become the focus of attentions in the development of electroluminescent diodes (LEDs), laser gain media or single-photon sources [1]. For all these various light-emitting devices, understanding the exciton-exciton annihilation, a process which ultimately limits the exciton density in these materials, becomes essential in order to control the device performances. For example, lasing threshold and LED efficiency are affected by the rapid non-radiative Auger recombination rate that limits the maximum electron-hole pair density in the photoactive material [2]. Auger recombination (*cf* description in **Chapter 1, part 2**) is the dominant recombination process that occurs in semiconductor nanostructures under high-excitation fluence [3,4].

Over the last few years, Auger recombination (AR) has been the subject of several investigations in weakly confined colloidal perovskite nanocrystals [5–7]. However, studies in strongly confined 2D perovskite samples are limited to a few cases: MAPI 2D thin films [8,9] and 5 ML-thick $CsPbBr_3$ NPLs [10,11]. While an increase of the AR rate is expected with the increase of the Coulomb interactions in confined systems, a slow bimolecular[1] AR rate of a few 10^{-4} and 10^{-3} cm^2/s was reported in 2D perovskite films in the strong confinement regime (1 to 5 MLs), leading to effective AR times on the order of hundreds of picoseconds to nanoseconds [8,9]. Interestingly, in a recent publication a decrease from 78 ps to 18 ps was reported in the effective biexcitonic recombination time of weakly confined $CsPbI_3$ NCs (size 12.1 nm) compared to in more-strongly confined ones (6.2 nm) [12]. Depending on the nature of the photoexcited species (free charge carrier or excitons), the AR process will follow third-or second-order kinetics [13,14]. Besides, the

[1] We use the term mono- and bimolecular kinetics by analogy with the chemical reactions involving one or two molecules.

anisotropic geometry of a system like the 2D quantum wells can induce further modifications in the measured kinetics such as asymmetric exciton-exciton interactions [15] and diffusion-limited recombination [9,16].

Here, we studied the multiple exciton dynamics of strongly confined lead iodide colloidal NPLs of 2 and 3 monolayers (MLs) by varying the excitation fluence from less than one to tens of μJ/cm^2. We found a fast-intrinsic AR rate with a corresponding effective recombination time of less than10 ps at high exciton density (~10^{11} cm^{-2}) while exciton diffusion delays the AR process to hundreds of ps when the initial exciton density is low.

On the other side, we studied the formation of multiple excitons in these NPL samples by the resulting AR that occurs after high photon energy and low fluence excitation. So far, multiple exciton generation (MEG) has only been observed in weakly confined iodide-based perovskite nanocrystals, $CsPbI_3$, and $FAPbI_3$, using transient absorption spectroscopy [12,17,18]. These indirect measurements are always very sensitive to photo-charging effects and/or a misinterpretation as a result of a too high excitation fluence [19,20] Surprisingly, MEG signatures were not observed by Klimov's group in his pioneering work in Cs-based perovskite NCs using time-resolved photoluminescence (TR-PL) techniques [5]. Here, we show that MEG induces a fast AR rate in 3 ML-thick NPLs due to the proximity of the two generated excitons that can be easily isolated from other non-radiative recombination processes occurring at a time scale larger by one order of magnitude.

4.2. Colloidal NPL samples and characterizations

Colloidal perovskite NPLs were synthesized at room temperature based on the LARP method [21]. Following this initial report of two-monolayer-thick $L_2[A PbI_3]PbI_4$ (MAPI, FAPI and CsPI) n=2 NPLs with L, an ammonium ligand and A an inorganic (cesium, Cs)

or organic (methylammonium, MA or formaminidium, FA) cation, we extended the synthesis to three-monolayer-thick $L_2[MAPbI_3]_2PbI_4$ NPLs (MAPI n=3). Unlike the ligand-assisted exfoliation procedures used in previously reported hybrid colloidal NPLs [22,23], the direct solution approach allows a more well-defined population (*i.e.* number of monolayers) in thinner NPLs.

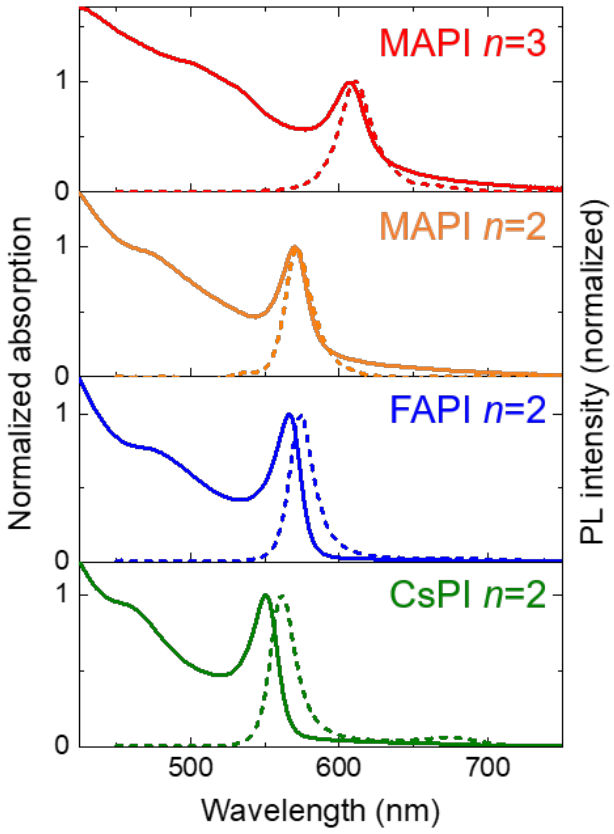

Figure 4.1. *Steady-state absorption (full line) and photoluminescence (dashed line) spectra of colloidal perovskite NPLs of three monolayers (MAPI n=3) and two monolayers (CsPI, FAPI, MAPI n=2).*

The steady-state absorption and photoluminescence (PL) spectra of the synthesized NPLs dispersed in toluene are shown in **Figure 4.1**. Except for CsPI n=2, all NPL samples present lateral dimensions from hundreds of nanometers to few micrometers (large disks on TEM images) and thus confinement in the lateral dimension can be neglected. The CsPI sample however might display some degree of confinement in one of the lateral

dimensions (nanoribbons with a width of 17 ± 3 nm and length of several hundreds of nm, see **Figure 2.32** in **Chapter 2, section 2**). While the small blue shift in the spectrum of Cs-based perovskite samples compared to MA- and FA-based ones is typical [24]. Here, it might be the consequence of the extra confinement effects, which could affect the AR rate [10].

4.3. Time-resolved photoluminescence experiments

Time-resolved photoluminescence (TR-PL) is a standard method to study multi-exciton dynamics in colloidal nanostructures. Since the PL signal is proportional to the average number of bounded electron-hole pairs in the excited nanoparticles, it allows to directly measure the exciton population in time following the different kinetic recombination processes [25]. Here, we employ the time-correlated single-photon counting (TCSPC) technique (see **Chapter 2, section 1**) with a time resolution of about 60 ps, to record luminescence decays of the four colloidal perovskite NPLs at the band-edge (560-620 nm depending on the NPL) after excitation at 400 nm. By varying the excitation fluence from 40 nJ/cm^2 to 15 μJ/cm2, multiexciton interactions may be revealed.

The TR-PL results for MAPI n=3 NPLs at different excitation fluences are shown in **Figure 4.2a**. The data for the n=2 NPL samples are displayed in **Figure 4.2b**. The PL decay traces could be well fitted by a multiexponential function. All the corresponding fit parameters are given in the **ANNEXE 4** (**Table A4-7**).

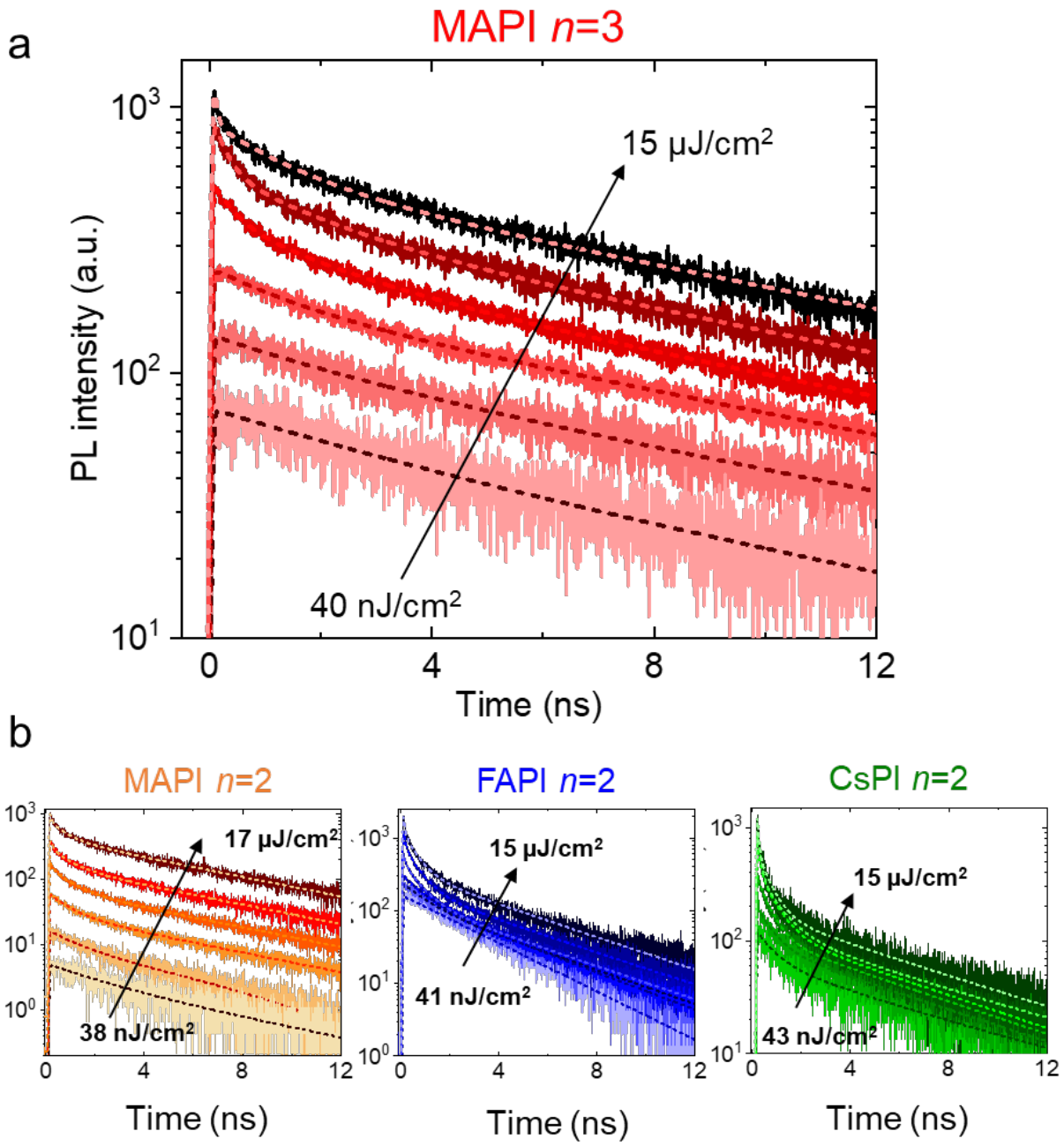

Figure 4.2. *Fluence-dependent PL decay traces of the perovskite NPLs excited at 400 nm (band-edge detection). Experimental data (full lines) and fit (dashed lines) for* ***(a)*** *MAPI n=3 NPLs and for* ***(b)*** *MAPI, FAPI and CsPI n=2 NPLs.*

4.3.1. Assignment of the multiple- and single- exciton dynamics

At low excitation fluencies, the dynamics are almost mono-exponential for MAPI and FAPI NPLs, but a better description is obtained for all the samples using a biexponential

decay function, having time constants τ_2 and τ_3. Starting at about 2 μJ/cm² (see the calculation of the excitation fluences in the **ANNEXE 4**), an extra short-lived component appears, characterized by a time constant τ_1 that decreases from a few hundreds to a few tens of ps with increasing excitation fluence. At the same time, the middle component τ_2 decreases from just below (or few ns) to a few hundreds of ps. The long component τ_3, however, remains almost constant and is 10 ± 1, 5.7 ± 0.1, 3.2 ± 0.6 and 5.9 ± 0.1 ns for MAPI *n=3*, MAPI *n=2*, FAPI *n=2,* and CsPI *n=2*, respectively.

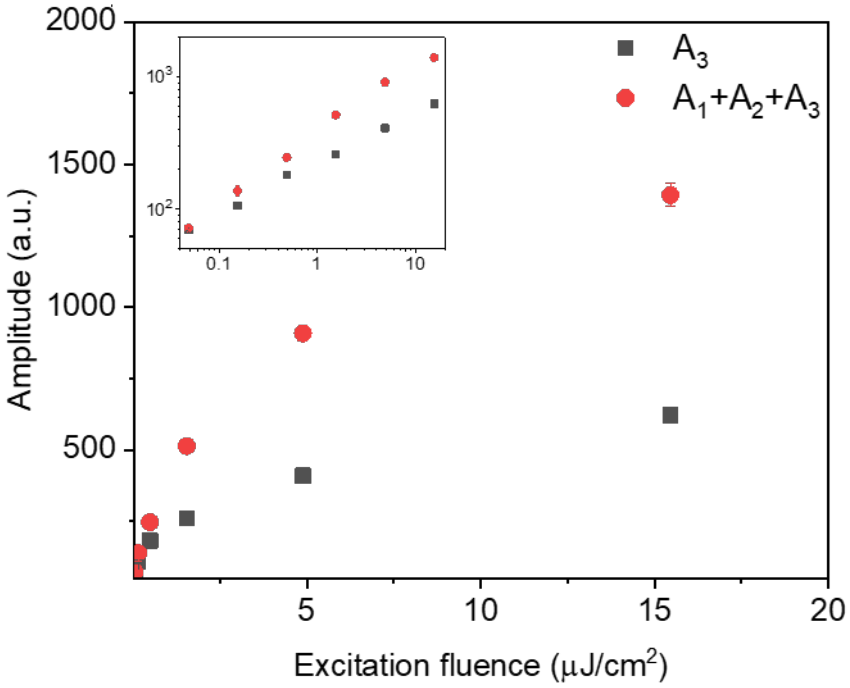

Figure 4.3. *Evolution of the total (A_1+A_2+A_3, red dots) and single-exciton (A_3, black dots) amplitude of the time components used in the multi-exponential fit of the TR-PL decay traces of n=3 MAPI NPLs, for different excitation fluences. Inset: same graph in the log-log scale.*

The constant value of the long component τ_3 for all excitation fluences shows that the PL signal detected at several ns is mainly associated to mono-exciton recombination. Indeed, recombination of free charged carriers will lead to bimolecular recombination, as previously observed in bulk halide perovskites [26]. The amplitudes associated with this long component saturate much faster than the total amplitudes (*i.e.* intensity at time *t*=0),

as seen in **Figure 4.3** for MAPI *n=3*. This means that while a high excitation density can generate several excitons within a single NPL, multiexciton recombinations are efficient enough to reduce the dynamics at long times to single excitons recombination. Thus, the nanosecond decays here reflect the dynamics of a single exciton, independently of the initial number of generated excitons [27].

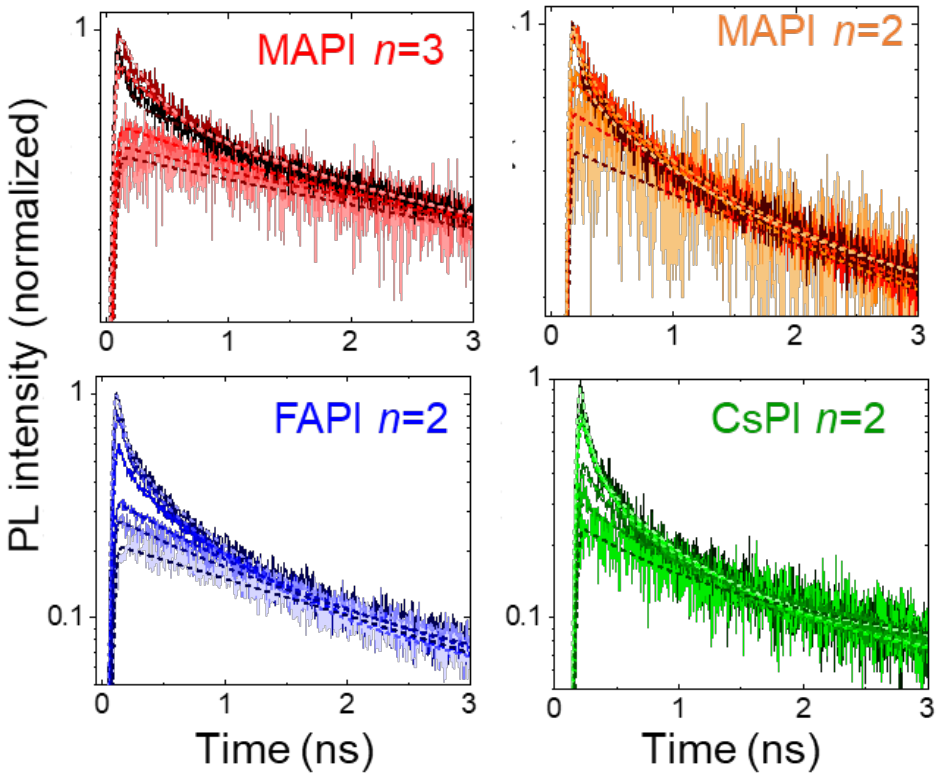

Figure 4.4. *TR-PL decay traces of the perovskite NPL samples normalized at long time to highlight the fast component arising at high-excitation density.*

The consistency of the long time dynamics due to mono-exciton allows us to normalize the PL decay traces at a long time to highlight the extra decay component at larger excitation density (**Figure 4.4**), similar to previous reports [6,27–29]. By subtracting the mono-exciton dynamics from the high fluence PL decay traces, the multiexciton dynamics are isolated. We found that the corresponding effective decay times decrease with the initial

number of created excitons, which is expected for quadratic multi-exciton recombination (see discussion below **part 4.3.2**).

As the multiexciton time constants (τ_1 and τ_2) extracted from the fit are on the order of hundreds to tens of ps, they correspond to non-radiative AR rather than radiative biexcitonic recombination. Indeed, the radiative biexciton lifetime ($\tau_{BX,rad}$) is related to the radiative single exciton lifetime ($\tau_{X,rad}$) according to the equation [30]:

$$\tau_{BX,rad} \approx \frac{1}{2}\tau_{X,rad} = \frac{1}{2}\frac{\tau_X}{PL\ QY} \quad [4.1]$$

where $\tau_x = \tau_3$ is the measured luminescence mono-exciton lifetime and PLQY is the photoluminescence quantum yield of the sample.

By taking the long time component of the PL decay τ_x = 10.0 ± 0.8 ns and PLQY = 0.31 of the *n=3* NPL sample, we found $\tau_{BX,rad} \approx 8$ ns, which is more than one order or magnitude longer than the observed time range of the multiexciton dynamics. Here, trion dynamics giving another kind of Auger recombination can be neglected since the samples were circulated within the 3 mm cell and the repetition rate decreased to 200 kHz to prevent from photo-charging and photo-degradation effects [3,31].

4.3.2 Discussion on the kinetics of the multi-exciton dynamics

4.3.2.1 Kinetic model

In the case of the main excite species are excitonic, Auger recombination follows bimolecular recombination kinetics and the total kinetic equation can be written as following [13]:

$$\frac{d\tilde{n}}{dt} = -k_X\tilde{n}(t) - \beta\tilde{n}(t)^2 \quad [4.2]$$

with $\tilde{n}(t)$ the time-dependent exciton density, $k_X = 1/\tau_X$ the "monomolecular" recombination rate of single excitons and β the "bimolecular" AR rate. For highly asymmetric 2D nanostructures, the exciton density is surfacic (number of excitons N per

NPL surface, in cm^{-2}), such as β is typically displayed in cm^2/s. We note that a factor ½ should normally be added in front of β because, for relatively low excitation photon energy, the re-excited exciton is not ionized and relax back to the band-edge at a cooling rate expected much higher than the Auger rate (*cf* **Chapter 3**). We note however that this factor was not taken into account previously so for a fair comparison we intentionally omit it but we remember that the real rate is twice faster.

The bimolecular Auger recombination requires a sufficiently high density of excitons to occur since it involves *short-range* exciton-exciton interactions that are described either by a collision process or a Förster energy transfer with efficiency scaling in $(1/d_{X\text{-}X})^6$, $d_{X\text{-}X}$ being the distance between the excitons (one exciton transfers its energy to re-excite the other exciton) [32]. In the two limiting cases of immobile excitons (*e.g.* self-trapped excitons) [33] and large exciton delocalization length in the 2D plane (wavefunction of the exciton center-of-mass motion extended well-above $d_{x\text{-}x}^2$) [34], the bimolecular AR rate (β) is constant in time and the solution to the **equation 4.2** has the analytical form [13]:

$$\tilde{n}(t) = \frac{\tilde{n}(0)exp(-t/\tau_X)}{1+\tilde{n}(0)\beta\tau_X[1-exp(-t/\tau_X)]} \qquad [4.3]$$

with $\tilde{n}(0)$, the initial exciton density.

4.3.2.2 Multiexponential fit vs. bimolecular kinetic model

The measured PL intensity is proportional to the averaged instantaneous number of excitons $N(t)$ and thus to the corresponding density $\tilde{n}(t)$. We thus use eq. 4.3 to fit our PL decay traces $I(t)$ = constant × $\tilde{n}(t)$, by fixing the initial $\tilde{n}(0)$ calculated from the excitation fluence, sample absorption cross-section, and surface (see **ANNEXE 4**) and fixing τ_X. This is shown in **Figure 4.5.**

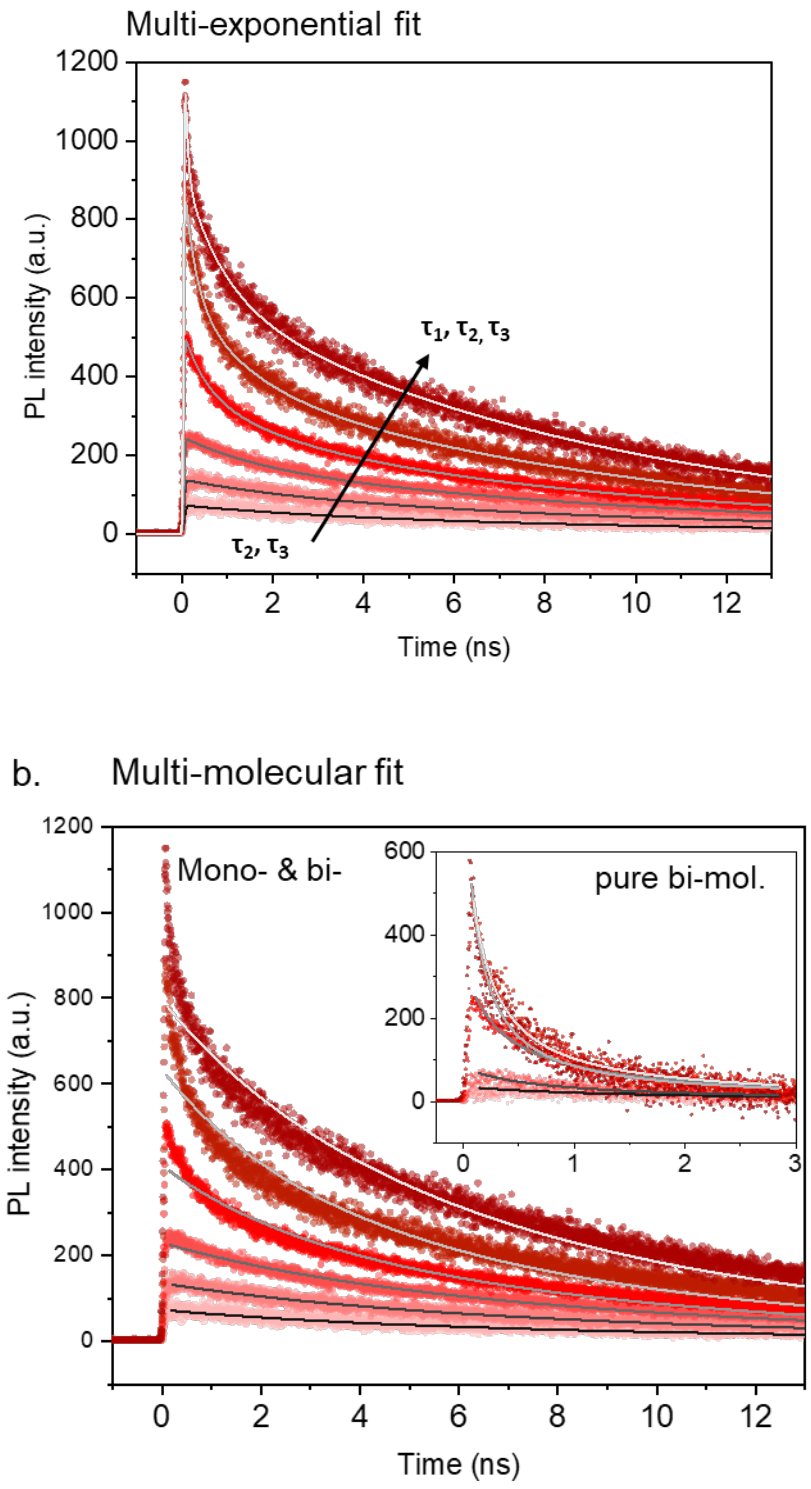

Figure 4.5. *Full TR-PL decay traces of MAPI n=3 NPLs excited at 400 nm with increasing fluence (from light to dark red dots) with* ***(a)*** *exponential fit (2 to 3 components) and* ***(b)*** *fit using the mono- and bi-molecular recombination kinetics (****equation 4.3****). In inset of* ***(b)*** *is shown the data subtracted from the mono-exciton dynamics with a pure bimolecular dynamic (****equation 4.4****).*

By comparing with the multiexponential fit (**Figure 4.5a**), the fit of the PL decay trace of MAPI n=3 NPLs using **Equation 4.3** does not reproduce the early-time dynamics associated with multiple excitons very well. The low excitation fluence data and long-time dynamics corresponding to non-interacting excitons present (at low exciton density) are however fairly well represented and give a bimolecular rate β that decreases from 5×10^{-3} to 8×10^{-5} cm^2/s with increasing excitation fluence. These values are comparable to the β-values of 5×10^{-4} and 5×10^{-3} cm^2/s reported by Delport *et al.* and *Deng et al.* respectively. [8,9] From our point of view, these values do not represent the multiexciton AR rates. They may be partially related to the presence of free carriers implying bimolecular non-geminate electron-hole recombination [35]. We should also note that these values are highly dependent on the initial value of $\tilde{n}(0)$ and τ_X, which make it difficult to physically interpret the results. We thus decided to fit only the isolated multiexciton dynamics, after subtraction of the low fluence trace, using a simplified equation describing pure bimolecular dynamics [13]:

$$\tilde{n}(t) = \frac{\tilde{n}(0)}{1+\tilde{n}(0)\beta t} \qquad [4.4]$$

The resulting fits are displayed in the inset of **Figure 4.5b**. In this case, experimental data are well reproduced and we obtain a bimolecular Auger recombination rate β decreasing from 8.2×10^{-2} to 1.1×10^{-2} cm^2/s with increasing excitation fluence from 0.15 to 15 µJ/cm^2.

4.3.2.3 Deviation from the "bimolecular" recombination of the multiexciton dynamics

The fact that β decreases with the excitation fluence can be surprising. It shows that the TR-PL dynamics deviate from bimolecular kinetics and in particular its dependency on $\tilde{n}$ is sub-quadratic. On the other hand, the effective AR rates extracted from the

multiexponential fit increase with the excitation fluence, thus expressing a super-linear dependency with the exciton density.

This trend can be understood if, in **equation 4.1**, the bimolecular Auger recombination rate β is time-dependent. Several works on the exciton-exciton annihilation in molecular systems presenting highly-limited delocalization length have taken into account the random walk of these excitons (diffusion) before the collision and resulting exciton-exciton recombination, at moderate excitation fluence [9,36]. For example, in one-dimensional samples such as linear J-aggregates, the bimolecular rate $\beta(t)$ is predicted to have a $t^{-1/2}$ dependency [37].

Excitons in 2D halide perovskites are expected to be much more spatially delocalized than their counterparts in molecular systems. However, due to the ionic nature of the perovskite structure, excitons within 2D perovskite might present reduced delocalization length along the 2D plane compared to transition metal dichalcogenides (MoS_2, WSe_2, etc…) or II-VI semiconductors such as CdSe. To the best of our knowledge, the effect of the exciton diffusion on the exciton-exciton annihilation process in perovskite nanostructures has only been discussed by Lian *and co.* and Deng *and co.*[9,10] The former authors did not investigate the evolution of the AR times with the excitation density but extracted the biexciton dynamics from transient absorption in n=5 $CsPbBr_3$ NPLs and found it very fast and sensitive to the geometry of the nanoplatelets (recombination time: 14 to 70 ps) [10]. However, the latter authors found that the exciton diffusion has no impact on the AR in 2D perovskite thin films (MAPI-based) by comparing the diffusion constant and Auger rate extracted from their analysis using transient absorption microscopy (reaction-limited and not diffusion-limited AR) [9].

To relate the AR rate in s^{-1} extracted from the multiexponential fit with the bimolecular AR rate in cm^2/s, we introduce the AR effective rate AR rate ($\tau_{Auger,\ eff}$), which is the

instantaneous rate that can be approximated by using the initial exciton density $\tilde{n}(0)$, according to $\tau_{\text{Auger, eff}} = 1/[\beta \times \tilde{n}(0)]$. The effective Auger recombination times are plotted against exciton density for the four NPL samples in **Figure 4.6**. It should be noted that $\tau_{\text{Auger, eff}}$ calculated from β contains in principle information on both τ_1 and τ_2 extracted from the multiexponential fit.

For moderate exciton fluence, the results clearly show a diffusion-limited exciton-exciton annihilation process. We further note that the AR time is increasing in NPL samples with larger dimensionality: MAPI n=3 NPLs seem to present a much-reduced AR rate than FAPI and MAPI n=2. Moreover, CsPI n=2 NPLs presenting a lateral confinement show the fastest rates at low exciton density, *i.e.* this latter sample displays a rate that is less diffusion-limited. We can conclude from these results that the diffusion constant is higher, or the exciton wavefunction delocalization in the 2D plane is larger, in more strongly-confined NPLs.

At higher excitation fluence, the effective Auger lifetimes attain asymptotically a limiting value that is comparable to the temporal resolution of our TCSPC setup (instrument response function (IRF) about 60 ps, *cf* **Chapter 2, part 1**). To determine the intrinsic Auger recombination rate (*i.e.* not diffusion-limited), we need to access the high fluence dynamics with a much higher temporal resolution using TA technique.

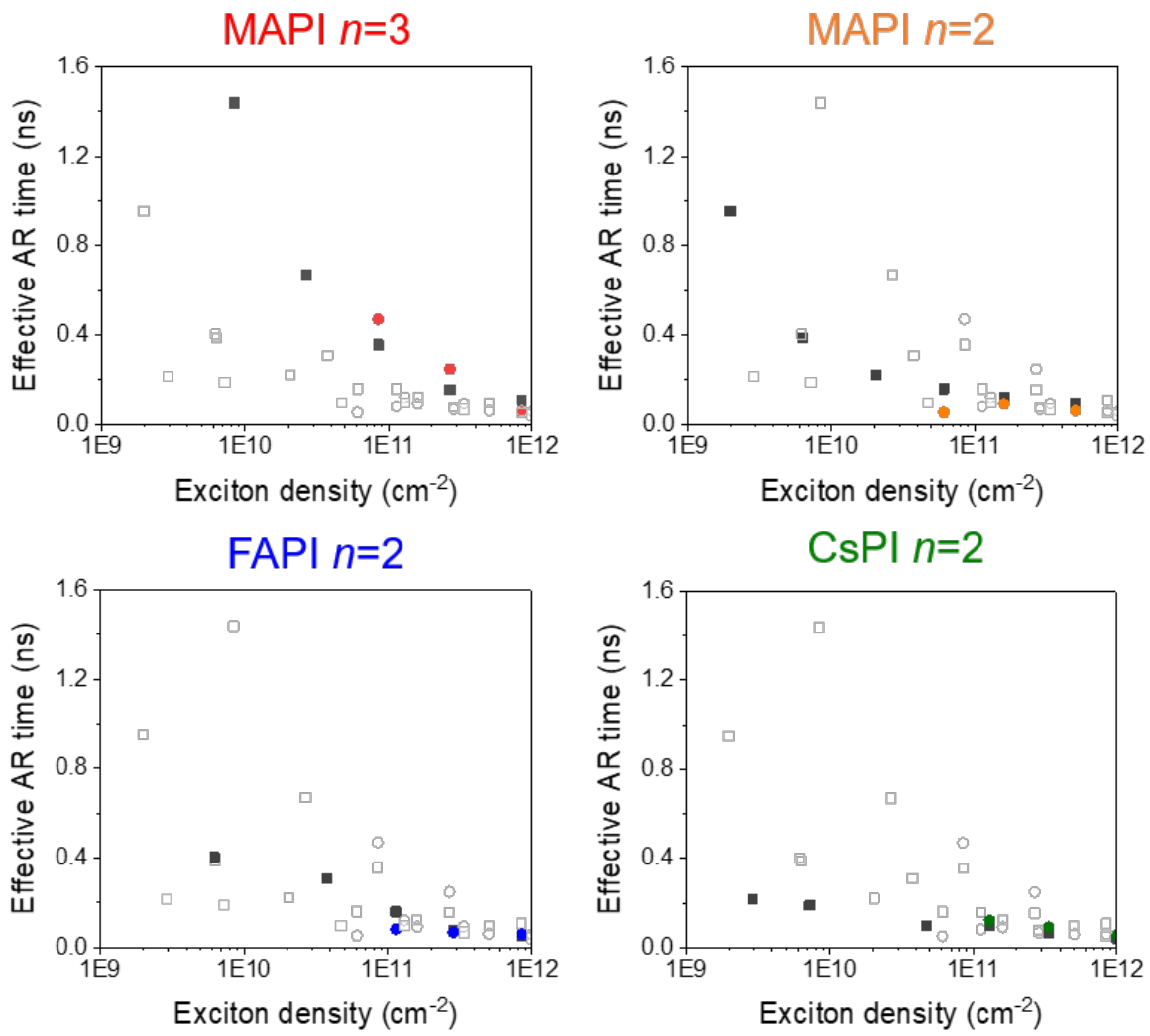

Figure 4.6. *Effective Auger recombination time ($\tau_{Auger,eff}$, full black squares) of the different perovskite NPL samples calculated using the bimolecular Auger recombination rate (β) from the multiexponential fit of the TR-PL decay. The multiexciton shortest time constants (τ_1, colored circles) are shown is each graph for comparison. The data of all samples are shown in light grey open circle/square.*

4.4. Visible transient absorption spectroscopy experiments

Transient absorption (TA) is a spectroscopic technique providing a much higher temporal resolution than TCSPC. Excitation fluence-dependent TA experiments were carried out on the four NPL samples using band-edge excitation to avoid the effect of relaxation in the early time dynamics (*cf* **Chapter 3**). The transient signal we focus on in this study corresponds to the photo-induced bleach (PIB) coming from the saturation of the band-

edge transition due to the presence of excitons generated by the pump in the lowest energy levels [29]. However, while the PL signal is always proportional to the population of excitons, the amplitude of the PIB signal is proportional only at low excitation fluence, as it saturates at high power due to the discrete character of the excited states available [14].

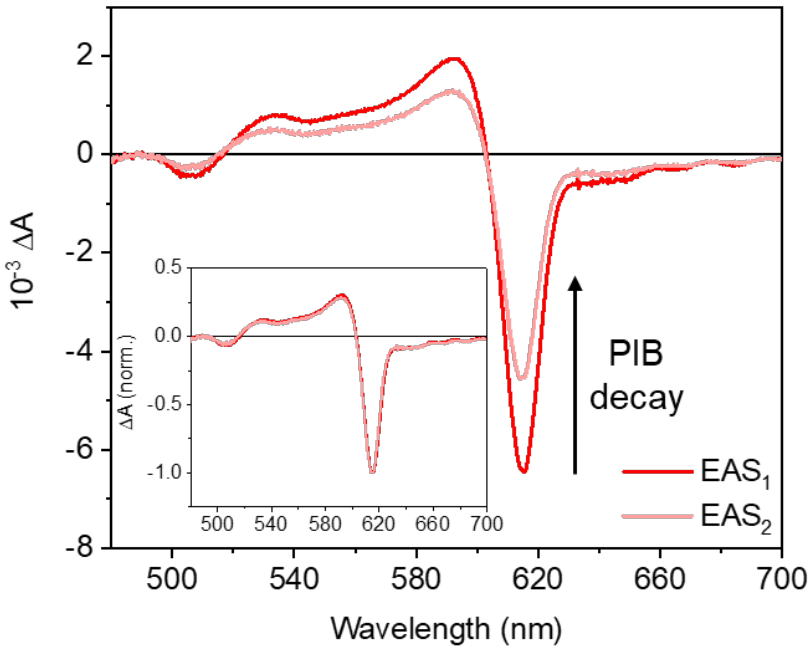

Figure 4.7. *Evolution Associated Spectra (EAS) extracted from global analysis of MAPI n=3 NPLs excited at* 620 *nm. The exponential decay time constants are 314 ps (EAS_1 to EAS_2) and 2.4 ns (amplitude decay of EAS_2). As EAS_1 and EAS_2 are only different in amplitude (same normalized lineshape in the inset), the decay dynamics are only due to depopulation.*

From a global fit analysis of the TA data, we found that the line-shapes where conserved within the time-range of interest (ps-ns), including no significant spectral shift in the PIB of the band-edge transition (**Figure 4.7**). Consequently, the kinetic trace at the PIB maximum averaged over a few nanometers can be fitted directly. The sign of the negative PIB signal was changed for easier comparison with TR-PL analysis.

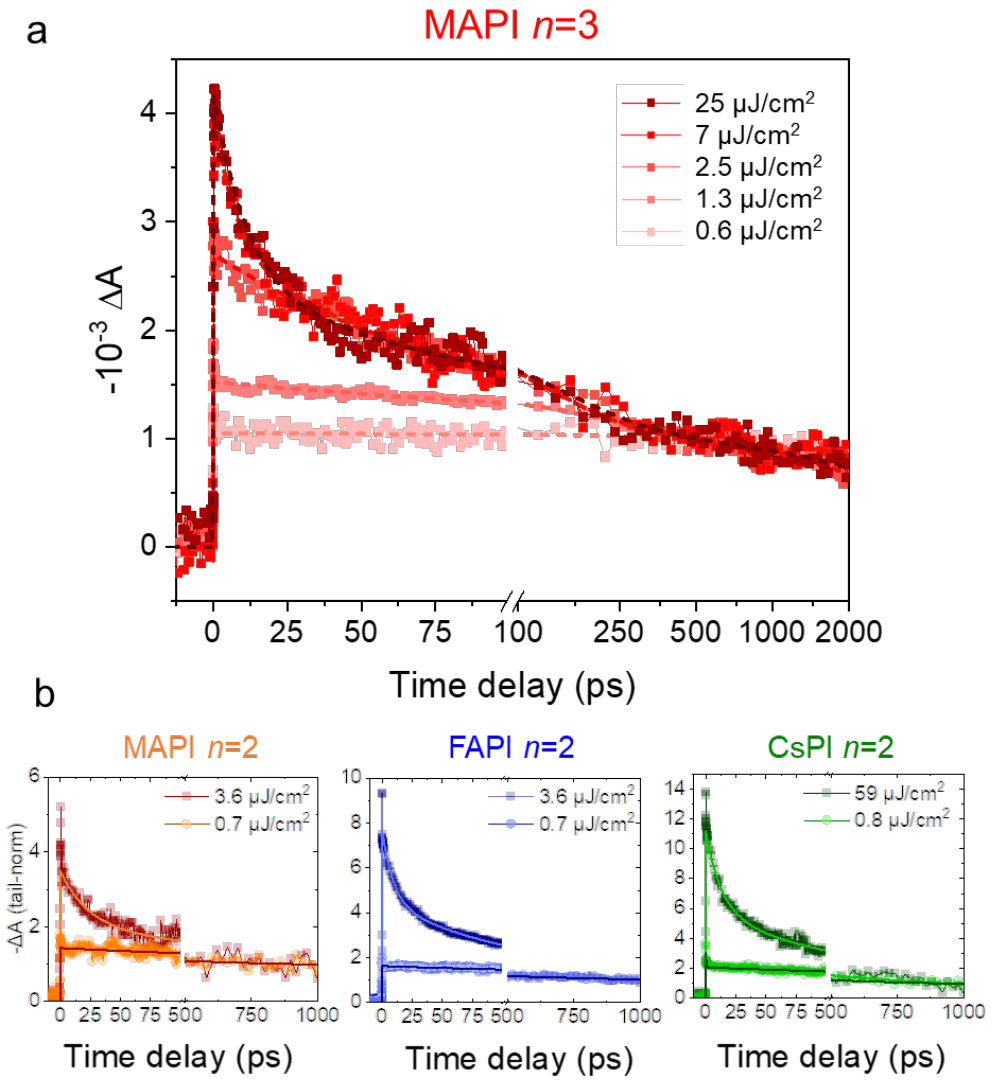

Figure 4.8. *Band-edge PIB traces of* ***(a)*** *MAPI n=3,* ***(b)*** *MAPI n=2,* ***(c)*** *FAPI n=2 and* ***(d)*** *CsPI n=2 NPLs normalized at long time for different excitation fluences and multiexponential fit (dashed lines). The PIB decays traces of the four NPL samples are shown in* ***Figure 4.8****. They are normalized at a longer time to highlight the extra decay appearing at high excitation fluence. As explained above in the treatment of TR-PL data, the time constants obtained by fitting with a multi-exponential decay function were satisfactory for the interpretation of the AR dynamics. Consequently, in the following, we only treat TA data in the same manner. The resulting fit parameters are given in* ***Table A8-11*** *in the* ***ANNEXE 4****.*

One kinetic component in the nanosecond time range was enough to fit the traces measured at the lowest excitation fluences (about 0.6-0.7 µJ/cm²), which is in agreement with TR-PL data (see the calculation of the number of excitons and exciton density in the

ANNEXE 4) The long-time constants are consistent with the nanosecond single-exciton recombination times measured in TR-PL for all the samples, even if the total TA time range is much reduced (about 2 ns).

Increasing the excitation fluence to of few μJ/cm^2 leads to additional kinetic components, a first on the order of a few hundreds of ps, and a second as short as sub-10 ps. Both time constants decrease with the excitation fluence. In line with the discussion of the TR-PL data, we assign these faster components to multiexciton processes, notably Auger recombination. However, the very fast (< 60 ps) dynamics could not be determined by TR-PL due to its limited IRF. The short time constants (τ_1) obtained by TA are plotted as a function of the exciton density for the four samples in **Figure 4.9**. The isolated τ_1 components tend to the same value for all the measured NPL samples, corresponding to the intrinsic Auger recombination time (not diffusion-limited). This show that the AR process can be described by a collision (or short-range energy transfer) without involving a probability of recombination per collision. We further note that this sub-10 ps component is much faster compared to other nanomaterials such as II-VI and III-V semiconductors that typically have an AR time on the order of a few hundreds of picoseconds. The second time component (τ_2) in the hundreds of ps is assigned to diffusion-limited Auger recombination.

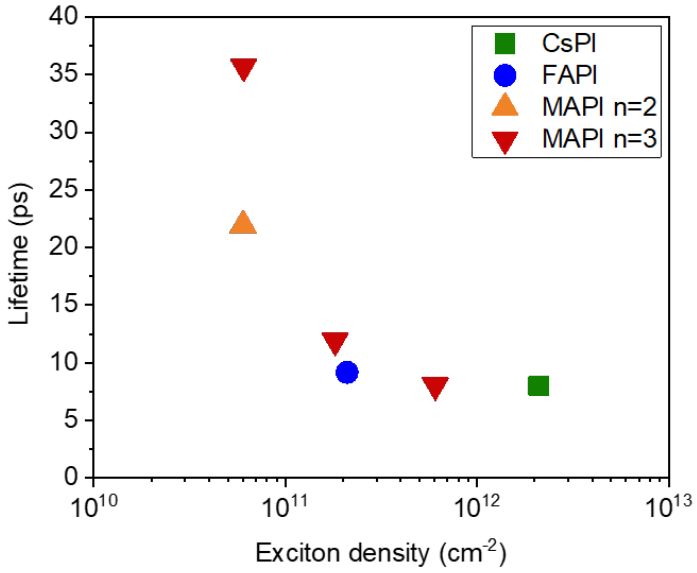

Figure 4.9. ***(a)*** *Early-time Auger recombination time constants (τ_1) extracted from high-excitation density TA date in MAPI n=3 NPLs at three different fluence and at the highest excitation density measured for, MAPI, FAPI, and CsPI n=2 NPLs.*

4.4.1. Diffusion- limited exciton-exciton recombination and intrinsic Auger rate

To further address how the multiexciton recombination rate depends of the density of excitons in two-dimensional structures, the corresponding inter-exciton distance $d_{X\text{-}X}$ can be calculated. In the case of MAPI n=3 NPLs, an additional component with a time constant in the hundreds of ps appear for an excitation fluence as low as 1.3 μJ/cm², corresponding to an initial exciton density of 3×10^{10} cm^{-2} (calculation in the **ANNEXE 4**). Assuming a Poisson distribution [14] for the number of excitons photo-created per NPL as a function of the excitation fluence and a homogeneous distribution of the excitons within a NPL (beam waist >> NPL size), this leads to an average inter-exciton distance $d_{x\text{-}x} \approx 57$ nm (center to center distance), with 68 % of the values in the 47-88 nm range (**Figure 4.10**). In the same manner, we estimated the exciton-exciton distance from the excitation density where an ultrafast component as short as 10 ps becomes predominant (> 40 % in amplitude at 25 ± 4 μJ/cm²). For this initial exciton density of $(6 \pm 2) \times 10^{11}$ cm^{-}

^{2}, the average inter-exciton distance $d_{x\text{-}x} \approx 13$ nm, with 68 % of the values between 12.2 and 13.7 nm. For this distance 4 to 6 times larger than the exciton Bohr radius a_B reported for $MAPbI_3$ perovskite ($a_B < 3$ nm [38]), the excitons overlap spatially as they recombine efficiently. Here, we only used the Poisson distribution for the statistical number of excitons photo-created for NPL. However, we should keep in mind that the excitation within the beam section is inhomogeneous. Thus, the range of the calculated $d_{x\text{-}x}$ is even broader.

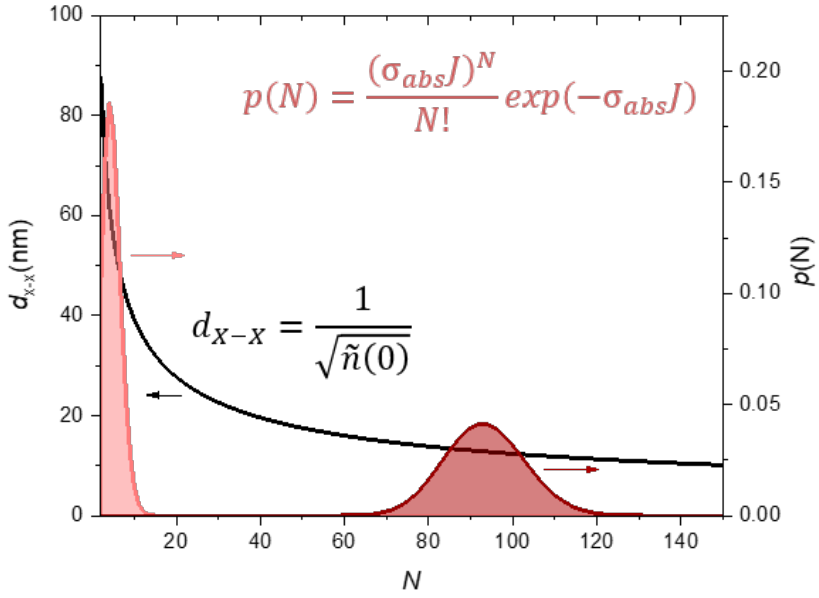

Figure 4.10. *Inter-exciton distance $d_{x\text{-}x}$ calculated from the initial exciton density $\tilde{n}(0)$ in MAPI n=3 NPLs following a band-edge excitation generating N excitons per NPL (curve and corresponding equation in black). The average number of excitons is given by the product of the sample absorption cross-section σ_{abs} (in cm^2) at the excitation photon energy hv (here 2 eV) and the photon excitation density (in cm^{-2}). The probability of having N exciton per NPL is given by the Poisson distribution (equation in pink). When the average number of N is large, this distribution can be approximated by the Normal distribution function, with 68 % of the values within one standard deviation away from the mean value of N. Here is represented two distributions, one corresponding to a low initial exciton density (light pink, 3×10^{10} cm^{-2}) and the other at high exciton density (dark pink, 6×10^{11} cm^{-2}).*

Assuming an isotropic exciton delocalization in the 2D plane, we can estimate the coherent exciton radius a_x (*i.e.* characteristic size of the extent of delocalization of the exciton center-of-mass motion [16] to be about $d_{x\text{-}x,min}/2 = 6.5$ nm. For $d_{x\text{-}x}$ much larger than the delocalization length, we can only assume that the multiexciton Auger recombination rate is limited by the exciton diffusion in the 2D plane. In that case, the effective Auger recombination time is highly dependent on the sample geometry. This could explain the range of AR rates reported by Lian *and co.* in 5 ML-thick $CsPbBr_3$ NPLs with different lateral sizes, without the need of invoking a probability of Auger recombination per exciton collision [10].

It means also that the mono-exponential decay usually extracted for discrete biexcitonic to mono-excitonic recombination in semiconductor nanostructures is not the intrinsic biexcitonic rate in anisotropic perovskite samples such as 2D NPLs. The intrinsic Auger rate can only be obtained at high excitation fluence where the initial photogenerated excitons overlap before diffusion takes place (reaction-limited AR). This is summarized in **Figure 4.11**.

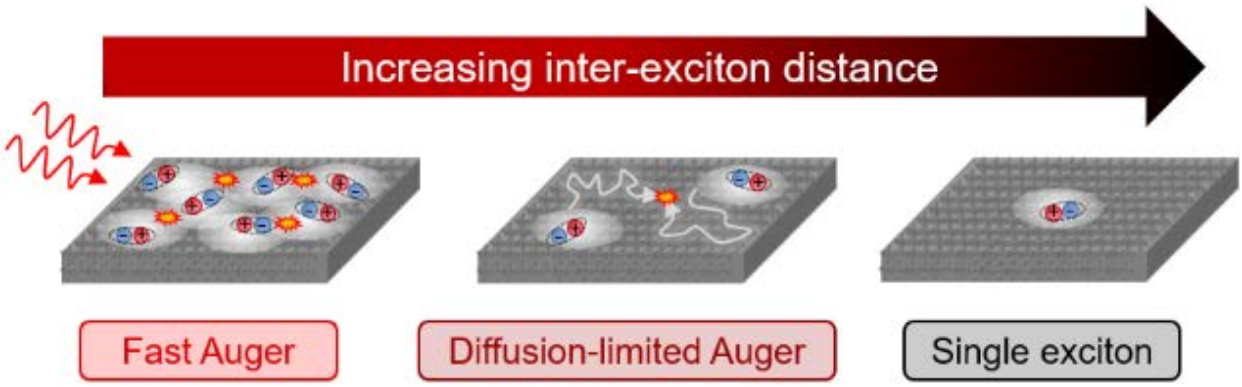

Figure 4.11. *Schematics of the exciton recombination processes as occurring with decreasing exciton density in time due to AR (from left to right) or with decreasing excitation fluence. TA decay rate is strongly dependent of the initial exciton density. At high exciton density, Auger is the main recombination pathway with intrinsic recombination time below 10 ps (reaction-limited Auger). Spatially separated excitons at moderate density have to diffuse in the 2D plane before they encounter each other and recombine non-*

radiatively, with typical lifetimes of hundreds of ps (diffusion-limited AR). Finally, single-excitons recombine on the ns timescale (electron-hole recombination).

4.5. Multiple exciton generation (MEG).

So far, the exciton-exciton interactions were probed at high excitation fluences, where each absorbed photon creates a unique electron-hole pair and multiple excitons within a single NPL decay predominantly through the Auger recombination process. We now investigate the case of very low excitation fluence with high photon energy, which can potentially lead to multiexciton generation.

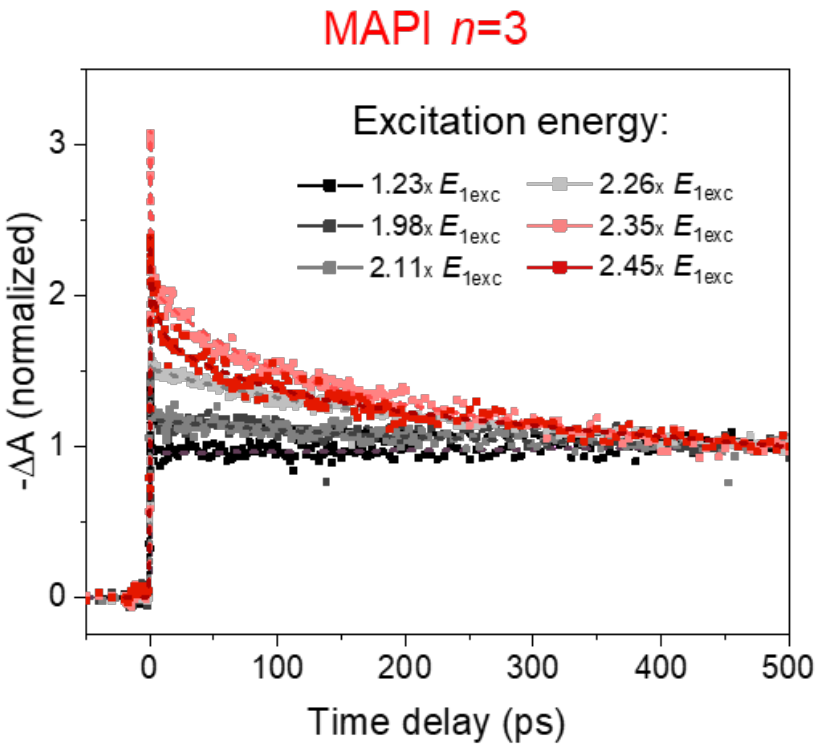

Figure 4.12. *PIB traces at low fluence of MAPI n=3 NPLs (band-edge detection, normalized at 500 ps) for different excitation photon energies (corresponding to 500, 310, 290, 270, 260 and 250 nm in wavelength). Experimental data are represented by squares, multi-exponential fits are represented by dashed lines.*

We focused the analysis on MAPI n=3 NPLs which present the lowest optical bandgap energy ($E_{1exc} \approx 1.95$ eV) within the synthesized samples. This allows us to excite the NPLs at various energies E in the ultraviolet (UV), using the second harmonic of the NOPA, well-above (about $2.45 \times E_{1exc}$, 250 nm, 4.96 eV) and below (*e.g.* about 320 nm, 3.88 eV) the minimum required threshold for MEG ($E = 2 \times E_{1exc}$.) To avoid as far as possible multiphoton absorption within a single NPLs, the excitation pulse energy was decreased to below 1 nJ, while keeping well-defined TA dynamics (ΔA from PIB signal around 0.5×10^{-3}). The extracted PIB dynamics at band-edge detection normalized at long time are displayed in **Figure 4.12** for six different excitation wavelengths. The corresponding fit parameters are in the **ANNEXE 4**).

While for a visible excitation, the PIB dynamics can be well described by a mono-exponential decay with a long-time component of about 10 ns (represented in black in **Figure 4.12**, excitation at $1.23 \times E_{1ex}$ corresponding to 500 nm), extra decay components with time constants ranging between 10 and 100 ps emerge for UV excitation. We also observe a coherent artifact at times below 300 fs that is taken into account in the exponential fit but not analyzed further for the extraction of the time constants and corresponding amplitudes. Similar to the previous analysis the faster components can be isolated from the long-time single-exciton dynamics by subtracting the trace obtained for visible excitation from the others after normalization at long times (**Figure 4.13)**. This faster component could be interpreted as the indirect observation of MEG, since the excitation fluence was reduced to a minimum while exciting the NPLs at a high photon energy. We should note that here, per opposition with visible TA experiments, we expected at most two excitons per NPL (for low enough excitation fluence).

The component characterized by a time constant on the order of hundreds of ps is directly observed at relatively low energy excitation ($1.98 \times E_{1exc}$ and $2.11 \times E_{1exc}$) with a relatively low amplitude. However, it becomes much more pronounced starting from $2.26 \times E_{1exc}$ (270

nm in wavelength). At $E \geq 2.35 \times E_{1exc}$, an additional component of a few picoseconds appears. It should be kept in mind that this time constant is much longer than the temporal resolution (< 300 fs for UV excitation).

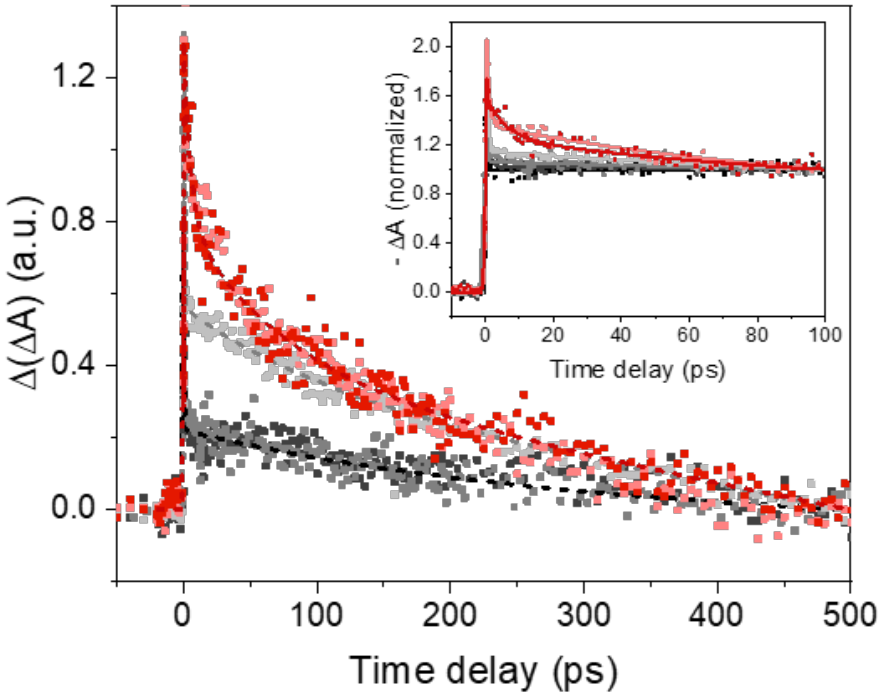

Figure 4.13. *(a) Isolated early-time PIB dynamics measured using UV excitation obtained by subtracting the trace acquired with visible excitation after normalization at 500 ps. Inset: Decay of the PIB normalized at 100 ps for all excitation photon energies. Experimental data are represented by squares with the same color scheme as in* ***Figure 4.12.***

The sum of amplitudes of the extra dynamics relative to the long one can be plotted versus the excitation energy relative to the optical bandgap one ($h\nu/E_{1exc}$). This leads to an apparent number of excitons generated by a single photon (exciton generation quantum yield, QY), seen in **Figure 4.14b** (black squares), as previously reported for perovskite nanocrystals [12,17] and other semiconductor nanostructures [39–41]. From this plot, it

seems that more than one exciton starts to be generated just below the theoretical threshold (1.98 ×E_{1exc}) and the maximum MEG efficiency (200 %) is reached at 2.45 ×E_{1exc}.

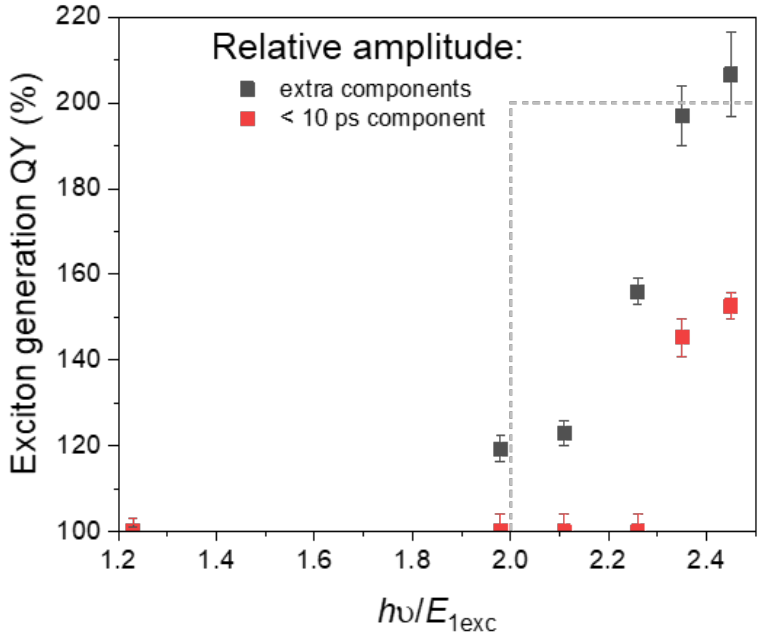

Figure 4.14. *Evolution of the amplitude of the early-time component relative to the single exciton one in MAPI n=3 NPLs, including the sub-10 to hundreds of ps components (black squares) and sub-10 ps only (red squares). Dashed grey lines represent the theoretical limit of the maximum quantum yield of generated excitons, 200 %, with an excitation threshold of 2 × E_{1exc}.*

In the following, we argue that only the fastest component of a few picoseconds corresponds to the indirect observation of MEG through the resulting fast Auger recombination (red squares **Figure 4.14**), while the intermediate component with a time constant of hundreds of picoseconds arises from side effects of high excitation photon energy.

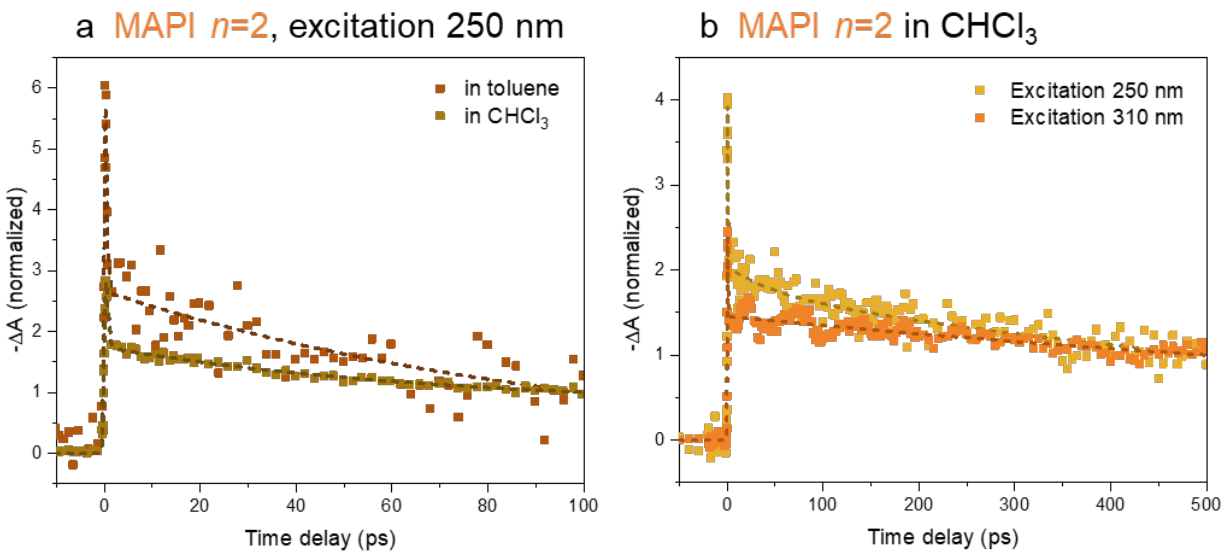

Figure 4.15. (a) *Comparison of the PIB traces (normalized at 100 ps) of MAPI n=2 NPLs synthesized in toluene and chloroform measured after excitation at 250 nm with identical fluences.* ***(b)*** *PIB traces (normalized at 500 ps) of MAPI n=2 NPLs synthesized in $CHCl_3$ for excitation at 250 and 310 nm.*

First, several experiments were performed to check that the short picosecond component did not arise from a solvent effect. The reason is that toluene starts to absorb light below 280 nm. Attempts to re-disperse the *n*=3 NPLs or to synthesize them directly in chloroform ($CHCl_3$) solvent with negligible absorption in the whole UV range of interest, were unsuccessful. Nevertheless, a collaboration with Philippe Cassette from the Liquid Scintillation Counting Working group (LNHB, CEA Saclay, France) reveals that no emission could be detected from the perovskite NPLs after excitation of the toluene molecules (liquid scintillation experiment), showing the absence of efficient energy transfer.

Furthermore, the direct synthesis of thinner MAPI *n*=2 NPLs in chloroform was possible and TA measurements on this sample do not show any picosecond component when exciting at 250 nm, even at higher excitation fluence (**Figure 4.15a**). From our point of

view, the MEG threshold was not reached in these materials since they have a higher optical bandgap.

TA measurements in the UV of this MAPI n=2 NPL sample synthesized in chloroform show an intermediate component characterized by a time constant on the order of hundreds of ps after excitation at 250 nm, but having a much-reduced amplitude compared to the same NPLs dispersed in toluene (**Figure 4.15a**). We interpret this result by the enhanced stability of the NPLs in chloroform versus toluene, which leads to a reduction of the intermediate component due to non-radiative pathways induced at high photon energy exposition. Similarly, to the NPL n=3 sample in toluene, we found a much higher proportion of this intermediate component when exciting at 250 nm compared to 310 nm (**Figure 4.15b**). If this dynamic was due to MEG, it will lead to an QY of about 134 % only at an excitation at 250 nm corresponding to an energy of 2.28 $\times E_{1exc}$.

Reported observations of MEG in colloidal semiconductor nanostructures have often been controversial. That is essentially because as the MEG process is not directly observed, measurements are subject to artefacts, such as photo-charging effects leading to other Auger recombination process (trion-related) [20]. In addition, experimentalists have to decrease the excitation fluence substantially to avoid direct generation of multiple excitons via multiphoton absorption. In perovskite NPLs however, the strong dependence of the AR rate on the average inter-exciton distance due to the limited exciton delocalization length allows us to unambiguously rule out the possibility that the short ps component could result from a too high excitation fluence: even if the low excitation fluencies used here can still generate more than one exciton per NPL (following the Poisson distribution), the resulting Auger recombination rate will be on the order of several hundreds of picoseconds (diffusion-limited AR, see above **part 4.4**). On the contrary, multiple excitons photogenerated from a *single* high energy photon will be spatially very close, resulting in a fast, in the diffusion-less AR rate, in the picosecond

time range (**Figure 4.16**). This is similar to what was measured for high excitation fluence in the visible, when the coherent exciton delocalization area overlap (> 25 µJ/cm^2). Auger recombination induced by MEG is a reaction of "*geminate*" biexciton formation (*i.e.* generated directly or indirectly from the same photon, depending on the mechanism [42]), while at high excitation density, the Auger process is due to recombination of excitons generated by the absorption of different photons. For nanostructures with highly delocalized center-of-mass motion wavefunction, no clear distinction can be made between the two different origins of the Auger recombination. Here, the limited exciton delocalization length in the 2D plane of the perovskite NPLs and their highly anisotropic shape allows to isolate the contribution of MEG-induced Auger by its characteristic decay rate. Finally, we can notice that the measured threshold for MEG in n=3 NPLs is well above the theoretical limit $2\times E_{1exc}$. This can explain why no observation of biexciton generation could be observed in the n=2 NPL samples with larger confinement effects.

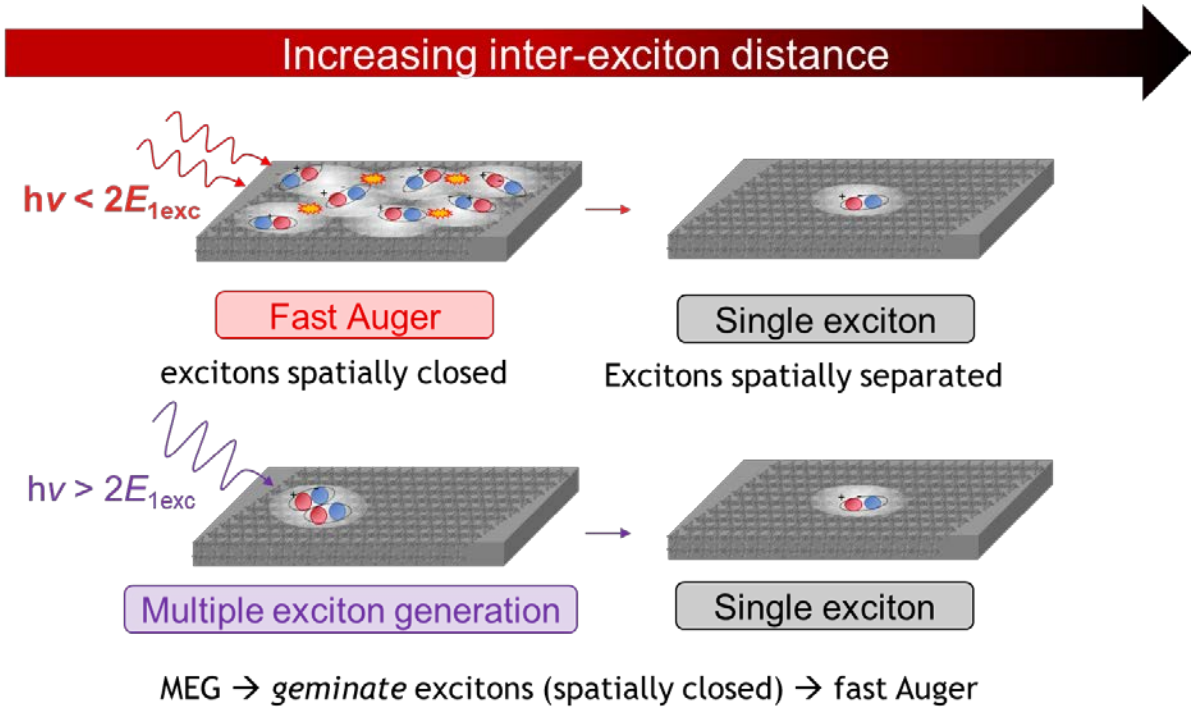

Figure 4.16 *Schematics of the exciton recombination processes at high exciton density where the excitons are spatially closed. After the MEG, the excitons are also generated close*

to each other (geminate excitons) even at low carrier density. In both cases, the intrinsic recombination time is below 10 ps (reaction-limited Auger).

ANNEXE 4

Calculation of the exciton density

The excitation fluence is:

$$J = \frac{E_{pulse}}{\Sigma_{laser}}$$

where E_{pulse} is the pump energy per pulse, and $\Sigma_{laser} = \pi(\omega_0)^2$ is the section of the pump laser beam with a beam waist ω_0 at the focus position for the different wavelength. (Σ_{laser} = 7.85x10^{-5} cm^2 for TCSPC and Σ_{laser} = 1.08 x10^{-3} cm^2 for TA).

We have $E_{pulse} = P_0/RR$ with RR, the pump repetition rate (200 kHz for TCSPC and 1.5 KHz for TA) and P_0, the average power of the pump beam corresponding to per-pulse energy fluence (J) in μJ/cm^2. To calculate the average photo-generated excitons per nanocrystal (<N>) the following expression is used.

$$\langle N \rangle = j\sigma_{abs}$$

There, the photon fluence per pulse (j) expressed in photons/cm^2 is calculate dividing the J (μJ/cm^2) by the excitation energy per one photon in μJ. The σ_{abs} at specific wavelength in cm^2 was estimated as follows.

Absorption cross-section

The absorption cross-section (σ_{abs}) at 400 nm was estimated using previous reports of σ_{abs} for colloidal NCs $FAPbI_3$ [7] and $CsPbI_3$ [43]. This was based on the consideration of the size-independent σ_{abs} at higher energies where the NCs behave as a bulk material [44]. Additionally, the linear absorption coefficient (μ_{abs}) for $MAPbI_3$ 2D perovskite thin films was used to estimate the μ_{abs} for *n=2* and *n=3* MAPI NPLs [9]. There, the calculation of the nanoparticle volume is needed using the nanoparticle dimension extracted using TEM images for the case MAPI 2D NPLs.

Table A4.1. Absorption cross-section estimations for the different samples.

NPLs	V (nm^3)	μ_{abs} (cm^{-1})	σ_{abs} (cm^2)	S (nm^2)	V (nm^3)	σ_{abs} (cm^2)
MAPI n=3		8.8×10^4 [9]	1.63×10^{-12}	15394	18472	1.92×10^{-11}
MAPI n=2		7.5×10^4 [9]	2.14×10^{-13}	2376	2851	3.34×10^{-13}
FAPI	2197 [7]		5.20×10^{-13} [7]	45239	54286	1.28×10^{-11}
CsPI	1405 [43]		5.60×10^{-13} [43]	6120	7344	2.04×10^{-12}

***[references]**

To account for the carrier-carrier interactions in 1D confined systems, we need to consider the exciton density ñ = <N>/S in cm^{-2}, where S the section of the NPLs. This points out the importance of comparing exciton density $\tilde{n}$ instead of N in the case of the colloidal 2D materials.

Table A4.2. Exciton density for TCSPC experiments in MAPI n=3 NPLs

P (µW)	J (µJ/cm^2)	j (#photons/cm^2)	<N> (#excitons)	ñ (cm^{-2})
227	0.037	2.91×10^{13}	56	3.63×10^{11}
74.2	0.11	9.50×10^{12}	18	1.19×10^{11}
30.4	0.73	3.89×10^{12}	7	4.86×10^{10}
11.01	2.02	1.41×10^{12}	2	1.76×10^{10}
1.66	4.94	2.13×10^{11}	0.4	2.66×10^{9}
0.56	15.11	7.17×10^{10}	0.1	8.96×10^{9}

Table A43. Exciton density for TA experiments in MAPI n=3 NPLs

P (µW)	J (µJ/cm^2)	j (photons/cm^2)	<N> (#excitons)	ñ (cm^{-2})
1	25	1.92×10^{12}	2	1.52×10^{10}
2	7.0	3.85×10^{12}	4	3.03×10^{10}
4	2.5	3.85×10^{12}	9	6.06×10^{10}
12	1.3	2.31×10^{13}	28	1.82×10^{11}
40	0.6	7.70×10^{13}	93	6.06×10^{11}

Time-resolved photo-luminescence (TR-PL) data analysis

Table A4.4-7. Fit parameters for a triexponential decay of the photoluminescence at different excitation fluence for the different samples (1) MAPI n=3 NPLs, (2) MAPI n=2 NPLs, (3) FAPI n=2 NPLs and (4) CsPI n=2 NPLs.

4. MAPI n=3 NPLs

J ($\mu J/cm^2$)	ñ (cm^{-2})	A_1	τ_1 (ps)	A_2	τ_2 (ns)	A_3	τ_3 (ns)
0.037	8.96×10^8			4 ± 2	3.4 ± 0.3	2 ± 2	11 ± 7
0.11	2.66×10^9			4.4 ± 0.7	2.5 ± 0.4	14.6 ± 0.8	10.8 ± 0.5
0.73	1.76×10^{10}			33.2 ± 0.7	1.54 ±0.06	93.3 ± 0.8	10.5 ± 0.1
2.02	4.86×10^{10}	120 ± 3	365 ± 17	114 ± 3	1.91 ± 0.06	213.0 ± 0.6	[10.4 ± 1] *
4.94	1.19×10^{11}	374 ± 6	244 ± 9	232 ± 5	1.78 ± 0.05	387 ± 1	[10.4 ± 1] *
15.11	3.63×10^{11}	820 ± 40	50 ± 2	326 ± 3	1.42 ± 0.02	543 ± 1	[10.4 ± 1] *

***[fixed values]**

5. MAPI n=2 NPLs

J ($\mu J/cm^2$)	ñ (cm^{-2})	A_1	τ_1 (ps)	A_2	τ_2 (ps)	A_3	τ_3 (ns)
0.038	1.03×10^9			60 ± 2	870 ± 52	57 ± 2	6.5 ± 0.2
0.115	3.13×10^9			128 ± 2	675 ± 19	99 ± 1	6.05 ± 0.08
0.777	2.10×10^{10}	208 ± 5	191 ± 8	184 ± 5	952 ± 23	114.7 ± 0.9	6.05 ± 0.05
2.28	6.16×10^{10}	467 ± 6	95 ± 3	320 ± 4	704 ± 10	120.7 ± 0.8	[6.05 ± 0.05] *
5.79	1.57×10^{11}	640 ± 11	128 ± 5	281 ± 9	840 ± 28	122 ± 1	[6.05 ± 0.05] *
17.4	4.72×10^{11}	1034 ± 25	60 ± 2	412 ± 9	552 ± 12	152 ± 1	[6.05 ± 0.05] *

***[fixed values]**

6. FAPI n=2 NPLs

J ($\mu J/cm^2$)	ñ (cm^{-2})	A_1	τ_1 (ps)	α_2	A_2 (ps)	A_3	τ_3 (ns)
0.041	2.36×10^9					158.5 ± 0.5	2.62 ± 0.01
0.109	6.25×10^9			109 ± 3	970 ± 41	126 ± 4	3.74 ± 0.07
0.661	3.77×10^{10}			157 ± 1	847 ± 10	144 ± 1	3.39 ± 0.02
1.98	1.13×10^{11}	248 ± 5	81 ± 3	317 ± 2	676 ± 6	139.7 ± 0.5	[3.5 ± 1] *
4.98	2.84×10^{11}	775 ± 14	67 ± 2	609 ± 6	571 ± 6	209 ± 1	[3.5 ± 1] *
14.87	8.51×10^{12}	1566 ± 25	59 ± 1	876 ± 8	520 ± 6	344 ± 2	[3.5 ± 1] *

*[fixed values]

7. CsPI n=2 NPLs

J (μJ/cm^2)	ñ (cm^{-2})	A_1	τ_1 (ps)	A_2	τ_2 (ps)	A_3	τ_3 (ns)
0.043	2.90 ×10^9			55 ± 1	729 ± 34	63.5 ± 0.6	5.9 ± 0.7
0.108	7.25 ×10^9			191 ± 2	667 ± 18	153.3 ± 0.8	6.0 ± 0.8
0.706	4.73 ×10^{10}			636 ± 3	537 ± 4	258.8 ± 0.9	5.9 ± 0.1
1.94	1.30 ×10^{11}	922 ± 11	122 ± 6	645 ± 8	787 ± 42	246 ± 1	[5.9 ± 1] *
5.00	3.35 ×10^{11}	1044 ± 20	93 ± 3	582 ± 19	684 ± 12	156 ± 1	[5.9 ± 1] *
15.02	1.01 ×10^{12}	1276 ± 21	57 ± 2	423 ± 8	526 ± 11	253 ± 3	[5.9 ± 1] *

*[fixed values]

Excitation density experiment at band-edge excitation (Auger) using TA.

Table A4.8-11. Fit parameters for a triexponential decay of the **PIB** at different excitation density for (a) MAPI n=3 NPLs, (b) MAPI n=2 NPLs, (c) FAPI n=2 NPLs and (d) CsPI n=2 NPLs.

8. MAPI n=3 NPLs

J (μJ/cm^2)	ñ (cm^{-2})	A_1	τ_1 (ps)	A_2	τ_2 (ps)	A_3	τ_3 (ns)
25	2.15×10^{12}	0.41 ± 0.03	11 ± 1	0.30 ± 0.02	126 ± 24	0.25 ± 0.02	5 ± 1
7.0	6.44×10^{11}	0.28 ± 0.03	8 ± 2	0.10 ± 0.02	95 ± 13	0.29 ± 0.07	9 ± 24
2.5	2.15×10^{11}	0.18 ± 0.09	35 ± 14	0.40 ± 0.08	155 ± 43	0.35 ± 0.02	5 ± 1
1.3	1.07×10^{11}			0.55 ± 0.01	259 ± 20	0.23 ± 0.01	4.5 ± 0.3
0.6	5.37×10^{10}					0.82 ± 0.03	11 ± 1

9. MAPI n=2 NPLs

J (μJ/cm^2)	ñ (cm^{-2})	A_1	τ_1 (ps)	A_2	τ_2 (ps)	A_3	τ_3 (ns)
3.6	1.80×10^{11}	6 ± 2	21 ± 9	4 ± 2	141 ± 13	5.6 ± 0.5	[6.0 ± 1.5] *
0.7	3.10×10^{10}			0.12 ± 0.01	171 ± 64	0.50 ± 0.01	[6.0 ± 1.5] *

*[fixed values]

10. FAPI n=2 NPLs

J (μJ/cm^2)	ñ (cm^{-2})	A_1	τ_1 (ps)	A_2	τ_2 (ps)	A_3	τ_3 (ns)
3.6	5.68×10^{11}	25 ± 2	9 ± 1	25 ± 1	106 ± 11	10.8 ± 0.4	[3.9 ± 0.5] *
0.7	1.14×10^{10}			0.41 ± 0.07	198 ± 1	1.71 ± 0.08	[3.9 ± 0.5] *

***[fixed values]**

11. CsPI n=2 NPLs

J (μJ/cm^2)	ñ (cm^{-2})	A_1	τ_1 (ps)	A_2	τ_2 (ps)	A_3	τ_3 (ns)
59	1.90×10^{13}	14.8 ± 0.4	8.42 ± 1	7.8 ± 0.4	316 ± 50	1.4 ± 0.3	[6 ± 1] *
0.8	2.44×10^{11}	0.31 ± 0.02	0.52 ± 0.09	0.29 ± 0.01	328 ± 42	0.32 ± 0.01	[6 ± 1] *

***[fixed values]**

Excitation energy experiment (MEG) using TA.

Table A4.11-14. Fit parameters for a triexponential decay of the averaged **PIB** at different excitation density for (a) MAPI n=3 NPLs, (b) MAPI n=2 NPLs, (c) FAPI n=2 NPLs

12. MAPI n=3 NPLs

λ (nm)	A_1	τ_1 (ps)	A_2	τ_2 (ps)	A_3	τ_3 (ns)
250	0.26 ± 0.02	5 ± 1	0.26 ± 0.01	160 ± 27	0.41 ± 0.01	[9.5 ± 0.5] *
270	0.24 ± 0.03	3 ± 7	0.27 ± 0.05	295 ± 137	0.48 ± 0.06	[9.5 ± 0.5] *
280			0.17 ± 0.02	114 ± 30	0.72 ± 0.01	[9.5 ± 0.5] *
290					0.63 ± 0.07	[9.5 ± 0.5] *

***[fixed values]**

13. MAPI n=2 NPLs

λ (nm)	A_1	τ_1 (ps)	A_2	τ_2 (ns)
250	0.22 ± 0.05	1.3 ± 0.8	0.77 ± 0.01	3.4 ± 0.5

310	0.41 ± 0.05	0.9 ± 0.3	0.59 ± 0.01	1.3 ± 0.1

14. FAPI n=2 NPLs

λ (nm)	**A_1**	**τ_1 (ps)**	**A_2**	**τ_2 (ns)**
250	0.10 ± 0.08	166 ± 7	0.64 ± 0.07	3.5 ± 0.3
310	0.26 ± 0.05	1.6 ± 0.9	0.67 ± 0.01	1.1 ± 0.1

Solvent effect in MAPI n=2 NPLs.

Table A4.15. Fit parameters for a triexponential decay of the **PIB** at different excitation density for MAPI n=2 NPLs.

J (μJ/cm^2)	**A_1**	**τ_1 (fs)**	**A_2**	**τ_2 (ps)**	**A_3**	**τ_3 (ps)**
0.8 (Tol)	0.56 ± 0.05	714 ± 225	0.36 ± 0.08	63 ± 20	0.10 ± 0.09	389 ± 29
0.8 ($CHCl_3$)	0.55 ± 0.09	684 ± 319	0.07 ± 0.01	55 ± 86	0.43 ± 0.06	909 ± 318

REFERENCES

[1] Y. Fu, H. Zhu, J. Chen, M.P. Hautzinger, X.Y. Zhu, S. Jin, Metal halide perovskite nanostructures for optoelectronic applications and the study of physical properties, Nat. Rev. Mater. 4 (2019) 169–188. https://doi.org/10.1038/s41578-019-0080-9.

[2] C. She, I. Fedin, D.S. Dolzhnikov, A. Demortière, R.D. Schaller, M. Pelton, D. V. Talapin, Low-threshold stimulated emission using colloidal quantum wells., Nano Lett. 14 (2014) 2772–7. https://doi.org/10.1021/nl500775p.

[3] V.I. Klimov, Multicarrier Interactions in Semiconductor Nanocrystals in Relation to the Phenomena of Auger Recombination and Carrier Multiplication, Annu. Rev. Condens. Matter Phys. 5 (2014) 285–316. https://doi.org/10.1146/annurev-conmatphys-031113-133900.

[4] V.I. Klimov, Spectral and Dynamical Properties of Multiexcitons in Semiconductor Nanocrystals, Annu. Rev. Phys. Chem. 58 (2007) 635–673. https://doi.org/10.1146/annurev.physchem.58.032806.104537.

[5] N.S. Makarov, S. Guo, O. Isaienko, W. Liu, I. Robel, V.I. Klimov, Spectral and Dynamical Properties of Single Excitons, Biexcitons, and Trions in Cesium–Lead-Halide Perovskite Quantum Dots, Nano Lett. 16 (2016) 2349–2362. https://doi.org/10.1021/acs.nanolett.5b05077.

[6] J.A. Castañeda, G. Nagamine, E. Yassitepe, L.G. Bonato, O. Voznyy, S. Hoogland, A.F. Nogueira, E.H. Sargent, C.H.B. Cruz, L.A. Padilha, Efficient Biexciton Interaction in Perovskite Quantum Dots under Weak and Strong Confinement, ACS Nano. 10 (2016) 8603–8609. https://doi.org/10.1021/acsnano.6b03908.

[7] H.-H. Fang, L. Protesescu, D.M. Balazs, S. Adjokatse, M. V. Kovalenko, M.A. Loi, Exciton Recombination in Formamidinium Lead Triiodide: Nanocrystals versus Thin Films, Small. 13 (2017) 1700673. https://doi.org/10.1002/smll.201700673.

[8] G. Delport, G. Chehade, F. Lédeé, H. Diab, C. Milesi-Brault, G. Trippé-Allard, J. Even, J.S. Lauret, E. Deleporte, D. Garrot, Exciton-exciton annihilation in two-dimensional halide perovskites at room temperature, J. Phys. Chem. Lett. 10 (2019) 5153–5159. https://doi.org/10.1021/acs.jpclett.9b01595.

[9] S. Deng, E. Shi, L. Yuan, L. Jin, L. Dou, L. Huang, Long-range exciton transport and slow annihilation in two-dimensional hybrid perovskites, Nat. Commun. 11

(2020) 1–8. https://doi.org/10.1038/s41467-020-14403-z.

[10] Q. Li, Y. Yang, W. Que, T. Lian, Size- and Morphology-Dependent Auger Recombination in CsPbBr 3 Perovskite Two-Dimensional Nanoplatelets and One-Dimensional Nanorods, Nano Lett. 19 (2019) 5620–5627. https://doi.org/10.1021/acs.nanolett.9b02145.

[11] B.R.C. Vale, E. Socie, A. Burgos-Caminal, J. Bettini, M.A. Schiavon, J.E. Moser, Exciton, Biexciton, and Hot Exciton Dynamics in CsPbBr3 Colloidal Nanoplatelets, J. Phys. Chem. Lett. 11 (2020) 387–394. https://doi.org/10.1021/acs.jpclett.9b03282.

[12] M. Cong, B. Yang, J. Chen, F. Hong, S. Yang, W. Deng, K. Han, Carrier Multiplication and Hot-Carrier Cooling Dynamics in Quantum-Confined CsPbI3 Perovskite Nanocrystals, J. Phys. Chem. Lett. 11 (2020) 1921–1926. https://doi.org/10.1021/acs.jpclett.0c00188.

[13] I. Pelant, J. Valenta, Luminescence Spectroscopy of Semiconductors, Oxford University Press, Oxford, 2012. https://doi.org/10.1093/acprof:oso/9780199588336.001.0001.

[14] V.I. Klimov, Nanocrystal Quantum dots -2nd edition, 2010. https://doi.org/10.1017/CBO9781107415324.004.

[15] V.I. Klimov, J.A. McGuire, R.D. Schaller, V.I. Rupasov, Scaling of multiexciton lifetimes in semiconductor nanocrystals, Phys. Rev. B - Condens. Matter Mater. Phys. 77 (2008) 195324. https://doi.org/10.1103/PhysRevB.77.195324.

[16] Q. Li, T. Lian, Exciton Spatial Coherence and Optical Gain in Colloidal Two-Dimensional Cadmium Chalcogenide Nanoplatelets, Acc. Chem. Res. 52 (2019) 2684–2693. https://doi.org/10.1021/acs.accounts.9b00252.

[17] M. Li, R. Begum, J. Fu, Q. Xu, T.M. Koh, S.A. Veldhuis, M. Grätzel, N. Mathews, S. Mhaisalkar, T.C. Sum, Low threshold and efficient multiple exciton generation in halide perovskite nanocrystals, Nat. Commun. 9 (2018) 637553. https://doi.org/10.1038/s41467-018-06596-1.

[18] C. de Weerd, L. Gomez, A. Capretti, D.M. Lebrun, E. Matsubara, J. Lin, M. Ashida, F.C.M. Spoor, L.D.A. Siebbeles, A.J. Houtepen, K. Suenaga, Y. Fujiwara, T. Gregorkiewicz, Efficient carrier multiplication in CsPbI3 perovskite nanocrystals, Nat. Commun. 9 (2018) 1–9. https://doi.org/10.1038/s41467-018-06721-0.

[19] C. Smith, D. Binks, Multiple Exciton Generation in Colloidal Nanocrystals, Nanomaterials. 4 (2013) 19–45. https://doi.org/10.3390/nano4010019.

[20] V.I. Klimov, Multicarrier Interactions in Semiconductor Nanocrystals in Relation to the Phenomena of Auger Recombination and Carrier Multiplication, Annu. Rev. Condens. Matter Phys. 5 (2014) 285–316. https://doi.org/10.1146/annurev-conmatphys-031113-133900.

[21] M.C. Weidman, M. Seitz, S.D. Stranks, W.A. Tisdale, Highly Tunable Colloidal Perovskite Nanoplatelets through Variable Cation, Metal, and Halide Composition, ACS Nano. 10 (2016) 7830–7839. https://doi.org/10.1021/acsnano.6b03496.

[22] V.A. Hintermayr, L. Polavarapu, A.S. Urban, J. Feldmann, Accelerated Carrier Relaxation through Reduced Coulomb Screening in Two-Dimensional Halide Perovskite Nanoplatelets, ACS Nano. 12 (2018) 10151–10158. https://doi.org/10.1021/acsnano.8b05029.

[23] I. Levchuk, A. Osvet, X. Tang, M. Brandl, J.D. Perea, F. Hoegl, G.J. Matt, R. Hock, M. Batentschuk, C.J. Brabec, H. Perovskite, F.X. Cl, I.C. Nanocrystals, I. Levchuk, A. Osvet, X. Tang, M. Brandl, J. Dar, F. Hoegl, G.J. Matt, R. Hock, M. Batentschuk, C.J. Brabec, Brightly Luminescent and Color-Tunable Formamidinium Lead Halide Perovskite FAPbX 3 (X = Cl, Br, I) Colloidal Nanocrystals, Nano Lett. 17 (2017) 2765–2770. https://doi.org/10.1021/acs.nanolett.6b04781.

[24] G.E. Eperon, S.D. Stranks, C. Menelaou, M.B. Johnston, L.M. Herz, H.J. Snaith, Formamidinium lead trihalide: A broadly tunable perovskite for efficient planar heterojunction solar cells, Energy Environ. Sci. 7 (2014) 982–988. https://doi.org/10.1039/c3ee43822h.

[25] E. Baghani, S.K. Oleary, I. Fedin, D. V. Talapin, M. Pelton, Auger-limited carrier recombination and relaxation in CdSe colloidal quantum wells, J. Phys. Chem. Lett. 6 (2015) 1032–1036. https://doi.org/10.1021/acs.jpclett.5b00143.

[26] M.B. Johnston, L.M. Herz, Hybrid Perovskites for Photovoltaics: Charge-Carrier Recombination, Diffusion, and Radiative Efficiencies, Acc. Chem. Res. 49 (2016) 146–154. https://doi.org/10.1021/acs.accounts.5b00411.

[27] N.S. Makarov, S. Guo, O. Isaienko, W. Liu, I. Robel, V.I. Klimov, Spectral and Dynamical Properties of Single Excitons, Biexcitons, and Trions in Cesium-Lead-Halide Perovskite Quantum Dots, Nano Lett. 16 (2016) 2349–2362.

https://doi.org/10.1021/acs.nanolett.5b05077.

[28] G.E. Eperon, E. Jedlicka, D.S. Ginger, Biexciton Auger Recombination Differs in Hybrid and Inorganic Halide Perovskite Quantum Dots, J. Phys. Chem. Lett. 9 (2018) 104–109. https://doi.org/10.1021/acs.jpclett.7b02805.

[29] V.I. Klimov, Optical Nonlinearities and Ultrafast Carrier Dynamics in Semiconductor Nanocrystals, J. Phys. Chem. B. 104 (2002) 6112–6123. https://doi.org/10.1021/jp9944132.

[30] G.A. Narvaez, G. Bester, A. Franceschetti, A. Zunger, Excitonic exchange effects on the radiative decay time of monoexcitons and biexcitons in quantum dots, Phys. Rev. B - Condens. Matter Mater. Phys. 74 (2006) 205422. https://doi.org/10.1103/PhysRevB.74.205422.

[31] D.J. Binks, Multiple exciton generation in nanocrystal quantum dots - Controversy, current status and future prospects, Phys. Chem. Chem. Phys. 13 (2011) 12693–12704. https://doi.org/10.1039/c1cp20225a.

[32] J.R. Lakowicz, Principles of fluorescence spectroscopy, Springer, 2006.

[33] M. Kirm, V. Nagirnyi, E. Feldbach, M. De Grazia, B. Carré, H. Merdji, S. Guizard, G. Geoffroy, J. Gaudin, N. Fedorov, P. Martin, A. Vasil'Ev, A. Belsky, Exciton-exciton interactions in CdWO4 irradiated by intense femtosecond vacuum ultraviolet pulses, Phys. Rev. B - Condens. Matter Mater. Phys. 79 (2009) 233103. https://doi.org/10.1103/PhysRevB.79.233103.

[34] L.T. Kunneman, M.D. Tessier, H. Heuclin, B. Dubertret, Y. V. Aulin, F.C. Grozema, J.M. Schins, L.D.A. Siebbeles, Bimolecular auger recombination of electron-hole pairs in two-dimensional CdSe and CdSe/CdZnS core/shell nanoplatelets, J. Phys. Chem. Lett. 4 (2013) 3574–3578. https://doi.org/10.1021/jz401970p.

[35] L.M. Herz, Charge-Carrier Dynamics in Organic-Inorganic Metal Halide Perovskites, Annu. Rev. Phys. Chem. 67 (2016) 65–89. https://doi.org/10.1146/annurev-physchem-040215-112222.

[36] U. Gösele, Anisotropic diffusion, long-range energy transfer and bimolecular exciton recombination kinetics, Chem. Phys. Lett. 43 (1976) 61–64. https://doi.org/10.1016/0009-2614(76)80756-7.

[37] M. Burgel, D.A. Van; Wiersma, The ultrafast dynamics of aggregate excitons in

water, s.n., 1999. http://www.rug.nl/research/portal. (accessed July 16, 2020).

[38] K. Tanaka, T. Takahashi, T. Ban, T. Kondo, K. Uchida, N. Miura, Comparative study on the excitons in lead-halide-based perovskite-type crystals CH3NH3PbBr3 CH3NH 3PbI3, Solid State Commun. 127 (2003) 619–623. https://doi.org/10.1016/S0038-1098(03)00566-0.

[39] R.D. Schaller, V.M. Agranovich, V.I. Klimov, High-efficiency carrier multiplication through direct photogeneration of multi-excitons via virtual single-exciton states, Nat. Phys. 1 (2005) 189–194. https://doi.org/10.1038/nphys151.

[40] R.J. Ellingson, M.C. Beard, J.C. Johnson, P. Yu, O.I. Micic, A.J. Nozik, A. Shabaev, A.L. Efros, Highly efficient multiple exciton generation in colloidal PbSe and PbS quantum dots, Nano Lett. 5 (2005) 865–871. https://doi.org/10.1021/nl0502672.

[41] M. Aerts, T. Bielewicz, C. Klinke, F.C. Grozema, A.J. Houtepen, J.M. Schins, L.D.A. Siebbeles, Highly efficient carrier multiplication in PbS nanosheets, Nat. Commun. 5 (2014). https://doi.org/10.1038/ncomms4789.

[42] A. Shabaev, C.S. Hellberg, A.L. Efros, Efficiency of Multiexciton Generation in Colloidal Nanostructures, Acc. Chem. Res. 46 (2013) 1242–1251. https://doi.org/10.1021/ar300283j.

[43] J. Puthenpurayil, O.H.C. Cheng, T. Qiao, D. Rossi, D.H. Son, On the determination of absorption cross section of colloidal lead halide perovskite quantum dots, J. Chem. Phys. 151 (2019) 154706. https://doi.org/10.1063/1.5126039.

[44] J. Maes, L. Balcaen, E. Drijvers, Q. Zhao, J. De Roo, A. Vantomme, F. Vanhaecke, P. Geiregat, Z. Hens, Light Absorption Coefficient of CsPbBr3 Perovskite Nanocrystals, J. Phys. Chem. Lett. 9 (2018) 3093–3097. https://doi.org/10.1021/acs.jpclett.8b01065.

GENERAL CONCLUSION

This thesis is focused on the investigation of the ultrafast dynamics of excitons and charge carriers in colloidal perovskite nanostructures. In particular, time-resolved optical spectroscopies such as time-correlated single photon counting (TCSPC) and femtosecond transient absorption (fs-TA) were used to study the effect of the confinement and exciton density on the hot exciton relaxation (cooling) and multiexciton Auger recombination process in strongly confined 2D lead iodide perovskite nanoplatelets with different composition.

We found that, contrary to the expected intrinsic phonon bottleneck effect, the cooling process occurs very rapidly, in hundreds of femtoseconds, and is faster in the strongly confined 2D perovskite nanoplatelets compared to the weakly-confined perovskite nanocrystals. Moreover, the cooling rate is similar for the different compositions of nanoplatelets (hybrid versus fully-inorganic perovskite) at low and high excitation fluences. The absence of an *intrinsic* phonon bottleneck at low excitation fluence is attributed to an efficient cooling mechanism involving a coupling between the exciton and surface ligand vibrational modes. This behavior was evidenced by comparing the excitation fluence-dependent cooling times of colloidal nanoplatelets in solution with mobile surface ligands and in 2D layered perovskite thin film where the ligands between perovskite layers can be considered as “frozen”.

The multiple exciton recombination in the strongly-confined 2D nanoplatelets is dominated by non-radiative Auger recombination. Due to the large asymmetric geometry of the perovskite nanoplatelets and limited exciton wavefunction delocalization, the Auger recombination rate depends strongly on the excitation fluence. At low fluence, when the initial average inter-exciton distance is several tens of nanometers, the Auger recombination is limited by exciton diffusion and occurs on a timescale of several

hundreds of picoseconds. In contrast, high excitation fluence produces “overlapping” excitons resulting in recombination times of less than 10 ps. This fast rate can explain why no efficient lasing could be obtained in these 2D materials.

Finally, the exciton density dependence of the Auger recombination rate allows us to identify and isolate the multiexciton dynamics resulting from the multiple exciton generation process occurring at high photon energy excitation (in the ultraviolet range). For the first time, we reported the energy threshold of this multiple exciton generation in 2D perovskites nanoplatelets.

PERSPECTIVES

In spite of the rapid development and potential low fabrication cost of perovskite solar cells certain issues should be addressed including thermal stability, ambient (particularly moisture) degradation, toxicity of the components, and scalability of the processing techniques. These challenges require not only an important engineering approach but also a strong fundamental approach, as a complete understanding of the device mechanisms is essential to propose successful tools to solve the mentioned issues. From our point of view, the wet chemical methods to obtain directly both colloidal perovskite nanocrystals and 2D layered perovskites with different morphologies and compositions are advantageous for all technologies, particularly light emitting devices. The selection of the material is clearly driven by the device targeted. For instance, the selection of colloidal 3D NCs or 2D NPLs for LEDs applications can be driven by the color purity but also related with the excitonic properties and transport inside each individual nanostructure. While, the selection between 2D layered perovskite thin films versus the conventional bulk thin films for solar cells has been more related with the stability issues. However, over all of these fundamental and general considerations, we thought that for real

practical purposes (one of the strengths of perovskite materials) the future spectroscopical studies of the photo-induced dynamics in low dimensional perovskite should be addressed in thin films under conditions close to the particular device operation. This is not straight forward considering the thin film deposition techniques and the adaptation of the spectroscopical techniques needed to study the ultrafast phenomena. Specially, to study the non-conventional phenomena as hot carrier/exciton relaxation or MEG in confined systems. However, we emphasized for future experiments go beyond the observation of a particular phenomenon in the active material and/or layer but also the conditions under those phenomena are relevant for real devices.

In principle, we tried to take in account the working principles of each device in the selection of the material and the relevant parameters such as carrier lifetimes, diffusion lengths, and diffusion coefficients, defects or trap densities. Those can be deduced indirectly from the study of photophysical processes and their recombination constants using ultrafast spectroscopies as TR-PL or TA. However, to realize the potential of these perovskite materials, both basic material characterization and device optimization studies are needed to advance simultaneously in the fundamental photo-physics and optoelectronic properties of perovskites. Regarding our main technique, TA spectroscopy can provide considerable insights into the ground and excited-state dynamics. However, it is important not to overgeneralize their findings. The conditions in the device architectures are more complex than solutions or films, where the morphology, interfacial traps and band alignments can have a significant influence on the dynamics. One should avoid drawing conclusions based on ultrafast optical spectroscopy studies alone. They should be complemented with materials and device characterization to gain a complete picture. For instance, the charge carrier dynamics associated to phenomena occurring inside the active layer as the charge generation, transport and recombination can be affected by the presence of the perovskite/charge transport layer interface. Such

interfacial effects relevant for the charge extraction/injection should be study parallel to the application of low dimensional perovskite in halide perovskite tandem solar cells. To illustrate this, we recalled the fact that recombination constants in the surface and bulk regions of perovskite single crystals are different. Then, it should be interesting to do experiments comparing liquid colloidal NPLs solutions, thin films of NPLs and 2D layered perovskite, where crystalline domains can be found.

On the other side, the excitonic nature in low dimensional materials together with their versatile fabrication methods hold great promise for high-stability LEDs and potentially laser applications. The pronounced excitonic behavior also gives rise to significant quasi-particle interactions, such as exciton–phonon and exciton–photon interactions. These quasi-particle interactions have potential applications for white LEDs and polariton lasers, which would otherwise be very difficult to achieve using the 3D systems. Hybrid perovskite nanostructures are potential candidates for these applications. However, one possible drawback can be its charge transport within the perovskite due to the presence of insulating organic layers. In spite of this, the recently developed quasi-2D perovskite LEDs are now at the forefront of perovskite-based electroluminescent devices, and have the potential to lead not only to efficient but also to very stable optoelectronic devices. Then, both of the material used in this thesis CsPI n=2 and MAPI n=3 NPLs can be good candidates to test on LED devices.

While, in the case of laser applications, further understanding of the electronic structure of the perovskites in function of the composition and synthesis methods for optimization should be done. In order to observed the optical gain under direct electrical operation at levels where photo- and thermal-sensitive materials can maintain device functionality without degradation. The first reported value of the amplified stimulated emission in the lead halide perovskites required predominant population of free carriers at carrier density around 10^{18} cm^{-3}. Also, although the non-radiative Auger loss can be modest at low

excitation levels, which is typically used in the LED devices, it affects the performance of devices under higher level injections and is aggravated further when the carrier injection is imbalanced due to the imperfect transport layers and interfaces. At even higher densities (~10^{19} cm^{-3}), which may be required for high-power laser operation whether optically or electrically pumped, the carrier dynamics enter a regime where added competition between bimolecular recombination and Auger process will occur. One possibility is to use cesium lead halide–based perovskite NCs with their larger bandgap and lower dielectric constant, where excitonic gain has been speculated to be the origin of the stimulated emission, given the observed excitons at room temperature. Then, further studies of optical gain can be carried out on the CsPI NPLs.

université PARIS-SACLAY

ÉCOLE DOCTORALE
Sciences Chimiques : Molécules, Matériaux, Instrumentation et Biosystèmes (2MIB)

Titre : Etude par spectroscopies optiques résolues en temps des dynamiques ultrarapides des excitons et porteurs de charge dans les nanostructures colloïdales de pérovskite

Mots clés : nanostructures de pérovskite colloïdales, spectroscopie optique femtoseconde, dynamiques des porteurs de charge & excitons

Résumé : Les matériaux semiconducteurs de pérovskite halogénée se sont révélés très prometteurs en raison de leurs propriétés exceptionnelles. Cette thèse porte sur la relaxation des porteurs de charge/excitons « chauds » et la recombinaison Auger advenant après une excitation de forte puissance ou à haute énergie. La spectroscopie de fluorescence résolue en temps et d'absorption transitoire (AT) femtoseconde sont utilisées afin d'étudier les effets du confinement et de la composition sur ces processus, en particulier dans les nanoplaquettes (NPLs) colloïdales de pérovskite bidimensionnelles (2D). Les dynamiques de relaxation ont été étudiées en utilisant une méthode d'analyse globale afin de décrire la relaxation dans les nanostructures de $FAPbI_3$ (FA= formamidinium) faiblement confinées et dans les NPLs 2D à fort confinement quantique et diélectrique. La nature des cations internes (FA, MA=méthylammonium ou Cs) n'influe pas ce taux, ni son evolution en puissance.

Ensuite, les recombinaisons multi-excitoniques dominées par la RA non radiative ont été étudiées dans les NPLs de pérovskite 2D fortement confinées. En revanche, une puissance d'excitation élevée produit des excitons dont les fonctions d'onde se recouvrent spatialement, entraînant des temps de RA inférieurs à 10 ps. Finalement, les dynamiques excitoniques dans les NPLs 2D ont été mesurées par AT après excitation dans l'ultraviolet afin d'observer le processus de multiplication d'excitons. Ce dernier implique la génération de plusieurs excitons "géminés", et donc proches spatiallement, suite à l'absorption d'un unique photon de haute énergie.

Title: Ultrafast dynamics of excitons and charge carriers in colloidal perovskite nanostructures studied by time-resolved optical spectroscopies

Keywords: colloidal perovskite nanostructures, femtosecond optical spectroscopy, charge carrier/exciton dynamics

Abstract: Halide perovskites have emerged as very promising photoactive materials due to their outstanding optoelectronic properties combined with low-cost processability. This thesis focuses on the study of two major fundamental processes occurring in colloidal halide perovskite nanostructures: the hot charge carrier/exciton relaxation ("cooling"), after excitation above the optical bandgap, and the non-radiative Auger recombination, taking place after high-fluence or high-photon energy excitation. In particular, time-resolved photoluminescence and femtosecond transient absorption spectroscopy were used to investigate the confinement and composition effects in strongly confined two-dimensional (2D) lead iodide perovskite nanoplatelets (NPLs). For the investigation of the cooling dynamics, a global analysis method based on single value decomposition was used to effectively describe the relaxation in weakly-confined $FAPbI_3$ nanoplates (FA=formamidinium) and strongly confined 2D NPLs. The cooling rate was found independent of the nature of the internal cations (FA, MA=methylammonium and Cs=cesium) and the expected *intrinsic* phonon bottleneck was not observed. Finally, the strong dependence of the AR with the inter-exciton distance allows the identification of multiple exciton generation (MEG), which involves the reaction of "geminate biexcitons" produced by the absorption of a single high-energy photon in the UV region.

Université Paris-Saclay
Espace Technologique / Immeuble Discovery
Route de l'Orme aux Merisiers RD 128 / 91190 Saint-Aubin, France